AC Susceptibility Study of Amorphous $(Fe_{1-x}Mn_x)_{75}P_{16}B_6Al_3$ Alloys

by

Anita Berndt

A thesis
submitted to the Faculty of Graduate Studies
in partial fullfillment of the requirements
for the degree of

Master of Science

Department of Physics
University of Manitoba
Winnipeg, Manitoba

ISBN 0-612-12983-7

Canada

Name Anita Glenda Berndt

Dissertation Abstracts International is arranged by broad, general subject categories. Please select the one subject which most nearly describes the content of your dissertation. Enter the corresponding four-digit code in the spaces provided.

Physics Solid State

SUBJECT TERM

0611

SUBJECT CODE

U·M·I

Subject Categories

THE HUMANITIES AND SOCIAL SCIENCES

COMMUNICATIONS AND THE ARTS

Architecture 0729
Art History 0377
Cinema 0900
Dance 0378
Fine Arts 0357
Information Science 0723
Journalism 0391
Library Science 0399
Mass Communications 0708
Music 0413
Speech Communication 0459
Theater 0465

EDUCATION

General 0515
Administration 0514
Adult and Continuing 0516
Agricultural 0517
Art 0273
Bilingual and Multicultural 0282
Business 0688
Community College 0275
Curriculum and Instruction 0727
Early Childhood 0518
Elementary 0524
Finance 0277
Guidance and Counseling 0519
Health 0680
Higher 0745
History of 0520
Home Economics 0278
Industrial 0521
Language and Literature 0279
Mathematics 0280
Music 0522
Philosophy of 0998
Physical 0523
Psychology 0525
Reading 0535
Religious 0527
Sciences 0714
Secondary 0533
Social Sciences 0534
Sociology of 0340
Special 0529
Teacher Training 0530
Technology 0710
Tests and Measurements 0288
Vocational 0747

LANGUAGE, LITERATURE AND LINGUISTICS

Language
- General 0679
- Ancient 0289
- Linguistics 0290
- Modern 0291

Literature
- General 0401
- Classical 0294
- Comparative 0295
- Medieval 0297
- Modern 0298
- African 0316
- American 0591
- Asian 0305
- Canadian (English) 0352
- Canadian (French) 0355
- English 0593
- Germanic 0311
- Latin American 0312
- Middle Eastern 0315
- Romance 0313
- Slavic and East European 0314

PHILOSOPHY, RELIGION AND THEOLOGY

Philosophy 0422
Religion
- General 0318
- Biblical Studies 0321
- Clergy 0319
- History of 0320
- Philosophy of 0322

Theology 0469

SOCIAL SCIENCES

American Studies 0323
Anthropology
- Archaeology 0324
- Cultural 0326
- Physical 0327

Business Administration
- General 0310
- Accounting 0272
- Banking 0770
- Management 0454
- Marketing 0338

Canadian Studies 0385
Economics
- General 0501
- Agricultural 0503
- Commerce-Business 0505
- Finance 0508
- History 0509
- Labor 0510
- Theory 0511

Folklore 0358
Geography 0366
Gerontology 0351
History
- General 0578
- Ancient 0579
- Medieval 0581
- Modern 0582
- Black 0328
- African 0331
- Asia, Australia and Oceania 0332
- Canadian 0334
- European 0335
- Latin American 0336
- Middle Eastern 0333
- United States 0337

History of Science 0585
Law 0398
Political Science
- General 0615
- International Law and Relations 0616
- Public Administration 0617

Recreation 0814
Social Work 0452
Sociology
- General 0626
- Criminology and Penology 0627
- Demography 0938
- Ethnic and Racial Studies 0631
- Individual and Family Studies 0628
- Industrial and Labor Relations 0629
- Public and Social Welfare 0630
- Social Structure and Development 0700
- Theory and Methods 0344

Transportation 0709
Urban and Regional Planning 0999
Women's Studies 0453

THE SCIENCES AND ENGINEERING

BIOLOGICAL SCIENCES

Agriculture
- General 0473
- Agronomy 0285
- Animal Culture and Nutrition 0475
- Animal Pathology 0476
- Food Science and Technology 0359
- Forestry and Wildlife 0478
- Plant Culture 0479
- Plant Pathology 0480
- Plant Physiology 0817
- Range Management 0777
- Wood Technology 0746

Biology
- General 0306
- Anatomy 0287
- Biostatistics 0308
- Botany 0309
- Cell 0379
- Ecology 0329
- Entomology 0353
- Genetics 0369
- Limnology 0793
- Microbiology 0410
- Molecular 0307
- Neuroscience 0317
- Oceanography 0416
- Physiology 0433
- Radiation 0821
- Veterinary Science 0778
- Zoology 0472

Biophysics
- General 0786
- Medical 0760

EARTH SCIENCES

Biogeochemistry 0425
Geochemistry 0996
Geodesy 0370
Geology 0372
Geophysics 0373
Hydrology 0388
Mineralogy 0411
Paleobotany 0345
Paleoecology 0426
Paleontology 0418
Paleozoology 0985
Palynology 0427
Physical Geography 0368
Physical Oceanography 0415

HEALTH AND ENVIRONMENTAL SCIENCES

Environmental Sciences 0768
Health Sciences
- General 0566
- Audiology 0300
- Chemotherapy 0992
- Dentistry 0567
- Education 0350
- Hospital Management 0769
- Human Development 0758
- Immunology 0982
- Medicine and Surgery 0564
- Mental Health 0347
- Nursing 0569
- Nutrition 0570
- Obstetrics and Gynecology 0380
- Occupational Health and Therapy 0354
- Ophthalmology 0381
- Pathology 0571
- Pharmacology 0419
- Pharmacy 0572
- Physical Therapy 0382
- Public Health 0573
- Radiology 0574
- Recreation 0575
- Speech Pathology 0460
- Toxicology 0383

Home Economics 0386

PHYSICAL SCIENCES

Pure Sciences

Chemistry
- General 0485
- Agricultural 0749
- Analytical 0486
- Biochemistry 0487
- Inorganic 0488
- Nuclear 0738
- Organic 0490
- Pharmaceutical 0491
- Physical 0494
- Polymer 0495
- Radiation 0754

Mathematics 0405
Physics
- General 0605
- Acoustics 0986
- Astronomy and Astrophysics 0606
- Atmospheric Science 0608
- Atomic 0748
- Electronics and Electricity 0607
- Elementary Particles and High Energy 0798
- Fluid and Plasma 0759
- Molecular 0609
- Nuclear 0610
- Optics 0752
- Radiation 0756
- Solid State 0611

Statistics 0463

Applied Sciences

Applied Mechanics 0346
Computer Science 0984
Engineering
- General 0537
- Aerospace 0538
- Agricultural 0539
- Automotive 0540
- Biomedical 0541
- Chemical 0542
- Civil 0543
- Electronics and Electrical 0544
- Heat and Thermodynamics 0348
- Hydraulic 0545
- Industrial 0546
- Marine 0547
- Materials Science 0794
- Mechanical 0548
- Metallurgy 0743
- Mining 0551
- Nuclear 0552
- Packaging 0549
- Petroleum 0765
- Sanitary and Municipal 0554
- System Science 0790

Geotechnology 0428
Operations Research 0796
Plastics Technology 0795
Textile Technology 0994

PSYCHOLOGY

General 0621
Behavioral 0384
Clinical 0622
Developmental 0620
Experimental 0623
Industrial 0624
Personality 0625
Physiological 0989
Psychobiology 0349
Psychometrics 0632
Social 0451

AC SUSCEPTIBILITY STUDY OF AMORPHOUS $(Fe_{1-x}Mn_x)_{75}P_{16}B_6Al_3$ ALLOYS

BY

ANITA BERNDT

A Thesis submitted to the Faculty of Graduate Studies of the University of Manitoba in partial fulfillment of the requirements of the degree of

MASTER OF SCIENCE

I hereby declare that I am the sole author of this thesis.

I authorize the University of Manitoba to other institutions or individuals for the purpose of scholarly research.

Anita Berndt

I further authorize the University of Manitoba to reproduce this thesis by photocopying or by other means, in total or in part at the request of other institutions or individuals for the purpose of scholarly research.

Anita Berndt

Abstract

A system described as 're-entrant' displays sequential magnetic phase transitions with a paramagnetic to ferromagnetic transition followed by a ferromagnetic to spin glass transition at lower temperatures. The zero field susceptibility for such a sample characteristically displays a sharp rise in the susceptibility as the paramagnetic to ferromagnetic transition is approached from above, which is followed by a plateau as the temperature is decreased, and finally a sharp drop in the susceptibility, which is often taken as marking the re-entrant phase boundary. As part of a detailed study of the 're-entrant' amorphous alloys $(Fe_{1-x}Mn_x)_{75}P_{16}B_6Al_3$ with $x = 0.235$, 0.26, 0.30, 0.32 and 0.41, the power law predictions of the scaling theory were used to analyze the field and temperature dependent a.c. susceptibility in the vicinity of the paramagnetic to ferromagnetic transition; critical temperatures were determined, along with the critical exponents δ, γ and the cross-over exponent, $\gamma + \beta$, which were found to have values consistent with the Heisenberg model predictions, with the influence of bond disorder evident away from the critical point. The lower candidate transition was investigated using both non-linear analysis (based on a mean field Ising model prediction that the coefficient of the leading field-dependent contribution to the susceptibility, $a_2(T)$, should diverge as the freezing temperature, T_f, is approached from below) and the interpretation of the low temperature features in terms of the Gabay-Toulouse (GT) and d'Almeida-Thouless (AT) lines predicted by the

mean field vector model. Both procedures failed to confirm the presence of a lower phase transition for the $x = 0.235$ and 0.26 samples, implying that the features observed in the zero field susceptibility must be a manifestation of other mechanisms, possibly thermally activated blocking processes. Likewise, the GT and AT analysis was unable to confirm the existence of a low temperature phase transition for the $x = 0.30$ and 0.32 samples; however, non-linear analysis, which is believed to be a more powerful technique at this time, revealed a distinct, but clearly non-divergent anomaly in the $a_2(T)$ versus temperature plots for the latter two concentrations, providing strong evidence, when considered along with previous neutron depolarization studies, that these two samples are indeed re-entrant. A modified magnetic phase diagram will be presented incorporating these new results.

Acknowledgements

I would like to express my appreciation to Dr. Gwyn Williams, my supervisor, whose suggestions and guidance greatly contributed to the success of this work. Special thanks also to Dr. Henry Kunkel, without whose valuable help this thesis would not have been possible. I would also like to thank Patricia Stampe and Scott King for their encouragement.

Finally, I would like to express my deepest graditude to my parents, and my husband, Marvin for their endless support and motivation. It is to them that I wish to dedicate my thesis.

Contents

Chapter 1

Introduction

The study of critical phenomena has provided insight into the behaviour of many physical systems in the vicinity of their phase transitions. Theories describing the properties of materials as they change from one equilibrium state to another have been developed to include liquid-gas, superconductor-normal, ferroelectric and magnetic transitions, amongst a host of others.

Of specific interest here are magnetic transitions, where the term 'critical phenomena' is applied to the thermodynamic behaviour of a system near its critical temperature undergoing a second order phase transition, or in some instances, a first order phase transition [1]. The study of critical phenomena has developed along two distinct branches, the first of which attempts to

[1] In Ehrenfest's classification scheme, the presence of a phase transition is characterized by a discontinuity in the n^{th} derivative of the Gibbs function, G where the order of the transition is taken to equal the smallest value of n for which the discontinuity appears. The transition from the paramagnetic to the ferromagnetic state represents a second order phase transition, in this sense, whereas the transition from the ferromagnetic to the antiferromagnetic state as in, for example, the rare earth intermetallic compound $Ce(Fe_{2-x}M_x)$ (Ali et al, 1992), where M is a transition metal substituted for Fe, represents a first order phase transition.

develop models describing in detail the interactions between magnetic moments. Using this approach, critical exponents describing the behaviour of thermodynamic properties of the system near its phase transition can be calculated. The appeal of using these critical exponents lies in the striking similarities that often exist between them for many physical systems, be they fluid, superconducting or magnetic, even though the systems may have interaction mechanisms/ranges or critical temperatures which are quite different.

This universality is investigated by a concept introduced in the mid 1960's, known as the static scaling hypothesis, which encompasses the second branch of the study of critical phenomena by exploring the relationship between the critical exponents rather than the exponents themselves. Since this aspect of the theory is model independent, its results can be applied to magnetic and non-magnetic systems alike. Furthermore, this hypothesis, also referred to as the homogeneous function approach provides valuable insights into possible forms for the magnetic equation of state.

In recent years, systems displaying 're-entrant' behaviour, i.e., having sequential phase transitions, have received considerable attention. This type of behaviour occurs in a sample, which over some composition range is paramagnetic (PM) at high temperatures, becomes ferromagnetic (FM) at T_c as the temperature is lowered (obeying the well established scaling relations described in Section 2.4), and then 're-enters' a (transverse) spin glass (SG)

phase at a freezing temperature, T_f, as the temperature continues to be decreased. The magnetic disorder in such systems, which is responsible for this type of behaviour, is characterized by the ratio, η, between the first and second moments of the exchange bond distribution, i.e. the mean, $\tilde{J}_o$ and width, $\tilde{J}$, which is used to model site disorder, thus $\eta = \tilde{J}_o/\tilde{J}$. According to the Sherrington-Kirkpatrick (SK) model, sequential phase transitions such as those just described occur for $1 \leq \eta \leq 1.5$, pure spin glass behaviour occurs for $\eta < 1$, and a single paramagnetic to ferromagnetic (PM-FM) phase transition takes place for $\eta > 1.5$. For alloys, η is often correlated to the magnetic impurity concentration.

The PM-FM transition is well understood; however, the nature of the potential FM-SG transition is the subject of on-going experimental and theoretical investigation and debate, as no universally agreed upon theory describing the characteristics of these interesting and unusual materials and the nature of their ground states has yet been found, although a number of theories have been proposed. An extension of the Sherrington and Kirkpatrick model (Sherrington et al, 1975), namely the vector spin models discussed in Chapter 2, suggest that the lower transition involves a transverse spin glass phase coexisting with longitudinal ferromagnetic order at a temperature, T_{GT} (Gabay et al, 1981), followed by a cross-over from weak to strong irreversibility at an even lower temperature, T_{AT} (de Almeida et al, 1978).

This type of behaviour was first proposed for AuFe (Coles et al, 1978),

probably first confirmed in PdFeMn (II Kunkel et al, 1988; Verbeck et al, 1978) and also observed in amorphous systems such as FeZr (Ma et al, 1991; Ryan et al, 1987; Kaul, 1987; Rhyne et al, 1988). Re-entrant behaviour is also believed to occur in systems with competing ferromagnetic and antiferromagnetic interactions (Mirebeau et al, 1990; Manheimer et al, 1983), such as those in $(Fe_{1-x}Mn_x)_{75}P_{16}B_6Al_3$ (henceforth referred to as FeMn). There is a great deal of motivation for considering the amorphous form of FeMn with some of the major reasons being as follows: (Salamon et al, 1980; Yeshurun et al, 1981)

(i) Amorphous systems are not subject to the compositional inhomogeneities, due to metallurgical constraints, often occurring in crystalline materials which can result in a magnetic response that 'mimics' that observed in true re-entrants systems, eg. NiMn (Kunkel et al, 1991). By manufacturing the samples using the melt spinning technique, which will be discussed in Chapter 4, the liquid state of the material is quenched in, thus preventing clustering or crystallization.

(ii) The samples can be prepared for any value of x without deviating from the amorphous phase in which the alloy exists.

(iii) Crystal-field and magnetocrystalline anisotropy effects are random in amorphous materials, and lattice imperfections or grain boundaries along which magnetic ions can precipitate, or domain wall pinning could occur, are absent.

(iv) Furthermore, it is believed by some researchers (Salamon et al, 1980; Yeshurun et al, 1981) that FeMn provides a physical realization of the bond-random model for a quenched magnetic system since the local moments of Fe and Mn have nearly the same spin.

The first three points listed above apply to any amorphous system, whereas (iv) may or may not be true for other materials, depending upon their composition.

Some discrepancies exist among the results published in the literature on the FeMn system, especially concerning the details of the supposed 're-entrant' spin glass phase. It is the purpose of this work to examine, in greater detail than has been done before, the nature of the ferromagnetic-spin glass 'transition', and attempt to determine whether or not FeMn is re-entrant over some composition range or whether the behaviour observed is due to other mechanisms, such as a temperature dependent magnetic coercivity.

The next chapter will include a summary of relevant background material, which will be followed by a review of previous experimental results in Chapter 3. Chapter 4 will provide a description of the experimental apparatus, as well as details about the different types of measurements performed. The data and analysis is presented in Chapter 5, along with a discussion and a comparison to the previous results reviewed in Chapter 3. Chapter 6 states the conclusions that can be made based on the present work on the FeMn system and the discussion presented in Chapter 5.

Chapter 2

Background

2.1 Magnetic Ordering

2.1.1 Ferro- and Antiferromagnetic Systems

The magnetic moments in materials, when not aligned/ordered in any regular fashion are said to exhibit paramagnetic behaviour, with the simplest theories of paramagnetism neglecting any interactions between the magnetic moments. However, there exist also substances exhibiting long range order, such as ferromagnets and antiferromagnets; the models describing the latter behaviour must take into account the coupling between moments to correctly describe the properties of these materials.

Ferromagnets are characterized by a ground state in which the electronic moments are aligned parallel to each other below a certain critical temperature, T_c, whereas in antiferromagnets the moments are arranged in an antiparallel fashion, resulting in zero net magnetization. Above their critical temperatures, thermal agitation causes these materials to assume a disor-

dered (paramagnetic) state, with the ordered state reappearing when the temperature drops below T_c again.

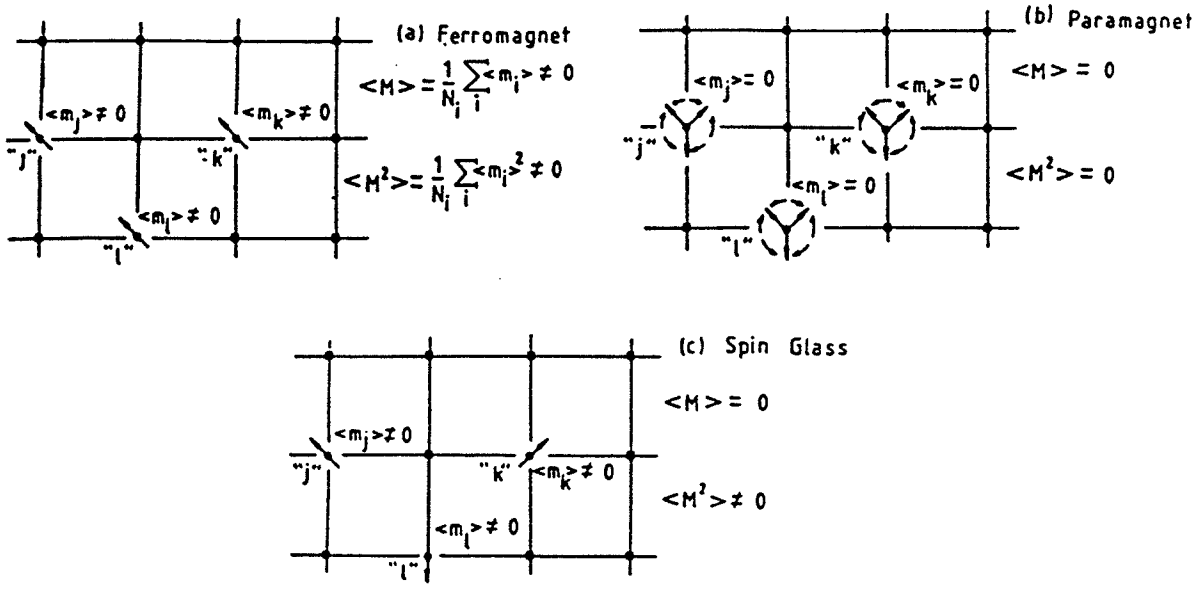

Figure 2.1: An illustration of the difference between (a) a ferromagnet below T_c (b) a paramagnet and (c) a spin glass below T_{sg}; the choice of the order parameter $q =< M^2 >$ for the latter is made apparent. (Williams, 1991)

2.1.2 Spin Glass Systems

In the early 1970's, a totally new type of ordering, unlike any other encountered before was discovered by Cannella and Mydosh (Cannella et al, 1972) in polycrystalline AuFe (in which a fraction of the (non-magnetic) Au sites are replaced substitutionally by moment bearing Fe atoms, so that the 'spins' (i.e. Fe atoms) in the system are distributed at random over the lattice sites).

The long range order present in ferromagnets and antiferromagnets is absent in these systems; however, they display a 'freezing transition' from a paramagnetic state in which the spins (moments) are randomly oriented and free to change their direction to one where the spins are randomly arranged but frozen, as illustrated in Figure 2.1(c).

Although the debate as to whether this magnetic structure represents a genuinely new phase or simply consists of a non-equilibrium state has not yet been completely resolved, there exists strong experimental evidence in some systems to support the case for a phase transition. This includes the divergence of the non-linear field dependent susceptibility at a temperature T_{sg}, in addition to the observation of a sharp peak (cusp) in the zero field ac susceptibility. This is the main point of contention in this area of magnetism, and if a phase transition indeed exists, additional questions then arise as to the nature of the order parameter. This topic, and the related theories will be further discussed in Section 2.3.4

2.2 Critical-Point Exponents

Before examining the various theories that attempt to describe the detailed behaviour of materials in the vicinity of a phase transition, it would be useful to first examine the so-called critical-point exponents which characterize the functional (power-law) behaviour of quantities such as the magnetization and susceptibility in the critical region. This requires selecting a quantity,

known as the order parameter, which is non-zero only in the ordered state of the material. For ferromagnetic systems, this requirement is fulfilled by the magnetization, M which is a measure of the degree of alignment of the magnetic moments in a sample.

2.2.1 Critical-Point Exponent Definition

In order to understand more clearly the behaviour of the various quantities in question, it would be useful to depict the relationship between the magnetic field, H, the magnetization, M and the temperature, T. The diagrams in Figure 2.2 are analogous to the familiar $P\rho T$ diagrams describing the liquid-gas transition, with H being equivalent to pressure, and M to density. (As H increases in a ferromagnetic material, the magnetization increases, just like the density of a gas rises as the pressure is increased.)

The relationships in Figure 2.2 may be combined into one three-dimensional diagram as illustrated in Figure 2.3, displaying simultaneously the connection between the magnetic field, the magnetization, and the temperature.

To understand the principles behind critical exponents, consider firstly a general function,

$$f(x) = Ax^a(1 + Bx^b + \cdots) \tag{2.1}$$

representing a state function such as the magnetization or the susceptibility near the transition point, where x is taken to be the appropriate state parameter. These include H, the applied field and t, the reduced temperature,

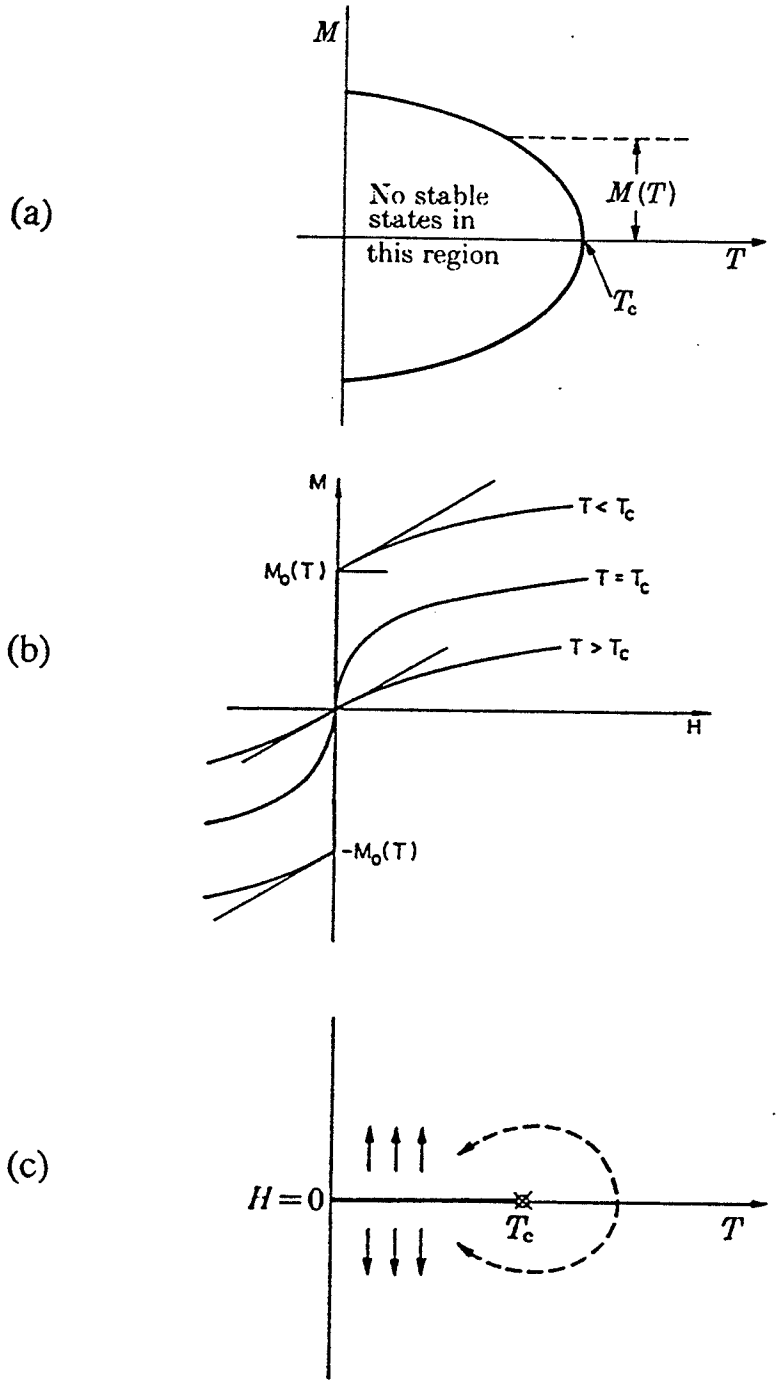

Figure 2.2: (a) Projection of the HMT surface onto the MT plane. (b) Isothermal cross-sections of the HMT surface. (c) Projection of the HMT surface onto the HT plane. (Stanley, 1971)

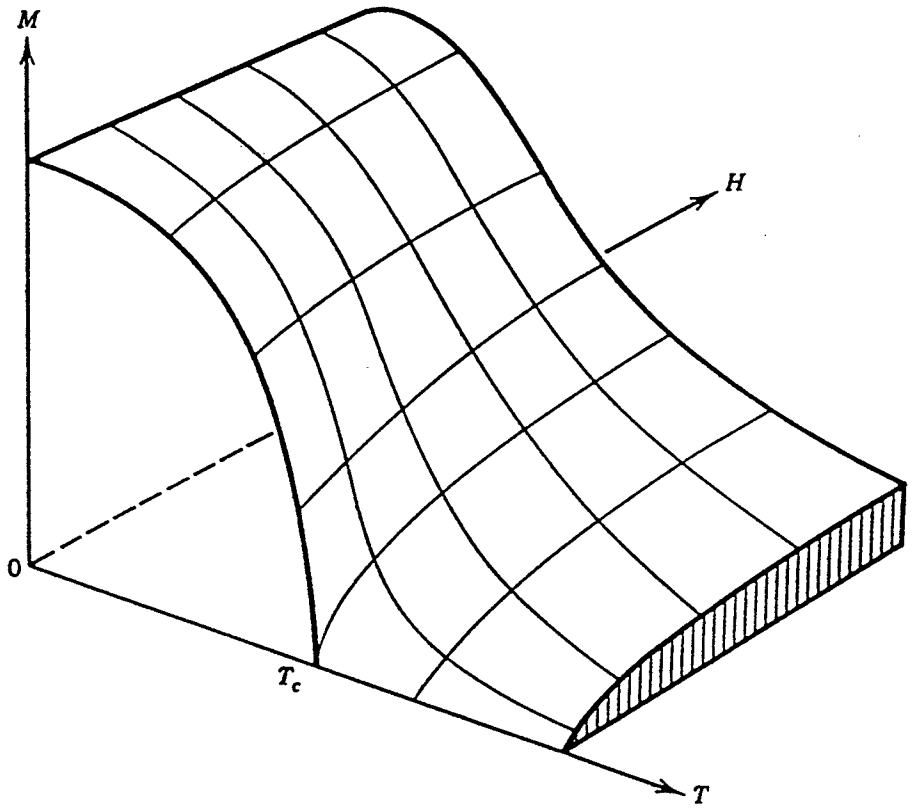

Figure 2.3: Surface representing the equation of state for a magnetic system undergoing a second-order phase transition at zero field ($H = 0$). The surface is symmetric under the reversal $M \rightarrow -M$, the lower half is not shown. (Huang, 1987)

given by

$$t \equiv \frac{T - T_c}{T_c}. \tag{2.2}$$

For convenience, $x = t$ will be used for the ensuing discussion, although the following comments are equally valid for $x = H$.

The critical-point exponents, 'λ' are then defined according to

$$\lambda \equiv \lim_{t \to 0^+} \frac{\ln f(t)}{\ln t}, \tag{2.3}$$

providing $f(t)$ is positive and continuous in the vicinity of small t. In the limit $t \to 0$, $f(t)$ simplifies to

$$f(t) = At^a \tag{2.4}$$

which yields, following (2.3) that

$$\lambda = a. \tag{2.5}$$

It is important to realize at this point that the critical exponent for $t > 0$ may not necessarily equal the critical exponent for $t < 0$, which will be henceforth denoted as λ'. However, according to many models the primed and unprimed exponents are equal, and are therefore often written in the unprimed form. In the event that $\lambda = 0$, the behaviour of $f(t)$ is not uniquely characterized, and may possess a logarithmic divergence as can be seen when considering

$$\lim_{t \to 0^+} \frac{\ln(\ln t)}{\ln t} = \lim_{t \to 0^+} \frac{\frac{1}{t}\frac{1}{\ln t}}{\frac{1}{t}} = \lim_{t \to 0^+} \frac{1}{\ln t} = 0. \tag{2.6}$$

However, $f(t)$ with $\lambda = 0$ may equally well vary continuously through T_c, or represent a finite discontinuity or cusp (eg. $f(t) \sim A - Bt^z$) at the critical temperature.

2.2.2 Critical-Point Exponents, α, β, γ and δ

Referring to the above equations and Figures 2.2 and 2.3, the exponents describing the static behaviour of a magnetic system can now be defined. There exist a great number of these describing the various aspects of critical behaviour; however, only the four most common exponents will be considered here.

Zero-Field Magnetization Exponent, β

The first of these is the zero-field magnetization exponent, β, which describes the spontaneous magnetization of the system, namely

$$M_o(T)/M_o(0) = \mathcal{B}(-t)^{\beta}(1 + \cdots), \tag{2.7}$$

where $M_o(T)$ represents the magnetization of a single-domain ferromagnet in zero applied field near the transition temperature. $M_o(0)$ is incorporated into the above equation so that the proportionality constant $\mathcal{B}$ changes only slightly between systems. The zero-field magnetization, or order parameter exponent, β can then be expressed as

$$\beta \equiv \lim_{t \to 0^-} \frac{\ln M}{\ln(-t)}. \tag{2.8}$$

Zero-Field Isothermal Susceptibility Exponents γ and γ'

Similarly, by studying Figure 2.2 (b) it can be deduced that the susceptibility at constant temperature,

$$\chi_T \equiv \left(\frac{\partial M}{\partial H}\right)_T \tag{2.9}$$

can be expressed as

$$\chi_T/\chi_T^o = \begin{cases} \mathcal{C}'(-t)^{-\gamma'}(1+\cdots) & [T<T_c,\ H=0] \\ \mathcal{C}(t)^{-\gamma}(1+\cdots) & [T>T_c,\ H=0] \end{cases} \tag{2.10}$$

with χ_T^o denoting the susceptibility of a paramagnetic system (i.e. non - interacting moments). Furthermore, it is important to note that even though χ diverges in the limit $T \to T_c$, the critical-point exponents describing the transition approached from below or above, γ' and γ respectively, are not necessarily the same. (The minus sign in front of the latter two exponents in (2.10) insures that both γ' and $\gamma > 0$.)

Critical Isotherm Exponent, δ

Referring to Figure 2.2 (b) once again, a third critical-point exponent can be defined according to

$$\frac{H}{H_c^o} = \mathcal{D}\left|\frac{M_H(T=T_c)}{M_o(T=0)}\right|^\delta \tag{2.11}$$

where $H_c^o \equiv kT_c/m_o$ with m_o representing the magnetic moment per spin. As can be seen, δ characterizes the curvature of the critical isotherm.

Constant-Field Specific Heat Exponents, α and α'

For magnetic systems, the expression for the specific heat is very similar to that for the susceptibility, and is given by

$$C_H = \begin{cases} \mathcal{A}(-t)^{-\alpha'}(1+\cdots) & [T < T_c,\ H = 0] \\ \mathcal{A}t^{-\alpha}(1+\cdots) & [T > T_c,\ H = 0]. \end{cases} \tag{2.12}$$

The behaviour predicted by simple models for the specific heat is often unphysical even though β, γ and δ may be approximately correct. Thus the comparison between the experimental and predicted values for the two exponents in (2.12) plays a particularly significant role in determining the validity of a new theory.

Overview

For temperatures sufficiently close to T_c the correction terms in the above equations become negligible, giving the set of expressions listed in Table 2.1.

At this point it would not be unjustified to ask why so much effort has been put into finding relationships that characterize the behaviour of a substance only near a phase transition instead of trying to find general formulae that describe the material's properties at all temperatures. There are several reasons for this, the first of which is that near a transition point, the first term in a power series expansion in field or temperature of a function describing say the magnetization, susceptibility or other response function would be dominant. The corresponding exponent is relatively easy to compute, as will be shown below, and therefore at least some information about

the functional form of the quantity in question can be deduced. Furthermore, the value of the critical-point exponents will provide insight into the nature of the magnetic order of the system.

Secondly, relationships arising from fundamental thermodynamic and statistical mechanical concepts exist between the critical exponents that are independent of the system being considered, be it magnetic, fluid or otherwise. Finally, striking similarities often exist between the critical exponents for many physical systems, be they fluid, superconducting or magnetic, even though the systems may have interaction mechanisms/ranges or critical temperatures which are quite different.

Some of the more common inequalities between the critical-point exponents introduced above are listed in Table 2.2. The inequalities often appear as equalities, thereby being consistent with the predictions of scaling theory (as will be shown in Section 2.4); however rigorous proofs exist only for the inequalities (Stanley, 1971, Chapter 4).

2.3 Theories of Magnetic Ordering

Within the last century many models have been proposed, attempting to understand the behaviour of magnetic materials. The main difference between the various theories lies in how they describe the interactions between the magnetic moments.

Table 2.1: Critical-point exponent definitions for magnetic systems

Exponent Definition	Conditions	Quantity
$M \sim (-t)^{\beta}$	$t \to 0^-, \quad H = 0, \quad M \neq 0$	zero-field magnetization
$\chi_T \sim t^{-\gamma'}$	$t \to 0^+, \quad H = 0, \quad M \neq 0$	zero-field isothermal susceptibility
$\chi_T \sim t^{\gamma}$	$t \to 0^-, \quad H = 0, \quad M = 0$	zero-field isothermal susceptibility
$M \sim H^{1/\delta}$	$t = 0, \quad H \neq 0, \quad M \neq 0$	critical isotherm
$C_H \sim (-t)^{-\alpha'}$	$t \to 0^-, \quad H = 0, \quad M = 0$	specific heat at constant magnetic field
$C_H \sim t^{-\alpha}$	$t \to 0^+, \quad H = 0, \quad M = 0$	specific heat at constant magnetic field

Table 2.2: Exponent Inequalities

Rushbrooke	$\alpha' + 2\beta + \gamma' \geq 2$
Griffiths	$\alpha' + \beta(\delta + 1) \geq 2$
Griffiths	$\gamma'(\delta + 1) \geq (2 - \alpha')(\delta - 1)$
Widom	$\gamma' \geq \beta(\delta - 1)$
Fisher	$(2 - \eta)\nu \geq \gamma$

2.3.1 Classical Mean Field Theory

The classical mean field or Weiss theory (Weiss, 1907) successfully accounts for such properties of ferromagnetism as the field and temperature dependent spontaneous magnetization and magnetic susceptibility. However, it provides little insight into the details of the interactions between the magnetic moments. The fundamental hypothesis of this model states that these interactions generate an effective internal molecular field, H_m, proportional to the average magnetization, namely

$$H_m = \lambda M, \tag{2.13}$$

with the proportionality constant, λ being referred to as the molecular field constant. Statistically, this is equivalent to assuming that each of the moments (spins) responds to the field independently (White, 1970). Neglecting the dipole-dipole and demagnetization fields, which are usually much smaller than the molecular field, the effective field is of the form

$$H_{eff} = H_a + \lambda M(T, H), \tag{2.14}$$

where H_a is the applied field.

To obtain an estimate of the magnitude of H_m, assume a not untypical Curie temperature on the order of 10^3 K (T_c(iron) = 1043 K). In this case atoms with a dipole moment of one Bohr magneton would have an internal magnetic field of approximately

$$\mu_B H_m \approx kT_c$$

$$H_m \approx 10^7 Oe.$$

This is much larger than the majority of fields capable of being generated in the laboratory, thereby giving an indication of the strength of the coupling between moments in a ferromagnet.

The Hamiltonian for an N atom system in the mean field theory is then given by

$$\mathcal{H} = -g\mu_B \sum_{i=1}^{N} \mathbf{J}_i \cdot \mathbf{H}_{eff}. \tag{2.15}$$

where $\mathbf{J}_i$ is the total angular momentum of the i^{th} atom, and

$$\mathbf{J}_i \cdot \mathbf{H} = m_i H \qquad (m_i = -J, -J+1, \ldots, 0, \ldots, J-1, J). \tag{2.16}$$

Using the above equation, the partition function, Z, defined to be

$$Z = \sum_i e^{-E_i/kT} \tag{2.17}$$

is related to the Gibbs free energy by

$$G(T,H) = -kT \ln Z. \tag{2.18}$$

Using the following thermodynamic relationship

$$M(T,H) = -\left(\frac{\partial G}{\partial H}\right)_T, \tag{2.19}$$

the magnetization can be expressed as

$$M(T,H) = NkT\frac{\partial \ln Z}{\partial H_{eff}} \tag{2.20}$$

$$= M_o B_J[(g\mu_B J/kT)(H_a + \lambda M(T,H))], \tag{2.21}$$

where M_o represents the maximum magnetization,

$$M_o \equiv M(T=0, H=0) = NJg\mu_B \tag{2.22}$$

and $B_J(x)$ is the Brillouin function, defined as

$$B_J(x) \equiv \frac{2J+1}{2J}\coth\left(\frac{2J+1}{2J}x\right) - \frac{1}{2J}\coth\left(\frac{1}{2J}x\right) \tag{2.23}$$

with

$$x = g\mu_B H_{eff}/kT. \tag{2.24}$$

Due to the appearance of $M = M(T, H)$ on both sides of (2.21), computer or graphical techniques are required to determine the spontaneous magnetization at a given temperature.

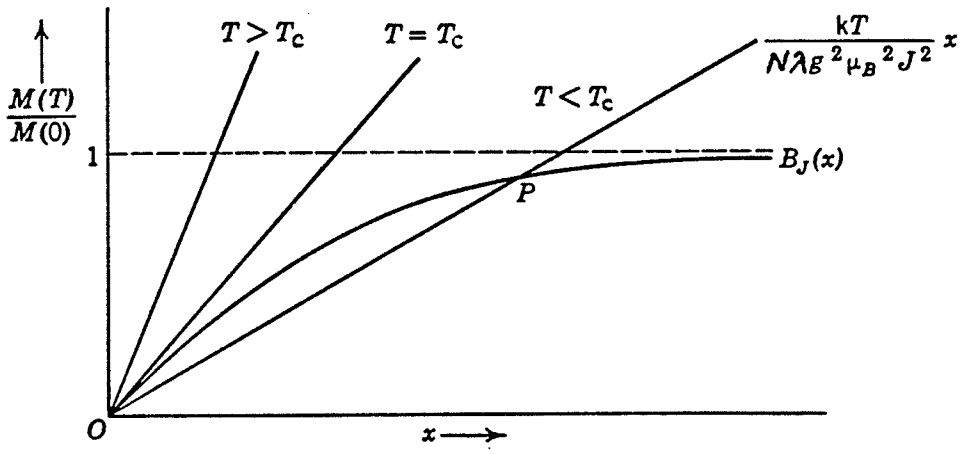

Figure 2.4: Illustration of a graphical method for the determination of the spontaneous ($H = 0$) magnetization at a temperature T. (Morrish, 1965)

In the above diagram T_c represents the ferromagnetic Curie temperature. Notice that $M = 0$ is the only solution above T_c, whereas for $T < T_c$ $M \neq 0$ is also permitted, indicating that below the critical temperature spontaneous magnetization exists in a ferromagnet. Obviously, during the transition to the paramagnetic state, occurring at $T = T_c$, the magnetization disappears.

Note that when $x \ll 1$, i.e. when the magnetization is small, the Brillouin function becomes

$$B_J(x) = \frac{J+1}{3J}x - \frac{J+1}{3J} \cdot \frac{2J^2+2J+1}{30J^2}x^3 + \ldots, \tag{2.25}$$

and in the limit $x \to 0$, the slope of the Brillouin function approaches $(J+1)/(3J)$. Comparing the latter to the slope of the straight line, $kT/N\lambda g^2\mu_B^2 J^2$ evaluated at $T = T_c$, provides a connection between the Curie temperature and the molecular field constant, namely,

$$T_c = \frac{Ng^2\mu_B^2 J(J+1)}{3k}\lambda = C\lambda, \tag{2.26}$$

where C is known as the Curie constant. From the above expression it can be seen that as the molecular field constant approaches zero, T_c also decreases, which is reasonable since $\lambda = 0$ represents a (non-interacting) paramagnetic system that does not have a critical temperature. Conversely, increasing λ increases the Curie temperature, since a larger value for the molecular field constant indicates stronger ferromagnetic coupling, which requires greater thermal agitation to destroy.

Mean Field Theory Critical Exponents

The critical point exponents predicted by this model can be found relatively easily using the derived expression for the magnetization, (2.21), as will now be demonstrated.

Magnetization Exponent, β

Since the region of interest is at temperatures near the critical temperature where the magnetization approaches zero, the small argument expansion of the Brillouin function (2.25) can be used. Taking $H_a = 0$, and inserting the latter into the expression for the magnetization (2.21) yields

$$\begin{aligned} M &= \left(M_o \frac{J+1}{3J} x\right) - \frac{2J^2+2J+1}{30J^2} x^2 \left(M_o \frac{J+1}{3J} x\right) + \ldots \\ &= \left(M_o \frac{J+1}{3J} x\right) - \frac{3}{10} \frac{J^2+(J+1)^2}{(J+1)^2 M_o^2} \left(M_o \frac{J+1}{3J} x\right)^3 + \ldots \end{aligned} \quad (2.27)$$

where $x = (g\mu_B J/kT)(\lambda M)$, and combining with (2.26) gives upon solving for M/M_o

$$\frac{M}{M_o} = \left[\frac{10}{3} \frac{(J+1)^2}{J^2+(J+1)^2}\right]^{1/2} \left(\frac{T}{T_c}\right) (-t)^{1/2}, \quad (2.28)$$

where $t = \frac{T-T_c}{T_c}$. In comparing this result to the expected power law dependence of the magnetization, $M \sim (-t)^\beta$, it can clearly be seen that $\beta = 1/2$.

Susceptibility Exponent, γ

In order to find the susceptibility exponent, consider the expression for the magnetization given above, (2.27) retaining only the first term and inserting $x = \frac{Jg\mu_B}{kT}(H_a + \lambda M)$. The resulting expression is

$$M = \frac{Ng^2\mu_B^2 J(J+1)}{3kT}(H_a + \lambda M), \quad (2.29)$$

which becomes

$$M = \frac{CH_a}{T - T_c} \tag{2.30}$$

upon incorporating (2.26). Now differentiating with respect to H_a yields

$$\chi_T = \left(\frac{\partial M}{\partial H_a}\right)_T = \frac{C}{T - T_c} = \frac{t^{-1}}{\lambda}. \tag{2.31}$$

In comparing this result to the expected power law dependence, $\chi_T \sim t^{-\gamma}$, it is obvious that $\gamma = 1$ in the mean field theory.

Critical Isotherm Exponent, δ

The critical isotherm exponent can be readily determined by evaluating x at T_c, namely

$$\begin{aligned} x(T_c) &= \frac{Jg\mu_B}{kT_c}(H_a + \lambda M) \quad ; \quad T_c = \frac{Ng^2\mu_B^2 J(J+1)}{3k}\lambda \\ &= \left(\frac{1}{M_o}\frac{3J}{J+1}\right)\left(M + \frac{H_a}{\lambda}\right), \end{aligned} \tag{2.32}$$

and substituting into (2.27)

$$M \approx \left(M + \frac{H_a}{\lambda}\right) - \frac{3}{10}\frac{J^2 + (J+1)^2}{(J+1)^2 M_o^2}\left(M + \frac{H_a}{\lambda}\right)^3. \tag{2.33}$$

For small applied fields

$$H_a = \frac{3}{10}\frac{J^2 + (J+1)^2}{(J+1)^2 M_o^2}\lambda M^3 \tag{2.34}$$

and from the expected power law dependence, $M \sim H^{1/\delta}$, it is apparent that $\delta = 3$.

Mean Field Theory: Advantages and Limitations

The beauty and elegance of the mean field theory lies in its simplicity – a closed form solution exists and can be found without wading through pages of laborious calculations. Furthermore, it fulfils the most fundamental requirement for a proposed theory of magnetic ordering, namely, it predicts a phase transition. Despite the fact that its predictions are not in quantitative agreement with experimentally observed phase transitions, qualitatively the mean field theory describes almost all available results, in particular when a mean field solution of the Sherrington-Kirkpatrick model (Section 2.3.4) is used to incorporate the effects of magnetic site disorder into calculations. In any event, the latter also provides a convenient starting point for more realistic, if not improved descriptions of magnetic systems.

However, the MFT fails to incorporate several important features that become especially crucial in the vicinity of a phase transition. Near the critical point, the MFT assumes that the only significant configuration is one of uniform spin density, which may be true at other temperatures, but is certainly invalid near T_c, where experimental evidence indicates that fluctuations in the spin density become prevalent.

Naturally, omitting such important aspects of the physical system results in incorrect values for the asymptotic critical point exponents, i.e. exponent values close to T_c, where critical fluctuations are largest. (See Table 2.3) The MFT predicts $M_{MFT} \sim t^{1/2}$, whereas experimental measurements, such as

those for PdFe (1.4 at.% Fe in Pd, Wang et al, 1992; Kaul, 1985) indicate that $M \sim t^{0.365}$ in the limit $T \rightarrow T_c^+$. Similarly, this theory suggests that $\chi_{MFT} \sim t^{-1}$, but the susceptibility of this PdFe alloy obeys $\chi \sim t^{-1.39}$ as $T \rightarrow T_c^+$.

The difference between the experimental and theoretical values for β, δ and γ is perhaps surprisingly small, and it is only in the case of α (the specific heat exponent) that the agreement between the MFT predictions and the qualitative behaviour of actual physical systems is not found. It can be shown that according to the MFT, the magnetic contribution to the specific heat in zero field disappears above the Curie temperature; this clearly contradicts experimental results which indicate the presence of a residual specific heat above T_c. More precisely, $C_H \sim \ln|T - T_c|$ when $T \rightarrow T_c^+$, in contrast to the behaviour illustrated in Figure 2.5.

The discrepancy concerning the specific heat is a direct consequence of the fact that the MFT disregards the short-range correlation between the spins, which are present in the majority of physical systems. The next set of models to be considered incorporate this short range coupling and are able account for the origin of the 'unknown' molecular field proposed by Weiss, but are considerably more difficult to work with than the mean field theory.

Nevertheless, despite its limitations, Weiss' theory (including the concept of domains) is still perhaps the most important theory for a practical discussion of most types of magnetic behaviour.

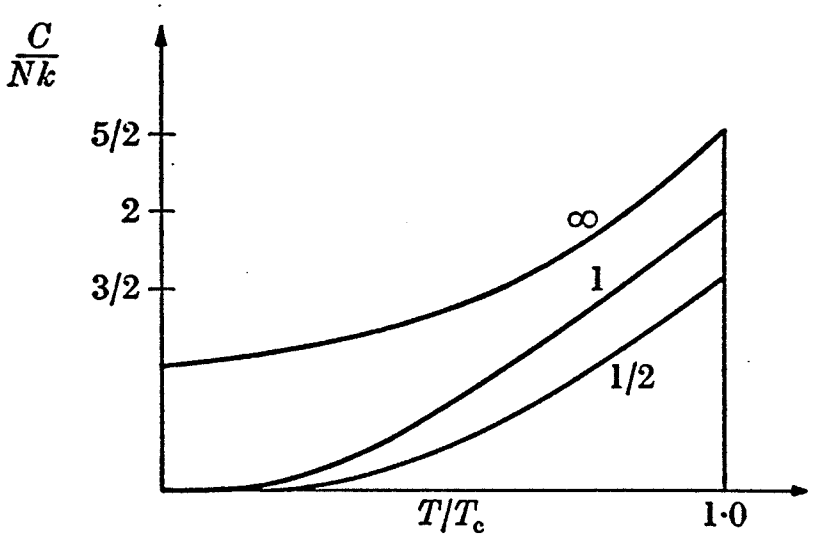

Figure 2.5: Dependence of C_H for $H = 0$ upon reduced temperature, T/T_c. Notice that although there is a simple jump discontinuity for all values of J (i.e. $\alpha = \alpha' = 0$), the magnitude of the discontinuity depends weakly upon J. (Stanley, 1971)

2.3.2 Ising and Heisenberg Models

The mean field theory predicts numerical values of the critical-point exponents, but does not provide any understanding about the nature of the molecular field constant, λ. Two other prominent models, namely the Heisenberg and Ising models, which were introduced after the development of quantum mechanics, attempt to provide a more realistic description of magnetic systems and also examine the nature of the aforementioned interaction. Both of these models propose that the magnetic moments are 'attached' to the lattice and interact via an exchange field whose strength is determined by an 'exchange coupling constant', denoted by J_{ij}. (Morrish, 1965)

The most general Hamiltonian for such a system may be expressed as (Stanley, 1971)

$$\mathcal{H}^{(D)} = -\sum_{i,j} J_{ij} \mathbf{S}_i^{(D)} \cdot \mathbf{S}_j^{(D)} \tag{2.35}$$

where $\mathbf{S}^{(D)}$ is the D-dimensional spin operator, with components obeying $\sum_{n=1}^{D} S_{in}^2 = 1$, where $(S_{i1}, S_{i2}, \ldots, S_{iD})$ are the Cartesian coordinates of $\mathbf{S}_i^{(D)}$. $D = 1, 2, 3$ and ∞ have been studied in detail, but only the two most common cases, $D = 1$ and $D = 3$ will be considered here. The exchange coupling constant in the above equation is electrostatic in origin and is a consequence of the necessity that the electrons in an atom be indistinguishable. It is important to note at this point that J_{ij} is positive for a ferromagnet (parallel spin arrangement), and negative for antiferromagnets (antiparallel spins).

The exchange coupling constant can also take on a variety of forms to account for the range of interactions present in materials. Most calculations within the framework of this model consider only nearest neighbour interactions in order to simplify the situation. However, this is a rather unphysical assumption and led to the development of the Sherrington-Kirkpatrick model in which J_{ij} has a Gaussian distribution, as will be discussed in more detail in Section 2.3.4.

Ising Model

The above named model was proposed by E. Ising in 1925 as part of his Ph.D. thesis; Ising considered a linear chain (one-dimensional lattice), taking only

isotropic nearest-neighbor interactions into account, with no external applied field. The Hamiltonian for such a system takes into consideration only the $z-$component of the spin and is given by

$$\mathcal{H} = -J \sum_{\langle i,j \rangle} S_{zi} S_{zj} \tag{2.36}$$

where J couples the spins located at sites i and j, and the notation $\langle i,j \rangle$ indicates that the summation is to be carried out only over the nearest neighbours of atom i. From the above expression it can be seen that the magnetic moments in this model can be taken to be classical 'vectors' with only two possible alignments, namely up or down. Moreover, the above equation also demonstrates that the interactions in this model are short-ranged, in contrast to the mean field theory. It is interesting to note that computations, assuming an isotropic exchange coupling constant extended over all atoms in the system, reduce to the mean field theory case, as expected (Stanley, 1971, Sec. 6.5).

Ising's solution for a one-dimensional system gave no indication of the phase transition observed in physical systems at any finite temperature. Furthermore, in its ground state at absolute zero all the spins in such a system would be aligned, but at any non-zero temperature this ordering would be destroyed and the system would assume a paramagnetic state. In 1952, Onsager and Yang published the solution to the two-dimensional Ising model in zero field, perhaps one the greatest triumphs in the theoretical study of critical phenomena. This result accurately predicts a logarithmic divergence

in the specific heat at T_c in contrast to the mean field theory result, but the critical exponents it yields do not agree with experimental values. No exact solution has been found for the three-dimensional Ising model, and is believed by some not to exist.

Heisenberg Model

In the Heisenberg model, the Hamiltonian is taken to equal the scalar product of the three-dimensional spin operators, multiplied by the exchange coupling constant. Since this model does not restrict the spins to the $(2S+1)$ discrete orientations permitted by quantum mechanics, it is said to be the $S \rightarrow \infty$, or classical limit of the quantum-mechanical Heisenberg model. The Heisenberg Hamiltonian for a lattice of spins is then usually expressed as

$$\mathcal{H} = -J_e \sum_{\langle i,j \rangle} \mathbf{S}_i \cdot \mathbf{S}_j, \tag{2.37}$$

where the exchange coupling constant is taken to be isotropic and non-zero only for nearest neighbors. Note that for only the products of the spin operators to be present, it is necessary to assume that the magnetic ions be sufficiently distant from each other that the electronic overlap be quite modest. Furthermore, if the magnetic ions have a non-negligible orbital angular momentum in addition to a spin component, the Hamiltonian may be a function of both the absolute and relative spin orientations. Whether or not these, and other additional requirements (Ashcroft et al, 1976, Chapter 32) are satisfied, depends upon the characteristics of the individual substance.

Approximation Techniques

Technically, a solution of the three-dimensional Heisenberg model Hamiltonian should constitute a superior theory of ferromagnetism, but unfortunately along with the (3D) Ising model Hamiltonian, none has yet been derived. Naturally, it would be desirable to find an alternative form of this Hamiltonian that can be solved exactly, but efforts to this end have not yet been successful either. This necessitates the use of approximation techniques to ascertain the properties of an Ising- or Heisenberg-like system near its phase transition, including its critical-point exponents and transition temperature. One prominent scientist states that such attempts have been so effective that 'one often forgets that they are only approximations'. Moreover, when compared with experimental outcomes, the error in the calculated numbers are often less than the experimental errors (Stanley, 1971).

However, in order to obtain these results, a tedious and complicated approach must be taken, known as the series expansion method. The latter expresses the thermodynamic function in question (eg. the Gibbs function) in increasing powers of either T ('low temperature expansion') or $1/T$ ('high temperature expansion'). These expansions are not performed about T_c, but rather about the zero value of T or $1/T$, and since knowledge of their asymptotic behaviour is required to achieve the desired results, the calculation of sufficient terms becomes so laborious that it can only be achieved using graph theory or computers. Although no rigorous proofs exist that these series are

in fact convergent, series expansions performed on solvable models (such as the two-dimensional Ising model) yield results agreeing with the exact values to within better that 0.01 %.

Ising and Heisenberg Model Limitations

Despite the precise critical exponent values generated by the $D = 3$ Ising and Heisenberg Hamiltonians (Table 2.3), these two models are by no means 'ideal', and are subject to a variety of restrictions.

Consider firstly the Ising model. Even though the $x-$ and $y-$components of the spin are neglected, it has found practical applications for systems such as one-component fluids and binary alloys. However, it is important to keep the aforementioned simplification in mind when evaluating the predictions of this theory. Moreover, the Ising model is invalid at low temperatures where the energy of the system depends upon the $x-$ and $y-$ spin components. In other words, the presence of spin waves is not permitted since the only way to introduce disorder into the system is to induce an actual spin flip.

In the case of the Heisenberg model, it must be said at this point that in spite of the more realistic description of a physical system it provides when compared to the mean field theory, or even the Ising model, it is still not applicable to many real materials. This is a consequence of the rather stringent restrictions this model places on the system, including well-localized spins and a complete uniformity (isotropy) of the interaction, as well as a variety

of other constraints [1] (Ashcroft et al, 1976, Chapter 32; Morrish, 1965, Sec. 6-3). Moreover, this model also requires the spins to be spatially ordered, which is certainly not the situation for the amorphous magnetic alloys of interest in this thesis. Despite these apparent limitations, the Heisenberg Hamiltonian has proven to be extremely useful in explaining the asymptotic experimental results obtained near T_c. It appears to be that in this limit of a diverging correlation length the observed behaviour is quite insensitive to the aforementioned restrictions.

The greatest deficiency of the Ising and Heisenberg models, more specifically their three-dimensional representations, is however that they cannot be solved exactly and the approximation techniques developed are very tedious and complicated. This provides sufficient justification for the formulation of a different approach, namely the Landau theory, which is not only easier to deal with than the latter two models, but also incorporates important physical effects not accounted for in the models discussed up to now.

2.3.3 Landau Theory

With his theory, Landau attempted to provide a more realistic equation of state for a magnetic system than suggested by the 'classical theories' available at the time, which included the mean field theory discussed above. Landau's theory utilizes similar concepts to the aforementioned theory and derives the

[1] Other details neglected in both the Ising and Heisenberg model include crystalline anisotropy terms which are of course present in any real material.

same critical exponents, but it also incorporates the concept of 'fluctuations', which strongly influences the behaviour of thermodynamic functions in the vicinity of a phase transition. Thus, the Landau theory has great heuristic usefulness even though it is quantitatively incorrect.

In essence, this theory suggests that the Helmholtz free energy, F of a magnetic system can be represented by the Taylor series, (Stanley, 1971)

$$F(T,M) = F_o(T) + F_2(T)M^2 + F_4(T)M^4 + \cdots \tag{2.38}$$

near the transition temperature, as here the magnetization, M, is small. Moreover, the temperature dependent coefficients in the above equation can also be expanded in power series, namely,

$$F_j(T) = \sum_{k=0}^{\infty} f_{jk}(T - T_c)^k = f_{j0} + f_{j1}(T - T_c) + \cdots. \tag{2.39}$$

Note that there are no odd terms in the expression for $F(T,M)$, as the free energy must remain unaffected if the sign of M is reversed.

Recalling that the magnetic field, H can be written as

$$H = \left(\frac{\partial F}{\partial M}\right)_T \tag{2.40}$$

yields

$$H(M,T) = \sum_{j=1}^{\infty} jF_j(T)M^{j-1} = 2F_2(T)M + 4F_4(T)M^3 + \cdots, \tag{2.41}$$

the Landau theory equation of state, from which the critical-point exponents can be determined.

Landau Theory Critical-Point Exponents

Magnetization Exponent, β

The magnetization exponent, β can easily be found from the equation of state, (2.41) by setting $H = 0$, and taking M to be small, which gives

$$0 = \{f_{21}(T - T_c) + \cdots\} + 2M^2\{f_{40} + f_{41}(T - T_c) + \cdots\} + \cdots. \quad (2.42)$$

Solving for M yields

$$M = \left(\frac{f_{21}}{2f_{40}}\right)^{1/2} (T_c - T)^{1/2}, \quad (2.43)$$

which upon comparing to $M \sim (-t)^\beta$ indicates that $\beta = 1/2$.

Isothermal Susceptibility Exponents, γ and γ'

From the definition of the susceptibility, $\chi_T = (\partial M/\partial H)_T$ and the expression for the field, $H(M,T)$ it can be seen that in this theory the inverse isothermal susceptibility,

$$\chi_T^{-1} = \left(\frac{\partial H}{\partial M}\right)_T = \left(\frac{\partial^2 F}{\partial M^2}\right)_T \quad (2.44)$$

can be written as

$$\chi_T^{-1}(T,M) = \sum_{j=2}^{\infty} j(j-1)F_j(T)M^{j-2} = 2F_2(T) + 12F_4(T)M^2 + \cdots. \quad (2.45)$$

At this point it is useful to recall that since the zero-field susceptibility is expected to diverge in the limit $T \to T_c^+$, χ_T^{-1} given by

$$\begin{aligned} \chi_T^{-1}(T,0) &= 2F_2(T) \\ &= 2\{f_{20} + f_{21}(T - T_c) + f_{22}(T - T_c)^2 + \cdots\} \end{aligned} \quad (2.46)$$

is required to approach zero, which in turn requires that $f_{20} = 0$. Also when $T > T_c$, the material is in the paramagnetic phase, and $M = 0$ when $H = 0$, so that $\chi_T^{-1}(T, 0)$ becomes

$$\chi_T^{-1}(T, 0) \approx 2f_{21}(T - T_c). \tag{2.47}$$

In the magnetically ordered region at temperatures below T_c, $M \neq 0$ for $H = 0$. Returning to (2.45), the inverse zero-field susceptibility can now be written as

$$\chi_T^{-1}(T, M) \approx 2\{f_{21}(T - T_c) + \cdots\} + 12M^2\{f_{40} + f_{41}(T - T_c) + \cdots\} \tag{2.48}$$

which becomes

$$\chi_T^{-1}(T, M) \approx 4f_{21}(T_c - T) \tag{2.49}$$

in combination with (2.43). Comparing the above to equations to $\chi_T \sim t^{-\gamma}$ and $\chi_T \sim (-t)^{-\gamma'}$ respectively, it can be seen that in the Landau theory, $\gamma = \gamma' = 1$. However, χ_T^{-1} increases twice as quickly for $T < T_c$ than for $T > T_c$, meaning that $\mathcal{C}' = 2\mathcal{C}$ (Section 2.2.2).

Critical Isotherm Exponent, δ

In order to ascertain the curvature of the critical isotherm, return to the expression for $H(M, T)$,

$$\begin{aligned} H(M,T) &= 2F_2(T)M + 4F_4(T)M^3 + \cdots \\ &= 2\{f_{20} + f_{21}(T - T_c) + \cdots\}M \\ &\quad +4\{f_{40} + f_{41}(T - T_c) + \cdots\}M^3 + \cdots \end{aligned} \tag{2.50}$$

and let $T = T_c$. Recalling that $f_{20} = 0$ then leads to

$$H(M, T_c) = 4f_{40}M^3 + \cdots \tag{2.51}$$

from which it can be seen, upon comparison with $H \sim M^\delta$ that $\delta = 3$.

Landau Theory Limitations

Similar to the mean field theory, the Landau theory provides a simple, solvable description of the properties of magnetic materials near their phase transition. Unfortunately, this theory also predicts the same incorrect critical point exponents that Weiss' molecular field theory does, so the discussion given above concerning the critical indices can also be applied here. In this case, the fault lies with the initial assumption that the Helmholtz function can be expanded as a power series about T_c – it has since been established that such a series diverges.

However, the one very important concept that the Landau theory incorporates, not accounted for in the mean field theory or the Ising and Heisenberg models is the presence of fluctuations from the equilibrium value in the order parameter, M near the phase transition. Since the discussion presented here concerns itself only with equilibrium situations (i.e. dynamical effects are not considered), it would be easy to assume that fluctuations in M be of little importance. This is indeed the case for temperatures far from T_c, but when approaching the critical temperature these fluctuations become so pronounced that they must be taken into consideration.

Detailed calculations exist showing how this concept is incorporated by the Landau theory (Patterson, 1971), which basically amounts to the study of the behaviour of fluctuations expressed as

$$M_z(r) - \langle M_z(r) \rangle, \tag{2.52}$$

and how the deviation of M_z from its average, $\langle M_z(r) \rangle$, at one location in the material is related to analogous fluctuations in neighbouring regions (Kadanoff et al, 1967). Mathematically, this behaviour is described by a correlation function given by

$$g(r, r') = \langle \{M_z(r) - \langle M_z(r) \rangle\} \{M_z(r') - \langle M_z(r') \rangle\} \rangle \tag{2.53}$$

which can be evaluated using the free energy of the system.

2.3.4 Spin Glass Theory

Edwards-Anderson Model

As stated in section 2.1.2 of this chapter, evidence for the existence of the spin glass state was first observed in the dilute alloys of the AuFe system (Cannella et al, 1972). Shortly thereafter a theory was proposed by Edwards and Anderson (EA model) (Edwards et al, 1975) to account for the cusp-like peak in the susceptibility of the latter dilute magnetic alloys. It was suggested that in such a system the exchange interaction, J_e, is not constant, but is instead represented by some distribution. Edwards and Anderson chose a Gaussian distribution centered at zero, concluding that since the sign of

Table 2.3: Critical-point exponent values

Critical Exponents	$T \leq T_c$			$T = T_c$	$T \geq T_c$	
	α'	β'	γ'	δ	α	γ
Landau/MFT	0	0.5	1	3	0	1
2-D Ising	0	0.125	1.75	15	0	1.75
3-D Ising	0.66	0.326	1.31	4.78	0.106	1.238
3-D Heisenberg	-	0.367	-	4.78	-.121	1.388
Experiment	0-0.2	0.2-0.4	1.0-1.2	3-6	-0.3-0.3	1.3-1.4

the interaction (i.e. sign of J_{ij}) oscillates with the distance between the interacting spins s_i and s_j (RKKY interaction – Appendix 1), a ground state will exist with the spins pointing in well defined, but apparently random directions, as illustrated in Figure 2.1(c). Upon inspecting any portion of the material, the ground state therefore results in the local magnetization $\langle s_i \rangle = 0$, which means that no ferromagnetic ordering is present, although the order parameter for a spin glass state is non-zero, as will be discussed below.

In introducing the EA model, an analogy is often presented which compares the formation of a spin glass phase to gelation in polymer science. As the density of long molecules increases in a mixture, a point is eventually reached where they become so entangled that they can no longer move. Although their positions are random, like the moments in a spin glass, below its critical temperature they do not change with time and remain at the same random orientations.

Applying the above situation to spin glasses, a logical choice for the order parameter describing the paramagnetic to spin glass transition is given by

$$q = \langle s_i(t_o) \cdot s_i(t) \rangle \qquad t \gg t_o \tag{2.54}$$

where $s_i(t_o)$ is the spin at site i at time t_o, and $s_i(t)$ is the same spin at some later time. At $T = 0$, $q = 1$, since at this temperature the spins are frozen in place with minimal thermal agitation. The order parameter decreases with increasing temperature until it reaches zero at $T = T_f$, the spin glass ordering temperature. (Recall that the order parameter for a ferromagnetic system was chosen to be the average magnetization $M \sim \langle s_i \rangle$, which is nonzero only below T_c.)

The EA model goes on to hypothesize that upon cooling a spin glass, the thermal agitation becomes sufficiently reduced below T_f that the presence of the RKKY coupling between the magnetic ion spins manifests a cusp in the susceptibility, an indication of spin glass ordering. Application of an external field suppresses this peak to a broad maximum.

Sherrington-Kirkpatrick Model

An alternate, more sophisticated theory than that proposed by Edwards and Anderson was introduced by Sherrington and Kirkpatrick (Sherrington et al, 1975). Assuming that the site disorder, such as that observed in amorphous alloys can be represented by an exchange bond disorder, they hypothesized that the Ising model Hamiltonian for such a quenched bond disordered system is

$$\mathcal{H} = -\frac{1}{2}\sum_{i \neq j} J_{ij} s_i s_j \quad ; \quad s_i = \pm 1 \tag{2.55}$$

with the exchange coupling constant having a Gaussian probability density given by

$$p(J_{ij}) = \frac{1}{J\sqrt{2\pi}} exp\left[\frac{-(J_{ij} - J_o)^2}{2J^2}\right]. \tag{2.56}$$

J_o and J, the first and second moments (mean and width) of the above distribution are scaled according to $J_o = \tilde{J}_o/N$ and $J = \tilde{J}/\sqrt{N}$, so that $\tilde{J}_o$ and $\tilde{J}$ are intensive parameters, independent of the size of the system.

It can be shown (Stanley, 1971) that in the thermodynamic limit (N, the number of magnetic ions $\rightarrow \infty$), the mean field theory is equivalent to an infinite range interaction model if a site independent exchange coupling constant ($J_{ij} = J$ for all i and j) is assumed. The SK model extends this problem to apply to disordered systems and considers the aforementioned 'infinite-range' calculations to arrive at a solution with the EA order parameter (2.54), describing a spin-glass in the appropriate temperature and composition range.

After a detailed calculation, an expression for the free energy was derived

along with the following two coupled equations:

$$q = 1 - \frac{1}{\sqrt{2\pi}} \int e^{-z^2/2} sech^2 \left[\left(\frac{\tilde{J}\sqrt{q}}{kT} \right) z + \frac{\tilde{J}_o m}{kT} \right] dz \qquad (2.57)$$

$$m = \frac{1}{\sqrt{2\pi}} \int e^{-z^2/2} tanh \left[\left(\frac{\tilde{J}\sqrt{q}}{kT} \right) z + \frac{\tilde{J}_o m}{kT} \right] dz \qquad (2.58)$$

representing the physical quantities,

$$m = \langle \langle s_i \rangle_T \rangle_J \qquad (2.59)$$

$$q = \langle \langle s_i \rangle_T^2 \rangle_J \qquad (2.60)$$

which are independent of i (i.e. site), and are valid for both finite and infinite-ranged interactions. The notation, $\langle\ \rangle_J$ represents an average over the exchange distribution, and $\langle\ \rangle_T$ denotes a thermal average.

Referring back to Figure 2.1, m and q are evidently analogous to $\langle M \rangle$ and $\langle M^2 \rangle$ respectively. It is then clear that $m = q = 0$ represents a completely disordered system, whereas $m \neq 0,\ q \neq 0$ indicates that the system is ordered (with a ferromagnetic component). This leaves the $m = 0,\ q \neq 0$ combination ($m \neq 0,\ q = 0$ is inconsistent) to describe a spin glass. From Figure 2.1 (c), this can be seen to be an eminently reasonable result, since the random orientation of the spins dictates that the net magnetization be zero; however, their 'frozen' orientations leads to $q \neq 0$, meaning that magnetic 'order' exists. This supports the EA claim of q as the order parameter for the spin glass phase.

Examination of the two coupled equations relating m and q, (2.57) and (2.58) respectively, suggests that as kT falls below the greater of $\tilde{J}_o$ or $\tilde{J}$,

magnetic ordering is established. More specifically, if $\eta = \frac{\tilde{J}_o}{\tilde{J}} > 1$ then $q \neq 0$, $m \neq 0$, and the system displays ferromagnetic behaviour. For $\eta < 1$, $m = 0$ and $q \neq 0$, and a spin glass state is established. A phase diagram as illustrated in Figure 2.6 can be drawn, which clearly illustrates that the two quantities of interest characterizing the magnetic behaviour in the SK model are the dimensionless parameters $kT/\tilde{J}$ and η.

The latter two parameters can be rescaled as follows to represent physically relevant quantities,

$$\begin{aligned} kT/\tilde{J} &\rightarrow T \\ \frac{\tilde{J}_o}{\tilde{J}} &\rightarrow x \end{aligned}$$

where x represents the impurity concentration. If the amorphous alloy being studied contains only one magnetic element, such as $(Fe_{1-x}Ni_x)_{75}P_{16}B_6Al_3$ (where the magnetic moment of Ni is suppressed by the phosphorous and boron (Geohegan et al, 1981)), $\tilde{J}$ and $\tilde{J}_o$ would be related to the magnetic ion concentration. However in the case of $(Fe_{1-x}Mn_x)_{75}P_{16}B_6Al_3$, both Fe and Mn possess magnetic moments; thus it should not automatically be assumed that the rescaling relationship is linear.

It is useful to note that the phase diagram can be broken down into three principal regions, namely $\eta \leq 1$, which represents a spin glass ground state, an intermediate region $1.0 < \eta < 1.25$, representing a double transition region, and $\eta \geq 1.25$, which has a ferromagnetic ground state. A further discussion concerning magnetization versus temperature curves in different

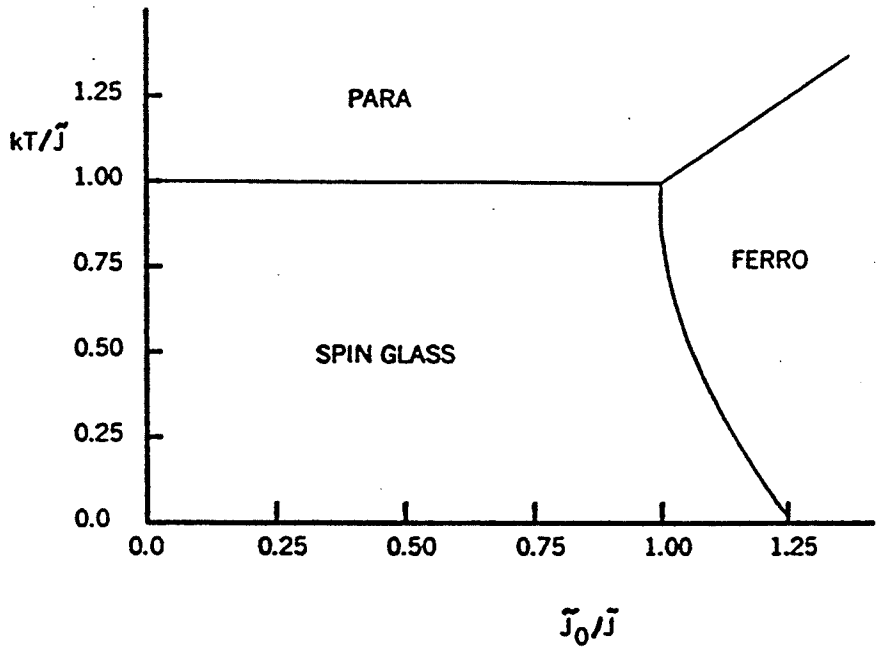

Figure 2.6: Sherrington-Kirkpatrick phase diagram (Sherrington et al, 1975)

applied fields, as well as the corresponding critical exponent values will be presented in Chapter 3, where they will be compared to experimental results on amorphous alloys.

A qualitative interpretation of the SK phase diagram as applied to magnetic ions randomly dispersed throughout a non-magnetic host material is useful for providing further insight into this theory (Geohegan et al, 1981). For small concentrations of the magnetic ions, the separations are large and the ions interact through an indirect exchange interaction (Appendix 1), that oscillates in sign with ion separation. Depending upon the location of a particular magnetic atom with respect to the other moment bearing impurities,

it will be acted on by a collection of fields, which will not necessarily align its moment with any one of the other surrounding moments. Thus, each spin will be oriented randomly, resulting in zero net magnetization.

With increasing (magnetic) impurity concentration, some magnetic ions will be sufficiently close to each other that they can interact directly, thereby forming clusters in which the moments are aligned. An indirect interaction occurs between the clusters however, resulting in zero net sample magnetization.

Beyond a certain critical concentration, x_{crit}, the clusters become sufficiently large to link together, thereby forming an 'infinite' cluster reaching to the sample boundaries. There still exist finite clusters, not connected to the 'infinite' cluster, which freeze with fields in random direction when the temperature is decreased. This affects the alignment of the moments within the 'infinite' cluster by reducing its net magnetization. Since higher temperatures are required to disorder larger clusters, T_c (PM to FM transition temperature) increases as x becomes larger. Similarly, it is clear that T_f (FM to SG transition temperature) is greatest at x_{crit} (coinciding with $\tilde{J}_o/\tilde{J} = 1.0$ in Figure 2.6), since lower temperatures are needed to 'freeze' the spins which are trying to align ferromagnetically, as x is increased. Thus it can be seen that $T_c \sim \tilde{J}_o$ and $T_f \sim \tilde{J}$ (I Kunkel et al, 1988).

As the concentration of the magnetic ions is further increased, the 'infinite' cluster will eventually engulf the finite clusters, until the entire piece

of material is ferromagnetic. This behaviour provides an explanation for the PM-FM transition line, and the raising of T_c with increasing magnetic ion concentration, as well as the disappearance of the reentrant phase beyond a certain concentration.

Effective Field Approach

An alternate calculation employs an effective field approach to an Ising Hamiltonian instead of the 'replica trick' incorporated by Sherrington and Kirkpatrick. A detailed study was carried out for $s = 1/2$ (Southern, 1976), where it was demonstrated that for a Gaussian distribution of exchange bonds, this technique yields the same phase diagram as that predicted by the SK model.

Subsequent analysis for arbitrary s using the following Hamiltonian

$$\mathcal{H} = -\sum_{i<j} J_{ij} s_i s_j - h' \sum_i s_i \quad ; \quad -s \leq s_i \leq s \tag{2.61}$$

where h' represents an applied field, yields the following set of equations (Roshko et al, 1985)

$$m = \frac{1}{\sqrt{2\pi}} \int_{-\infty}^{\infty} s B_s[(kT)^{-1} s(\tilde{J}_o m + \tilde{J}\alpha\sqrt{q} + h')] e^{-\frac{\alpha^2}{2}} d\alpha \tag{2.62}$$

$$q = \frac{1}{\sqrt{2\pi}} \int_{-\infty}^{\infty} s^2 B_s^2[(kT)^{-1} s(\tilde{J}_o m + \tilde{J}\alpha\sqrt{q} + h')] e^{-\frac{\alpha^2}{2}} d\alpha \tag{2.63}$$

It can be shown that the above expressions reduces to (2.57) and (2.58) for $s = 1/2$ and $h' = 0$.

2.3.5 Vector-Spin Model

Having discussed the nature of spin glasses, it would now be useful to examine the behaviour at the 're-entrant' ferromagnetic-spin glass transition, and its manifestation in terms of physical quantities.

In AuFe, the system in which spin-glass behaviour was first observed, the susceptibility increases rapidly as the paramagnetic-ferromagnetic transition is approached from above, displays a plateau as the temperature is decreased further until the ferromagnetic-spin glass transition is approached, and at this point the susceptibility rapidly drops, thereby denoting the 're-entrant' phase transition in this system.

The paramagnetic-ferromagnetic transition is well understood and can be analyzed in light of the discussion presented in the previous sections. However, a rigorous quantitative analysis for the ferromagnetic-spin glass transition has not yet been developed, although a number of theories exist.

Using the SK model, it has been shown (Kornick et al, 1989; II Kunkel et al, 1988) that the nature of this phase transition can also be studied by examining the behaviour of the non-linear component of the susceptibility. It has been suggested that a peak in the non-linear component of the susceptibility, occurring in the low temperature edge of the zero-field susceptibility plateau (i.e. at the proposed critical temperature, T_f) is indicative of a phase transition.

Consider the expression,

$$\chi = \chi_o - a_2 H^2 + a_4 H^4 - \cdots, \tag{2.64}$$

where the odd terms have not been included, in accordance with the symmetry of χ under a field reversal. To ensure the convergence of the above power series, the terms decrease in magnitude and alternate in sign. For small applied fields, the susceptibility can be approximated by

$$\chi \approx \chi_o - a_2 H^2, \tag{2.65}$$

where the coefficient a_2 may be found experimentally by plotting the susceptibility at constant temperature versus H_i^2. For sufficiently small values of H^2, the curve can be approximated by a straight line with a slope of a_2. It has been found in some samples (FeZr, Ma et al, 1991; PdFeMn, II Kunkel et al, 1988) that the slope becomes larger as the susceptibility shoulder is approached from above and below, whereas the range over which the curves can be approximated by a straight line decreases. The resulting behaviour is a peak in the $a_2(T)$ versus temperature graph.

The difficulty with this approach is that it is based upon an Ising mean-field model, which does not account for the 3D (Heisenberg-like nature of most real systems (Gabay et al, 1981). The predicted temperature dependence $a_2(T) \sim (T_{sg} - T)^{-4}$ for $T \leq T_{sg}$ therefore is not expected to describe experimental behaviour. Measurements on potentially re-entrant systems display a peak in $a_2(T)$ that is substantially smaller than expected, which

may also be due to dynamical constraints. This model, does however, predict both the double peaked structure, as well as the peak behaviour in an applied field (lower peak being larger than upper peak in high fields, and lower peaks moving down in temperature with increasing field while upper peaks increase in temperature as the field is increased) observed in several physical systems, including the samples studied in this work.

As stated above, the analysis based on the SK model is theoretically incomplete at low temperatures even though it correctly predicts the observed field and temperature dependence of the susceptibility. To take into account the Heisenberg-like (three dimensional) nature of the spins, an extended theory was proposed using vector spins $\mathbf{S_i}$, with m components, $S_{i\mu}(\mu = 1, ..., m)$, and the following Hamiltonian

$$\mathcal{H} = -\sum J_{ij} \sum S_{i\mu} S_{j\mu} - H \sum S_{i1} \tag{2.66}$$

where J_{ij} is the same as that used for the SK model.

This constitutes one of the most prominent theories describing the ferromagnetic-spin glass transition, and is known as the vector mean-field model (Gabay et al, 1981; Dubiel et al, 1987). It suggests that longitudinal ferromagnetic order is established below the paramagnetic-ferromagnetic transition, and transverse spin-glass order (associated with replica symmetry breaking), along with weak irreversibility [2] occurs at T_f. The line anal-

[2]Recall, for a ferromagnet $\langle\langle m_z\rangle_T\rangle_J \neq 0$, $\langle\langle m_\perp\rangle_T\rangle_J = 0$ and $\langle\langle m_\perp^2\rangle_T\rangle_J = 0$, whereas $\langle\langle m_z\rangle_T\rangle_J \neq 0$, $\langle\langle m_\perp\rangle_T\rangle_J = 0$ and $\langle\langle m_\perp^2\rangle_T\rangle_J \neq 0$, for a transverse spin glass.

ogous to the paramagnetic-ferromagnetic cross-over line is known as the Gabay-Toulouse, or GT line. At even lower temperatures, the possibility of a cross-over from weak to strong irreversibility is suggested, delineated by the d'Almeida-Thouless, or AT line. Unfortunately, the theory predicts nothing about how the above two features are physically manifested, but suggestions have been made that identify them with low temperature peaks sometimes appearing in the field dependent susceptibility data. More will be said concerning this possibility in Chapter 5.

To perform a detailed analysis to determine whether or not the susceptibility displays GT behaviour, the temperature at which the first peak below the ferromagnetic-paramagnetic transition occurs must be compared with the following equation. The peak temperature is predicted to vary with field according to (Dubiel et al, 1987)

$$t_{GT} = \frac{T_{GT}(0) - T_{GT}(H_a)}{T_{GT}(0)} = \sqrt{2}\frac{g\mu_B}{k_B T_{GT}(0)} c H_a, \tag{2.67}$$

where

$$c = \frac{m^2 + 4m + 2}{4(m+2)^2}, \tag{2.68}$$

$T_{GT}(0)$ is the spin glass 'critical temperature' in zero field, and m is the spin dimensionality, taken here to be 3.

The low temperature AT feature is expected to behave according to

$$T_{AT}(0) - T_{AT}(H_a) \sim H_a^n, \tag{2.69}$$

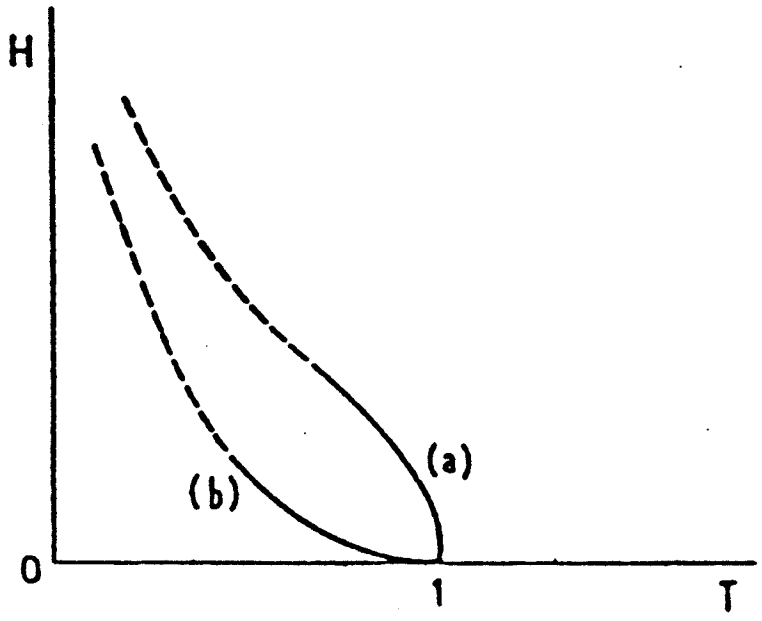

Figure 2.7: Phase diagram of the infinite-range model for classical vector spins. Line (a) corresponds to the freezing of the transverse degrees of freedom, line (b) to the d'Almeida-Thouless line (Gabay et al, 1981).

where $n \approx 2/3$ is predicted. Use of this relationship allows $T_{AT}(0)$ and n to be determined.

The phase diagram corresponding to the vector spin model is illustrated in Figure 2.7.

There exist questions as to where exactly replica symmetry breaking occurs (at the GT or AT line), and whether or not an AT line even exists (Cragg et al, 1982). Later research has resulted in claims that physical systems with two lower transitions have been found (Dubiel et al, 1987), and the appropriate analysis for the samples studied here will be presented in Chapter 5.

2.4 Scaling Theory

The complications encountered in trying to develop a reasonable and solvable model describing the behaviour of magnetic systems near their phase transitions have motivated scientists to examine a revolutionary new proposal, now known as scaling theory, or the homogeneous function approach. Starting in the mid 1960's, suggestions were made that relationships exist between the critical-point exponents that allow all of them to be expressed as a function of two unspecified parameters. Thus, scaling theory does not actually predict numerical values for the critical-point exponents, but rather relates them to each other, and leads to the inequalities listed in Table 2.2 being replaced by equalities. Furthermore, this approach to critical phenomena provides insights into possible forms for the equation of state of a magnetic system.

Although the scaling approach is based on the unproven hypothesis that certain thermodynamic state functions can be expressed as homogeneous functions, it has provided considerable understanding of critical phenomena. Moreover, its predictions have been confirmed by various experimental evidence, which supports their validity.

2.4.1 Static Scaling Hypothesis

According to the static scaling hypothesis, the Gibbs potential $G(T, H)$, which can alternatively can be written as $G(t, H)$ where t is the reduced temperature, can be expressed as a generalized homogeneous function, de-

fined as follows

$$G(\lambda^{a_t}t, \lambda^{a_H}H) = \lambda G(t, H). \tag{2.70}$$

If a function is homogeneous and if a_t and a_H are known at some point, say t_o and H_o, then its value at any other location can be determined by a simple scale change, which is mathematically expressed as follows

$$f(\lambda^{a_t}t_o, \lambda^{a_H}H_o) = \lambda f(t_o, H_o). \tag{2.71}$$

This statement embodies the entire concept behind the homogeneous function approach, namely, that if the scale of the system is changed, in other words, if the parameters that the Hamiltonian depends on, (i.e. H and t) are varied, the form of the Hamiltonian remains unaffected. This indicates that for any number λ, the two indices referred to in the introduction of this section, a_t and a_H, can be found, from which all of the critical exponents may then be determined. Note that all of the other thermodynamic state functions, $F(t, M)$, $U(S, M)$, and $E(S, H)$ are also potential candidates for finding the critical indices; however $G(t, H)$ is the most convenient for exploring the quantities of interest, particularly the magnetization, the susceptibility and the specific heat.

2.4.2 Scaling Theory: Critical Point Exponents

Applying $M(t, H) = -\left(\frac{\partial G}{\partial H}\right)_t$ to the Gibbs scaling relation (2.70) yields the following result,

$$\lambda^{a_H}M(\lambda^{a_t}t, \lambda^{a_H}H) = \lambda M(t, H) \tag{2.72}$$

which is sometimes referred to as the magnetic equation of state. Clearly this expression is also a generalized homogeneous function.

Magnetization Exponent, β

In order to find the magnetization exponent, β, recall that $H = 0$, giving

$$M(t,0) = \lambda^{(a_H-1)} M(\lambda^{a_t} t, 0). \tag{2.73}$$

Since the above expression holds for all values of λ, select $\lambda^{a_t}(-t) = 1$ or $\lambda = \left(-\frac{1}{t}\right)^{1/a_t}$ so that (2.73) becomes

$$M(t,0) = (-t)^{(1-a_H)/a_t} M(-1,0) \sim (-t)^{(1-a_H)/a_t}, \tag{2.74}$$

where the minus sign is required to make the argument in (2.74) positive since $T < T_c$. Recalling the power law dependence of the magnetization in the limit $t \to 0^-$, $M \sim (-t)^\beta$, and comparing the latter to (2.74) yields

$$\beta = \frac{1 - a_H}{a_t}. \tag{2.75}$$

Susceptibility Exponents, γ and γ'

The susceptibility exponents, γ and γ', may be determined using (2.70) in conjunction with the following thermodynamic relationship,

$$\chi_t \equiv \left(\frac{\partial M}{\partial H}\right)_t = -\left(\frac{\partial^2 G}{\partial H^2}\right)_t \tag{2.76}$$

which gives,

$$\lambda^{2a_H} \chi_t(\lambda^{a_t} t, \lambda^{a_H} H) = \lambda \chi_t(t, H). \tag{2.77}$$

For temperatures below T_c, setting $H = 0$ and choosing $\lambda = (-t)^{-1/a_t}$ gives

$$\chi_t(t,0) = (-t)^{-(2a_H-1)/a_t}\chi_t(-1,0) \sim (-t)^{-(2a_H-1)/a_t}. \tag{2.78}$$

When $t \to 0^-$, $\chi_t \sim (-t)^{-\gamma'}$. Comparing this to the above equation indicates that

$$\gamma' = \frac{2a_H - 1}{a_t}. \tag{2.79}$$

Similarly to find γ, which applies to temperatures $T > T_c$, take $\lambda = t^{-1/a_t}$, from which it can be shown that

$$\gamma = \frac{2a_H - 1}{a_t}. \tag{2.80}$$

This demonstrates one of the properties of scaling theory, namely that the primed and unprimed critical-point exponents it predicts are equal. Consequently, the divergence on both sides of the critical temperature will be symmetric.

Critical Isotherm Exponent, δ

The critical isotherm exponent, δ can be found by returning to (2.72) and letting $t = 0$, which gives

$$M(0,H) = \lambda^{a_H-1}M(0,\lambda^{a_H}H). \tag{2.81}$$

Choosing $\lambda = H^{-1/a_H}$ and inserting this quantity into (2.81), one obtains

$$M(0,H) = H^{(1-a_H)/a_H}M(0,1) \sim H^{(1-a_H)/a_H}. \tag{2.82}$$

By comparing this to the power law dependence for the critical isotherm, valid in the limit $H \to 0$, namely $M \sim H^{1/\delta}$, it can be seen that

$$\delta = \frac{a_H}{1 - a_H}. \tag{2.83}$$

Specific Heat Exponents, α and α'

The fourth set of critical exponents, α and α', which describe the behaviour of the specific heat in a constant magnetic field, can be calculated using the expression relating C_H to the Gibbs function,

$$C_H \equiv -T \left(\frac{\partial^2 G}{\partial T^2} \right)_H. \tag{2.84}$$

Applying the latter equation to (2.70) yields

$$\lambda^{2a_t} C_H(\lambda^{a_t} t, \lambda^{a_H} H) = \lambda C_H(t, H). \tag{2.85}$$

Inserting $H = 0$ and $\lambda = (-t)^{-1/a_t}$ into this equation, and then comparing the latter to the power law form of the specific heat, $C_H \sim (-t)^{-\alpha'}$ gives

$$\alpha' = 2 - \frac{1}{a_t}. \tag{2.86}$$

Using similar techniques to find α, it is elementary to demonstrate that

$$\alpha = \alpha' \tag{2.87}$$

as required by scaling theory.

2.4.3 Exponent Equalities

It has thus been confirmed through the above derivation that in the scaling approach all of the critical exponents can be expressed in terms of only the two parameters, a_t and a_H. Using this property, the inequalities listed in Table 2.2 can be replaced by equalities. It is important to realize that this is a direct result of the scaling assumption, since the only two variables, H and t involved in the Gibbs potential enter without any relationship between them being specified, aside from the homogeneity of the Gibbs function. Thus, the connection between the exponent values does not depend on the system being studied; however, the actual values of the critical indices vary from model to model (Wang, 1990).

2.4.4 Scaling Law Equation of State

Besides predicting the relationship between the critical point exponents, scaling theory also provides insights into the functional form of the magnetic equation of state, which have been verified by experimental results. Returning to the scaling law equation of state (2.72), which can be rewritten as

$$M(t,H) = \lambda^{a_H-1} M(\lambda^{a_t} t, \lambda^{a_H} H), \tag{2.88}$$

and taking $\lambda = t^{-1/a_t}$, gives

$$M(t,H) = t^{(1-a_H)/a_t} M\left(1, \frac{H}{t^{a_H/a_t}}\right). \tag{2.89}$$

The above expression may be simplified by recalling the definition of β and δ in terms of a_H and a_t, and incorporating the Widom equality, $\gamma = \beta(\delta - 1)$; the equation of state may then be written as follows

$$M(t,H) = t^{\beta} M\left(1, \frac{H}{t^{\beta\delta}}\right) = t^{\beta} M\left(1, \frac{H}{t^{\gamma+\beta}}\right) = t^{\beta} F\left(\frac{H}{t^{\gamma+\beta}}\right). \qquad (2.90)$$

From the latter equation it can be clearly seen that scaling theory says nothing about the functional form of F, indicating only the nature of its argument. However, this expression provides the basis for deriving the asymptotic power law dependencies, valid in the limit $t \to 0$ and used earlier (Table 2.1).

The scaling expression for the isothermal susceptibility may be found by simply differentiating (2.90) with respect to H, giving

$$\chi(t,H) = \left(\frac{\partial M}{\partial H}\right) = t^{-\gamma} F'\left(\frac{H}{t^{\gamma+\beta}}\right), \qquad (2.91)$$

where $F'(H/t^{\gamma+\beta})$ represents the derivative of $F(H/t^{\gamma+\beta})$ with respect to its argument, $H/t^{\gamma+\beta}$. This can be rewritten as (Williams, 1991)

$$\begin{aligned} \chi(t,H) &= \left(\frac{1}{t^{\gamma+\beta}}\right)^{\frac{\gamma}{\gamma+\beta}} F'\left(\frac{H}{t^{\gamma+\beta}}\right) = H^{\frac{-\gamma}{\gamma+\beta}} \left(\frac{H}{t^{\gamma+\beta}}\right)^{\frac{\gamma}{\gamma+\beta}} F'\left(\frac{H}{t^{\gamma+\beta}}\right) \\ &= H^{(1/\delta)-1} G\left(\frac{H}{t^{\gamma+\beta}}\right) \end{aligned} \qquad (2.92)$$

using

$$G(x) = x^{\frac{\gamma}{\gamma+\beta}} F'(x) \quad ; \quad x = \left(\frac{H}{t^{\gamma+\beta}}\right). \qquad (2.93)$$

Alternatively, the last line in (2.92) can be much more simply derived by letting $\lambda = H^{-1/a_H}$ in (2.77), so that the latter becomes

$$\chi(t,H) = H^{(1-2a_H)/a_H} \chi(H^{-a_t/a_H} t, 1). \qquad (2.94)$$

Substituting in for β, γ and δ, and designating $\chi(H^{-a_t/a_H}t, 1)$ as $K\left(\frac{t}{H^{1/(\gamma+\beta)}}\right)$ gives

$$\chi(t, H) = H^{1/\delta - 1} K\left(\frac{t}{H^{1/(\gamma+\beta)}}\right), \tag{2.95}$$

which has the same $H-$dependence as (2.92).

One particularly interesting feature of the susceptibility versus temperature behaviour is the shift of the susceptibility peak with increasing field as seen in Figure 2.8.

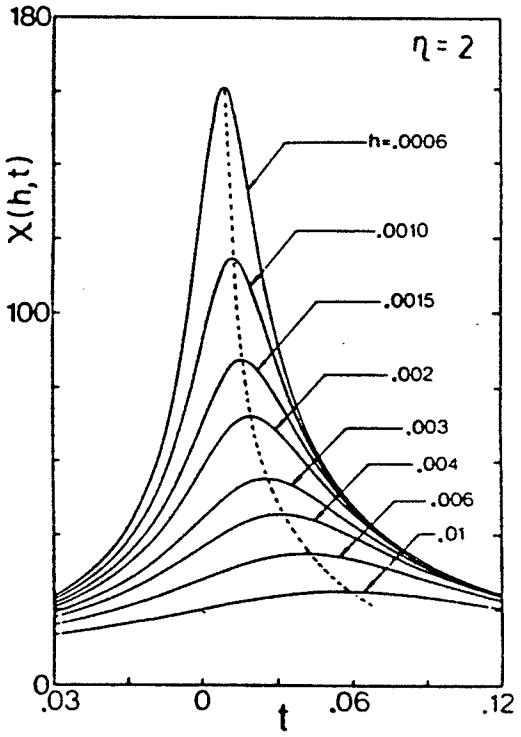

Figure 2.8: The susceptibility $\chi(h, t)$ in various fixed fields h; the dotted line represents the cross-over line. (Williams, 1991)

This feature of the susceptibility is incorporated in (2.92) or (2.95) as can be seen when differentiating these expressions with respect to temperature, and then setting the result equal to zero. Using (2.92), the following is obtained

$$\left(\frac{\partial \chi}{\partial t}\right)_{H,t=t_p} = H^{(1/\delta)-1}\frac{(\gamma+\beta)H}{t^{\gamma+\beta+1}}G'\left(\frac{H}{t^{\gamma+\beta}}\right)_{t=t_p} = 0. \tag{2.96}$$

Obviously, the above expression will hold only if $G'(H/t_p^{\gamma+\beta}) = 0$, where t_p represents the reduced temperature at which the susceptibility peaks. This requires that the scaling function $G(H/t^{\gamma+\beta})$ at t_p in a fixed field be a constant, requiring in turn that

$$\frac{H}{t_p^{\gamma+\beta}} = const. \tag{2.97}$$

Thus, the temperature at which the maximum occurs (along the so-called 'cross-over' line) increases as H increases according to

$$\frac{T_p - T_c}{T_c} = t_p \propto H^{1/(\gamma+\beta)} \tag{2.98}$$

where $\gamma + \beta$ is known as the 'cross-over' exponent. Moreover, because $G(H/t_p^{\gamma+\beta})$ is a constant, it can be seen from (2.92) that

$$\chi(H, t_p) \propto H^{(1/\delta)-1} \tag{2.99}$$

which indicates that the height of the maximum is solely field-dependant and decreases with increasing H ($\delta > 1$), thereby reproducing the experimentally observed behaviour of the susceptibility in the vicinity of T_c. The advantage

of using (2.99) instead of (2.11) to find δ is that the former expression is independent of the critical temperature, whereas any analysis involving the latter equation requires previous knowledge of T_c. In order to find the cross-over exponent, T_c must, however, be determined.

Although scaling theory has been a great success, its postulates have not been proven, and hence there remain scientists who still consider it to be an '*ad hoc* assumption, entirely devoid of physical rationale'. Attempts to resolve this situation have prompted the development of yet another approach, namely the Renormalization Group theory (Huang, 1987; Fisher, 1983), whose most fundamental purpose is to provide a rationale for scaling and justify the universality observed between the behaviour of apparently unrelated physical systems. This theory also provides methods for calculating actual numerical values for the critical-point exponents (not just the relationships between them), as well as providing insight into the nature of scaling functions.

Chapter 3

Review of Previous Results

$Fe_{1-x}Mn_x$ [1] samples with varying composition have been investigated using a variety of experimental techniques, some of the more important and interesting of which will now be considered as part of a general review of previous experimental results. More specifically, existing magnetization and susceptibility data will be presented, along with analysis techniques which yield critical exponent values and critical temperatures characterizing the various phase transitions. Finally, a brief summary of neutron scattering and Mössbauer experiments will be presented to give insight into other methods used to investigate amorphous alloys.

3.1 FeMn Phase Diagram

Materials with competing exchange interactions, such as amorphous FeMn (elemental Fe is ferromagnetic, whereas Mn is antiferromagnetic), generally

[1] It is important to note that the alloys studied actually have a chemical composition $(Fe_{1-x}Mn_x)_{75}P_{16}B_6Al_3$ even though they are generally referred to as $Fe_{1-x}Mn_x$.

become spin glasses over some composition range. Evidence has been published that would indicate that the spins in FeMn 'freeze' from a paramagnetic state to form a spin glass for Mn concentrations (i.e. x) between 0.35 and 0.47 (Mirebeau et al, 1990).

In the event that the mean of the exchange coupling constant distribution ($\tilde{J}_o$) becomes comparable to its width ($\tilde{J}$), which according to Mirebeau et al, 1990, [2] occurs for $0.22 \leq x \leq 0.35$, theoretical models such as the SK model predict more complex behaviour. The sample is paramagnetic at higher temperatures, and becomes ferromagnetic with decreasing temperature before finally entering a spin glass phase as the temperature is lowered further. This type of behaviour is the qualifying feature for a reentrant system.

At lower Mn concentrations ($x \leq 0.22$, Mirebeau et al, 1990), the sample enters a ferromagnetic ground state, but apparently displays no lower temperature transition. This behaviour results in a FM-PM transition line intersecting a line bounding the spin glass phase at a multicritical point, as illustrated in the phase diagram in Figure 3.1. In accordance with the latter, three 'critical' temperatures can be defined, namely T_c representing the usual FM-PM transition temperature, T_{sg} defining the PM-SG line, and T_f denoting the FM-SG critical temperature. Upon comparing the proposed FeMn phase diagram shown in Figure 3.1 to that predicted by Sherrington and Kirkpatrick (Figure 2.6), a striking similarity would seem apparent,

[2]This is based on magnetization measurements, where T_f was found following the technique used by Manheimer et al, 1982 discussed in Section 3.2.2.

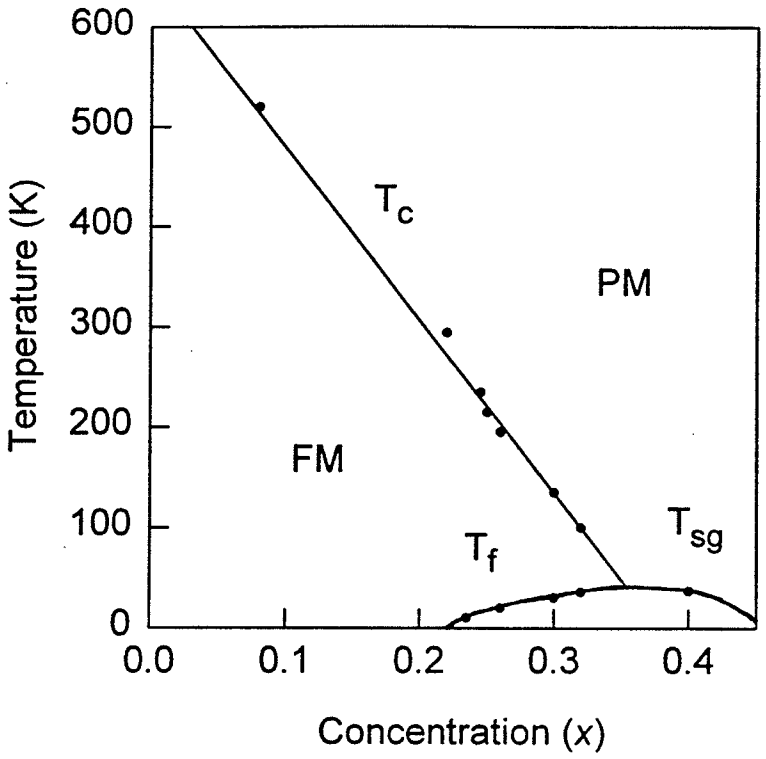

Figure 3.1: FeMn phase diagram. (Mirebeau et al, 1990)

with the main difference between the two diagrams being that the PM-SG line in Figure 3.1 does not extend to $x = 1$, as suggested by the SK model. However this similarity is only qualitative and is based on a phase diagram constructed using magnetization measurements, the interpretation of which can sometimes be misleading.

It is the objective of this work to re-examine the above conclusions based on a detailed linear and non-linear field and temperature dependent susceptibility study, combined with existing microscopic investigations of the FeMn system.

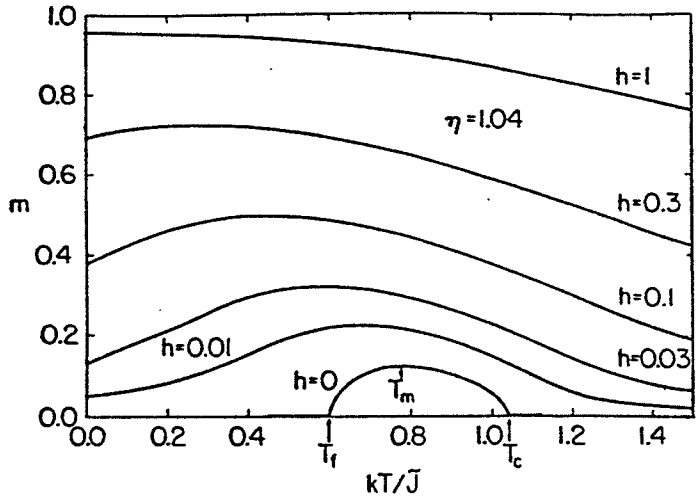

Figure 3.2: Model predictions for magnetization versus temperature with various reduced fields ($h = \mu B_a/\tilde{J}$) for $\eta = \tilde{J}_o/\tilde{J} = 1.04$. (Geohegan et al, 1981)

3.2 Magnetic Behaviour of FeMn

3.2.1 Theoretical Predictions

Returning to the effective field approach (Section 2.3.4), magnetization and susceptibility curves can be generated by solving the coupled equations (2.62) and (2.63). This was done for various $\tilde{J}_o/\tilde{J}$ values and a number of applied fields in order to provide a complete representation of the predicted magnetization and susceptibility for the different regions of the phase diagram. The results displayed in Figures 3.2 and 3.3 have excellent qualitative agreement with the experimental measurements presented below, indicating that amorphous alloys such as FeMn display several features which are generally well described by the SK model.

Although the theoretical curves in Figure 3.2 and 3.3 are somewhat more

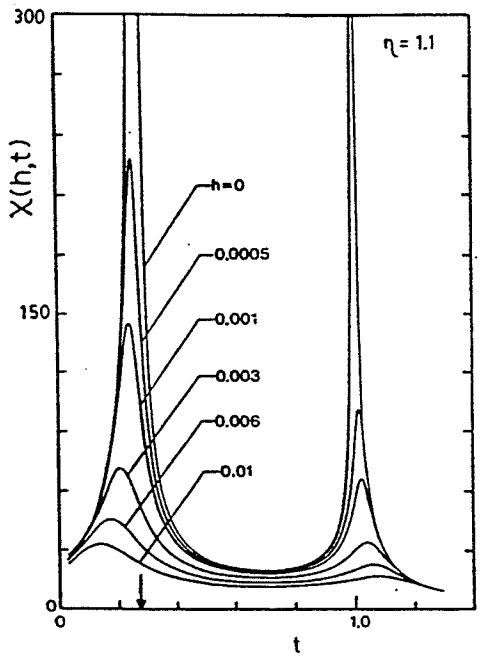

Figure 3.3: Effective field model predictions for susceptibility versus temperature with different reduced fields ($h = H_{appl}/T_f$)for $\eta = \tilde{J}_o/\tilde{J} = 1.1$. The arrow indicates the location of T_f. (Kornik, 1990)

symmetric than those obtained experimentally (Figure 3.4 and Figure 3.7 respectively), the resemblance between the diagrams is still truly remarkable. As can be seen for the magnetization data, applying a field causes the peak temperature to move down in temperature, as well as generating a nonzero magnetization in the temperature ranges $T < T_f$ and $T > T_c$. Furthermore, if H_{appl} is large enough, M remains at its peak value below T_f, instead of dropping to zero, presumably eliminating the low temperature transition. As for the susceptibility measurements; a double peaked structure is observed as well as the correct field dependent behaviour, i.e. the lower temperature peaks move down in temperature with increasing field, and the high temper-

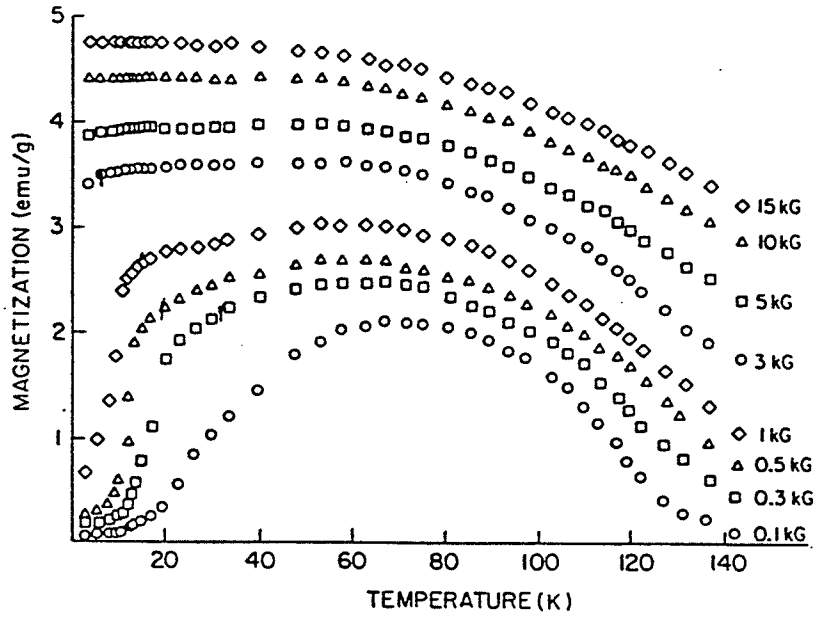

Figure 3.4: Magnetization versus temperature for $x = 0.32$ in various applied fields. (Yeshurun et al, 1980)

ature peaks move up in temperature with increasing field. Referring back to Figure 2.9, which shows effective field model predictions for the susceptibility when $\eta = 2.0$, a single peak and the corresponding field dependence is observed in agreement with the behaviour of the well-understood paramagnetic to ferromagnetic transition.

3.2.2 Experimental Results

Paramagnetic-Ferromagnetic Transition

Magnetization versus temperature curves are among the most often used measurements for determining critical exponents and temperatures. In the vicinity of T_c the magnetization should obey the usual ferromagnetic-paramagnetic transition power laws listed in Table 2.1 with the critical exponents

tabulated in Table 2.3. Originally, the latter were found by means of Arrott plots, namely by plotting $M^{1/\beta}$ versus $(H/M)^{1/\gamma}$, and adjusting the exponents until a best straight line is obtained. A sample graph is shown in Figure 3.5 consisting of a collection of isotherms above and below the critical temperature from which it is estimated that $\gamma = 1.6$ and $\beta = 0.4$. The third critical exponent can then easily be found via the (scaling) relationship $\gamma = \beta(\delta - 1)$. The isotherms are almost straight parallel lines, and suggest a critical temperature (the straightest line, which extrapolates to the origin represents the critical isotherm) in the vicinity of 100 K. This technique is not particularly reliable though since several different exponent combinations may yield straight line fits.

Scaling theory avoids this problem by providing an alternate, improved method for finding the critical exponents. Recalling the expression

$$M(H,t) = t^{\beta} F\left(\frac{H}{t^{\gamma+\beta}}\right) = t^{\beta} F\left(\frac{H}{t^{\beta\delta}}\right) \tag{3.1}$$

from Section 2.4.4 and defining $y \equiv (t/|t|)(H/|t|^{\beta\delta})$ allows the magnetization to be expressed as

$$M(H,t) = t^{\beta} F(y) \tag{3.2}$$

for convenience.

The behaviour of the scaling function $F(y)$ can then be divided into two parts, namely $F_+(y)$ for $T > T_c$, and $F_-(y)$ for $T < T_c$. If the correct exponents and critical temperature can be chosen, all of the data will collapse onto two curves in a plot of $\log(M/t^{\beta})$ versus $\log(h/t^{\beta\delta})$, – one for $T > T_c$, and

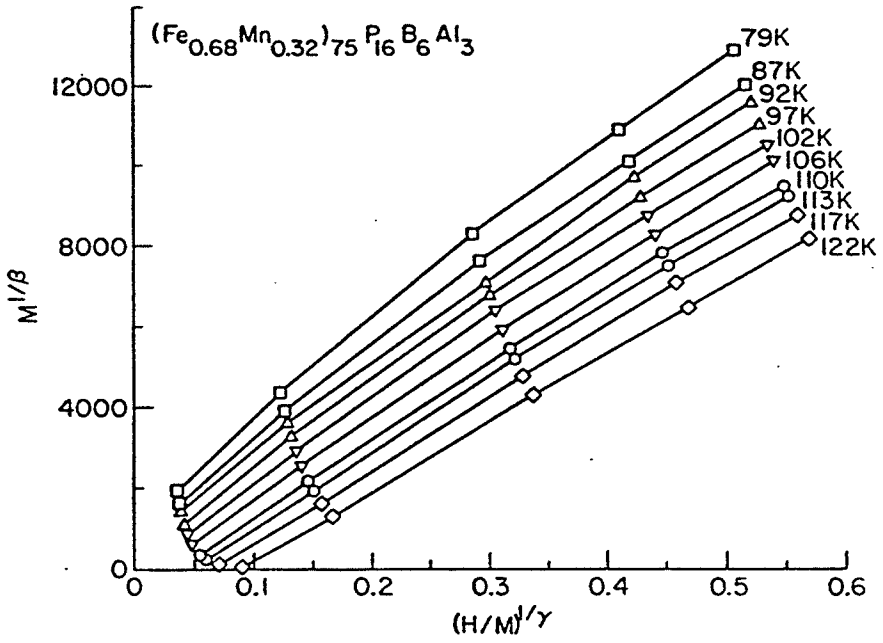

Figure 3.5: Arrott plot for isotherms near T_c for $x = 0.32$ alloy (Yeshurun et al, 1981)

another for $T < T_c$. Note that M/t^{β} versus $H/t^{\beta\delta}$ would serve the same purpose, but taking the logarithm of each of these quantities facilitates detection of deviations from the 'universal' curves when T_c or the critical exponents are varied. A sample plot is shown in Figure 3.6, the two branches represent the best fits possible using reasonable exponent values, i.e. restricting possible exponent values to $2 \leq \delta \leq 6$, $0.03 \leq \beta \leq 0.50$ and allowing T_c to vary as much as 10%. The exponents thus determined are unique, with an assigned error denoting the variation permitted before a deviation from the 'best curve' fit becomes discernable. The values found using this method are listed in Table 3.1 along with the corresponding critical temperatures

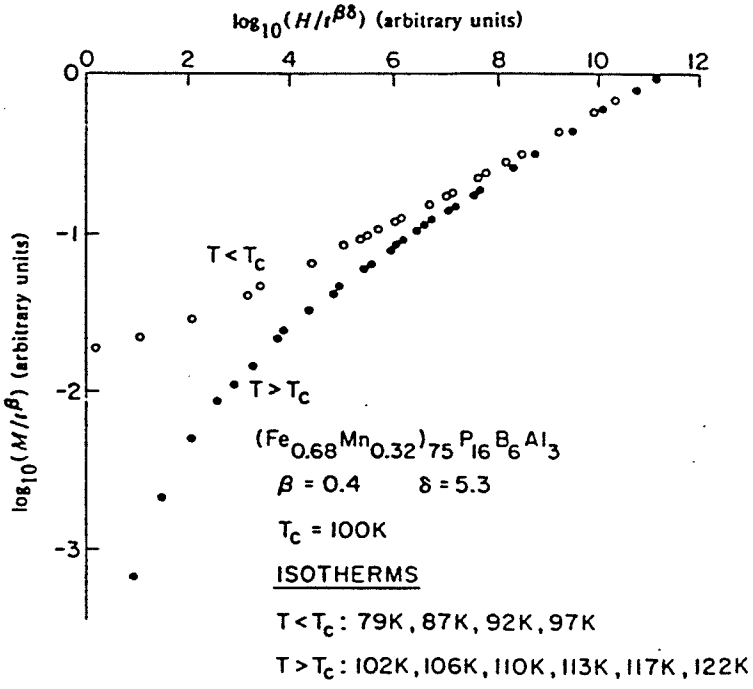

Figure 3.6: Scaled magnetic data for the PM-FM transition. (Yeshurun et al, 1981)

for the various Mn concentrations. Notice how the values found by different researchers vary, suggesting that this technique, although superior to Arrott plots, is still not definitive. This could be due to variations in composition, although the samples appear to have been prepared in the same laboratory (Chen et al, 1976). Note also that the sample composition for Yeshurun et al, 1981 were rechecked using microprobe analysis; the x values were found to be somewhat lower than the nominal values.

Some a.c. susceptibility measurements (Geohegan et al, 1981; Salamon et al, 1980) have also been performed and used to generate a set of critical exponents. Although the measurements included samples with a greater composition range than will be examined here, the data collected was neither

Table 3.1: Critical Values from Magnetization Measurements (Yeshurun et al, 1981 (top); Manheimer et al, 1983 (bottom))

x	T_c	β	δ [γ]	T_f (T_{sg})	$\tilde{\beta}$	$\tilde{\delta}$ [$\tilde{\gamma}$]
0.20	293 ± 4	0.40 ± 0.03	5.1 ± 0.3 [1.64]*	14 ± 2		
0.30	107 ± 2	0.40 ± 0.04	5.0 ± 0.3 [1.60]	31 ± 2	0.4 ± 0.03	4.5 ± 0.3 [1.4]
0.32	100 ± 2	0.40 ± 0.03	5.3 ± 0.3 [1.72]	38 ± 2	0.4 ± 0.03	4.5 ± 0.03 [1.4]
0.36	42 ± 2	0.40 ± 0.05	2.5 ± 0.5 [0.60]			
0.20	280	0.41	[1.45]	28		
0.30	112	0.47	[1.42]	29	0.4	1.4
0.35	101	0.30	[1.55]	65	0.3	2

* Calculated $\gamma/\tilde{\gamma}$ values using Widom equality (for comparison to Manheimer values)

over as large a field or temperature range as that presented here, nor was the analysis as complete. Only the critical exponent $\delta(\tilde{\delta})$ was found, and the supposed FM-SG critical temperature (T_f) was simply estimated from the position of the lower temperature feature of the double peaked structure observed in an applied field. There was, furthermore, no mention of a third peak at very low temperatures for samples in the concentration range $0.23 < x < 0.26$, as will be presented in Chapter 5.

In order to determine the critical exponents the sample susceptibility was measured in the presence of several applied fields, after which scaling relationships similar to those in the Section 2.4.4 were used to extract the desired information.

In the presence of an applied field a double peaked structure illustrated in Figure 3.7 was observed. Clearly the high temperature peaks move to higher temperatures as the field is increased, in agreement with the SK model predictions, as well as scaling (Figure 3.3).

The critical exponents found using this technique are listed in Table 3.2 (Geohegan et al, 1981). The uncertainty in δ as well as the low values for the compositions $x = 0.20$ and 0.30, is a consequence of the curvature observed in the $\log(\chi_{peak})$ versus $\log(H)$ plots (Figure 3.8), making it impossible to determine a unique slope. The low values are likely an average value obtained in fitting the data. An improved value could have been obtained by calculating the low field asymptotic slope.

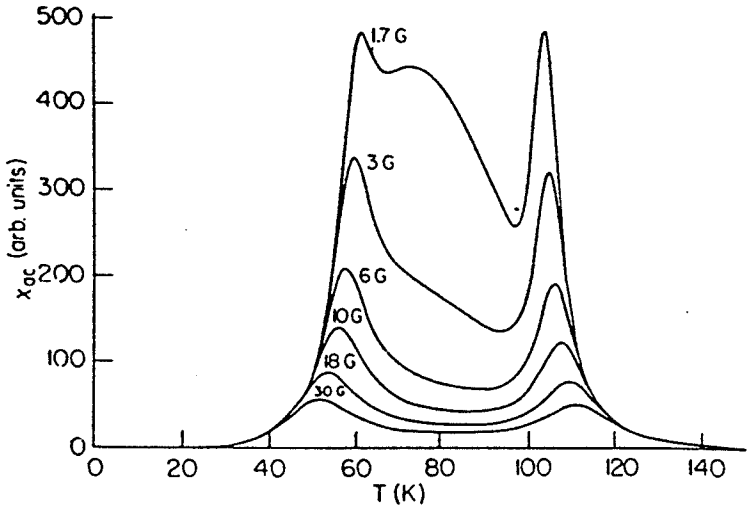

Figure 3.7: A.C. susceptibility temperature dependence of $x = 0.35$ alloy in several applied fields (Geohegan et al, 1981)

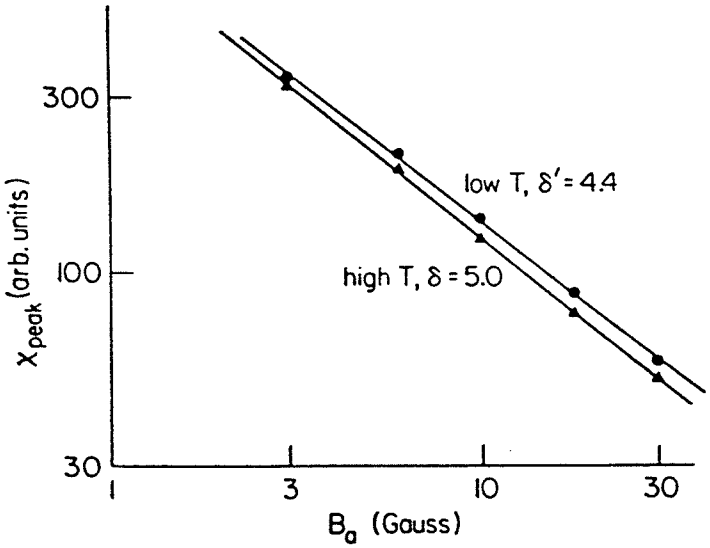

Figure 3.8: δ plot: $\log(\chi_{peak})$ versus $\log(H_a)$ for $x = 0.35$ (Geohegan et al, 1981)

Table 3.2: Critical Values from Susceptibility Measurements (Geohegan, 1981)

x	T_c (K)	T_f (K)	T_{sg} (K)	δ	$\tilde{\delta}$
0.10	$> T_{room}$				
0.15	$> T_{room}$	<5			
0.20	280	34		≈ 3.5	
0.30	114	54		≈ 4	
0.35	104	63		5.0	4.4
0.36			42.0†		
0.40			42		
0.44			29.5†		
0.45			29*		
0.47			28.6†		
0.50			27*		
0.53			27.3†		
0.55			26.5*		
0.59			24.9†		
0.60			26*		

*(Salamon et al, 1980) †(Yeshurun et al, 1981)

Ferromagnetic-Spin Glass Transition

The drop in magnetization illustrated in Figure 3.4 indicates that for $x = 0.32$ the ferromagnetic state may not be stable as the temperature is decreased: the material undergoes a potential phase change to enter a new state with reduced M, either a spin glass or anti-ferromagnetic state. Alternatively, the system may simply undergo a canting (asperomagnetic) or cluster glass (non-critical) transition. A ferromagnetic to spin glass transition is similar to the paramagnetic to ferromagnetic transition, at least to the extent that both the paramagnetic and spin glass phases have zero net magnetization.

Some researchers (Yeshurun et al, 1980; Yeshurun et al, 1981; Salamon et al, 1981) also believe that the relationships

$$M(0,T) \sim \left(\frac{T}{T_f} - 1\right)^{\tilde{\beta}} \tag{3.3}$$

and

$$M(H,T_f) \sim H^{1/\tilde{\delta}} \tag{3.4}$$

are valid in the vicinity of T_f suggesting that a critical transition also occurs along the FM-SG line; general consensus concerning the validity of the above two equations has not been reached though. More will be said about this behaviour below.

A scaling plot for this proposed transition, obtained by adjusting T_f, $\tilde{\beta}$ and $\tilde{\delta}$, then yields a graph like the one illustrated in Figure 3.9. The latter plot is very similar to Figure 3.6, however with the temperature axis

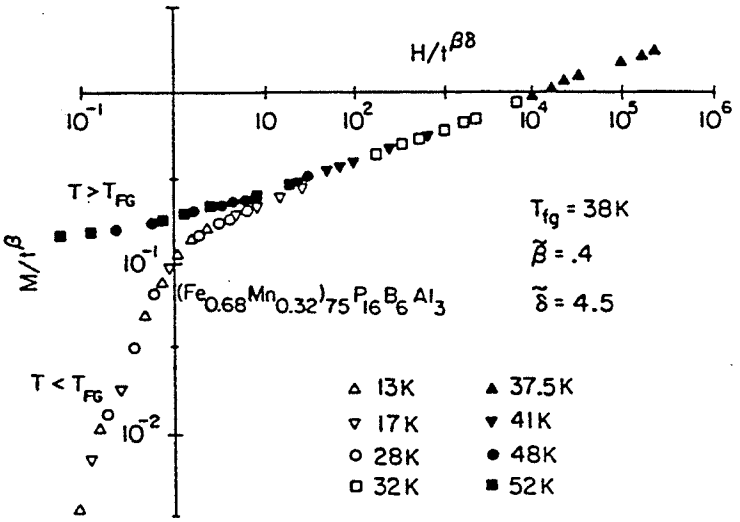

Figure 3.9: Scaled magnetic data for the FG transition (Yeshurun et al, 1981)

reversed; consequently, the two branches are interchanged, with the isotherms in the ferromagnetic regime always constituting the upper branch. Critical exponents and T_f extracted from the data are listed in Table 3.1 for the different Mn concentrations. When looking at the latter values though, it is important to realize that it has not yet been established whether or not the linear magnetic properties for this transition are expected to conform to scaling law predictions or not.

In fact, it is still debated whether or not the material undergoes a phase transition, or the spins just gradually freeze when going from a ferromagnetic to perhaps a cluster glass state. Further evidence suggesting that the behaviour is indeed critical was found by (Yeshurun et al, 1980; $0.2 < x < 0.36$) and (Geohegan et al, 1981; $0.15 < x < 0.35$) where it is documented

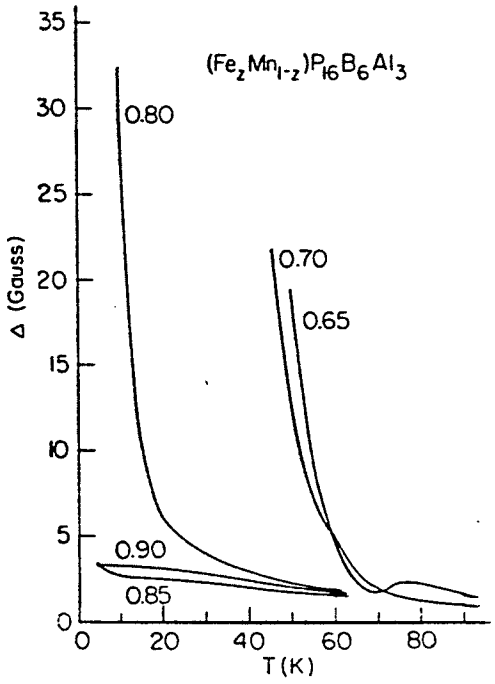

Figure 3.10: Temperature dependence of the coercivity, Δ (Geohegan et al, 1981)

that the magnetic susceptibility along the FM-SG line also obeys the scaling hypothesis.

As with the magnetization, the temperature axis for the FM-SG transition is 'reversed' with respect to that of the PM-FM transition. A manifestation of this can be seen in Figure 3.7, the low temperature field dependant peaks occur at a lower temperature than the zero field peak. The following argument can be used to explain this phenomena; for this transition M decreases with decreasing temperature, but since $M(T_f) > M(\tilde{T}_{peak})$, the susceptibility maximum must occur below the FM-SG critical temperature. Hence the location of $\chi(\tilde{T}_{peak})$ provides an lower limit for T_f.

A plot of $\log(\chi_{peak})$ versus $\log(H_a)$ can then be used to find $\tilde{\delta}$, as illustrated in Figure 3.8, and the exponent values found using this method are listed in Table 3.2. As with the magnetization, the Hopkinson maximum is not expected to interfere with the analysis since it is predicted to have a negligible contribution below T_f. Furthermore, hysteresis effects, which would complicate the situation are insignificant in the temperature region of interest (Figure 3.10).

The $\tilde{\delta}$ plot shown in Figure 3.8 is virtually identical to the δ plot in the same diagram, except that the entire line is shifted up a little. This type of agreement, namely the accuracy with which scaling behaviour is reproduced, suggests that this transition is indeed critical.

Paramagnetic-Spin Glass Transition

Zero field susceptibility versus temperature measurements are useful for identifying spin glasses since their susceptibility is usually substantially smaller than that of a system with a ferromagnetic phase, as can be seen when considering Figure 3.11.

As stated in Section 2.3.4, this transition is identified by a sharp cusp in the zero field susceptibility, agreeing with the SK prediction for this region of the phase diagram. Examples of this type of behaviour are illustrated in Figures 3.8 and 3.12. The peak positions, used to determine T_{sg} are listed in Table 3.2.

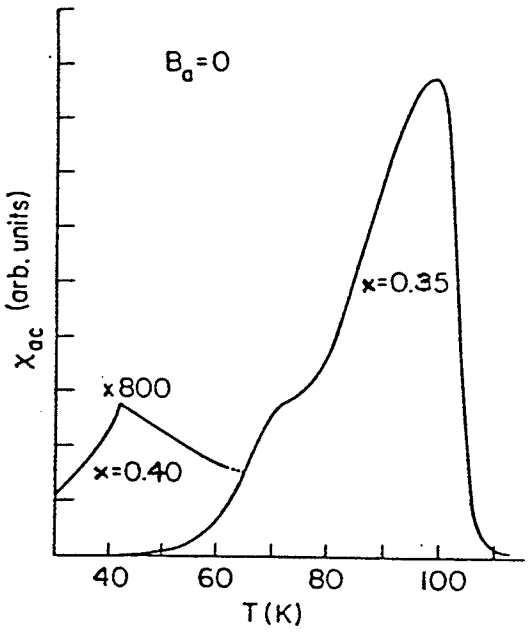

Figure 3.11: A.C. susceptibility versus temperature. Note that the $x = 0.40$ data has been multiplied by 800. Also, the composition $x = 0.40$ is a spin glass, whereas $x = 0.35$ has a ferromagnetic phase. (Geohegan et al, 1981)

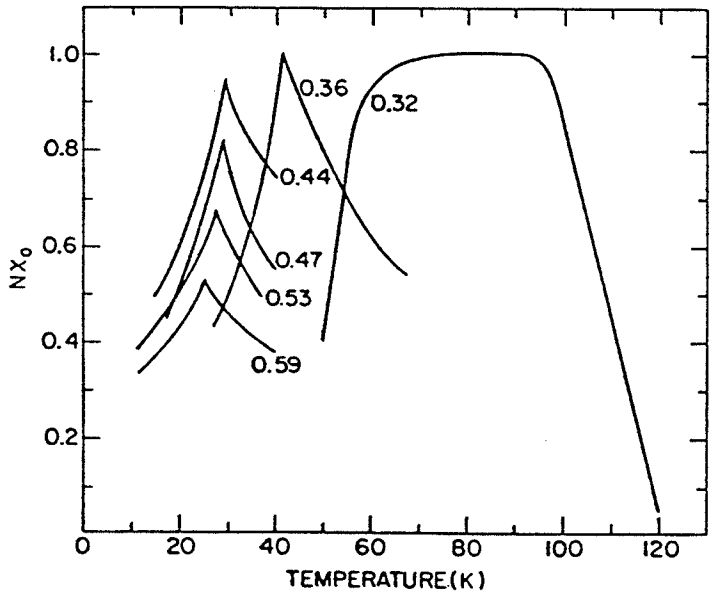

Figure 3.12: A.C. susceptibility versus temperature (Salamon et al, 1980)

The peak height in Figure 3.12 is expected to increase with decreasing x as the multicritical point is approached along the PM-SG line (Salamon et al, 1981) because the susceptibility diverges in the vicinity of the ferromagnetic phase boundaries. No concensus has yet been reached as to whether or not the 'PM-SG' transition in FeMn is critical; however, attempts have been made to describe this phase change using the following scaling equation (Salamon et al, 1981; Yeshurun et al, 1981)

$$\chi(T,x) = \lambda^{\gamma}\chi(\lambda\mu(T,x), \lambda^{\phi}g(T,x)), \tag{3.5}$$

where the scaling fields, μ and g depend upon the shape of the phase diagram and the location of the multicritical point, taken to be situated at $x_{\mathrm{MCP}} = 0.36$ and $T_{\mathrm{MCP}} = 41$ K on the phase diagram. Choosing the MCP to coincide with the origin of the scaling axes, i.e. $g = \mu = 0$, the $g = 0$ axis is taken to be an extension of the FM-SG line, and the $\mu = 0$ axis is chosen to lie along the PM-FM line. Taking $\lambda^{\phi}g = 1$ then gives

$$\chi(T,x) = g^{-\gamma/\phi}\chi\left(\frac{\mu}{g^{1/\phi}}\right) \tag{3.6}$$

which displays a cusp at $\mu/g^{1/\phi} = const.$, thereby defining the FM-SG line.

The cross-over exponent, ϕ may be found by plotting $\log(\mu)$ versus $\log(g)$, using the peak temperatures in Figure 3.12 to generate a graph with a slope of $1/\phi$. Having done this, $\chi/g^{-\gamma_t/\phi}$ (where γ_t is the tricritical susceptibility exponent) can be plotted versus the scaling variable $\mu/g^{1/\phi}$, as illustrated in Figure 3.13. Values of $1/\phi = 1.36 \pm 0.1$ and $\gamma_t = 1.1 \pm 0.1$ were found using

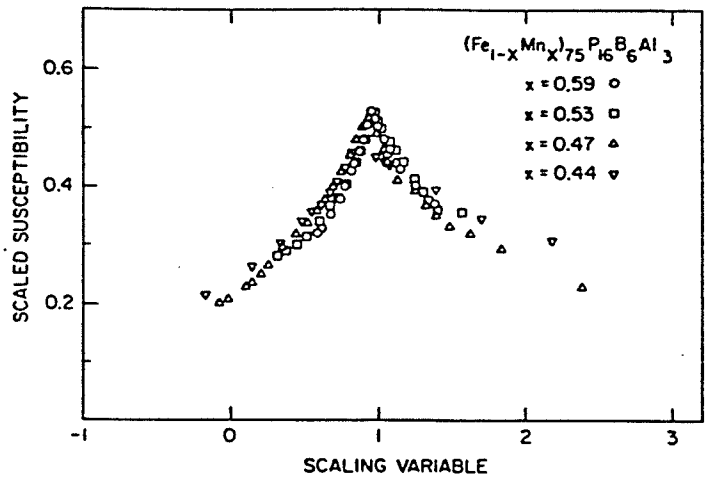

Figure 3.13: Scaled susceptibility along the PM-SG line (Yeshurun et al, 1981)

the above technique.

The success of the above procedure by no means resolves the uncertainty as to whether or not the 'PM-SG' transition is actually a true phase transition. Only further theoretical analysis and experimental measurements could confirm if the above analysis and its results are indeed valid.

3.2.3 Overview

When comparing the results in Tables 3.1 and 3.2, it can be seen that sizable discrepancies exist between some of the critical temperatures and exponents. Considering in particular the values for T_f, those obtained from magnetization measurements are much lower than those determined from susceptibility temperature sweeps. It is important to realize though that there is no physi-

cal feature unambiguously agreed upon as identifying the FG-SG critical temperature, so the latter must be determined, along with the other adjustable variables solely from the scaling plot.

The differences in T_f would affect the location of the FM-SG line in the phase diagram, and also the points at which it intersects the PM-SG and PM-FM lines, which in turn would cause variations in the critical concentration and temperature. It is this ambiguity that has been in part, motivation for this detailed study of the FeMn system, using not only linear, but also non-linear susceptibility measurements.

3.3 Neutron Scattering Results

Another type of probe which is sensitive to the microscopic, as opposed to macroscopic properties of the sample, is neutron diffraction. Although this technique can be used to study the distribution, orientation and ordering of magnetic moments, the discussion here will concentrate on the magnetic ordering, and how neutron diffraction can be used to investigate phase transitions.

Using neutrons, basically two techniques, involving either scattering or polarization analysis, can be used to study magnetic materials. Considering first scattering techniques; in paramagnetic (disordered) substances, the atomic moments have random orientations causing the neutrons, which have a dipole moment even though they are electrically neutral, to be scattered

incoherently. On the other hand, in ferromagnetic (and other ordered) substances, the atomic moments are parallel (or antiparallel in the case of an antiferromagnetic sample) resulting in coherent scattering, and therefore a diffraction pattern.

Using polarization analysis, a beam of polarized neutrons becomes depolarized after passing through a ferromagnetic sample with several large domains (as opposed to many small ones). It is interesting to note that in the more common scattering experiments mentioned above, the microscopic neutron-spin interaction is probed, whereas polarization analysis measures the neutron spin precession over the much larger mean domain size. In paramagnets and spin glasses, where disorder occurs at microscopic levels, the neutrons pass through the sample without becoming depolarized.

This can be understood by recalling that the neutron's spin undergoes Larmor precession in a field, such as that within a ferromagnetic sample, thus causing depolarization of the beam. In a paramagnet and spin glass, however, $B(t)$ fluctuates much more rapidly than the time required for one Larmor precession; thus the neutrons remain polarized.

The latter technique was used to investigate the properties of Fe$_x$Mn (Mirebeau, 1990), for concentrations in the range $0.07 < x < 0.41$, a range that includes non-frustrated ferromagnets, weakly frustrated alloys, samples displaying reentrant behaviour, and pure spin glasses. The results are illustrated in Figure 3.14.

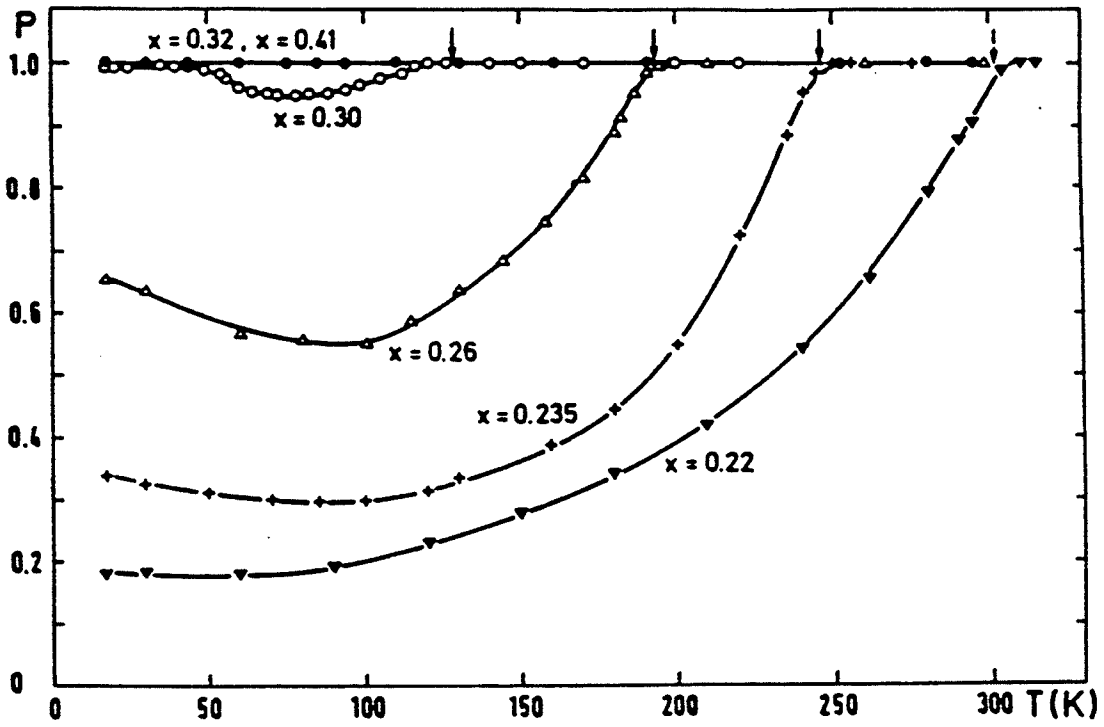

Figure 3.14: Polarization, P as a function of temperature for $Fe_{1-x}Mn_x$, where the arrows indicate the Curie temperature. A neutron wavelength of $\lambda = 5$ Angstroms was used, along with an applied field of 5 Oe. Not shown are the results for the $x = 0.07$ sample, which display strong neutron depolarization over the whole temperature range. (Mirebeau et al, 1990)

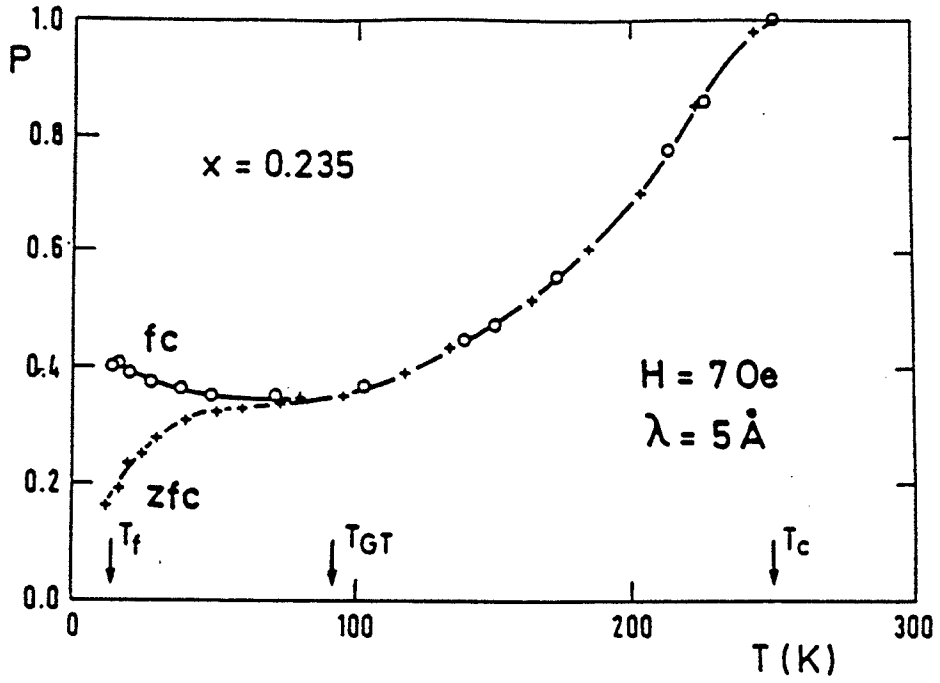

Figure 3.15: Polarization versus temperature for $Fe_{1-x}Mn_x$, $x = 0.235$, where the first, second and third arrows represent the AT, GT and Curie temperatures respectively. The FC curve represents the field cooled polarization, and the ZFC curve is the zero field cooled data. (Mirebeau et al, 1990)

Depolarization measurements performed on the $x = 0.235$ sample at lower temperatures were used to make predictions concerning a low temperature phase transition. Examining Figure 3.15, it can be seen that the depolarization for field cooled and zero field cooled measurements deviates below about 90 K. This onset of irreversibility is interpreted as delineating the GT transition, whereas the sharp decrease in the ZFC depolarization indicates the presence of strong irreversibility, and thus the AT transition.

Conclusions were also drawn by studying the average domain size at different temperatures and concentrations. The latter quantity was determined by analyzing the wavelength dependence of the depolarization (decreased

dependence was interpreted as being a manifestation of larger domains, because then the field, and thus the Larmor precession axis changed less often within the sample). As expected, the average domain size decreases as the disorder (increasing x) increases. Most importantly, for the weakly frustrated $Fe_{1-x}Mn_x$ alloys with $0.22 < x < 0.26$, large domains were found that persist into the supposed reentrant spin-glass phase. This was found not to be the case for larger x values.

3.4 Mössbauer effect

Another technique which can be used to study the magnetic properties of materials involves the Mössbauer effect. Mössbauer spectra found for $Fe_{1-x}Mn_x$ ($x = 0.35$) at different temperatures are illustrated in Figure 3.16. It was determined that quadrupole splitting and the isomer shift were the predominant effects responsible for the structure observed; the actual data was fit using the function

$$P(H) = \sum a_n[cos(n\pi H/H_m) - (-1)^n], \tag{3.7}$$

where H_m is the cut-off field, chosen to be between 150 kOe and 500 kOe, depending upon the temperature.

A plot of $P(H)$ versus H is shown in Figure 3.17. From the behaviour of the peaks in this plot, critical exponents and temperatures were found using

$$\Delta H = H_{av} - H_p \tag{3.8}$$

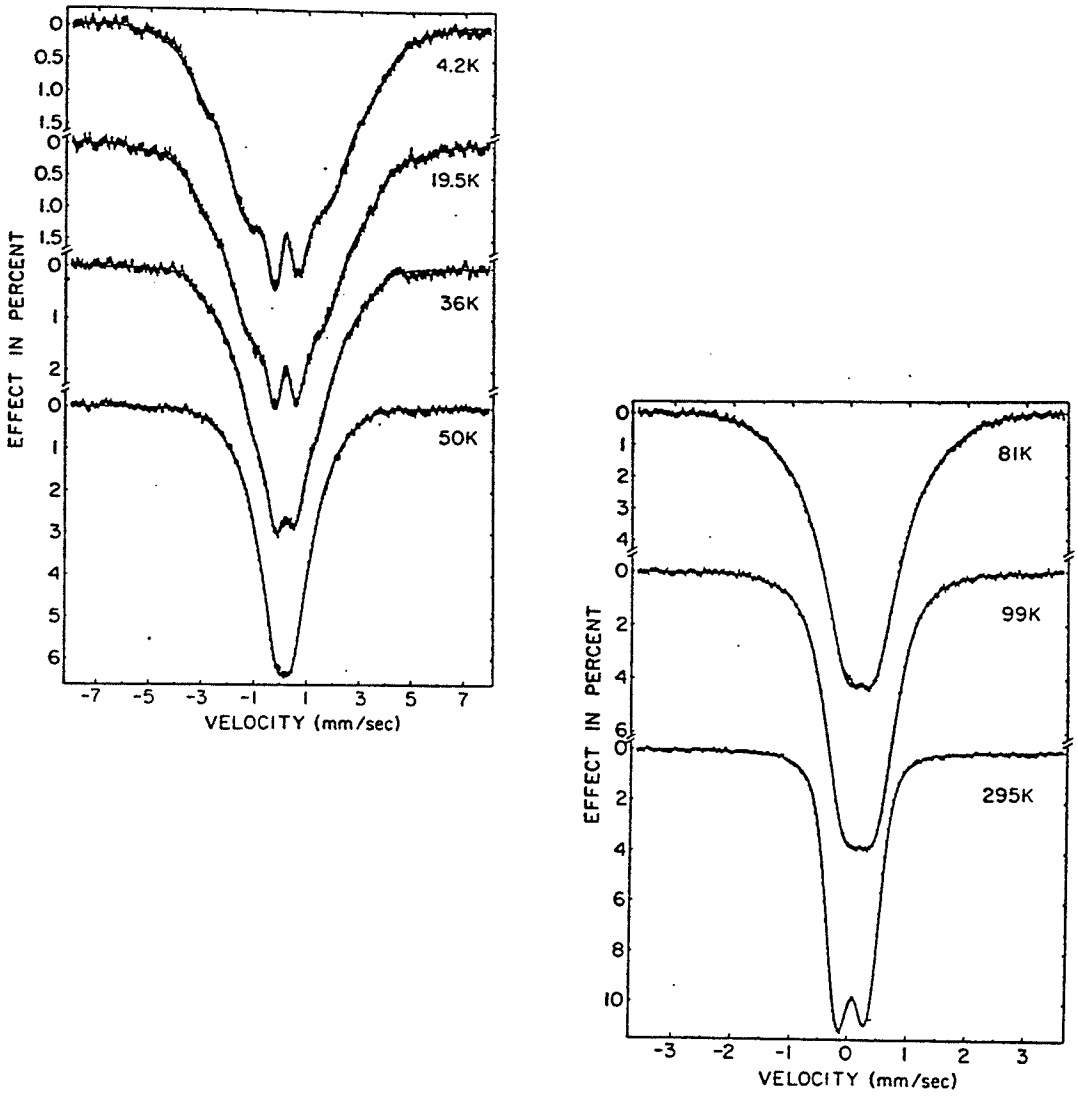

Figure 3.16: Mossbauer spectra for $Fe_{1-x}Mn_x$ ($x = 0.35$). (Keller et al, 1981)

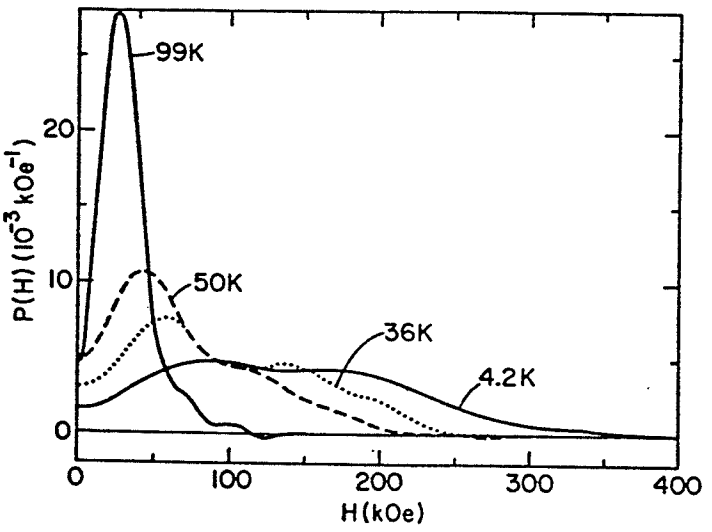

Figure 3.17: $P(H)$ for selected temperatures, from Figure 3.17. (Keller et al, 1981)

in conjunction with

$$\Delta H = \Delta H_{fo}(1 - T/T_f)^{\beta_f}, \tag{3.9}$$

where H_{av} and H_p are the average and (lower) peak field, and the subscript 'f' denotes the paramagnetic to ferromagnetic transition parameters. A similar expression was used for the ferromagnetic to spin glass transition. The results were found to be $\beta_f = 0.42 \pm 0.14, T_f = 100 \pm 2$K for the paramagnetic-ferromagnetic transition and $\beta_s = 0.52 \pm 0.19, T_s = 50.2 \pm 1.4$ K for the ferromagnetic-spin glass transition.

Chapter 4

Experimental Methods

4.1 Sample Description

4.1.1 Introduction

The samples used for this investigation, $(Fe_{1-x}Mn_x)_{75}P_{16}B_{\ 6}Al_3$ where x = 0.235, 0.26, 0.30, 0.32, 0.41, were prepared by Bigot and Peynot (Centre d' Etudes de Chimie-Metallurgie, Vitry sur Seine) using the melt spinning technique to produce a thin foil, which was encased with masking tape for protection because of its extreme fragility, and then cut into narrow strips using a sharp knife. The sample length and width were measured with a travelling microscope (Precision Tool & Instrument Co. Ltd.), and the thickness was calculated, based on the measured mass (found using a Mettler microbalance) and estimated density of each sample.

Several attempts were made to experimentally ascertain the density using a displacement method (Pratten, 1981). Unfortunately the amount of sample available was so small ($\sim$ 10 mg) in all but perhaps one case that even the

Mettler microbalance was not sufficiently sensitive (± 3 μg) to carry out such measurements. Extreme care must also be taken as the samples were so fragile that they would usually break into many fragments before the entire procedure could be completed.

Despite these difficulties, a density measurement for the $x = 0.26$ specimen was completed, although the error is estimated to be as high as 10%. The procedure was as follows:

(i) The sample was first weighed in air, s_{air} (buoyancy effect of air is negligible).

(ii) The sample mass was then determined in toluene [1] by using a small copper V-shaped holder suspended by a gold plated tungsten (to reduce surface tension effects) wire (diameter = 50 μm). The empty holder, h_{tol} and then the holder containing the sample, $(h+s)_{tol}$ was weighed in toluene, the difference between the two measurements giving the sample weight in toluene

$$s_{tol} = (h+s)_{tol} - h_{tol}.$$

(iii) The buoyancy 'force', which is equal to the mass of toluene displaced was calculated using

$$mass_{tol} = s_{air} - s_{tol}.$$

(iv) The sample volume could then be determined from

$$s_{vol} = \frac{\rho_{tol}}{mass_{tol}} = \frac{0.8669\text{g/cm}^3}{mass_{tol}}.$$

[1] Note that toluene is a volatile and hazardous solvent. Inhalation and contact must be avoided. This measurement was conducted with the apparatus in a fume hood.

(v) Finally, the sample density could be found

$$\rho_{sample} = \frac{s_{air}}{s_{vol}}.$$

Using this procedure $\rho_{0.26} = 5.94$ g/cm^3 was found. Unfortunately, attempts to find the densities of the other samples were unsuccessful.

After an extensive literature search failed to yield the density of $(Fe_{1-x}Mn_x)_{75}P_{16}B_{\ 6}Al_3$ for any other values of x, it was decided to estimate the densities using a weighted average over the individual densities,

$$\rho_{sample} = 0.75\{\rho_{Fe}(1-x) + \rho_{Mn}x\} + 0.25\{0.16\rho_P + 0.06\rho_B + 0.03\rho_{Al}\}. \quad (4.1)$$

This approach is based on the general result that for metal-metalloid amorphous alloys the density usually varies linearly with metalloid concentration (Konczos et al, 1985). As a check, the calculation was applied to several other amorphous materials for which the density is known (Krebs et al, 1985; Cargil, 1975). The discrepancies between the calculated and measured values were usually quite small, and never more than 10%. The densities determined using this method are listed in Table 4.1. Note that our measured density for the $x = 0.26$ sample agrees with the calculated density to within the experimental error. Given the relatively large error in the measurement and good agreement generally obtained by the calculation, it was decided to use the calculated values exclusively in the analysis.

Table 4.2 lists the various sample properties, with the significance of the demagnetizing and calibration factors listed in Table 4.3 being discussed in

Table 4.1: Calculated Density

Concentration (x)	Density (g/cm^3)
23.5	6.33
26.0	6.32
30.0	6.31
32.0	6.30

Sections 5.1.3 and 4.2.5 respectively. The calibration and demagnetizing factors for the various samples are a weighted average, based on the mass and dimensions of the individual pieces comprising the sample. In other words, the composite calibration factor is given by

$$c_{sample} = \frac{\sum_i c_i m_i}{\sum_i m_i} \tag{4.2}$$

where c_i is the individual calibration factor (see Section 4.2.5) determined by the dimensions of each individual piece. The composite demagnetizing factor may be found in a similar fashion.

Table 4.2: Sample Specifications

Piece #	Length (mm)	Width (mm)	Mass(g)
23.5-1	15.74	0.77	0.0020
23.5-2	17.09	1.62	0.0044
23.5-3	17.50	1.67	0.0048
26-1	12.54	0.55	0.0011
26-2	15.60	1.12	0.0037
26-3	17.30	1.20	0.0044
26-4	17.20	1.45	0.0053
30-1	17.05	1.33	0.0032
30-2	17.01	1.54	0.0037
30-3	17.10	1.05	0.0025
30-4	16.30	1.43	0.0033
30-5	17.24	1.39	0.0034
30-6	16.68	1.69	0.0040
30-7	16.58	1.83	0.0043
30-8	16.15	1.28	0.0029
32-1	16.55	1.48	0.0038
32-2	16.95	1.34	0.0035
32-3	16.93	1.21	0.0032
32-4	17.05	1.19	0.0031
32-5	16.60	1.14	0.0029

Table 4.3: Calibration and Demagnetizing Factors

Sample	Pieces	Mass (g)	Cal. Factor (emu/g-Oe)	Demag. Factor (cm^3)
23.5-I	1	0.0020	7.10×10^{-4}	0.0213
23.5-II	2 - 3	0.0092	7.36×10^{-4}	0.0255
26-I	1	0.0011	6.49×10^{-4}	0.0449
26-II	2 - 4	0.0134	7.28×10^{-4}	0.0496
30-I	1 - 8	0.0273	7.27×10^{-4}	0.0276
30-II	7 - 8	0.0072	7.21×10^{-4}	0.0301
32-I	1 - 5	0.0165	7.28×10^{-4}	0.0258

4.1.2 Preparation of Metallic Glasses

Although the samples were kindly provided in foil form by Bigot and Peynot (Centre d' Etudes de Chimie-Metallurgie, Vitry sur Seine), a brief overview of the two most common techniques for preparing amorphous samples will now be presented for completeness. (Zallen, 1983) (Güntherodt et al, 1981)

Splat Quenching

Making metallic glasses in film form essentially involves rapidly quenching a liquid droplet, or jet onto a good heat conducting metal to produce 'splats' or ribbons, using the procedures described below. The most important requirement for producing these films is that the melt cools to a sufficiently low temperature rapidly enough that it does not have the opportunity to

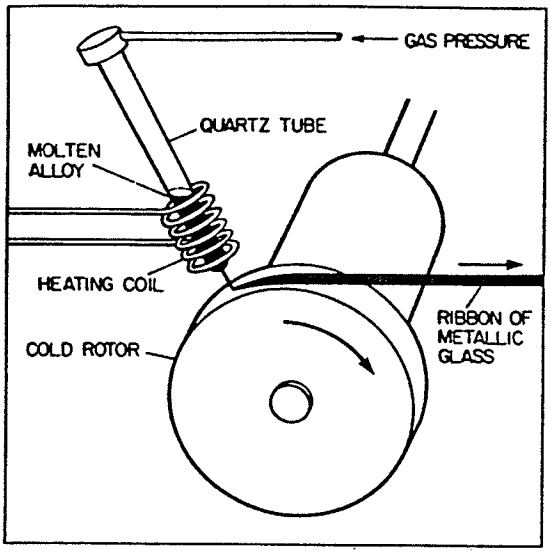

Figure 4.1: Melt Spinning (Zallen, 1983)

crystallize. Forming an ordered solid requires time, since nucleation must occur for crystal growth to take place. Thus, the liquid must be cooled to below the glass transition temperature, T_g, without being allowed to become ordered at the freezing temperature, T_f ($T_g < T_f$).

Melt Spinning

This technique, which was employed to make the samples studied in this thesis, uses a rapidly spinning wheel (tangential speed $\sim$ 2 km/min.) to conduct heat away from a molten jet of alloy, as can be seen in Figure 4.1. The rotor must possess excellent thermal conductivity, and is therefore often made of copper, which is maintained at room temperature with water cooling. The 'ribbon' manufactured in this way can have a thickness ranging from 20 to 60 μm. Since the film is extremely thin and makes good thermal contact with an excellent heat sink, it cools rapidly ($\sim 10^6$ K/s) before it solidifies.

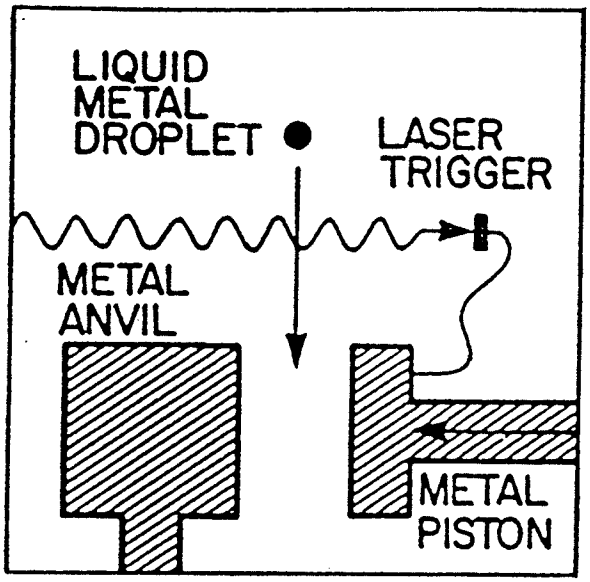

Figure 4.2: Splat cooling (Zallen, 1983)

Depending upon whether or not the alloy oxidizes easily, the 'ribbon' may be made in air or in a vacuum/inert atmosphere such as argon.

Splat Cooling

Splat-cooling, which is a variation of the melt spinning technique, was developed especially for the purpose of making metallic glasses, and consists of letting a molten droplet of the material fall between an anvil and a hammer, as illustrated in Figure 4.2. There it is flattened into a 15 to 30 mm diameter 'splat' with a thickness ranging from 20 to 80 μm. This method cools the liquid metal from both sides, and exhibits cooling rates in the range 10^5 K/s to 10^8 K/s.

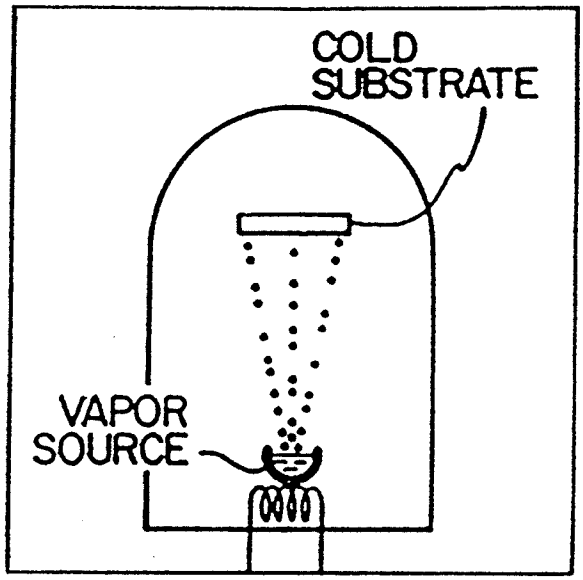

Figure 4.3: Vapor condesation (Zallen, 1983)

Vapor Condensation

Vapor condensation, a technique which employs an entirely different approach than the one discussed above can also be used to form amorphous solids. (Zallen, 1983) This method bypasses the liquid state of the material entirely, and essentially constructs the amorphous solid one atom at a time, therefore possessing the highest effective quenching rate obtainable.

There exist a variety of vapor condensation techniques, the simplest of which is illustrated in Figure 4.3, and involves heating the desired material until a vapor is formed, which can then condense on the cold substrate. The material forming on the substrate will be amorphous, providing the thermal energy of the vapor atoms is removed before they reconfigure into a crystalline form. Another approach involves using an electron or ion beam to bombard

the source material (sputtering). Vapor condensation is useful in forming thin films with a thickness of 5 - 50 μm.

4.2 Experimental Apparatus

The data collected for this thesis involved measuring the a.c. susceptibility of a series of FeMn samples over a wide range of temperatures and static biasing fields. To accomplish this goal requires the development of three separate experimental systems; the cryostat system, the susceptometer (susceptibility measuring device) and the data collection system, all of which will now be described in some detail.

4.2.1 Cryostat System

Although the name suggests that this equipment is solely related to temperature control, in actual fact, the cryostat system also includes the sample probe, static biasing field solenoids, and the sensing/pickup coils connected to the susceptometer. The arrangement of this equipment is illustrated in Figure 4.4, and the function of the individual components will be described in the ensuing sections.

As can be seen in the diagram, the cryostat consists of two double-walled, concentric chambers (dewars). The outer dewar surrounds the various coils and always contains liquid nitrogen; it is insulated from the outside by means of a vacuum space between its double walls. The inner dewar in which the

sample is placed, is appropriately named the sample space, and can be filled with liquid helium or liquid nitrogen for constant temperature measurements at 4.2 or 77 K, respectively.

4.2.2 Sample Probe

The construction of the sample probe itself involves a machined OFHC (oxygen-free, high thermal conductivity) copper block around which an insulated nichrome heater is wound and to which a large bundle of 32 gauge copper wires (braid) was soft-soldered, into which the sample to be measured could be inserted. The purpose of the copper bundle is to provide a means by which the temperature of the sample (having good thermal contact to the bundle) can be varied, and yet allow the a.c. driving field generated by the susceptometer to easily penetrate to the sample; the skin depth of copper is much greater than the diameter of the wires. Before placing the sample into the copper braid, it was wrapped in masking tape to electrically insulate it from the latter, but still maintain good thermal contact to the heater.

Before proceeding with a measurement it was necessary to correctly position the sample with respect to the pickup coils. This was accomplished by initially placing the centre of the sample $\sim$ 8.0 cm below the bottom of the copper block within the Cu bundle. After cooling the sample to a temperature at which it had a non-zero a.c. susceptibility, the sample position was fine-tuned by means of an adjustment screw at the top of the thin-walled stainless steel tube supporting the copper block. The screw is

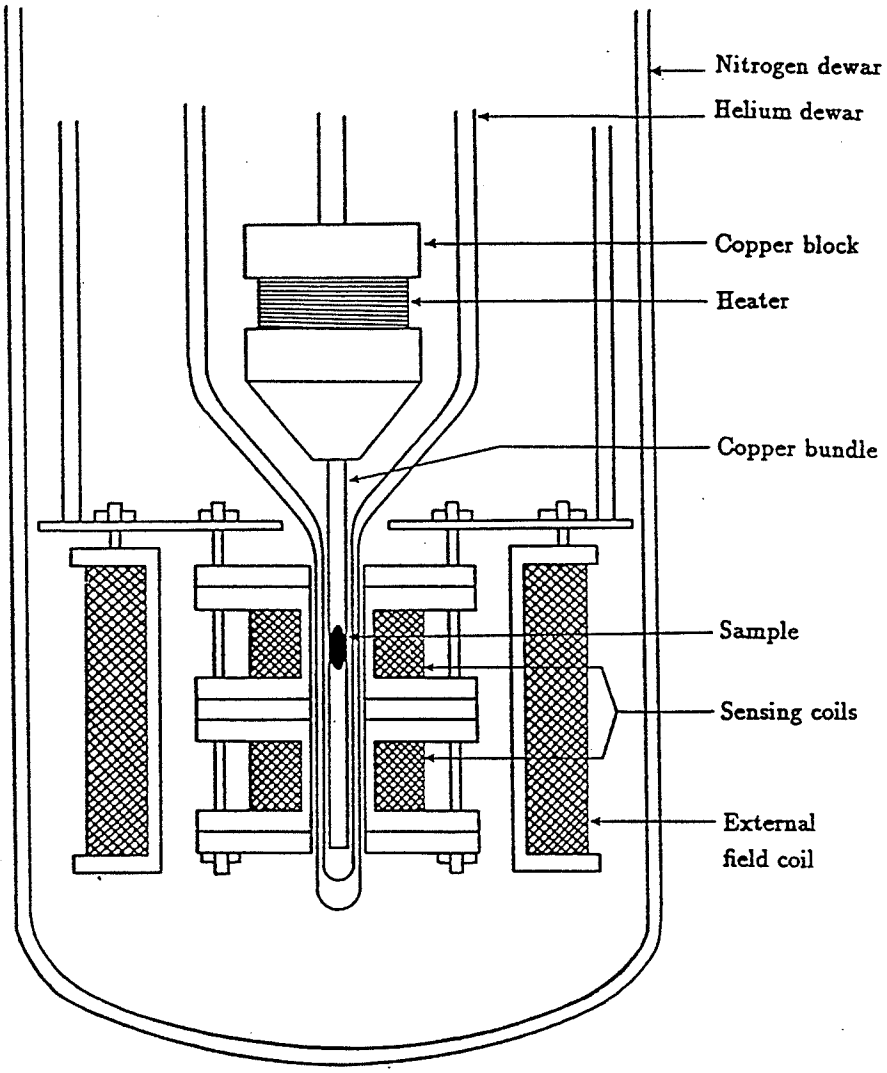

Figure 4.4: Cut away view of the lower portion of the cryostat system, including the sample probe and the various coils providing the sensing and D.C. biasing-field. (Ma, 1990)

threaded onto a plate at the top of the cryostat system, and provides a convenient means for moving the sample. Stainless steel is used since it is a relatively poor thermal conductor, thus limiting the heat transfer into the cryostat from outside. The entire sample probe was thereby moved up or down with respect to the sensing coils until a maximum signal was obtained on the susceptometer output.

4.2.3 Static Biasing Field

Zero Field Measurements

When doing either temperature or field sweeps, the sample was initially cooled from well above T_c ($\sim 1.2T_c$) to the desired temperature in 'zero' field; i.e., the local 0.52 Gauss vertical component of the Earth's field was backed off. This was done by passing the appropriate current (2.43 mA) from a constant current source through the biasing solenoid (215 Oe/amp) within which the sample was located (Figure 4.4). The purpose of this procedure was to ensure that each run was always started with the sample in the same magnetic ground state. In other words, any history dependent effects i.e. hysteresis, which could affect the reproducibility of the results, were removed. It should be noted that no measures were taken to compensate for the local horizontal component of the Earth's field, which is approximately 0.24 Oe. Although this is inconsequential when doing high field measurements, it had to be considered when doing experiments at smaller fields.

Temperature Sweeps

When performing temperature sweeps, the sample was subjected to a series of static biasing fields (applied along its largest dimension) ranging from $\sim$ 0.5 Oe to 1000 Oe. For fields less than about 500 Oe, the 215 Oe/amp solenoid was used, whereas for higher fields an additional solenoid producing 186 Oe/amp was connected in series with the first solenoid, giving a total of 401 Oe/amp. The two coaxial solenoids were both constructed by winding 22 gauge enamelled copper wire on a brass former, and were maintained at a constant temperature of 77 K during any experiment by immersing them in liquid nitrogen. This serves to reduce the coil resistance, important because large currents will cause considerable Joule heating, and maintaining the coils at a constant temperature helps to stabilize the current. The current passing through the solenoid(s) was generated by a Lambda LK344A FM Model current regulated power supply and monitored for stability by measuring voltage across a standard resistor with a DANA multimeter.

4.2.4 Temperature Control

For all experiments performed it was imperative to constantly monitor the temperature. For the temperature sweeps, this quantity was recorded at regular intervals using a computer controlled data acquisition system, as will be described below; and for the field sweeps, it was necessary to ensure that the the temperature remained sufficiently constant throughout the run.

The sample temperature was determined by means of a calibrated Chromel P-Au + 0.03 at.% Fe thermocouple with one junction immersed in an ice bath, and the other placed as near the sample as possible, i.e. at the top of the wire bundle, $\sim$ 5 cm above the sample. It was not possible to place the junction at the site of the sample because AuFe at this concentration is weakly magnetic; the thermocouple itself could contribute to the signal detected by the sensing coils. Temperature gradients between the sample and the thermocouple junction were minimal due to the good thermal conductivity of the copper braid, provided the heating rate (for temperature sweeps) was kept sufficiently low. The thermocouple emf was displayed on a Racal-Dana 5001 DVM and could be converted to a temperature in Kelvin using the appropriate calibration data.

Since most of the experiments were carried out at temperatures much lower than room temperature, it was necessary to cool the sample using liquid helium and/or liquid nitrogen. For $T \geq 77$ K the nitrogen dewar was filled until the biasing field and pickup coils were completely immersed. In order to facilitate more rapid cooling of the sample, the vacuum space of the inner/helium dewar could be softened to provide better thermal contact with the sample space. (Thermal contact between the nitrogen and helium dewar was controlled, in general, by changing the vacuum in the helium dewar jacket.) For data collected at 77 K, nitrogen was poured into the 'helium' dewar (sample space) to provide an stable temperature environment.

Between 4.2 K and 77 K the nitrogen dewar was completely filled to provide maximum thermal isolation of the helium dewar, which was then cooled with cold helium gas obtained from a liquid helium storage dewar through a liquid helium transfer tube. For constant temperature experiments at 4.2 K, a small amount of liquid helium was transferred into the sample space.

To warm the sample to the desired temperature after cooling (it was impossible to cool to exactly the required temperature with the exception of 4.2 K or 77 K), an electric (nichrome) heater was used. The latter was constructed by wrapping about 10 turns of 0.010″ diameter heater wire (13.2 Ω/ft, 50 Ω total resistance at room temperature) around the copper block, as illustrated in Figure 4.4. By adjusting the heater current, various warming rates could be achieved, depending upon the experiment being performed. At 'very high' temperatures, near room temperature, the warming rate could be increased without resorting to very high heater currents by pumping on the inner dewar vacuum space through a nitrogen-filled cold trap with a diffusion pump to decrease the thermal contact with the nitrogen dewar.

4.2.5 The Susceptometer

Principle of Operation

The susceptibility measurements were carried out using a phase locked 2.4 kHz susceptometer (Maartense, 1970, 1982). Essentially, this consists of two LCR resonators, configured as shown in Figure 4.5, with natural frequencies

$\omega_1 = \frac{1}{\sqrt{L_1 C_1}}$, and $\omega_2 = \frac{1}{\sqrt{L_2 C_2}}$ respectively. The first resonator is part of an oscillator, which is connected so that both circuits have an initial driving frequency, $\omega_1 = \omega_2$. When a piece of magnetic material is inserted into L_2 the self-inductance of the latter changes to $L_2 + \Delta L_2$, which in turn causes $\omega_2 \rightarrow \omega' = \frac{1}{\sqrt{(L_2+\Delta L_2)C_2}}$, as well as affecting the phase, ϕ, associated with ω_2. The quantity ϕ, which represents the phase by which the emf leads the current, is given by

$$\phi = \frac{\omega L - \frac{1}{\omega C}}{R} = \frac{\omega^2 LC - 1}{\omega RC} \quad ; \quad \omega = \omega_1,\ \omega_2. \tag{4.3}$$

Thus, changing the inductance, capacitance or resistance of any of the elements comprising the two circuits affects their respective phase angles. The output of the two circuits is fed into a phase detector, monitoring the phase, but not the amplitude difference between the two signals. The phase detector generates a D.C. voltage change proportional to $\Delta\phi = \phi(L_1) - \phi(L_2 + \Delta L_2)$, which is passed via a feedback loop to a voltage dependent reactance element that attempts to compensate for ΔL_2 and re-establish the condition $\Delta\phi = \phi(L_1) - \phi(L_2)$. The susceptibility of the sample can then be determined since it is proportional to the voltage generated by the phase detector, which is in turn related to ΔL_2.

Specifications

The two inductors, or sensing coils used in the susceptometer are comprised of 4000 turns of 35 gauge enamelled copper wire counter-wound on nylon coil

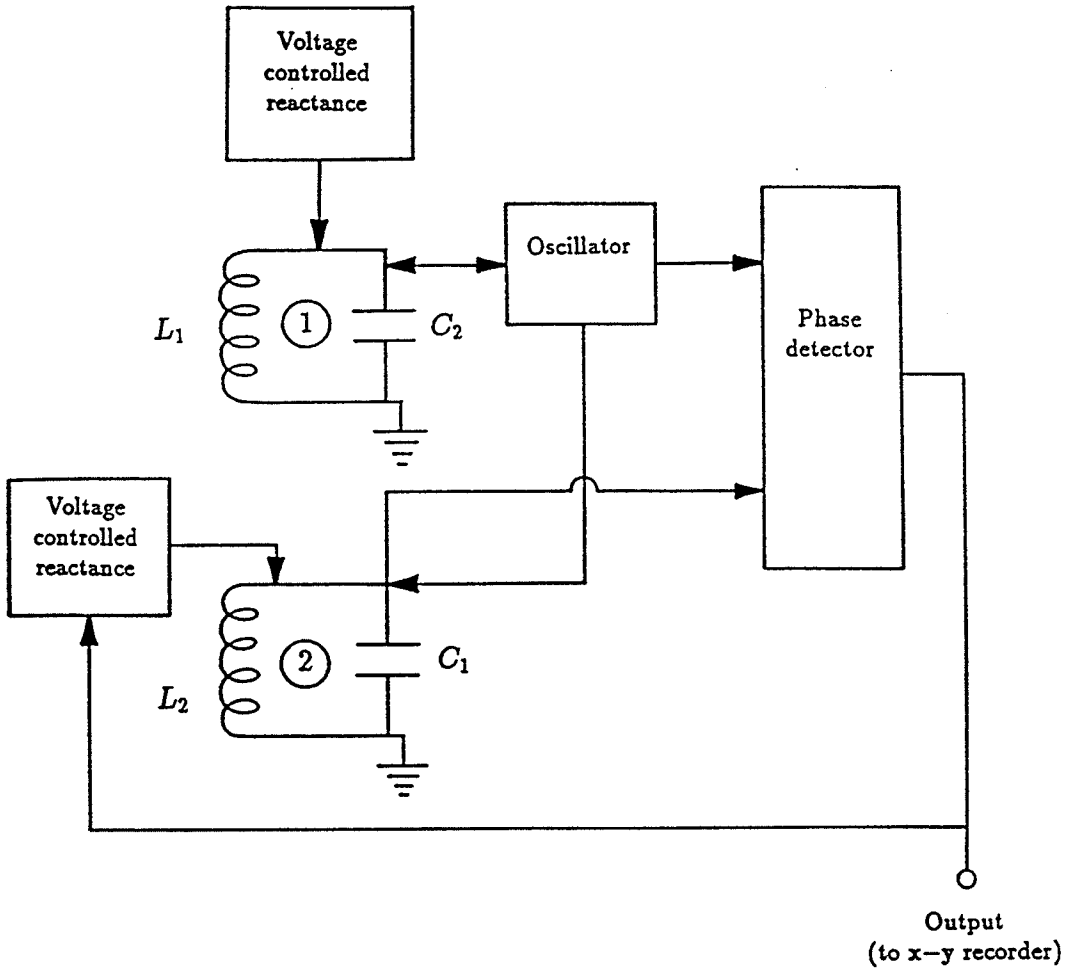

Figure 4.5: Block diagram of the susceptometer (Ma, 1990)

formers, with inductances measured to be 205 and 202 mH (Roshko, 1979). The arrangement of the coils with respect to the sample position can be seen in Figure 4.4; the coils were always immersed in liquid nitrogen during operation of the susceptometer to reduce their resistance and increase the Q of the LCR circuits, thus reducing the noise factor resulting from changes in sensitivity due to temperature drift.

A driving frequency of 2.4 kHz was employed, with a driving field strength of 30 mOe used for most of the measurements. A driving field of 50 mOe was required for a few trials in order to improve the signal to noise ratio. A smaller field strength is naturally preferred, since the purpose of the measurements was to find the a.c. susceptibility, which involves the differential slope on an M versus H curve. However, the finite resistance of the sensing coils (even at 77 K) limits the possible driving field levels available, as the oscillations would get damped out below a certain threshold.

It is important to note that the copper braid containing the sample passed through both counter-wound sensing coils in order to balance out the diamagnetic signal from the Cu braid itself. Differences between the component values of the two circuits, which of course are not necessarily equal as in the ideal case, cause a non-zero voltage output even in the absence of a sample. This is taken into account when making measurements, as described in Section 4.3.1.

Calibration

As previously mentioned, the susceptometer generates an output reading in volts; in order to obtain absolute susceptibility measurements in emu/g-Oe, a calibration factor is necessary. The susceptibility may be calculated directly from the ΔL (change in inductance) introduced by the presence of the sample using the following expression (Maartense, 1970)

$$\Delta\chi = 4\pi\eta\rho\left(\frac{\Delta L}{L}\right) \tag{4.4}$$

where η is the 'effective volume filling fraction' of the sample inserted into L_1, and ρ is its density. However, since η is very difficult to determine, the susceptometer was instead calibrated using a 99.999% pure Gd_2O_3 powder which has a theoretically well understood magnetic behaviour. This sesquioxyde of gadolinium is paramagnetic at 77 K, and exhibits a large susceptibility displaying excellent agreement with the Curie-Weiss law,

$$\chi = \frac{N\mu_{eff}^2}{3k_B(T-\theta)} = \frac{Ng^2\mu_B^2 J(J+1)}{3k_B(T-\theta)}, \tag{4.5}$$

where the paramagnetic Curie point, θ, equals -13 K for Gd_2O_3 (Schinkel et al, 1973). The powder was placed in a series of glass tubes with different dimensions, and the susceptibilities were then measured at 77 K (fresh liquid nitrogen).

Inserting $\mu_{eff} = (7.70 \pm 0.04)\mu_B$ into (4.5) gives the calculated susceptibility, which in conjunction with the expression

$$\chi = \frac{c\chi_v}{m}, \tag{4.6}$$

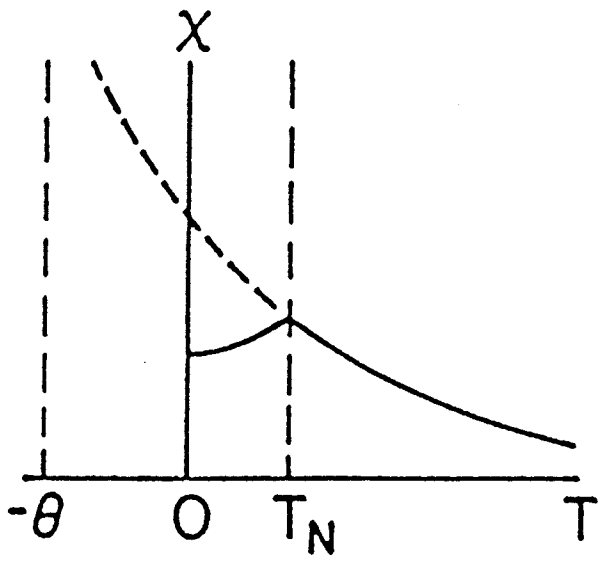

Figure 4.6: Susceptibility of an antiferromagnet above its Neel point; T_N is the Neel temperature and θ is the paramagnetic Curie point. (Jiles, 1991)

where m is the sample mass, and χ_v is the measured susceptibility in volts, yields the calibration factor, c. It is important to mention that in order to make the final results independent of the size of the FeMn specimen used, all susceptibility measurements will be expressed in emu/g-Oe. This requires an expression which incorporates the sample mass, as has been done in (4.6).

To within experimental error, the diameter of the sample did not affect the calibration factor, whereas a difference in length resulted in the following relationship (Wang, 1994)

$$c = (0.20 \text{ emu/V-Oe-mm})(\text{sample length}) + 5.56 \text{ emu/V-Oe}.$$

The above value is only valid to within $\pm 5\%$ due to inherent limitations on the sensitivity of the susceptometer. This is not a major concern, however, since the relative (which can measured to better than 1 part in 10^4), as opposed to the absolute susceptibility is usually the quantity of interest.

4.2.6 Data Collection System

Throughout all of the experiments, the data was collected and stored using a data acquisition system controlled by RALPH [2], while simultaneously being recorded on a Philips PM 8143 XY recorder, if desired. RALPH could be set to collect susceptibility versus current (field) or temperature data, depending upon the particular experiment in progress, as will now be discussed. It should be noted that all data was read in volts from two Hewlett-Packard 34401A multimeters and could be converted to the desired units (Kelvin, Oe, etc.) by means of appropriate conversion tables and analysis routines.

4.3 A.C. Susceptibility Measurement Procedure

4.3.1 Temperature Sweeps

In order to collect temperature sweep data it was necessary to vary the sample temperature within the range 4.2 to 300 K while keeping the D. C. biasing field constant. The steps involved in this procedure were as follows:

(i) The sample was first warmed to well above its critical temperature ($\sim 1.2T_c$), see Section 4.2.3 and subsequently cooled in 'zero' field.

(ii) Depending upon the temperature range of interest, the sample was cooled with nitrogen, or nitrogen and helium (Section 4.2.4).

[2] A program designed to run on a personal computer, written by J. Schachter, University of Manitoba, 1991.

(iii) After reaching the desired temperature and disconnecting the zero-field constant current supply (backing off the Earth's field), the Lambda LK344A FM current supply was connected to the appropriate solenoid combination (215 or 401 Oe/amp) and adjusted to generate the desired applied field.

(iv) Having completed all of the above preliminary steps, RALPH was initiated and a 'zero' reading was taken (see (v)). The data collection system was set to read the susceptibility (in volts) and the temperature (in μV) every 1 to 5 μV in temperature. The heater current was then slowly increased so that the warming rate remained approximately constant. The latter was monitored by RALPH and maintained at about 5-7 s/μV (1-2 min/K) – heating at a faster rate may introduce a temperature gradient between the sample and the thermocouple junction. It should be noted that higher temperatures required greater heating currents to achieve the same warming rate; for example, near 4.2 K, a 10-30 mA heater current was required, whereas at 77 K, 130-150 mA was used. For all samples except $Fe_{76.5}Mn_{23.5}$, the heater current was kept below 210 mA at even the highest temperatures. However, in this one case, temperatures as high as 300 K were required, which made heater currents as high as 350 mA necessary. To ensure consistency between the temperature sweeps at various fixed fields, care was taken to keep the heater current approximately the same at a given temperature.

(v) Additional 'zeros' were taken at regular intervals to correct for any drift in the 'zero-susceptibility' readings [3]. These readings were obtained by using the support rod (Section 4.2.2) to extract the sample from the upper sensing coil until a minimum in the susceptibility was observed on the XY recorder/DVM, and then prompting RALPH to record a 'zero-susceptibility' reading. The sample was then reinserted to allow data collection to resume.

(vi) After acquiring data in the temperature region of interest, the sample was again warmed above T_c and the entire procedure could be repeated at a different field.

4.3.2 Field Sweeps

The field sweeps were conducted with a procedure that was, in some ways, similar to the temperature sweeps, except that here the temperature is kept constant and the field is varied. To some degree, these runs required greater care to complete than the temperature sweeps as temperature stability was quite difficult to maintain, especially between 4.2 K and 77 K. However, as each individual field sweep could be completed within a few minutes (not including warming and cooling times), this difficulty could be reduced to an acceptable level by monitoring the temperature during the field sweep and introducing small heater current adjustments if necessary.

(i) As with the temperature sweeps, the sample was first warmed to well above its critical temperature and then cooled to the required temperature in

[3]The zero corrections will be discussed in detail in Section 5.1.

'zero' field, to ensure that each measurement was carried out along a 'virgin magnetization curve'.

(ii) Using a low heater current, a temperature stability from ± 1 μV to $\pm$ 4 μV ($\pm$ 70 mK to $\pm$300 mK) was achieved, depending upon the temperature at which the measurement was performed.

(iii) The current supply for the field sweeps consisted of a 6824A Hewlett - Packard DC Power Supply-Amplifier, driven by a Stanford Research Systems Model DS335 Synthesized Function Generator. The supply was adjusted to give an initial output of 2.43 mA through the 215 Oe/amp solenoid in order to begin the sweep from true zero field.

(iv) After starting RALPH and taking a zero, the field sweep was begun by setting the function generator ramp time to a value much slower than either the susceptometer time constant or the magnetization relaxation time, typically $(5 - 25)\text{x}10^{-5}$ Hz. The data acquisition system was set to read the susceptibility (in volts) and applied current (in volts – measured across a 1 Ω standard resistor) at appropriate intervals to collect enough data points for analysis.

(v) Once the desired maximum field was reached another zero was taken; then the back-off field was reset, and the sample was warmed in preparation for the next measurement.

4.3.3 'Butterfly' Loops

Butterfly loops, so named due to their shape (Figures 5.56 and 5.57) are actually 'complete' field sweeps, with the applied field being swept, using a saw-toothed waveform from negative to positive, and then back to negative again. These measurements determine the magnetic 'hardness' or coercivity of the sample, and evaluate the importance of hysteretic effects at different temperatures. These measurements were by far the least time-consuming since it was not necessary to warm the sample above T_c before each run. However, it was even more difficult to control the temperature than with field sweeps, as each individual run took longer to complete, and therefore required the temperature to remain stable for a greater period of time.

(i) For this type of experiment, it was not necessary to cool in zero field, as mentioned above. Instead, once the temperature was stabilized, the current passing through the 215 Oe/amp solenoid was swept through a preliminary closed loop between $\pm$ 1 A before the actual measurement. The coercivity was then measured by sweeping the sample through the same hysteresis loop.

(ii) RALPH was set up in the same manner as for field sweeps, except that the field range over which data was collected now included both positive and negative fields.

(iii) The next butterfly loop could be recorded as soon as the next temperature of interest was established.

Chapter 5

Data Analysis and Discussion

5.1 Data Correction

Before any results can be extracted from these raw data, three separate correction factors must be incorporated. The zero and background adjustments are required because of the non-ideal characteristics of the sample probe, and the demagnetization correction results from the finite size/geometrical shape of the samples used. Each of these aspects will now be discussed in detail.

5.1.1 Zero Correction

As described in the 'Experimental Methods' chapter of this thesis, 'zero readings' were taken regularly when performing any susceptibility measurements. The reason this is necessary was to monitor that portion of the signal which is not due to the sample, but is rather a contribution from the sample probe. Even though the sensing coils in the susceptometer are counter wound, eddy currents induced in the copper block (Figure 4.4) will affect the inductance

of each sensing coil to a different extent. Withdrawing the sample from L_2 (Figure 4.5), yields a residual signal which is generated only by the presence of the copper block. The error introduced by this effect can then be accounted for by subtracting these residual 'zero-susceptibility' readings from the 'sample-susceptibility' measurements.

Since in general, the magnitude of eddy currents depends upon the resistivity of the materials in which they are induced, the above contribution will be more pronounced at lower temperatures where the resistivity of the copper block will be lower. Furthermore, larger driving fields will also introduce a greater 'zero-susceptibility' signal.

5.1.2 Background Correction

The copper bundle (braid) containing the sample also affects the susceptibility readings even though, ideally, the effect of the braid, which links both sensing coils, should cancel. However, due to inhomogeneities in the bundle, a diamagnetic contribution of about -0.045 V at 4.2 K results, which decreases in magnitude with increasing temperature and can be measured upon removal of the sample from the probe.

For the present measurements, this effect is most significant at low temperatures, where the magnitude of the susceptibility approaches that of the background correction. A complete temperature sweep in the absence of a sample in the probe will determine the temperature dependence of the background susceptibility, which can then be subtracted from the measured signal

along with the zero correction to obtain the 'true' measured susceptibility.

5.1.3 Demagnetizing Correction

The susceptibility obtained by incorporating the background effects is still not the true susceptibility of the sample, because of the finite size of the FeMn specimen. A magnetized sample possesses uncompensated poles at its surface, with a distribution depending upon the geometry of the sample. Taking the specimen to be uniformly magnetized, as is the case for an ellipsoid (Morrish,1965), results in a uniform internal magnetic field given by

$$H_i = H_a - H_d = H_a - NM \tag{5.1}$$

where H_a and H_d are the applied and demagnetizing fields respectively, and N is the shape-dependent demagnetization factor. [1] $H_i < H_a$ for all magnetic materials except diamagnets, which have a negative susceptibility and are therefore magnetized in a direction opposite to that of the applied field. The demagnetization correction is usually negligible in dia- and paramagnets; however, in the case of ferro- and ferrimagnets, it must be considered.

Although the FeMn pieces used in the present study have a rectangular shape (Table 4.1), they were approximated by ellipsoids with the principal axes equalling the sample dimensions, since this is the only shape for which

[1] For an 'infinitely' thin, needle-like sample aligned along the direction of the applied field, $N \rightarrow 0$, whereas for a flat disc with its surface perpendicular to the field direction, $N = 4\pi$. The FeMn specimen studied here are long flat strips, with their longest dimension parallel to the field direction, and therefore have a very small demagnetization factor (Table 4.1).

the demagnetization factor can be exactly calculated. Evaluating the appropriate elliptic integral (Osborn, 1945), the demagnetization factor for each sample was calculated.

Once the demagnetization factor is known, the actual, or 'true' susceptibility of the sample,

$$\chi_t = \frac{\partial M}{\partial H_i}, \tag{5.2}$$

as compared to the measured susceptibility,

$$\chi_m = \frac{\partial M}{\partial H_a}, \tag{5.3}$$

can be calculated. By combining the above two expressions using (5.1), it is trivial to show that

$$\chi_t = \frac{\chi_m}{1 - N\chi_m}. \tag{5.4}$$

From the above expression it can be seen that the measured susceptibility is limited to

$$\chi_m \leq \frac{1}{N}, \tag{5.5}$$

where $\chi_m = \frac{1}{N}$, or $1 - N\chi_m = 0$ represents the demagnetization limit at which the true sample susceptibility diverges ($\chi_t \rightarrow \infty$).

A final requirement before we can proceed to analyze the data will be to establish a procedure for evaluating the internal field, H_i, given an applied field, H_a. Referring to (5.1) it can be seen that it will be necessary to determine the magnetization, which can be obtained by integrating (5.2)

yielding

$$M(T) = \int_0^{H_i} \chi_i(T) \cdot dH_i. \tag{5.6}$$

It follows trivially from (5.2) and (5.3) that this is equivalent to the more useful expression

$$M(T) = \int_0^{H_a} \chi_m(T) \cdot dH_a, \tag{5.7}$$

which can be approximated numerically using

$$M_j = \chi_{m_1} \cdot H_{a_1} + \sum_{k=1}^{j-1} (H_{a_{k+1}} - H_{a_k}) \cdot \frac{1}{2}(\chi_{m_{k+1}} + \chi_{m_k}) \;\; ; \;\; 1 \leq j \leq n-1 \tag{5.8}$$

which is simply the trapezoidal rule, where n is the number of data points collected and j is the data point label. By using the above equation in conjunction with (5.1), the internal field may be written as

$$H_{i_j} = H_{a_j} - NM_j. \tag{5.9}$$

The trapezoidal approximation given by (5.8) results in an overestimation of the magnetization, but the error becomes negligible if sufficient number of data points are collected.

5.2 Zero Field Susceptibility

Before examining the susceptibility versus temperature curves in various applied fields, it would be interesting to consider the behaviour of the zero field (I_a = 2.43 mA to back off the vertical component of the Earth's field) susceptibility for the various samples. It is apparent that the susceptibility increases sharply with decreasing temperature for all of the samples, as can be seen in Figure 5.1, thus denoting the paramagnetic to ferromagnetic phase transition. The nature of the decrease in susceptibility at lower temperatures is not as well understood, and is believed to be either indicative of another phase transition, or simply due to an increase in coercivity, as will be discussed in more detail below.

The broad maximum in the intermediate region of the temperature sweeps, referred to as the Hopkinson peak, or principal maximum is not the result of critical behaviour, but rather due to 'technical processes' (Williams, 1991) such as domain wall motion. As the temperature decreases, thermal effects diminish, allowing the relative strength of the spin-orbit coupling to increase, which in turn may result in greater anisotropy. This would result in the gradual decrease in susceptibility below the paramagnetic to ferromagnetic transition, as is observed in the $x = 0.235$ and 0.26 samples.

Note that none of the zero field runs reach the demagnetization limit, unlike some of the previous results published (Salamon et al, 1980). To

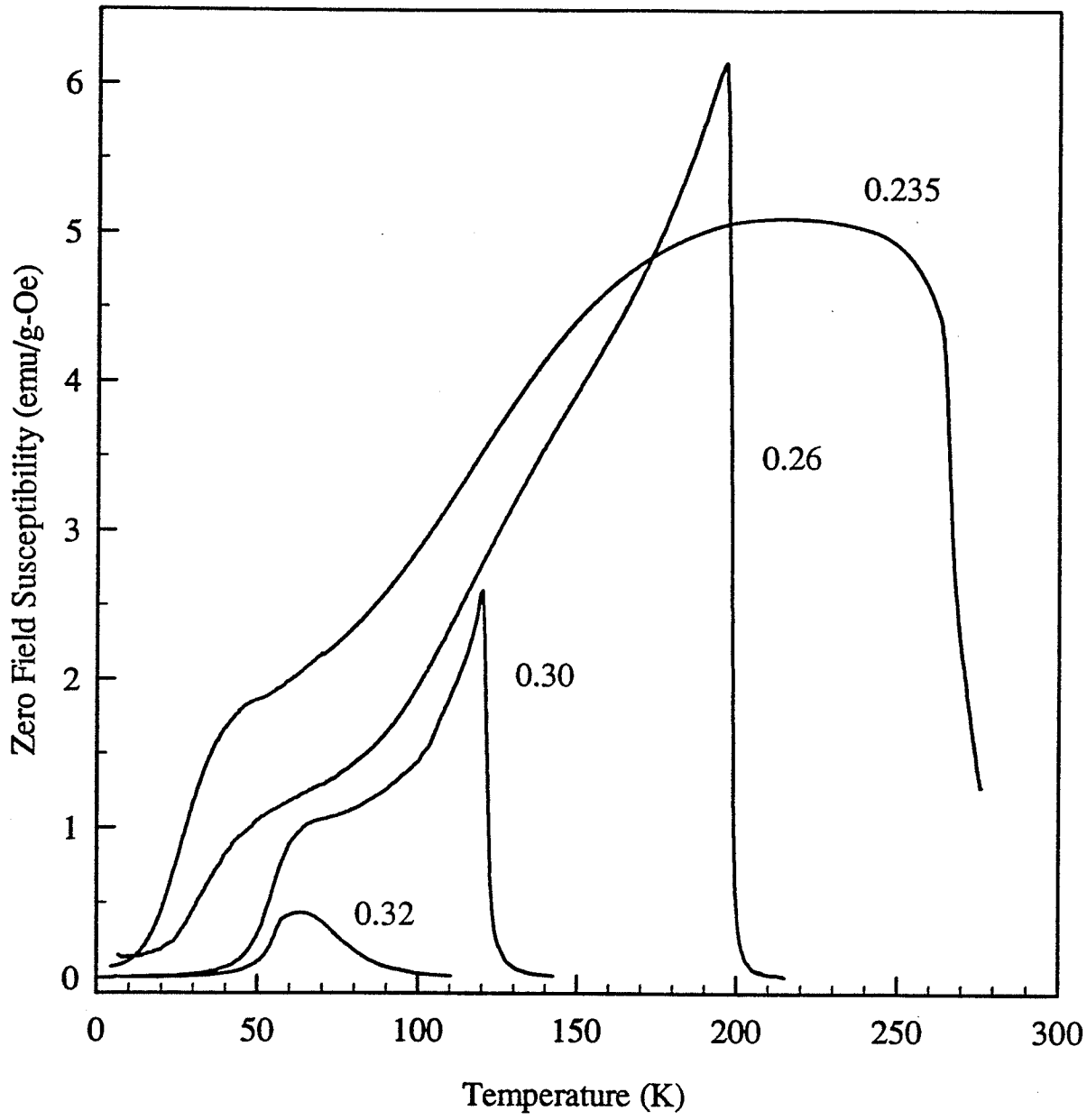

Figure 5.1: The zero field a.c. susceptibility, $\chi(H,T)$ (in emu/g-Oe), corrected for background and demagnetising effects, plotted against temperature (in K) for the x= 0.235, 0.26, 0.30 and 0.32 samples.

understand this, recall the equation

$$H_i = H_a - NM,$$

which can be used to show that

$$\chi_t = \frac{\chi_m}{1 - N\chi_m}$$

with the limitation, $\chi_m \leq \frac{1}{N}$. In other words, at the demagnetization limit: $\chi_m = \frac{1}{N}$, $H_i = 0$ and $H_a = NM$. For this to be the case in an oscillating driving field (such as the one used to measure the a.c. susceptibility), the magnetization must also oscillate with a magnitude specified by $\Delta M = \frac{\Delta H_a}{N}$. Clearly, the larger the demagnetization factor, N, the smaller the oscillations that are required. The accurate determination of N is difficult for the long, thin samples used in this study, but since this quantity is quite small under these circumstances, an accurate determination is not important. If N is small, however, a greater amount of coherent rotation and domain wall motion is needed to satisfy $\Delta M = \frac{\Delta H_a}{N}$. Therefore, anisotropy effects become more prevelant, and the demagnetization limit is not as easily reached as it would be in a sample with large N (Williams, 1991).

5.3 Upper Transition

As described in the experimental section, temperature sweeps were carried out in various static external biasing fields. The results of these measurements for the different concentrations are shown in Figures 5.2 to 5.5; the

suppression of the Hopkinson peak amplitude, and reduction in peak temperature in a sufficiently strong magnetic field reveals a set of critical, or secondary peaks [2]. Whereas the Hopkinson peak decreases in amplitude and temperature as H_a is increased, the critical peaks also decrease in height (although not nearly as quickly as the Hopkinson peak), but move upwards in temperature ($T_p > T_c$), as illustrated in Figures 5.2, 5.4 and 5.5. The detailed behaviour of the critical peaks are shown in Figures 5.6 to 5.9, which also show a cross-over line (dashed line - recall Figure 2.8) below which the behaviour of the susceptibility is field dominated, and above which it is controlled by thermal fluctuations.

The latter can be understood, at least qualitatively, in terms of the fluctuation dissipation theorem (III Kunkel et al, 1988) using the expression

$$\chi(H,T) \sim \frac{1}{T}(\langle S_z \rangle^2 - \langle S_z^2 \rangle). \tag{5.10}$$

Considering the high temperature limit ($t >> h$), $\langle S_z \rangle \rightarrow 0$ and $\langle S_z^2 \rangle \rightarrow S(S+1)$ in non-zero applied field, giving $\chi(H,T) \sim \frac{1}{T}$ (which is simply Curie's law, Section 2.3.1), and thus $\left(\frac{\partial \chi}{\partial t}\right) < 0$. To understand the behaviour when $h >> t$, i.e., in the field dominated regime, consider the approach to T_c from above in finite field, H_a. In this situation the magnetization approaches saturation as the critical temperature is approached, meaning that the fluctuations, and thus χ decreases as $T \rightarrow T_c^+$, giving $\left(\frac{\partial \chi}{\partial t}\right) > 0$.

[2]It should be noted that it is assumed that any contribution to the susceptibility from the tail of the Hopkinson maximum, i.e. regular contribution is negligible. It is expected that this assumption is valid for all but the lowest fields.

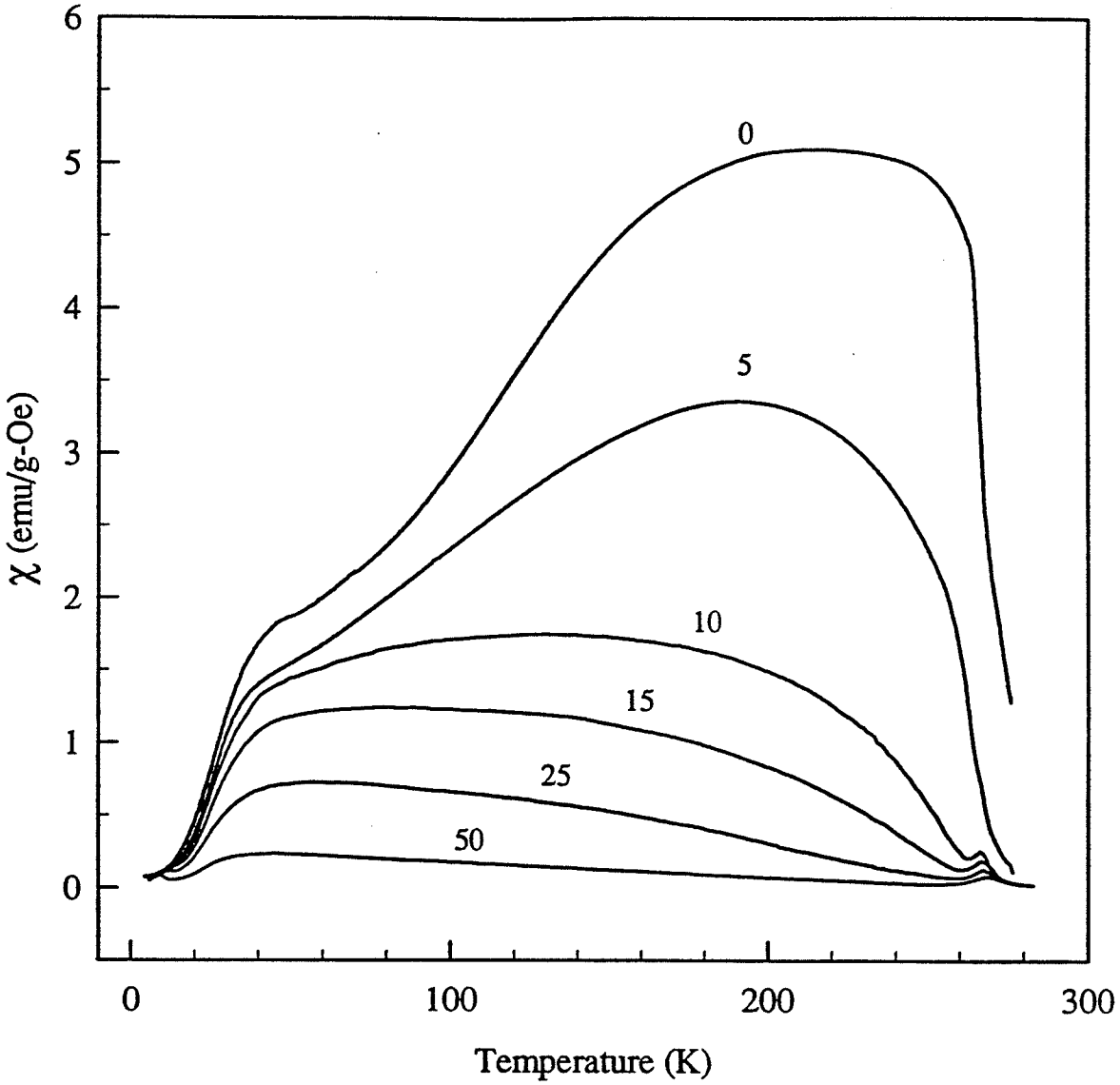

Figure 5.2: The a.c. susceptibility, $\chi(H,T)$ (in emu/g-Oe), corrected for background and demagnetizing effects, plotted versus temperature (in K) for the $x = 0.235$ sample. The numbers beside each curve represent the static biasing field (in Oe).

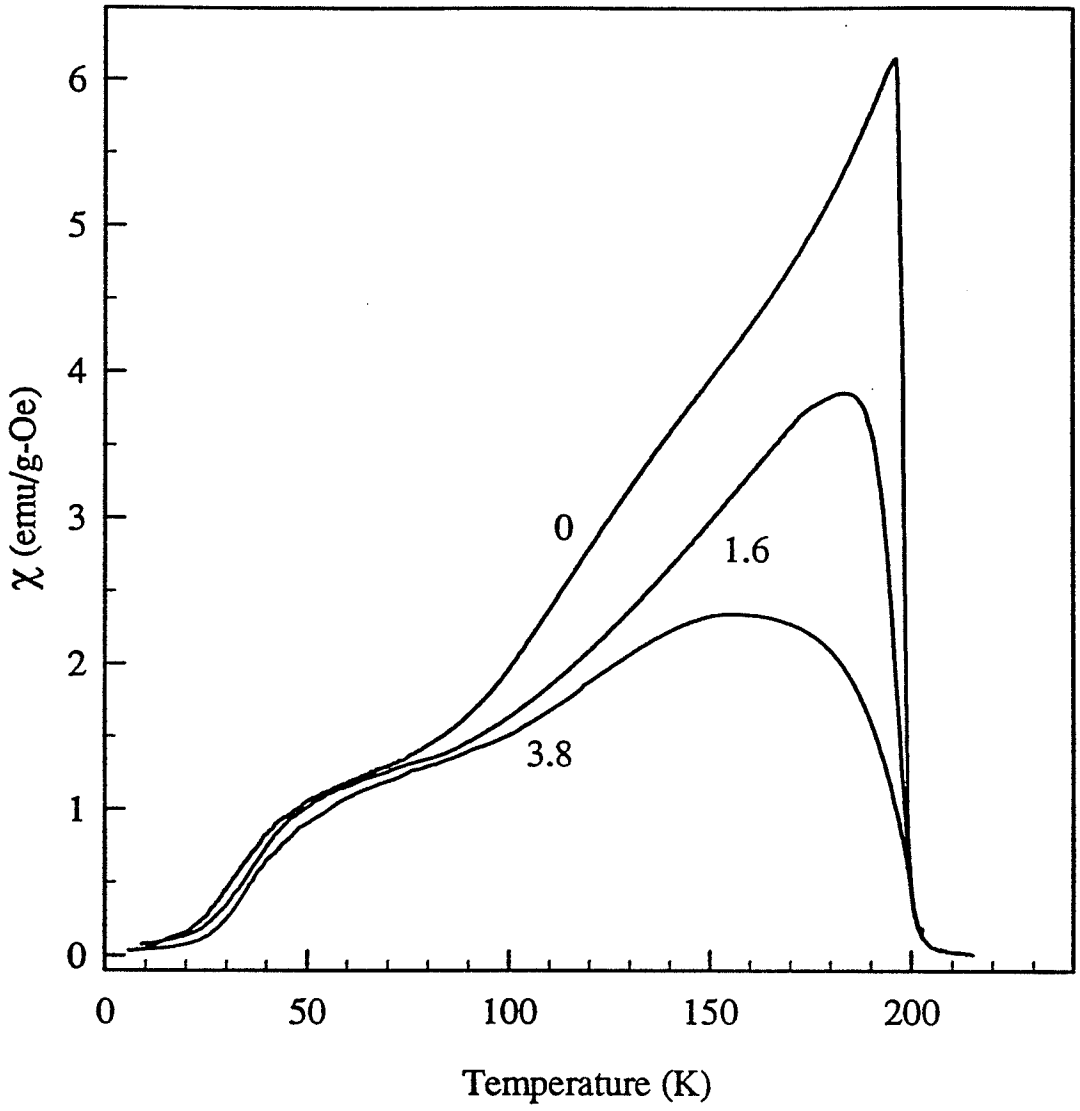

Figure 5.3: The a.c. susceptibility, $\chi(H,T)$ (in emu/g-Oe), corrected for background and demagnetizing effects, plotted versus temperature (in K) for the $x = 0.26$ sample. The numbers beside each curve represent the static biasing field (in Oe).

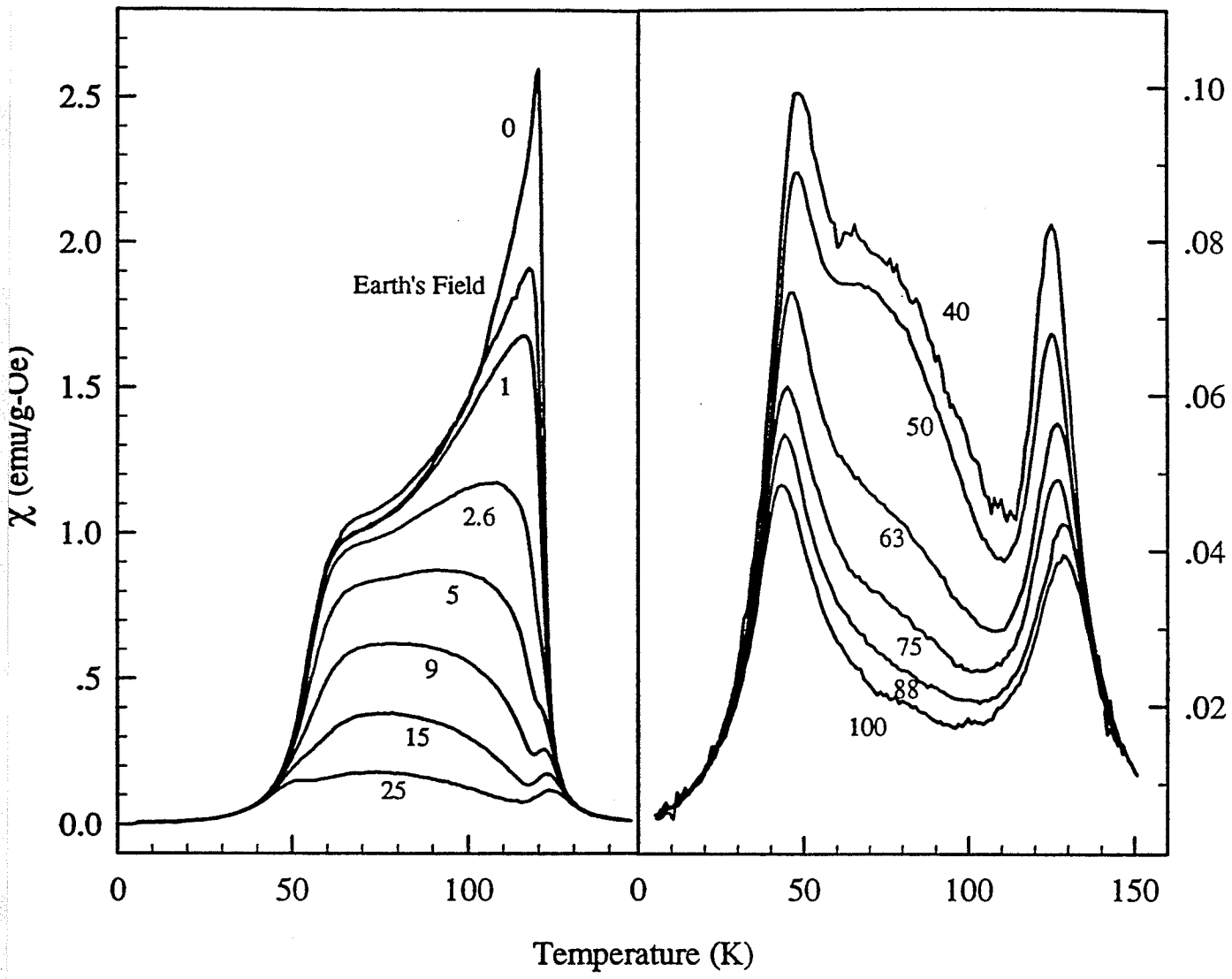

Figure 5.4: The a.c. susceptibility, $\chi(H,T)$ (in emu/g-Oe), corrected for background and demagnetizing effects, plotted versus temperature (in K) for the $x = 0.30$ sample. The numbers beside each curve represent the static biasing field (in Oe).

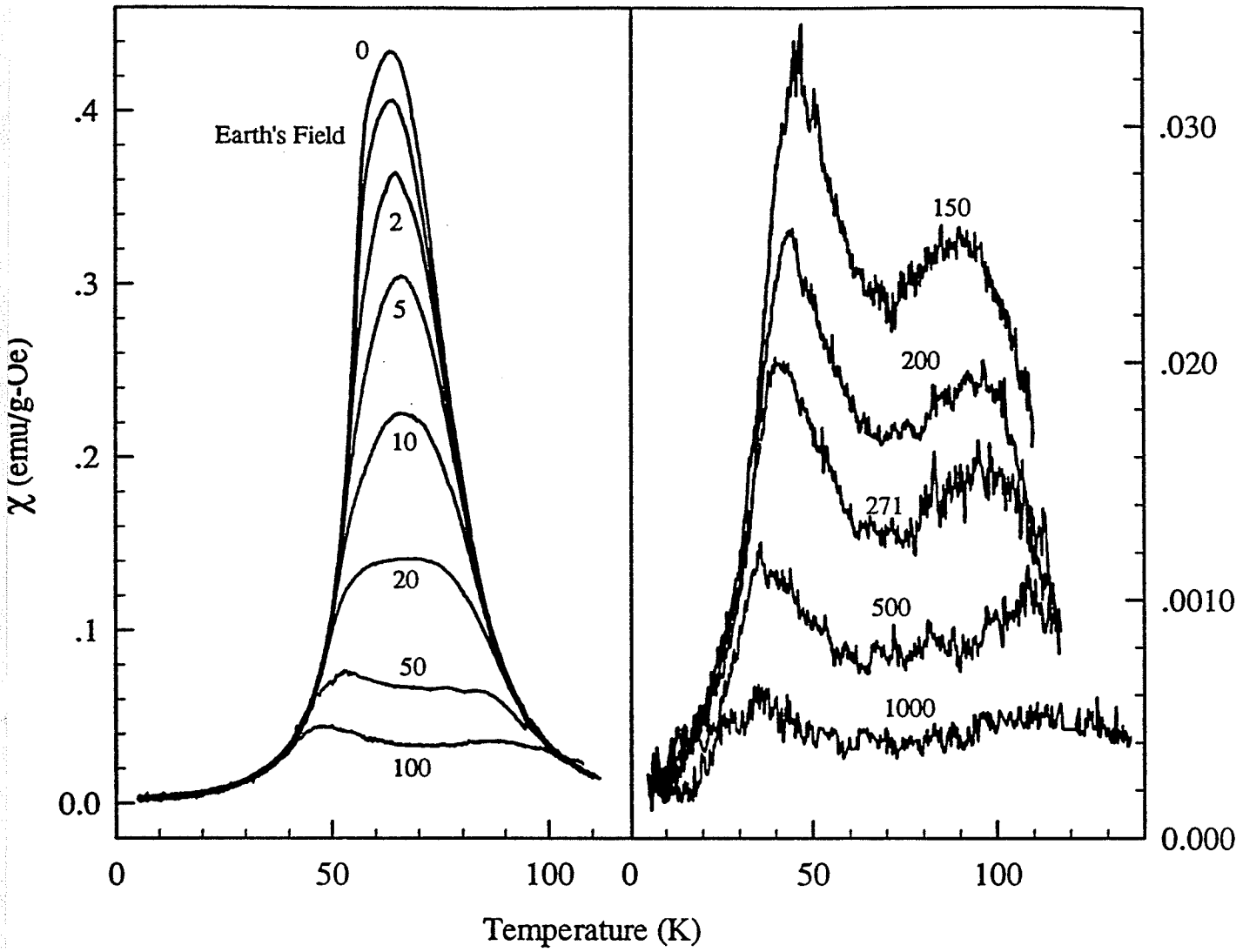

Figure 5.5: The a.c. susceptibility, $\chi(H,T)$ (in emu/g-Oe), corrected for background and demagnetizing effects, plotted versus temperature (in K) for the $x = 0.32$ sample. The numbers beside each curve represent the static biasing field (in Oe).

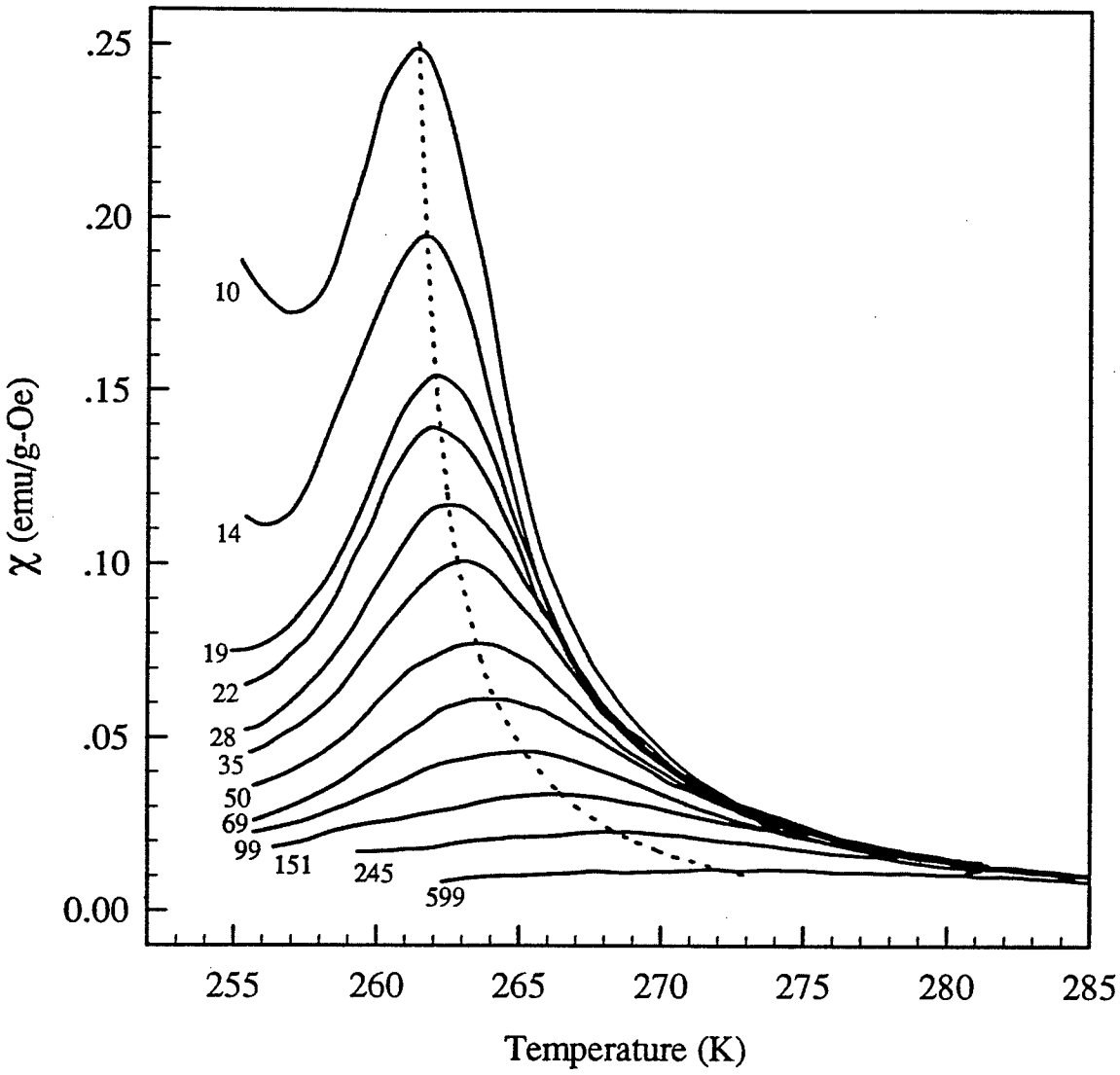

Figure 5.6: Critical peak structure for the $x = 0.235$ sample. The numbers beside each curve represent the static biasing field (in Oe), and the dotted line represents the cross-over line, illustrating the relationship, $\chi_p \sim t_p^{-\gamma}$.

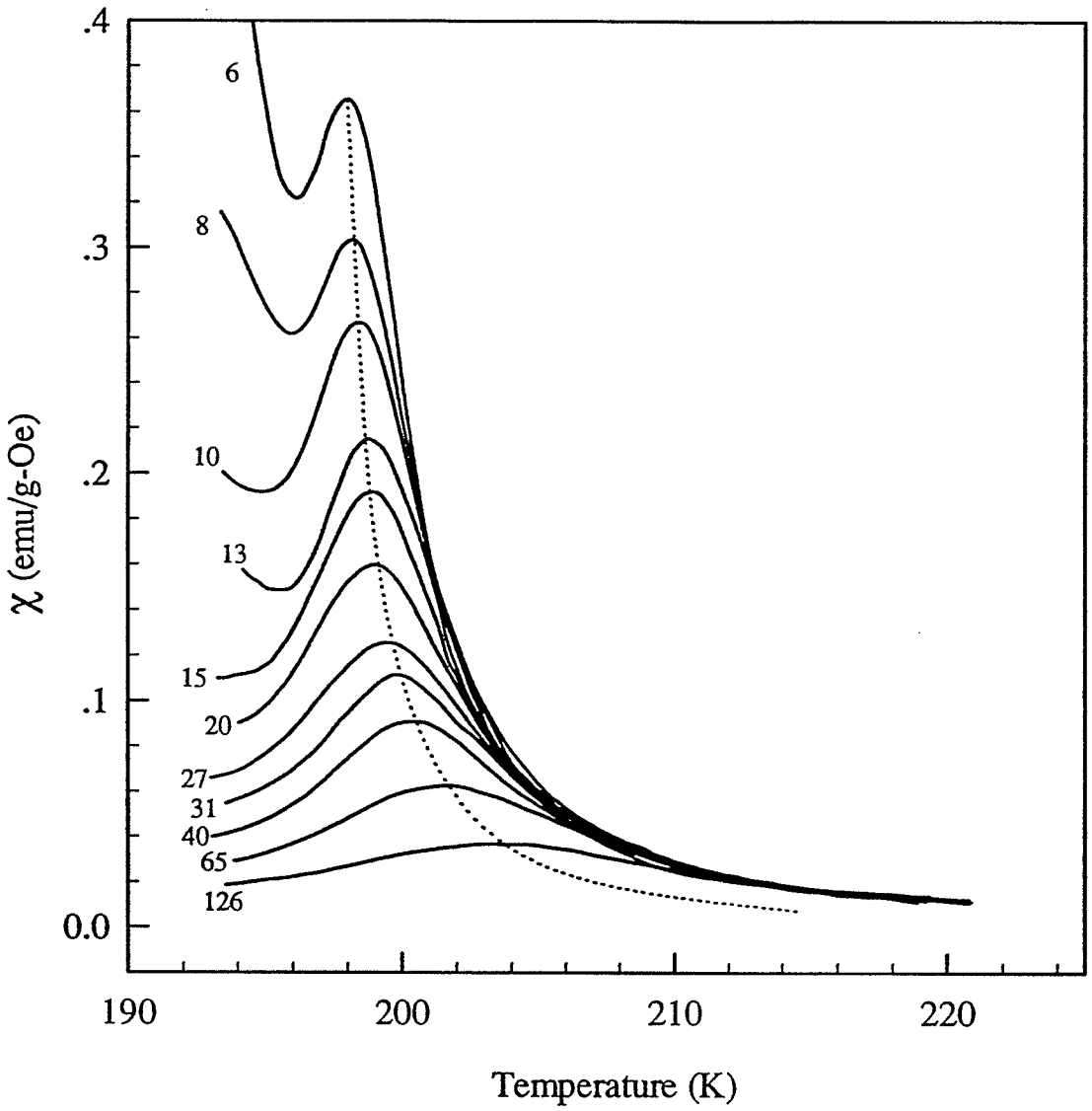

Figure 5.7: Critical peak structure for the $x = 0.26$ sample. The numbers beside each curve represent the static biasing field (in Oe), and the dotted line represents the cross-over line, illustrating the relationship, $\chi_p \sim t_p^{-\gamma}$.

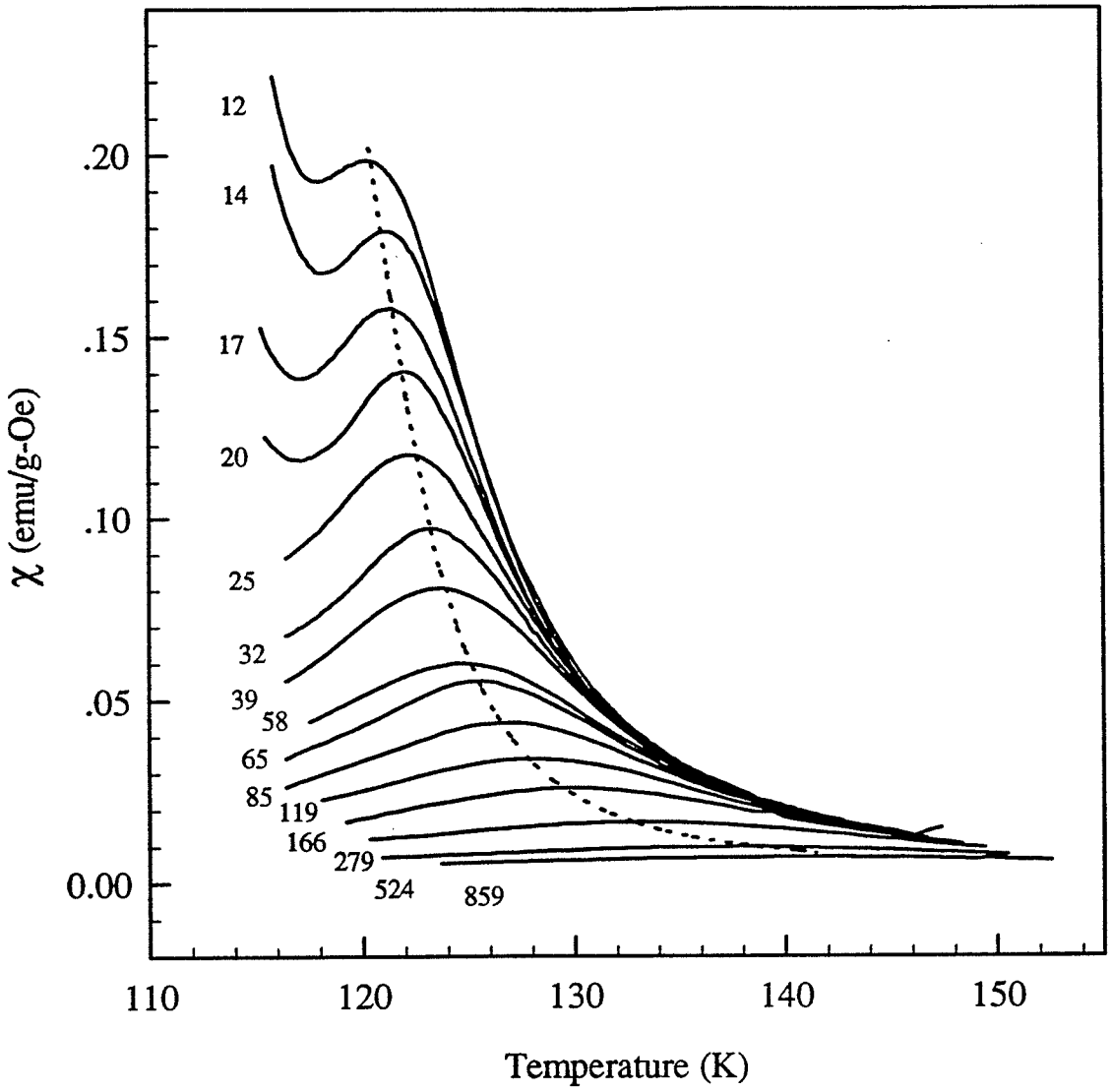

Figure 5.8: Critical peak structure for the $x = 0.30$ sample. The numbers beside each curve represent the static biasing field (in Oe), and the dotted line represents the cross-over line, illustrating the relationship, $\chi_p \sim t_p^{-\gamma}$.

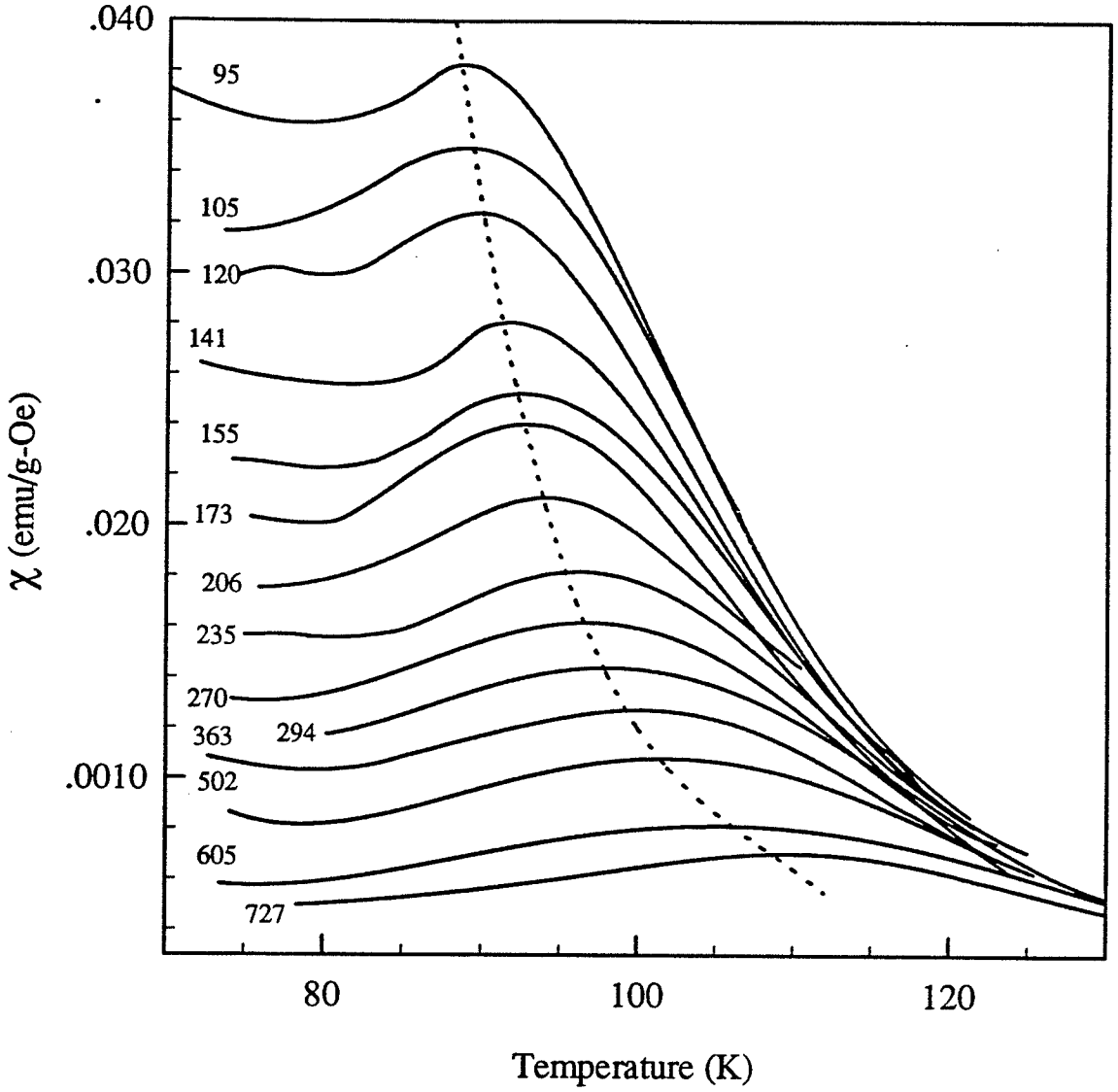

Figure 5.9: Critical peak structure for the $x = 0.32$ sample. The numbers beside each curve represent the static biasing field (in Oe), and the dotted line represents the cross-over line, illustrating the relationship, $\chi_p \sim t_p^{-\gamma}$.

Thus a peak must exist for $T > T_c$ between the two limiting constraints.

Recalling the discussion in Section 2.4.4; the functional form of the expression relating the singular component of the susceptibility to the internal field, H_i and the reduced temperature, $t = (T - T_c)/T_c$, is given by the scaling relation

$$\chi(H_i, t) = t^{-\gamma} F'\left(\frac{H_i}{t^{\gamma+\beta}}\right) = H_i^{1/\delta - 1} G\left(\frac{H_i}{t^{\gamma+\beta}}\right). \tag{5.11}$$

Several relationships derived from the above equation describing the behaviour of the critical peaks will now be considered in light of the experimental data collected.

Firstly, from (5.11) the critical isotherm exponent, δ can be determined by plotting $\chi(H_i, T_p)$ against H_i on a double logarithmic scale to obtain a straight line with a slope of $\frac{1}{\delta} - 1$ in accordance with the equation

$$\chi(H_i, T_p) \propto {H_i}^{1/\delta - 1}, \tag{5.12}$$

where H_i is the internal field, T_p is the peak temperature, and $\chi(H_i, T_p)$ is the peak susceptibility for a particular field.

The combination $\gamma + \beta$ can be found in a similar manner by plotting t_p against H_i on a double logarithmic scale, with the justification for this choice coming from the scaling prediction

$$t_p = \frac{T_c - T_p}{T_c} \propto {H_i}^{1/(\gamma+\beta)} \tag{5.13}$$

where T_c is the critical temperature. (Recall the discussion for (2.98), Section 2.4.4.) However, the above expression contains two unknowns, namely T_c and

the combination $\gamma + \beta$. To determine the critical temperature, T_p is plotted versus $\sqrt{H_i}$ (i.e. assume $\frac{1}{\gamma+\beta} = 0.5$), and T_c is initially estimated from the intercept of the best-fit line, given by

$$T_p \approx c(H_i)^{.5} + T_c, \tag{5.14}$$

where c is some constant. Inserting this T_c into (5.13), a new value of $\frac{1}{\gamma+\beta}$ is found and used in (5.14) to replace the original estimate of 0.5, which in turn permits an 'improved' T_c to be calculated. Adjusting the critical temperature slightly with each iteration, this procedure is repeated until the two graphs yield consistent values for T_c and $\frac{1}{\gamma+\beta}$.

A method of finding γ by itself, using temperature sweep data involves combining (5.12) and (5.13), and then using the Widom equality, $\gamma = \beta(\delta-1)$ to give

$$\chi_p(H, t_p) \propto {t_p}^{-\gamma}. \tag{5.15}$$

Thus, when the logarithm of the peak susceptibility is plotted versus the logarithm of the reduced peak temperature, the result should be a straight line with a slope of $-\gamma$.

Finally, the effective susceptibility exponent, $\gamma^*(t)$ can be found by plotting the zero field susceptibility versus reduced temperature, $(T > T_c)$ on a double-logarithmic scale, and then finding the slope of the curve. $\gamma^*(t)$, also known as the Kouvel-Fisher susceptibility exponent, is thus defined as:

$$\gamma^*(t) = \frac{\mathrm{d}[ln\chi(0,t)]}{\mathrm{d}[lnt]} \tag{5.16}$$

and represents the point to point, or instantaneous slope of the $\chi(0,T)$ versus t plot. Further discussion concerning the 'expected behaviour' of the resulting $\gamma^*(t)$ versus t curve will follow below.

The ferromagnetic to paramagnetic transition for the various samples and the exponents found will now be presented.

5.3.1 $\mathbf{Fe_{1-x}Mn_x}$ $(x = 0.235)$

The procedure described above was used to find δ for the $x = 0.235$ sample, as illustrated in Figure 5.10. The best fit line was found using a well established procedure (Bevington, 1969) and included all of the data points (10 Oe $< H_i <$ 600 Oe) to yield a value for δ of 3.84 ± 0.03. Comparing the exponent value found experimentally to the 3-dimensional Heisenberg model, it can be seen that the experimental value does not agree particularly well with the 'expected' value of 4.78.

A double logarithmic plot of t_p versus H_i, fit over the range 10 Oe $< H_i <$ 300 Oe (points 1 to 13), along with a plot of T_p versus $H_i^{1/(\gamma+\beta)}$, fit over the same range, gives $\gamma + \beta = 1.7(6) \pm 0.1(0)$ and $T_c = 260.17 \pm 0.09$ K in accordance with (5.13). Note that the points at higher fields were not included due to the pronounced downward curvature, caused by the bond disorder present in the sample. The 3D Heisenberg value for $\gamma + \beta$ is $1.388 + 0.367 = 1.755$, which agrees very well with the experimental result. The plots and corresponding best fit lines are shown in Figures 5.11 and 5.12 respectively.

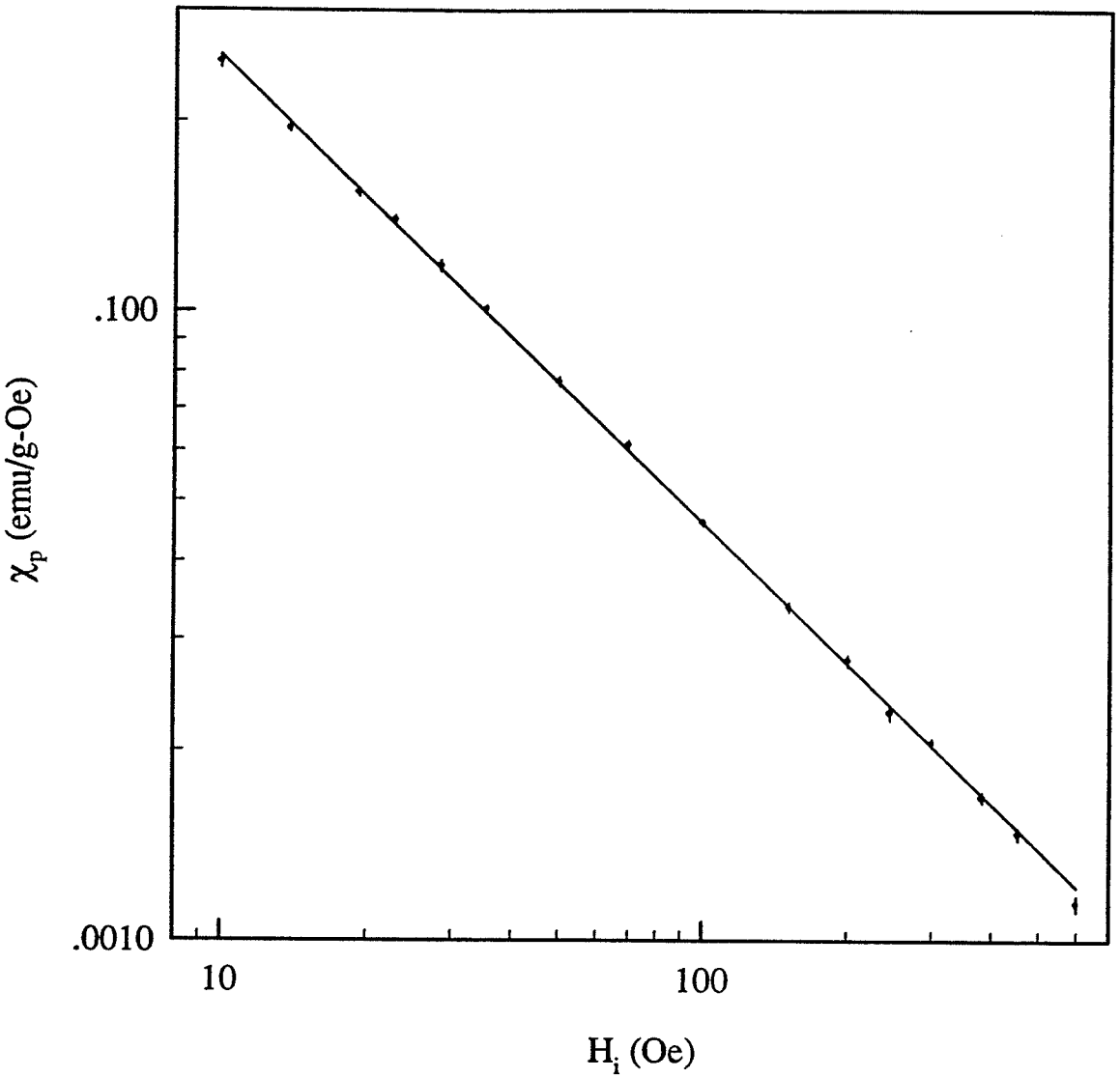

Figure 5.10: The critical peak amplitude, $\chi(H, T_p)$ (in emu/g-Oe) plotted against internal field (in Oe) on a double logarithmic plot for the $x = 0.235$ sample. The solid line represents the best fit line using all of the data points, the slope of which gives $\delta = 3.84 \pm 0.03$.

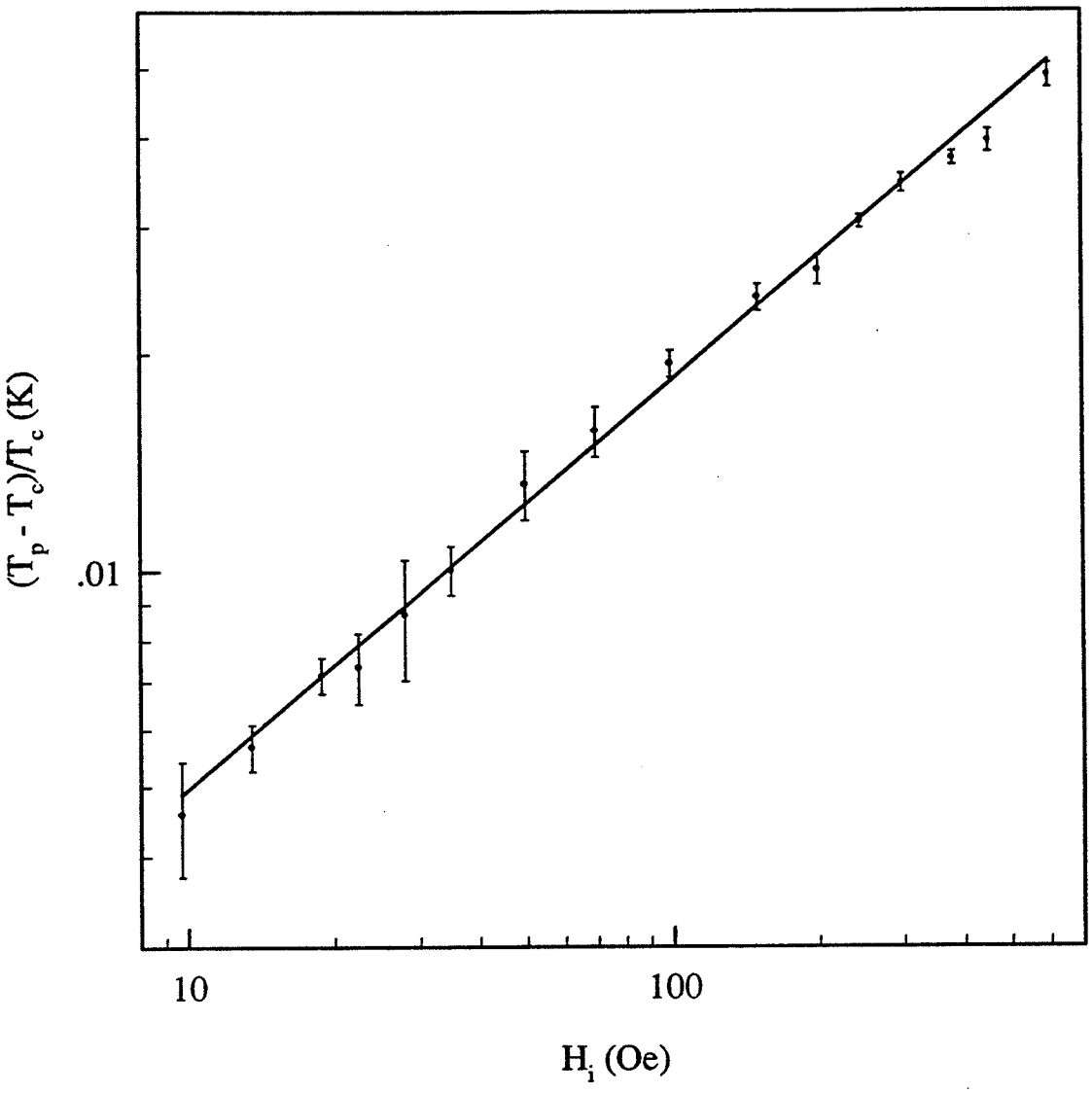

Figure 5.11: The reduced temperature versus the internal field (in Oe), plotted on a double logarithmic plot for the $x = 0.235$ sample. The points are shown with their corresponding errors, which reflect the uncertainty in the peak temperatures. The solid line represents the best fit line, found over the field range 10 Oe $< H_i <$ 300 Oe, and gives a value for $\gamma+\beta$ of 1.7(6)$\pm$0.1(0).

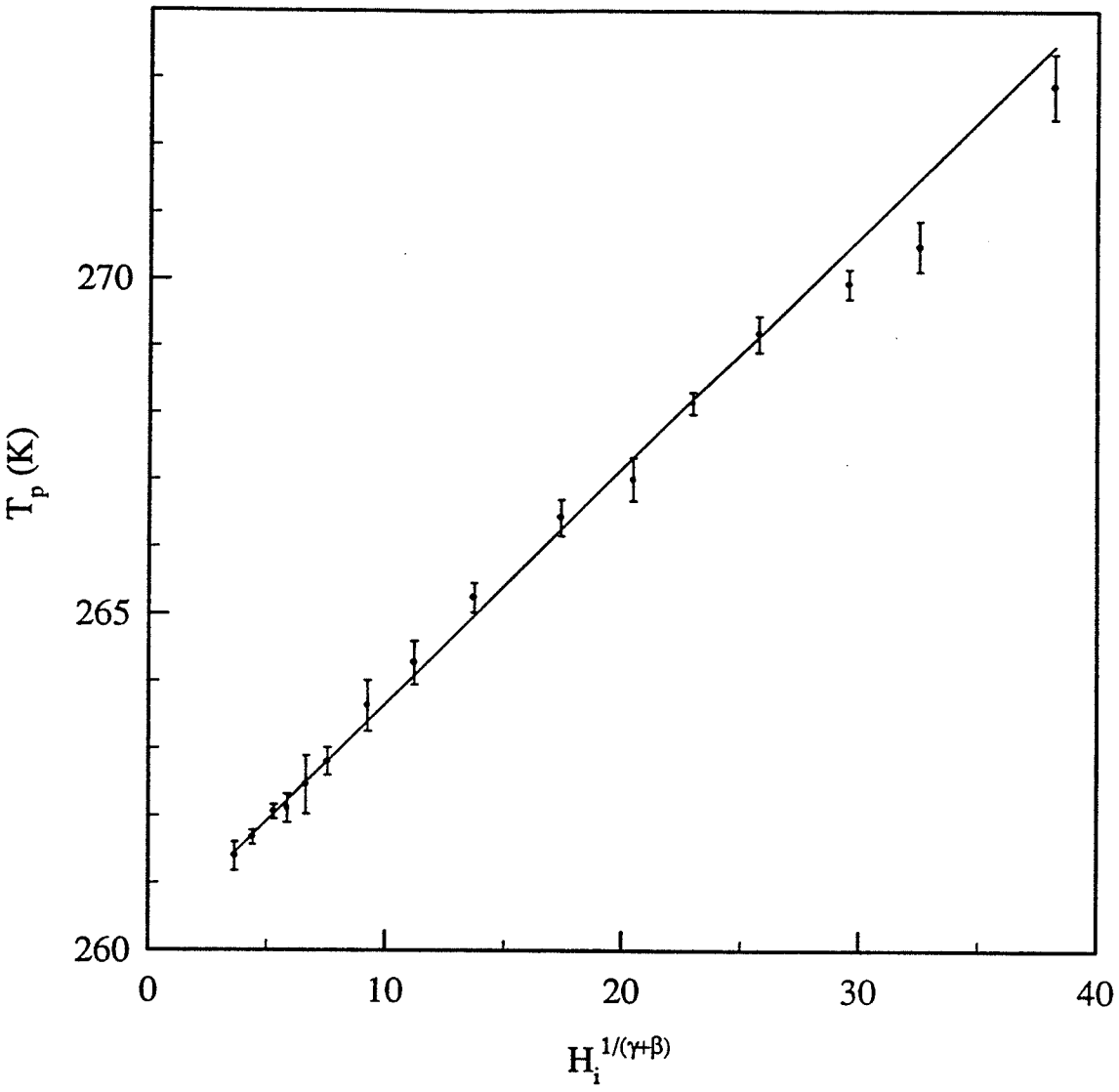

Figure 5.12: The peak temperature (in K) versus $H_i^{1/(\gamma+\beta)}$ for the $x = 0.235$ sample, where $\gamma + \beta = 1.76 \pm 0.10$ from the previous figure. The best fit line, found over the field range 10 Oe $< H_i <$ 300 Oe, has an intercept (critical temperature) of 260.17 ± 0.09 K.

Comparing Figures 5.10 and 5.11, it is apparent that a unique δ value exists over the entire field range, 10 Oe $< H_i <$ 600 Oe, whereas the cross-over exponent, $\gamma + \beta$ was found between 10 Oe and 300 Oe. It is unusual not to observe a corresponding curvature in the δ plot, i.e. have a decreasing $\delta^*(H)$ with increasing field (Berndt et al, 1995). However, the $\gamma + \beta$ value of 1.76 ± 0.10 agrees extremely well with the 3D Heisenberg model value of 1.755.

The γ exponent, itself, can be found using (5.15), as illustrated in Figure 5.13. The fit is not nearly as good as for the previous figures and yields γ values of 1.24 ± 0.02 and 1.29 ± 0.01 when fields 10 Oe $< H_i <$ 300 Oe (as in the $\gamma + \beta$ plot) and 10 Oe $< H_i <$ 600 Oe (δ plot range) respectively are used. Both values are somewhat lower than the 3D Heisenberg value of 1.388. A small reduction of T_c (within error) is unable to improve these fits appreciably.

Returning to the zero field temperature sweep, the temperature dependence of γ, i.e. $\gamma^*(t)$ can now be determined. A plot of $\log(\chi)$ versus $\log(t)$ is shown in Figure 5.14 with a 'high temperature' ($0.093 < t < 0.124$) slope of -1.03 ± 0.39, and a 'peak' ($0.020 < t < 0.060$), or maximum slope of -1.80 ± 0.03. At high temperatures, the susceptibility is expected to agree with the Mean Field Theory prediction of $\gamma = 1$, as is indeed the case for this sample.

The derivative, or local slope of the corresponding $\ln(\chi)$ versus $\ln(t)$ plot

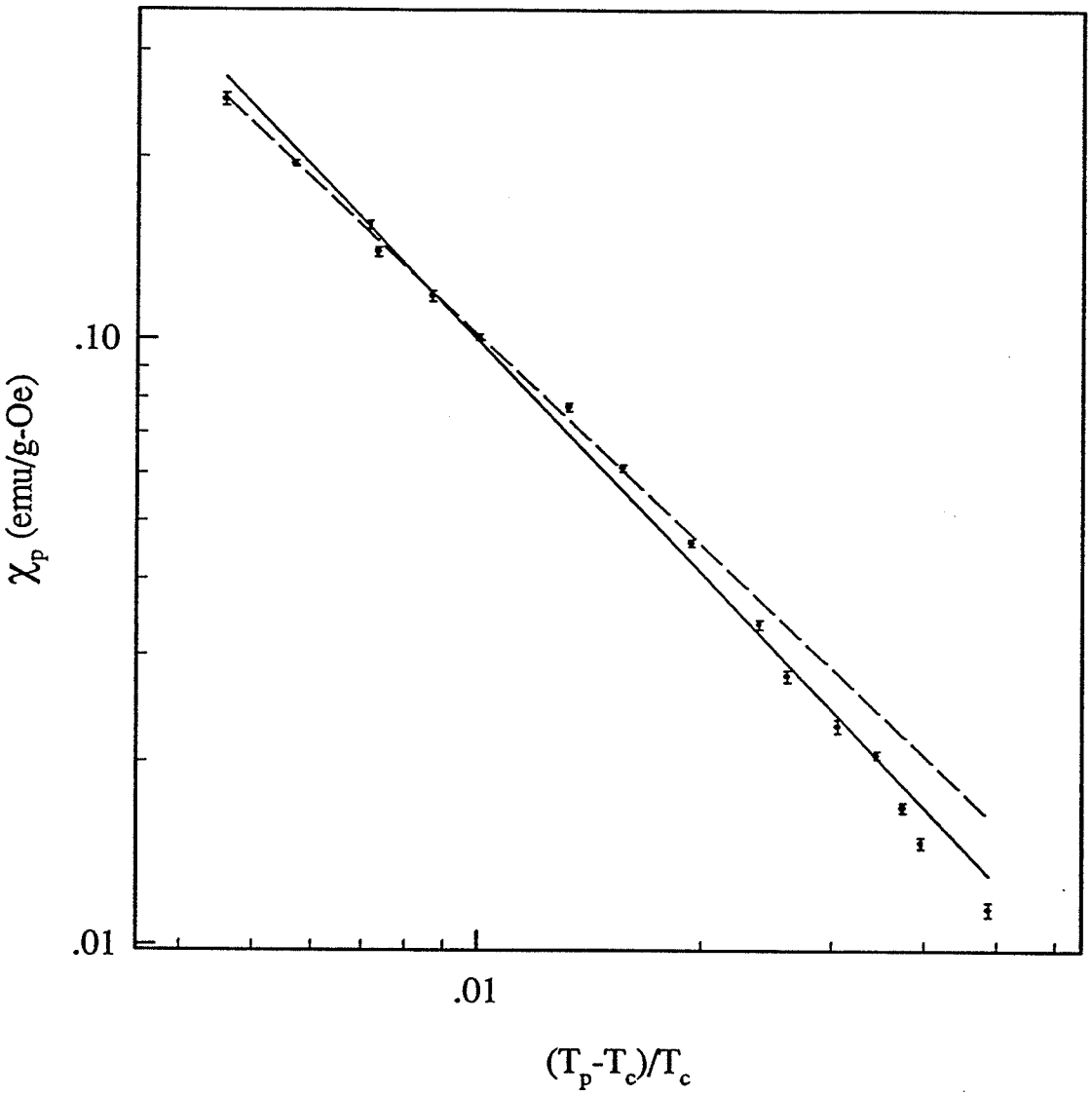

Figure 5.13: The peak susceptibility (in emu/g-Oe) versus $t_p = (T_p - T_c)/T_c$ for the $x = 0.235$ sample, shown on a double logarithmic plot. The solid line represents the best fit line over all of the data points (i.e. δ plot range) and gives $\gamma = 1.29 \pm 0.01$, whereas the dashed line is the best fit line over 10 Oe $< H_i <$ 300 Oe ($\gamma + \beta$ plot range) and gives $\gamma = 1.24 \pm 0.02$.

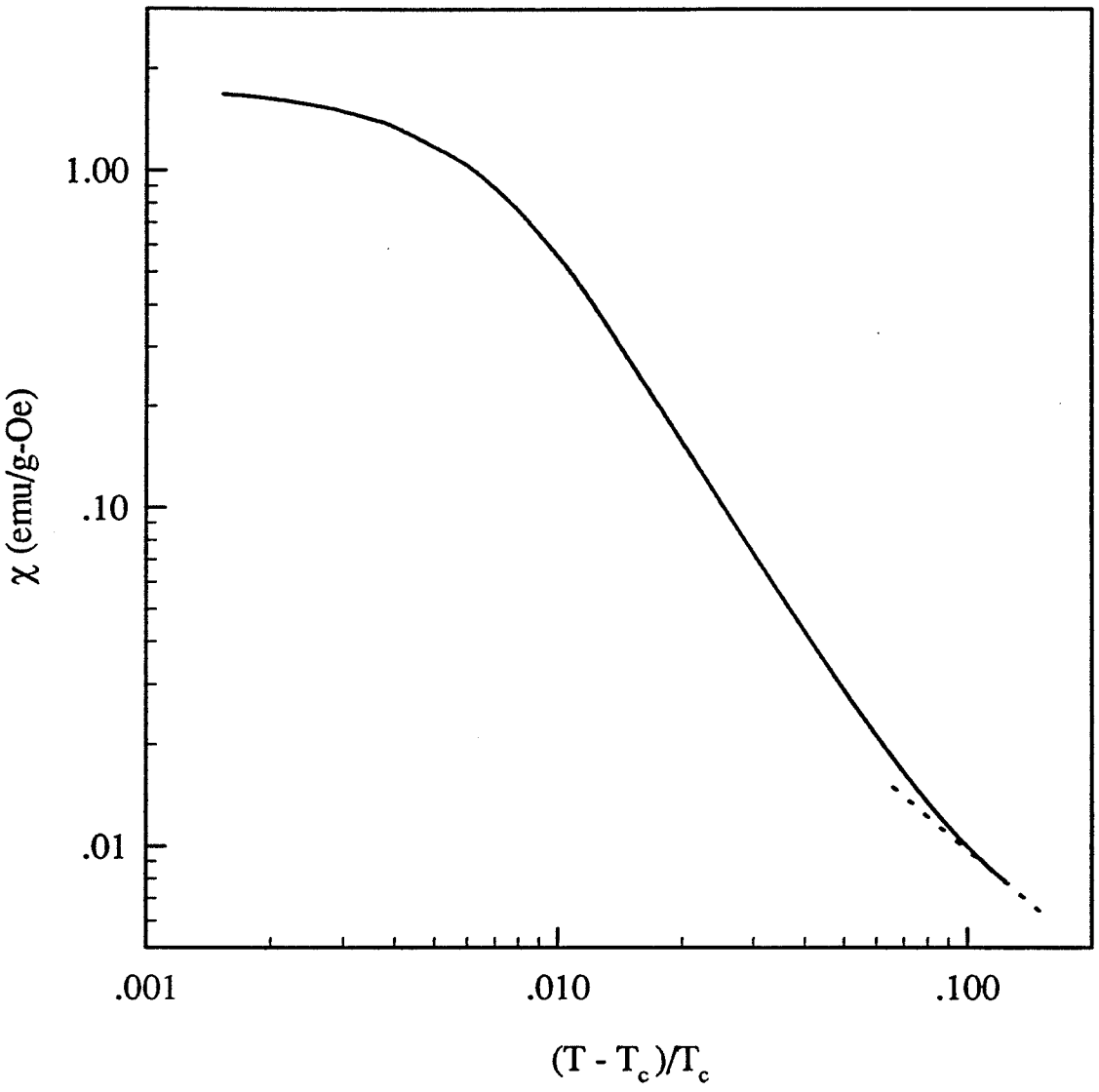

Figure 5.14: The $x = 0.235$ zero field susceptibility (in emu/g-Oe) plotted against reduced temperature for $T > T_c$ on a double logarithmic plot. The dotted line at the high temperature end of the graph is the best fit line, found over the temperature range, $0.093 < t < 0.124$, and has a slope of -1.03 ± 0.39.

(identical graph to Figure 5.14, different scale) is illustrated in Figure 5.15, where $\gamma^*(t)$ rises rapidly between $0 < t < 0.03$, reaching a maximum of 1.94 at $t = 0.031$ and then decreases again at higher temperatures, asymptotically approaching the Mean Field Theory value of 1. The 'peak' γ value determined from Figure 5.15 is in fairly good agreement with that determined from Figure 5.14, the difference being explained by the fact that in Figure 5.14, $\gamma = 1.80 \pm 0.03$ was an average over a number of points (and is therefore lower), whereas $\gamma^*(t = t_{peak}) = 1.94$ is found from the local slope. Notice that $\gamma^*(t)$ approaches zero at small reduced temperatures rather than approaching the 3D Heisenberg value of 1.388 as $t \rightarrow 0$. This is an inevitable consequence of the zero field susceptibility failing to reach the demagnetization limit, as previously discussed.

It is also interesting to confirm whether or not the Widom equality, $\gamma = \beta(\delta - 1)$ is obeyed. This is most easily done by rearranging the latter to get

$$\gamma = \frac{(\gamma + \beta)(\delta - 1)}{\delta}. \tag{5.17}$$

The above expression uses the values found for $\gamma + \beta$ and δ, namely $1.7(6) \pm 0.1(0)$ and 3.84 ± 0.03 respectively, to 'predict' a value for γ, which can then be compared to the results obtained using (5.15) and the $\gamma^*(t)$ plot. It can easily be shown that (5.17) yields a value of 1.30 ± 0.07, which nearly encompasses the 3D Heisenberg value, but more importantly, agrees to within error with the γ values found by plotting χ_p versus t_p (Figure 5.13). This suggests that the Widom inequality can be expressed as an equality.

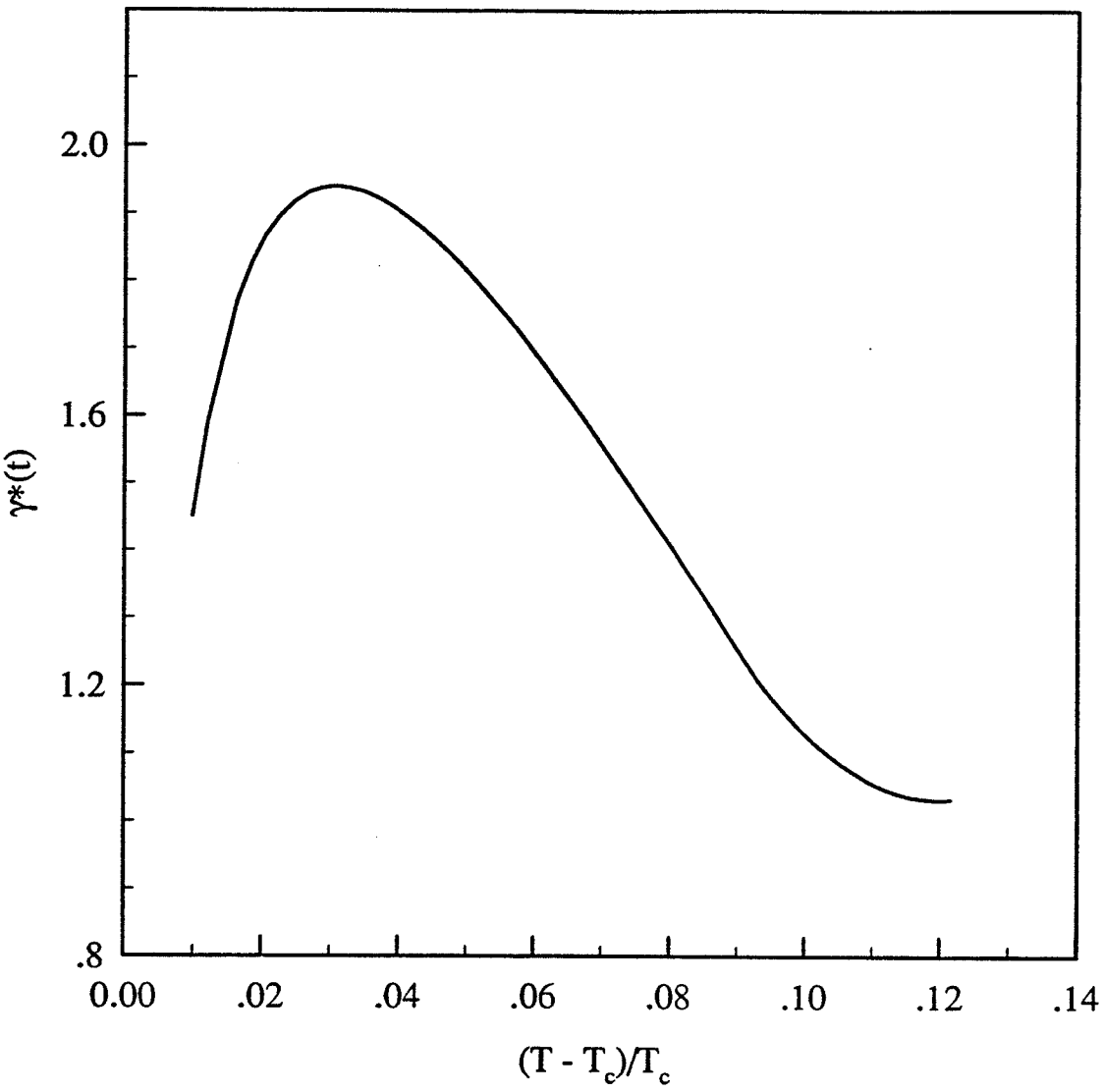

Figure 5.15: The effective Kouvel-Fisher susceptibility exponent, $\gamma*(t)$ (5.16) for $x = 0.235$ plotted versus temperature.

5.3.2 $Fe_{1-x}Mn_x$ ($x = 0.26$)

Carrying out similar calculations on the data collected for the $x = 0.26$ sample yields the following results. From the data shown in Figure 5.16 a value for δ of 4.69 ± 0.01 can be found when all of the data points (6 Oe $< H_i <$ 1000 Oe) are used to find the best-fit line. This agrees quite well with the 3D Heisenberg value of 4.78. As with the $x = 0.235$ sample, no curvature is apparent over the field range of the measurements.

The combination $\gamma+\beta$, along with T_c were found, as illustrated in Figures 5.17 and 5.18 to be $1.7(5) \pm 0.1(7)$ and 196.6 ± 0.1 K respectively, using the field range 8 Oe $< H_i <$ 82 Oe (points 2 to 16). The first point was not used in the calculation as it is substantially lower than the best-fit line. A possible reason for this is that at low fields, a large regular contribution will affect the position of the critical peak. The latter two figures display even more pronounced downward curvature than the corresponding plots for the $x = 0.235$ sample, although measurements taken for the $x = 0.26$ sample extend to higher fields.

Using the alternate method to find an asymptotic γ gives values of $1.386 \pm$ 0.003 and 1.477 ± 0.001 when the field ranges 8 Oe $< H_i <$ 82 Oe ($\gamma + \beta$ plot range) and 6 Oe $< H_i <$ 1000 Oe (as in the δ plot), respectively are used. Both of these slopes, along with the data used, are shown in Figure 5.19. These values are in much better agreement with the 3D Heisenberg value than those found for the $x = 0.235$ sample, one of them being slightly

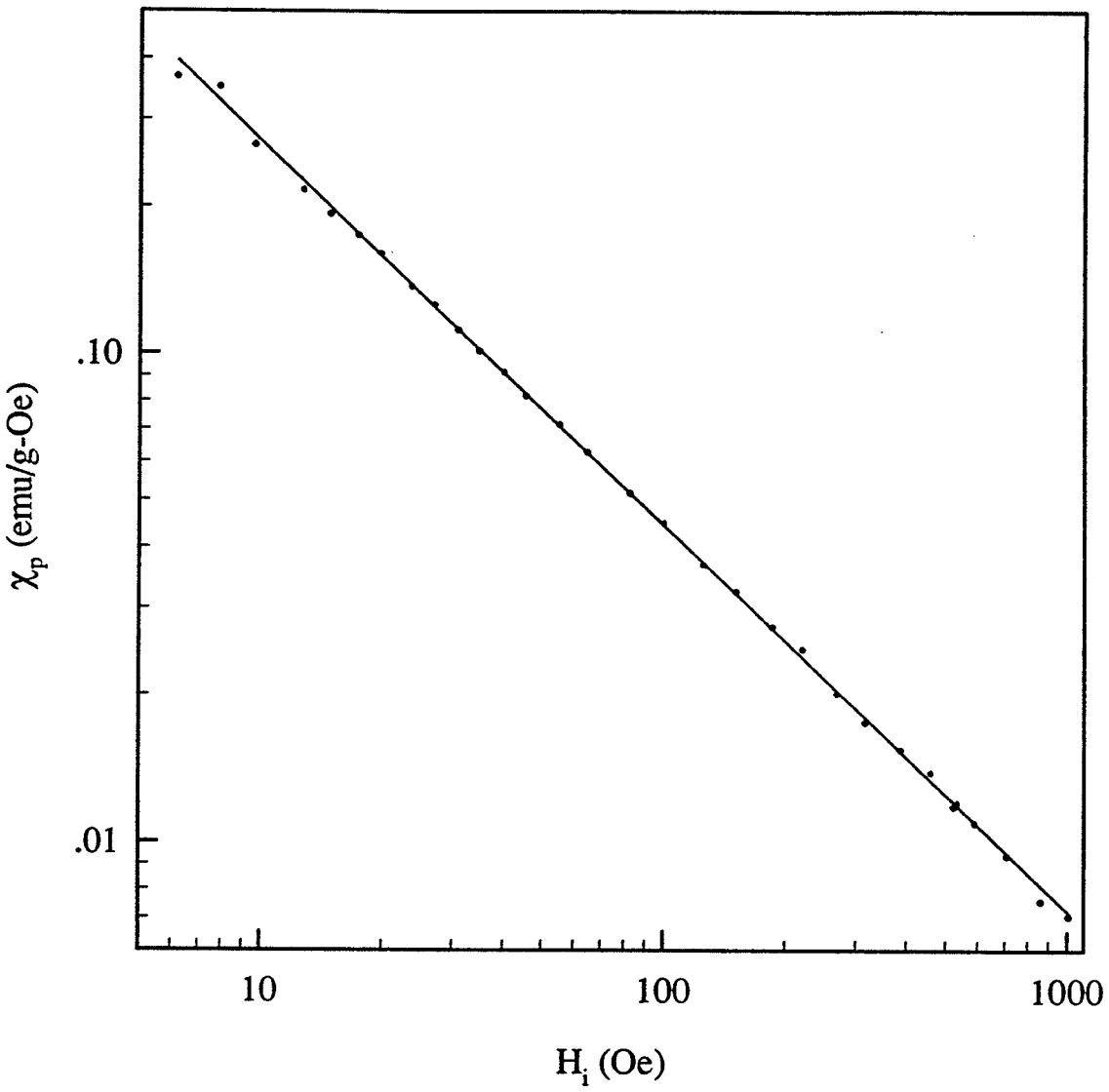

Figure 5.16: The critical peak amplitude, $\chi(H, T_p)$ (in emu/g-Oe) plotted against internal field (in Oe) on a double logarithmic plot for the $x = 0.26$ sample. The solid line represents the best fit line using all of the data points, the slope of which gives $\delta = 4.69 \pm 0.01$.

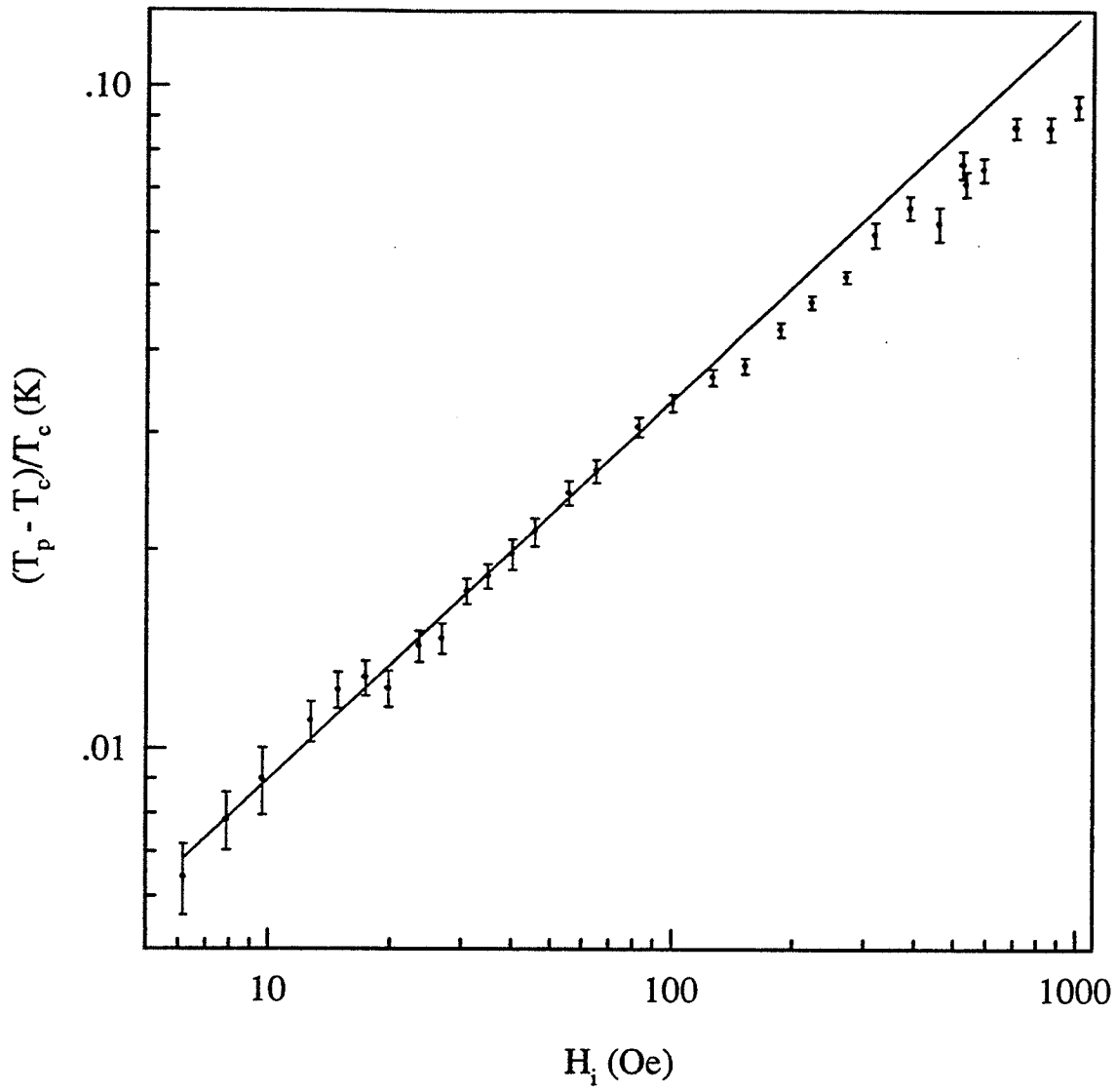

Figure 5.17: The reduced temperature versus the internal field (in Oe), plotted on a double logarithmic plot for the $x = 0.26$ sample. The points are shown with their corresponding errors, which reflect the uncertainty in the peak temperatures. The solid line represents the best fit line, found over the field range 8 Oe $< H_i <$ 82 Oe, and gives a value for $\gamma + \beta$ of $1.7(5) \pm 0.1(7)$.

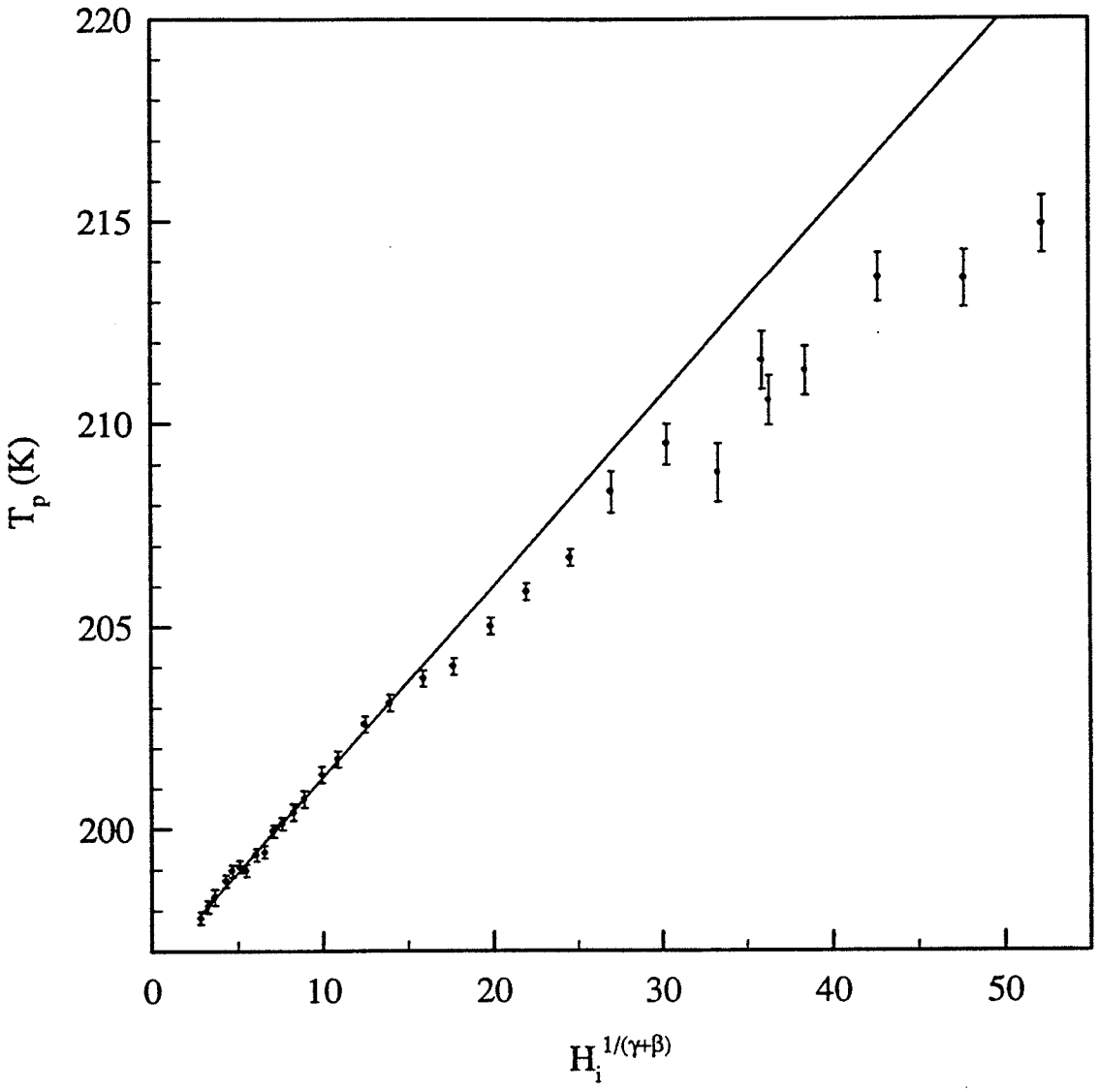

Figure 5.18: The peak temperature (in K) versus $H_i^{1/(\gamma+\beta)}$ for the $x = 0.26$ sample, where $\gamma + \beta = 1.75 \pm 0.17$ from the previous figure. The best fit line, found over the field range 8 Oe $< H_i <$ 82 Oe, has an intercept (critical temperature) of 196.6 ± 0.1 K.

lower, and the other being somewhat higher.

The effective susceptibility exponent for $x = 0.26$ can also be found as before, with the susceptibility versus reduced temperature plot being shown in Figure 5.20. At higher temperatures, the data does not curve upwards to approach the Mean Field behaviour as was the case for $x = 0.235$, suggesting that data should have been collected to even higher temperatures. In order to do so however, a larger sample would have been required to increase the signal to noise ratio to an acceptable level. Otherwise the data would simply decrease to the 'background' level, and not accurately reflect the response of the sample. Notice also that a high temperature value of $\gamma \approx 1$ was found for the $x = 0.235$ sample, using reduced temperatures in the range $0.093 < t < 0.124$, which is much lower than 0.221, the highest reduced temperature in Figure 5.20. This implies that the temperature at which the short range order is destroyed, in other words, that at which the Mean Field Theory becomes valid, depends upon the concentration, x. A 'maximum' slope can still be calculated however, and was found to be -1.69 ± 0.05, using the temperature range, $0.031 < t < 0.079$.

Using (5.16), the curve illustrated in Figure 5.21 was obtained, representing the temperature dependence of γ. The latter achieves a maximum of 1.77 at $t = 0.12$, which agrees quite well with the 'average' value found above.

Checking the Widom equality using (5.17) yields a value of $1.3(8) \pm 0.1(3)$ for γ, which not only agrees very well with the 3D Heisenberg value, but is

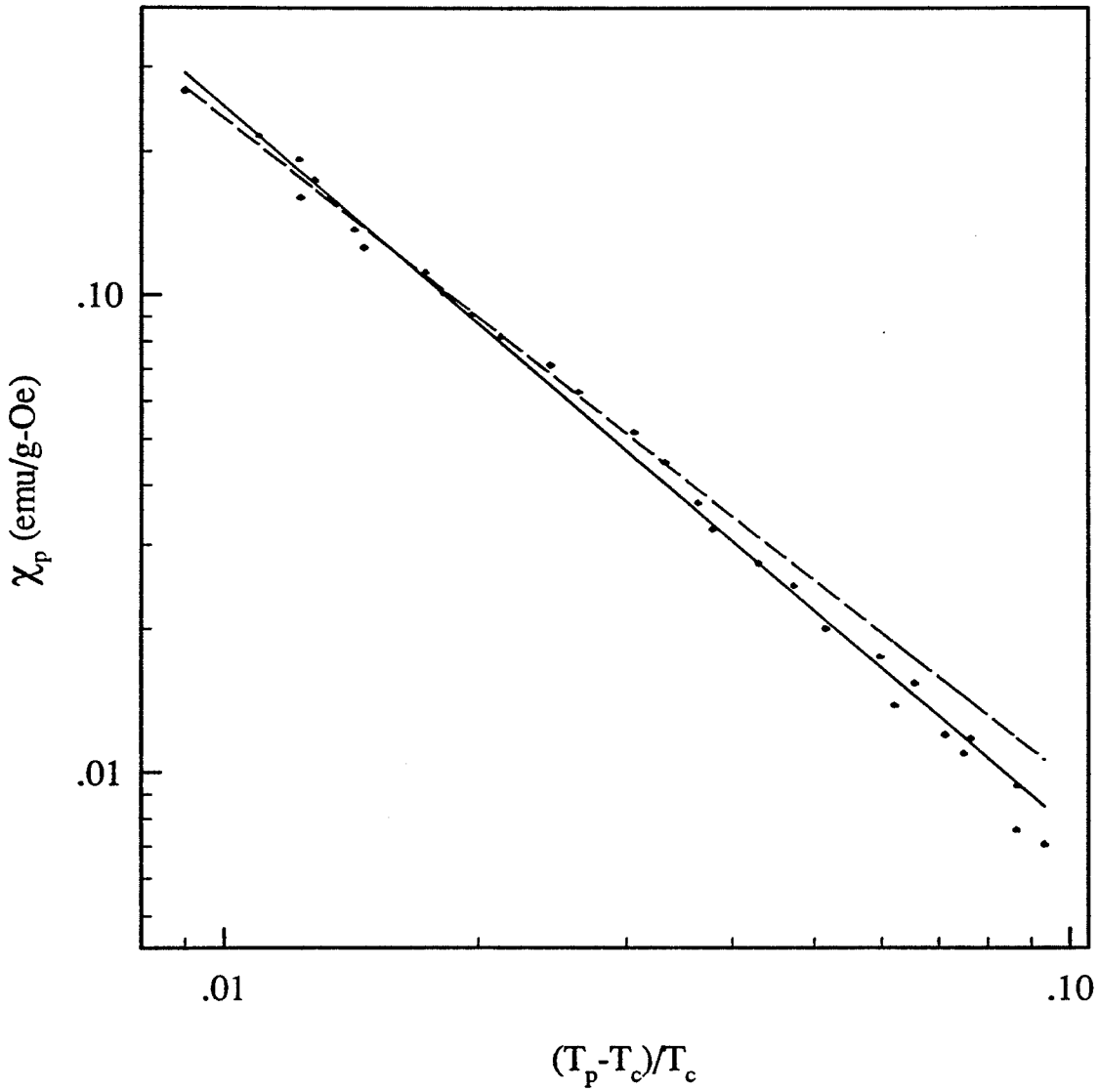

Figure 5.19: The peak susceptibility (in emu/g-Oe) versus $t_p = (T_p - T_c)/T_c$ for the $x = 0.26$ sample, shown on a double logarithmic plot. The solid line represents the best fit line over all of the data points (i.e. δ plot range) and gives $\gamma = 1.477 \pm 0.001$, whereas the dashed line is the best fit line over 8 Oe $< H_i <$ 82 Oe ($\gamma + \beta$ plot range) and gives $\gamma = 1.386 \pm 0.003$.

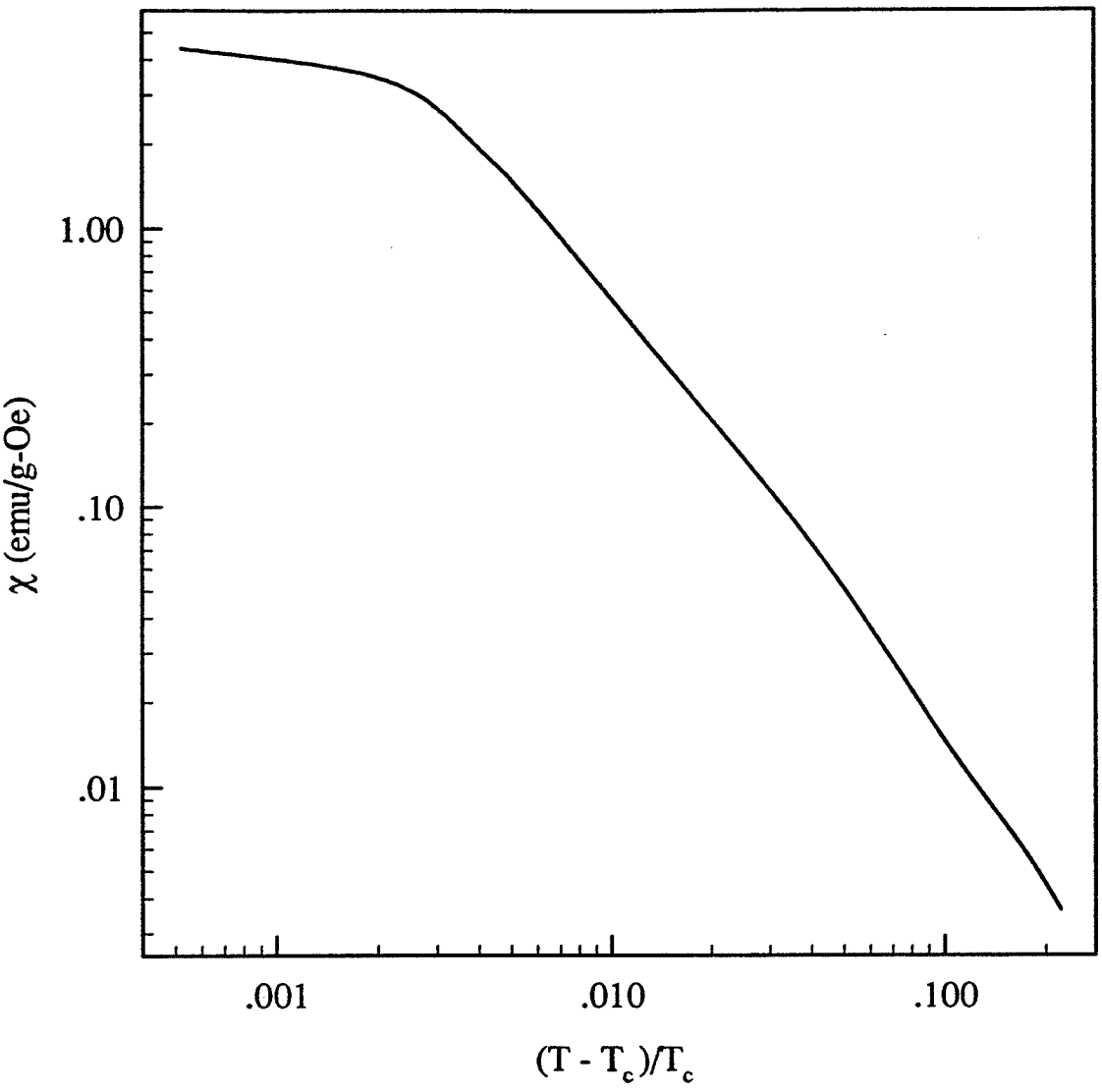

Figure 5.20: The $x = 0.26$ zero field susceptibility (in emu/g-Oe) plotted against reduced temperature for $T > T_c$ on a double logarithmic plot.

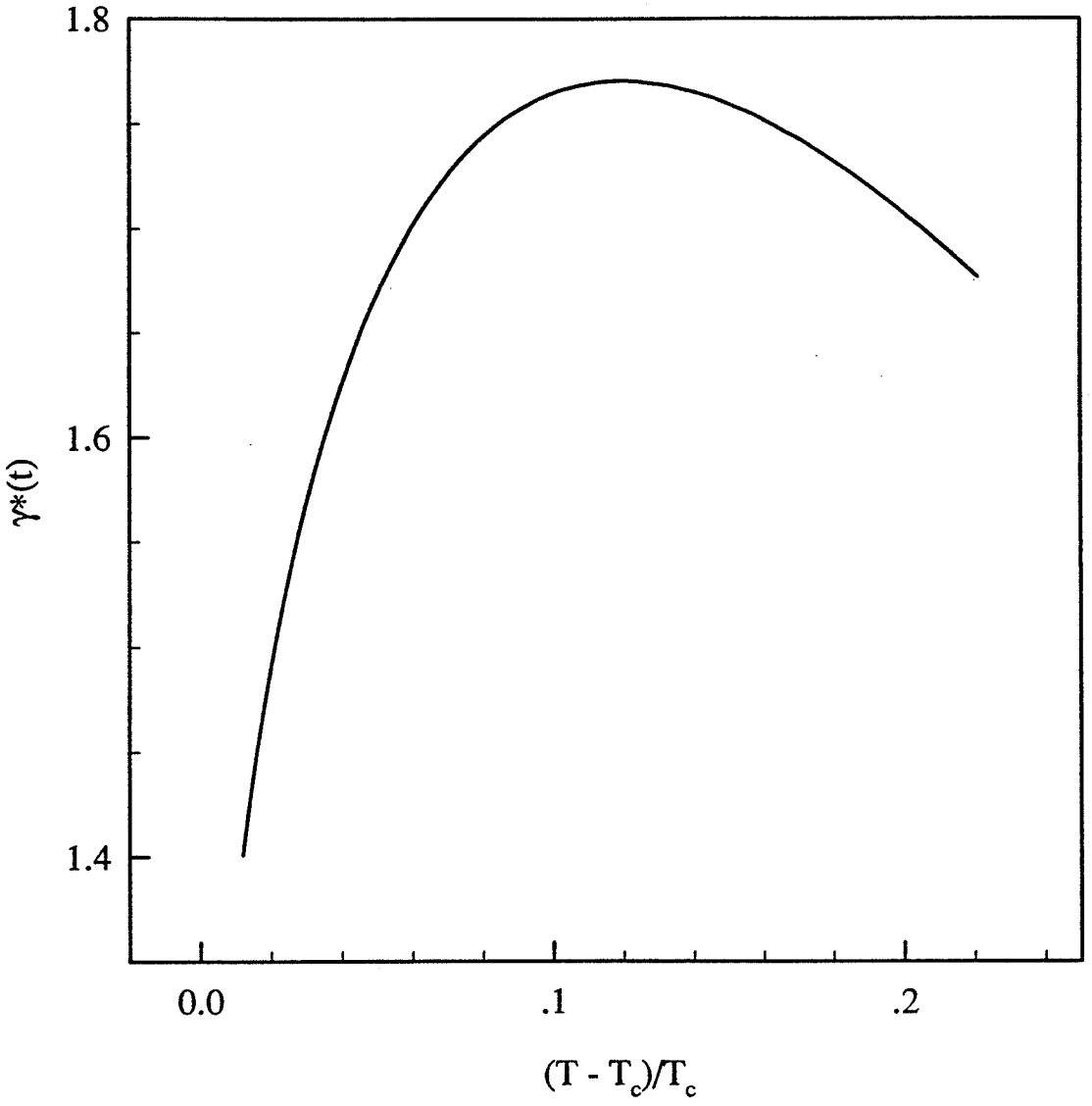

Figure 5.21: The effective Kouvel-Fisher susceptibility exponent, $\gamma*(t)$ (5.16) for $x = 0.26$, plotted versus temperature.

also consistent with the value obtained from the γ plot, using (5.15). Thus the Widom inequality can again be expressed as an equality.

5.3.3 $Fe_{1-x}Mn_x$ ($x = 0.30$)

Following the same procedures as outlined above, the values for the various $x = 0.30$ critical exponents can be found. Using all of the data points (12 Oe $< H_i <$ 1000 Oe) shown in Figure 5.22, δ was found to be 4.86 ± 0.02. This agrees quite well with the 3D Heisenberg value of 4.78, and as with the previous samples, no curvature is visible, even at the highest fields.

The critical temperature and $\gamma+\beta$ were found from Figures 5.23 and 5.24 to equal 118.0 ± 0.2 K and $1.7(5) \pm 0.1(3)$ respectively, where the latter value agrees excellently with the 'predicted' 3D Heisenberg value of 1.755. A field range, 14 Oe $< H_i <$ 85 Oe (points 2 to 12), similar to that of the $x = 0.26$ sample was used to find the above values; however, the downward curvature at higher fields is possibly even more pronounced than with the previous two samples. As before, the first data point was omitted since it deviates visibly from the best fit line.

Using (5.15) to find γ gives slopes of -1.31 ± 0.02 and -1.53 ± 0.03 for the field ranges 12 Oe $< H_i <$ 1000 Oe and 14 Oe $< H_i <$ 85 Oe respectively. The first value almost agrees with the theoretical value of 1.388, whereas the latter number is substantially larger than the 3D Heisenberg value due to the obvious curvature in the data points, as illustrated in Figure 5.25.

The temperature dependence of the zero field susceptibility on a double

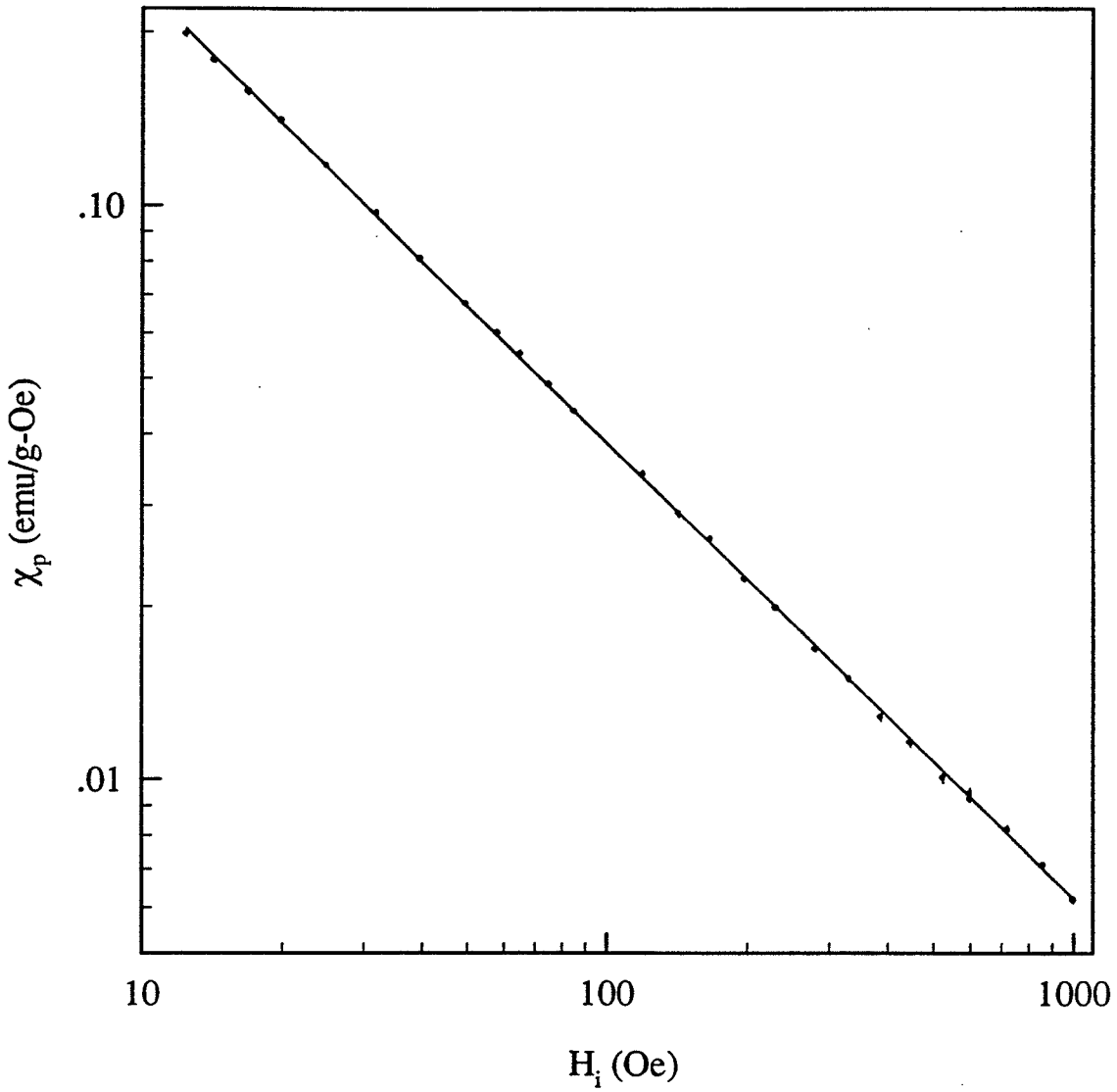

Figure 5.22: The critical peak amplitude, $\chi(H, T_p)$ (in emu/g-Oe) plotted against internal field (in Oe) on a double logarithmic plot for the $x = 0.30$ sample. The solid line represents the best fit line using all of the data points, the slope of which gives $\delta = 4.86 \pm 0.02$.

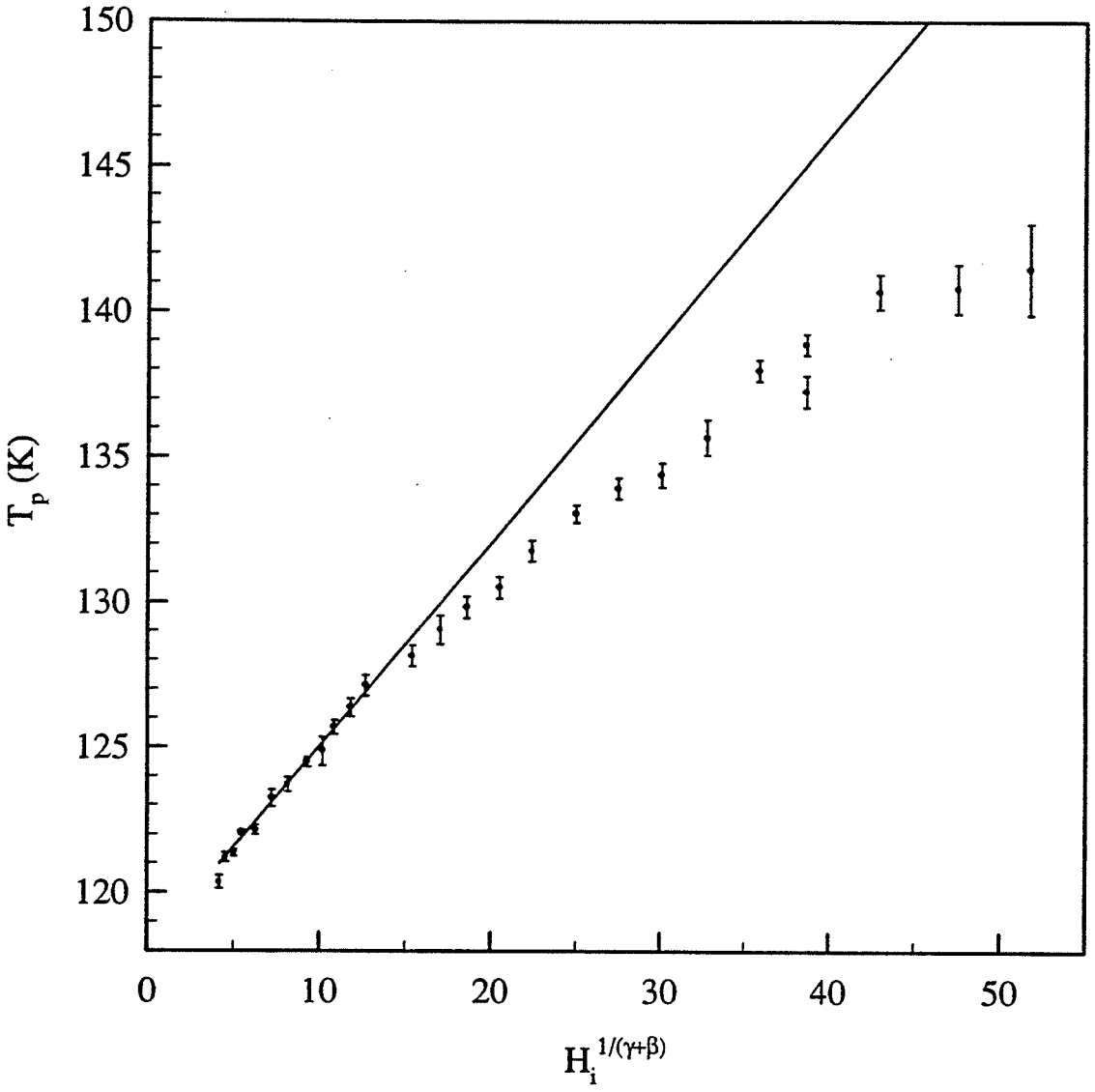

Figure 5.23: The reduced temperature versus the internal field, plotted on a double logarithmic plot for the $x = 0.30$ sample. The points are shown with their corresponding errors, which reflect the uncertainty in the peak temperatures. The solid line represents the best fit line, found over the field range 14 Oe $< H_i <$ 85 Oe, and gives a value for $\gamma + \beta$ of $1.7(5) \pm 0.1(3)$.

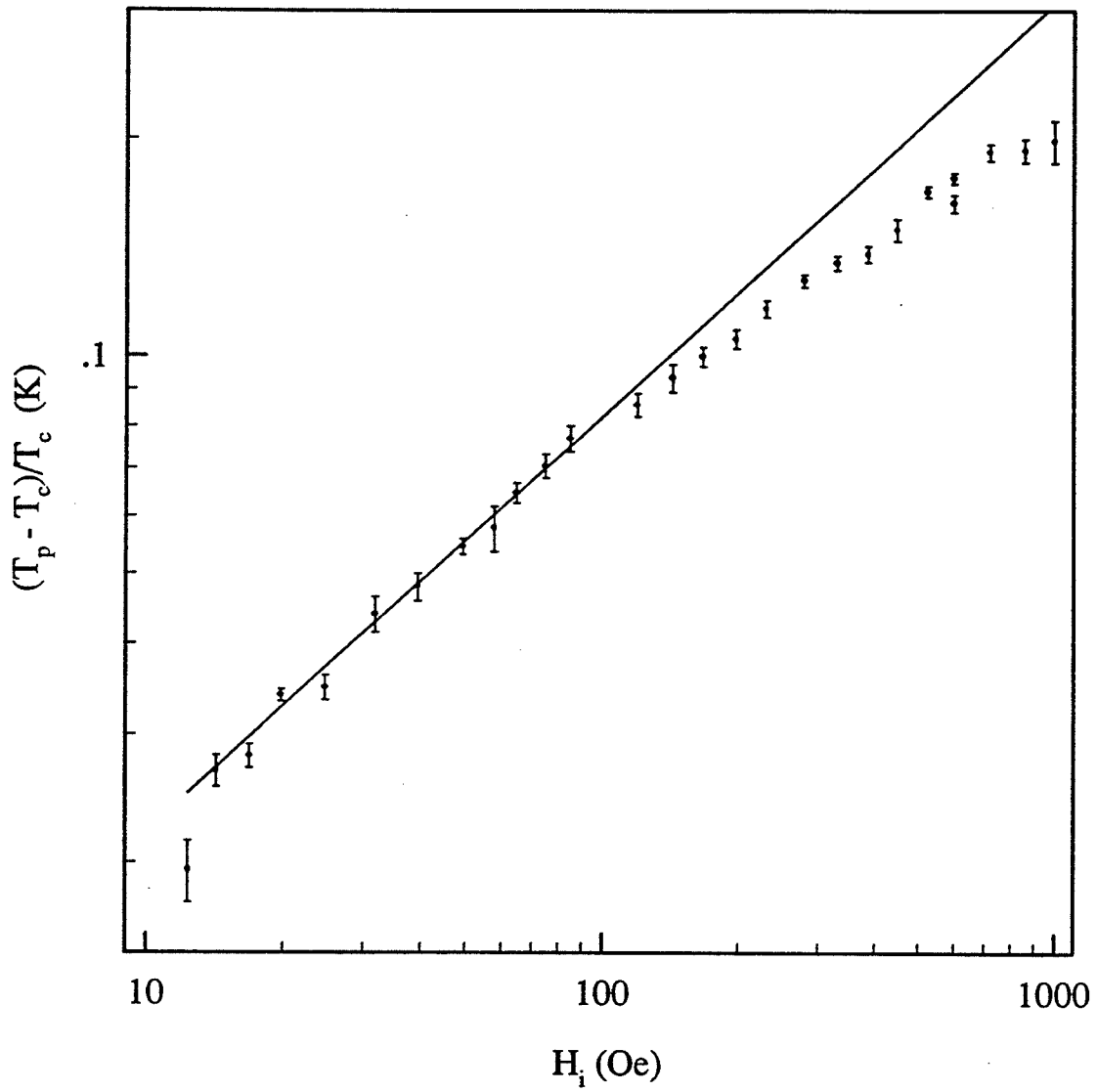

Figure 5.24: The peak temperature (in K) versus $H_i^{1/(\gamma+\beta)}$ for the $x = 0.30$ sample, where $\gamma + \beta = 1.75 \pm 0.13$ from the previous figure. The best fit line, found over the field range 14 Oe $< H_i <$ 85 Oe, has an intercept (critical temperature) of 118.0 ± 0.2 K.

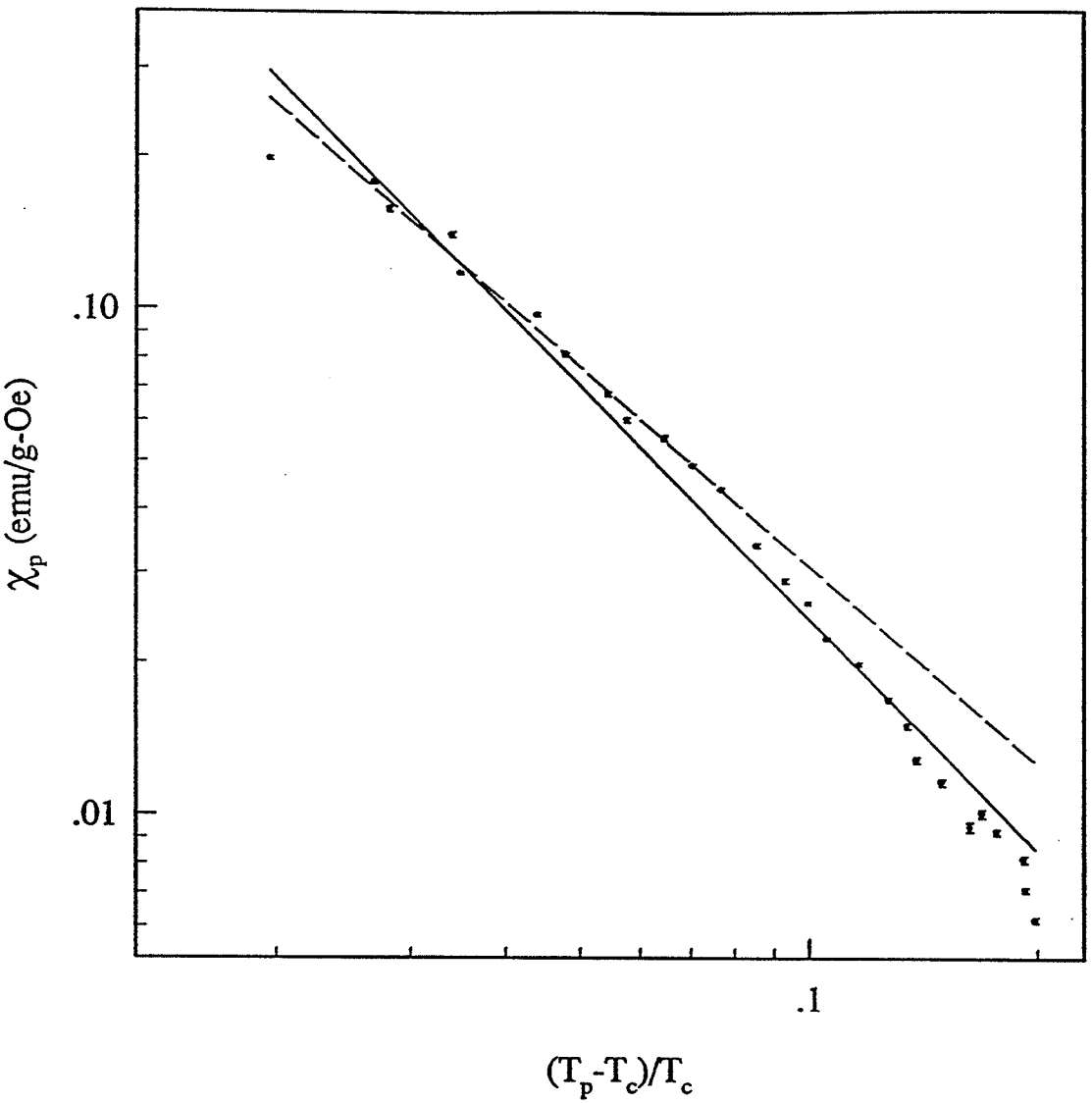

Figure 5.25: The peak susceptibility (in emu/g-Oe) versus $t_p = (T_p - T_c)/T_c$ for the $x = 0.30$ sample, shown on a double logarithmic plot. The solid line represents the best fit line over all of the data points (i.e. δ plot range) and gives $\gamma = 1.53 \pm 0.03$, whereas the dashed line is the best fit line over 14 Oe $< H_i <$ 85 Oe ($\gamma + \beta$ plot range) and gives $\gamma = 1.31 \pm 0.02$.

logarithmic plot is shown in Figure 5.26. As with the $x = 0.26$ sample, the data displays no significant upward curvature, although the slope at higher temperatures is somewhat less steep than in the range, $0.1 < t < 0.2$. The reasons for this behaviour are the same as before; only additional data could determine the true high temperature characteristics of the sample. The maximum slope was found to be -2.74 ± 0.08 using temperatures in the range $0.037 < t < 0.063$.

The $\gamma^*(t)$ versus t curve shown in Figure 5.27 peaks at $t = 0.043$ with a value of $\gamma^*_{peak} = 3.14$. This value is somewhat higher than the maximum slope found above, as expected.

Applying (5.17) to verify the Widom equality gives $\gamma = 1.39 \pm 0.10$. As with the other samples, this value is in excellent agreement with the 3D Heisenberg value, as well as agreeing with the low field gamma found using (5.15). As before, this implies that the Widom inequality can be written as an equality.

5.3.4 $Fe_{1-x}Mn_x$ $(x = 0.32)$

Finally, analysing the $x = 0.32$ data, the critical temperature and exponents for this sample can be determined. From the data illustrated in Figure 5.28, δ was found to be 6.99 ± 0.07 when all of the data points are used (90 Oe $< H_i <$ 1000 Oe), which is substantially (46%) higher than the 3d Heisenberg value. The large error bars at high fields are a result of the noise in the signal, which played a larger role for this sample than with the others because of

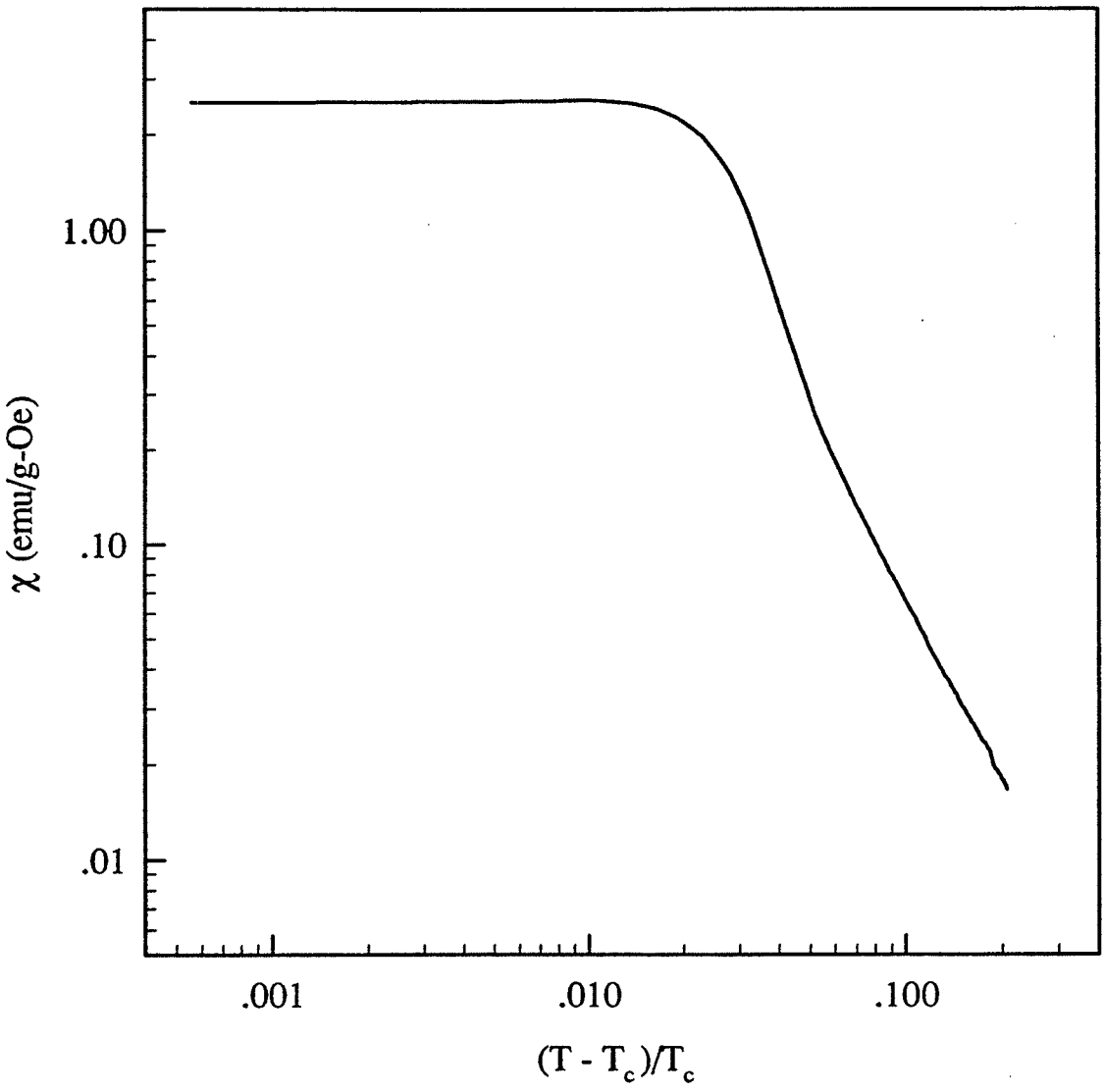

Figure 5.26: The $x = 0.30$ zero field susceptibility (in emu/g-Oe) plotted against reduced temperature for $T > T_c$ on a double logarithmic plot.

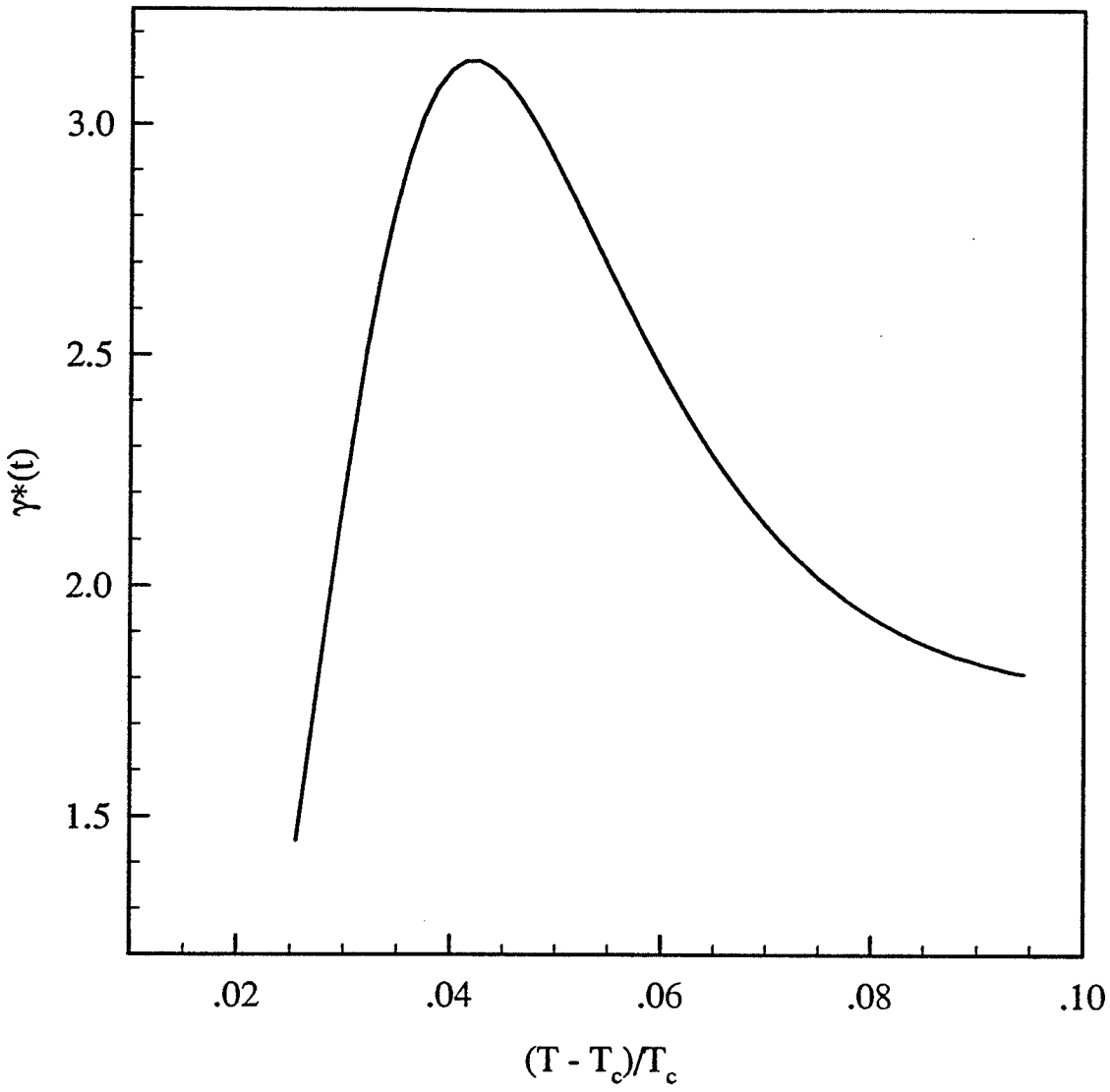

Figure 5.27: The effective Kouvel-Fisher susceptibility exponent, $\gamma*(t)$ (5.16) for $x = 0.30$, plotted versus temperature (in K).

the small signal size. This could have been avoided had more sample been available.

Using the field range 90 Oe $< H_i <$ 300 Oe (points 1 to 12), similar to that used for the $x = 0.235$ sample, the following values were obtained from Figures 5.29 and 5.30; $\gamma + \beta = 1.7(5) \pm 0.2(8)$ and $T_c = 78.2 \pm 0.9$ K. The curvature appearing at high fields is not quite as pronounced as in the previous two samples, although there seems to much more scatter among the data points. As before, the result for the $\gamma + \beta$ combination agrees extremely well with the 'theoretical' value.

Using a χ_p versus t_p plot, as shown in Figure 5.31, γ was found to be 1.54 ± 0.02 and 1.58 ± 0.02 for the ranges 90 Oe $< H_i <$ 1000 Oe and 90 Oe $< H_i <$ 300 Oe respectively. These are both considerably higher than the 3D Heisenberg value, which can possibly be attributed to the fact that sufficiently low fields (such as those used for the other samples) were not used. This is because of the inability to observe critical peaks at lower fields due to the anisotropy present in this sample.

The temperature dependence for the zero field susceptibility on a double logarithmic plot is illustrated in Figure 5.32. Considering the behaviour of the previous two samples, the absence of pronounced upward curvature is not surprising, enabling only the 'peak' susceptibility to be found. Using temperatures in the range $0.556 < t < 0.666$ gives an average 'peak' slope of -2.13 ± 0.02.

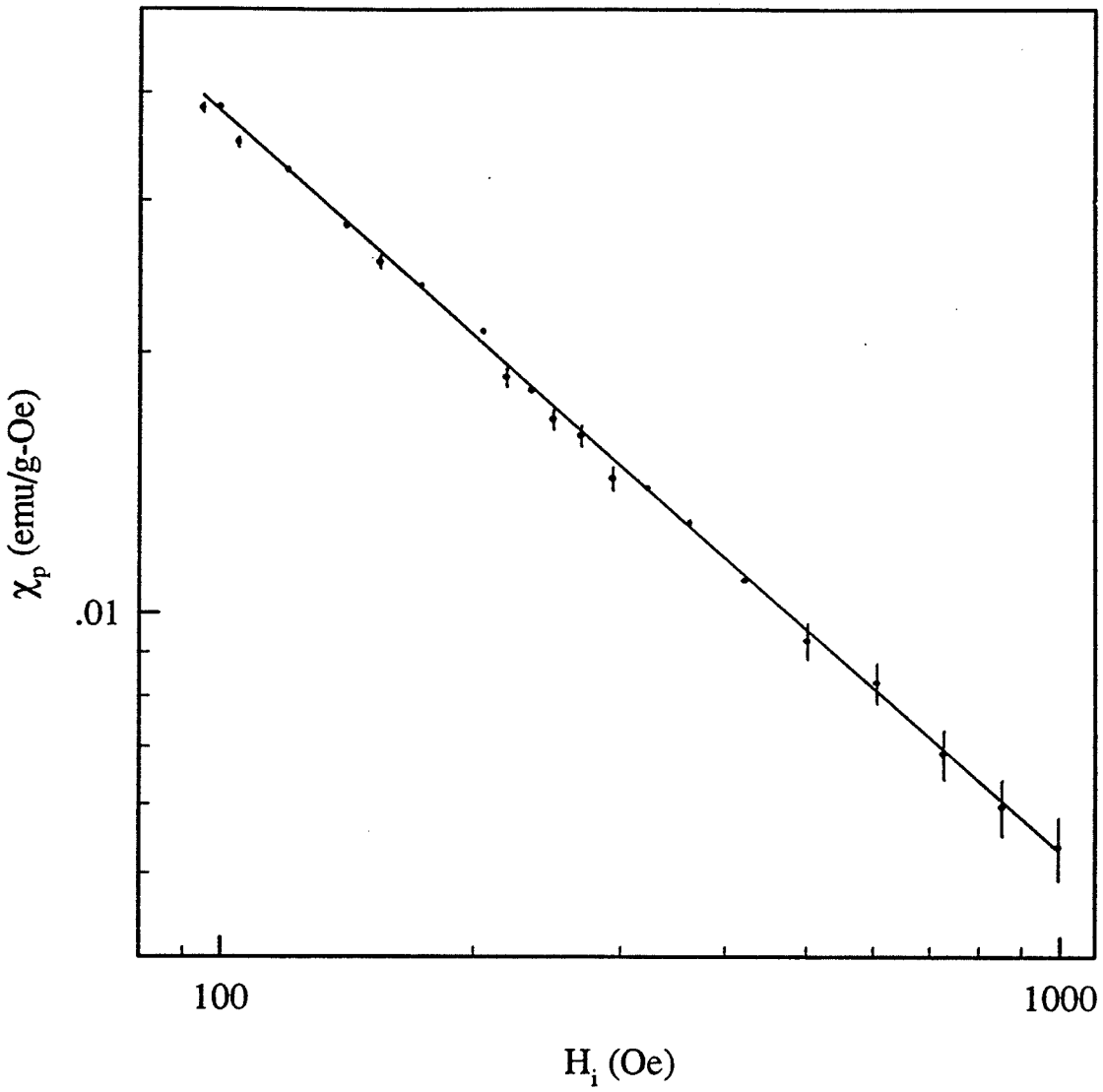

Figure 5.28: The critical peak amplitude, $\chi(H, T_p)$ (in emu/g-Oe) plotted against internal field (in Oe) on a double logarithmic plot for the $x = 0.32$ sample. The solid line represents the best fit line using all of the data points, the slope of which gives $\delta = 6.99 \pm 0.07$.

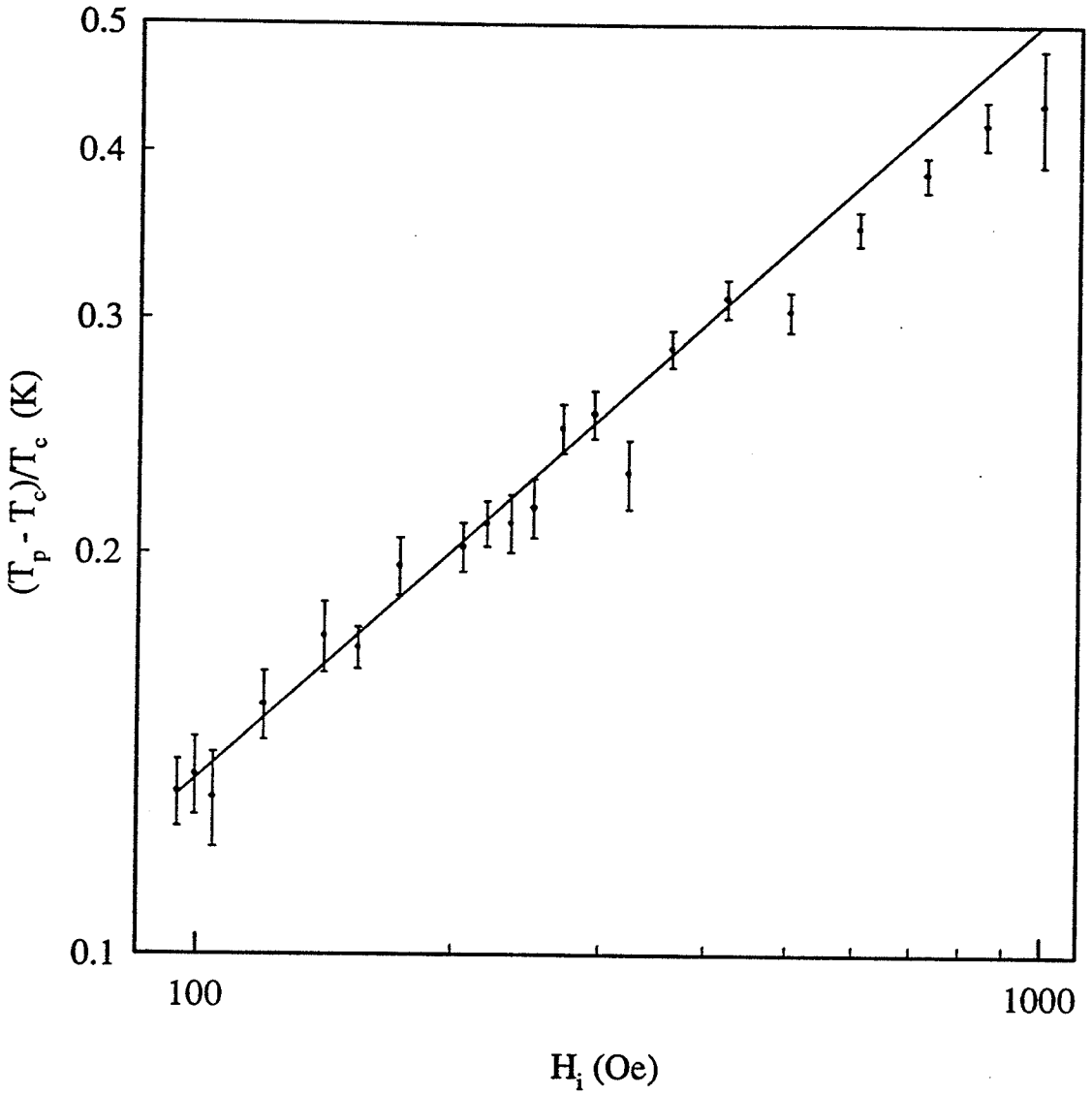

Figure 5.29: The reduced temperature versus the internal field (in Oe), plotted on a double logarithmic plot for the $x = 0.32$ sample. The points are shown with their corresponding errors, which reflect the uncertainty in the peak temperatures. The solid line represents the best fit line, found over the field range 90 Oe $< H_i <$ 300 Oe, and gives a value for $\gamma+\beta$ of 1.7(5)$\pm$0.2(8).

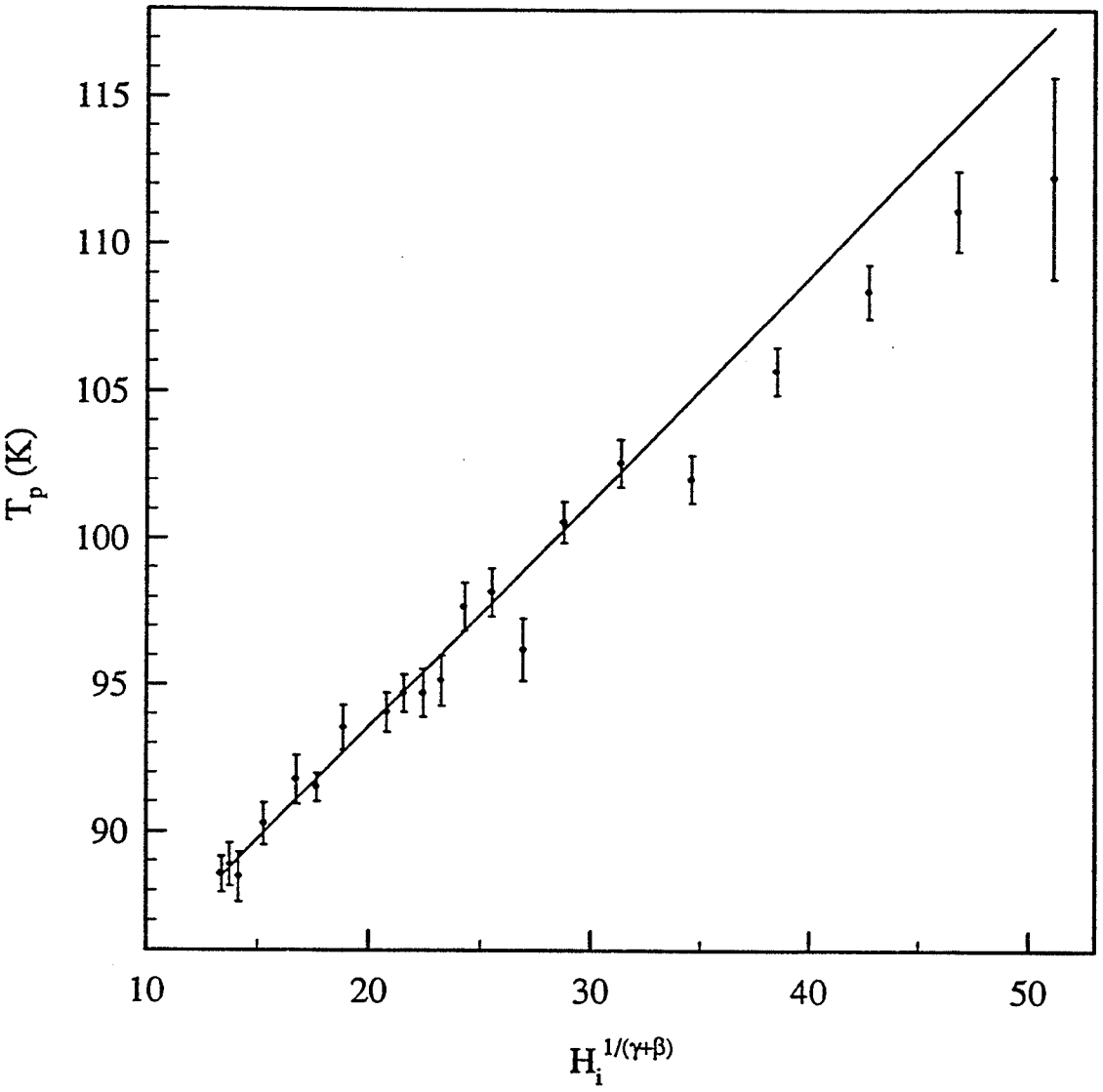

Figure 5.30: The peak temperature (in K) versus $H_i^{1/(\gamma+\beta)}$ for the $x = 0.32$ sample, where $\gamma + \beta = 1.75 \pm 0.28$ from the previous figure. The best fit line, found over the field range 90 Oe $< H_i <$ 300 Oe, has an intercept (critical temperature) of 78.2 ± 0.9 K.

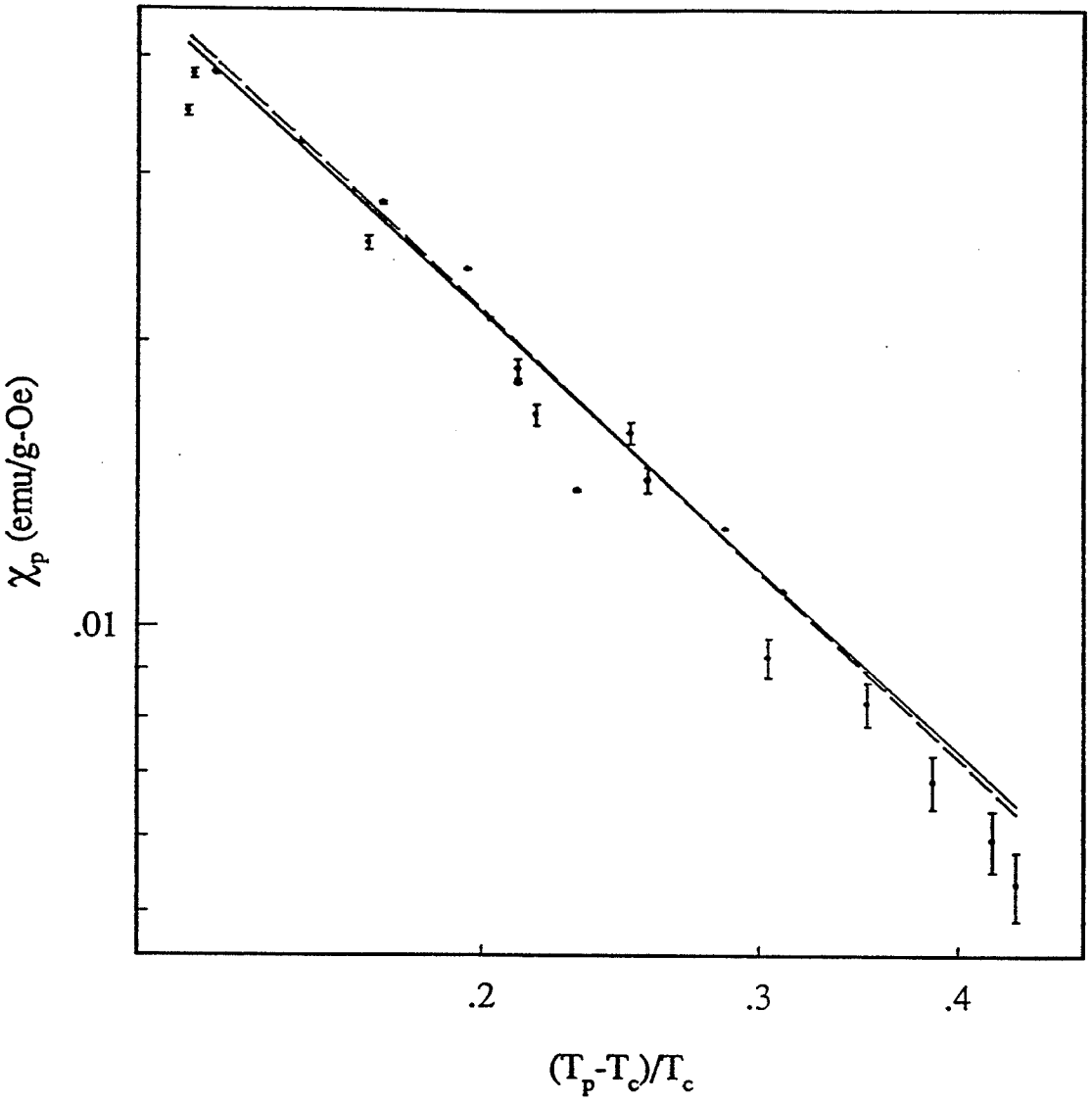

Figure 5.31: The peak susceptibility (in emu/g-Oe) versus $t_p = (T_p - T_c)/T_c$ for the $x = 0.32$ sample, shown on a double logarithmic scale. The solid line represents the best fit line over all of the data points (i.e. δ plot range) and gives $\gamma = 1.54 \pm 0.02$, whereas the dashed line is the best fit line over 90 Oe $< H_i <$ 300 Oe ($\gamma + \beta$ plot range) and gives $\gamma = 1.58 \pm 0.02$.

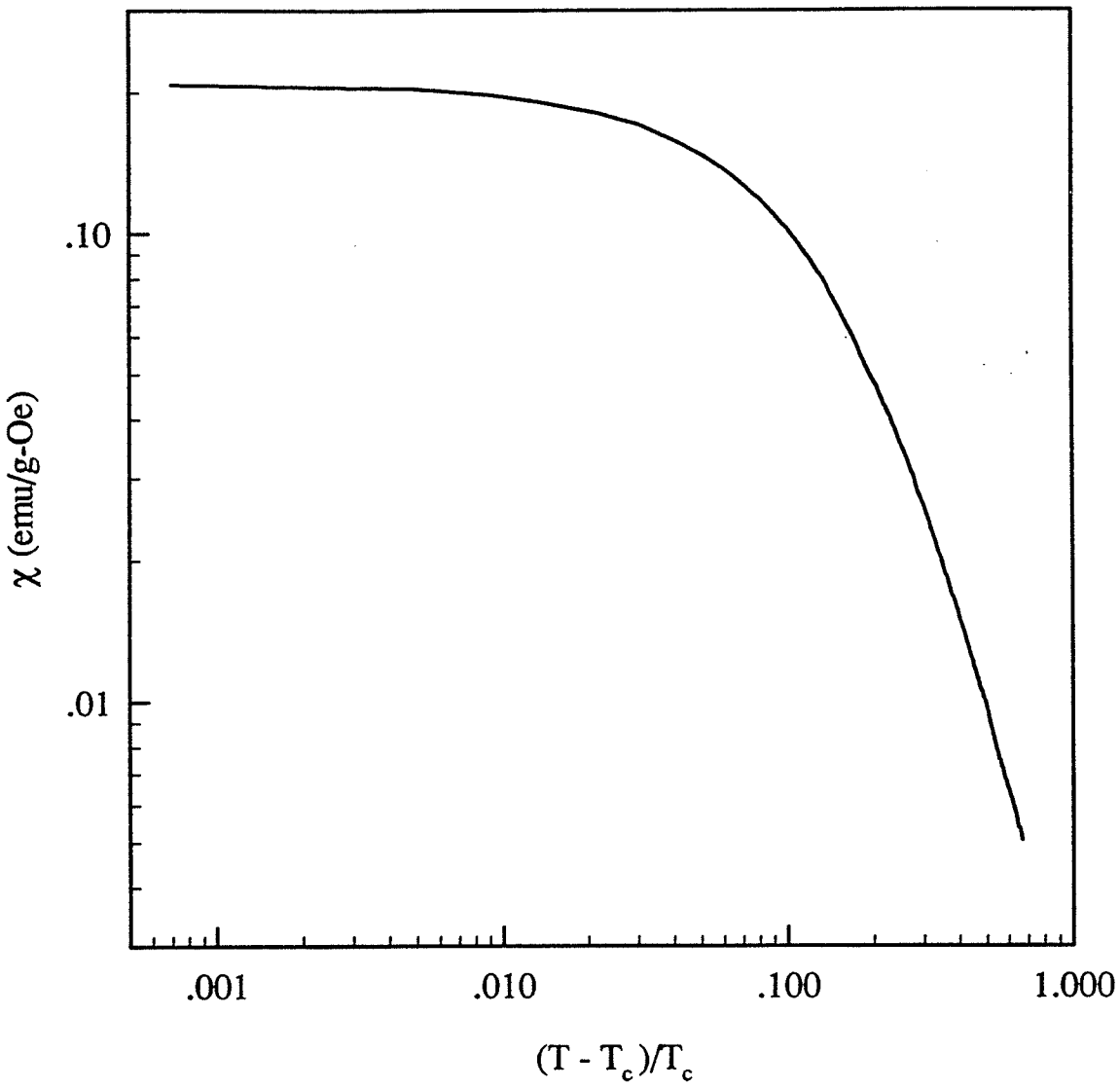

Figure 5.32: The $x = 0.32$ zero field susceptibility (in emu/g-Oe) plotted against reduced temperature for $T > T_c$ on a double logarithmic scale.

The corresponding $\gamma^*(t)$ plot is shown in Figure 5.33 and can be seen to peak at a value of 2.21 at $t = 0.560$, which is in good agreement with the value found above.

Checking whether or not the Widom equality is valid for this sample gives a γ value of 1.50 ± 0.24 using (5.17). The large error can be attributed to the large error in $\gamma + \beta$, which is due to the scatter in the data points. Even though the above quantity agrees with the 3D Heisenberg value of 1.388 essentially because of its large error, it is also in reasonably good agreement with the two γ values found from the χ_p versus t_p plot (Figure 5.31), which once again confirms the validity of the Widom equality.

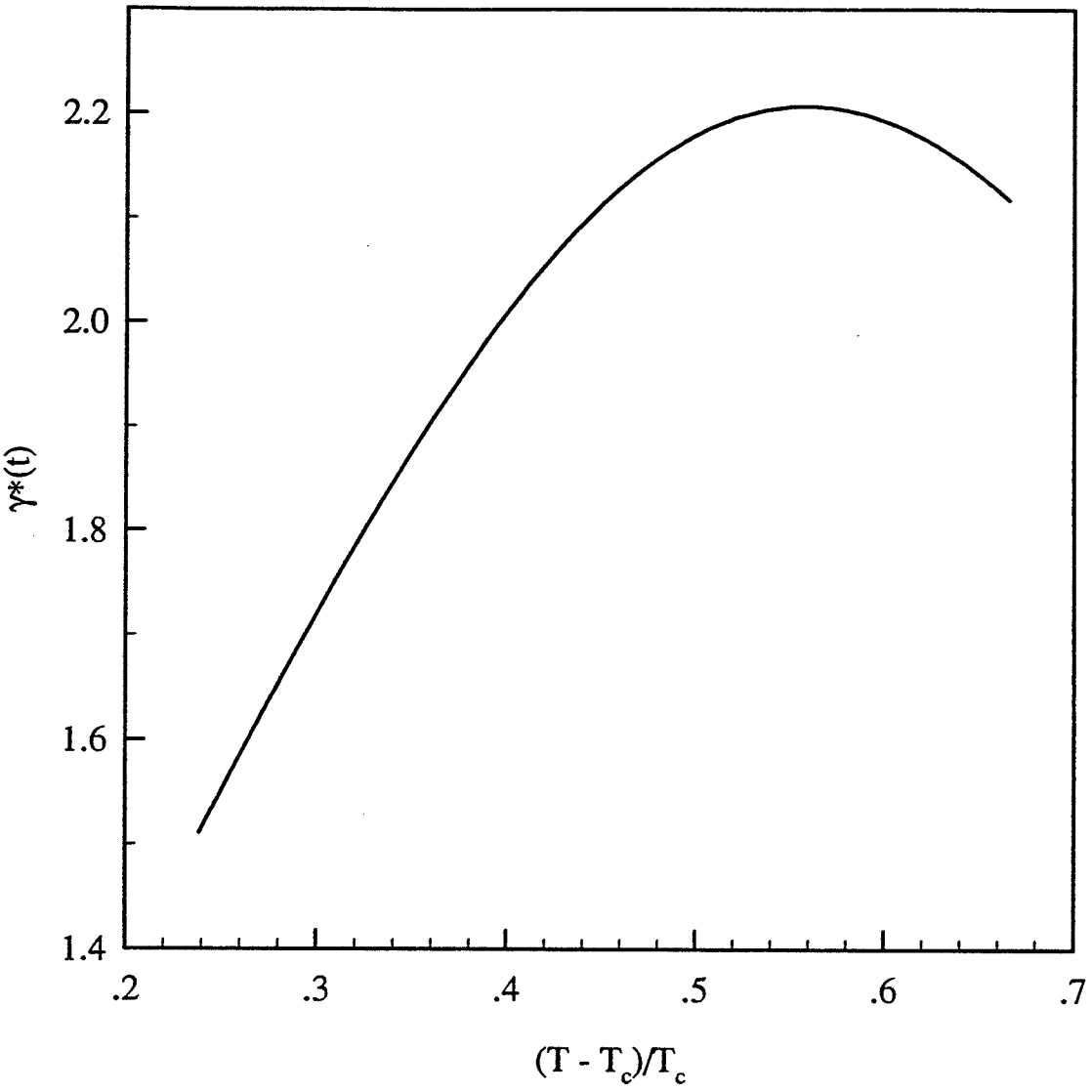

Figure 5.33: The effective Kouvel-Fisher susceptibility exponent, $\gamma*(t)$ (5.16) for $x = 0.32$, plotted versus temperature (in K).

5.4 Discussion: Ferromagnetic Transition

Using conventional scaling predictions, the presence of a paramagnetic to ferromagnetic transition has been confirmed in four of the $Fe_{1-x}Mn_x$ alloys studied here ($x = 0.235, 0.26, 0.30, 0.32$). A summary of the critical temperatures and exponents found is listed in Table 5.1, and will now be examined and compared to previous experimental results where available.

Figure 5.34 shows a plot of T_c against composition, x, incorporating both the present data along with previous measurements which use a variety of experimental methods. The slope of the fit to all the available data is $\frac{dT_c}{dx} = -1700$ K/at.%. The large scatter in the T_c values obtained could be as a result of compositional variations of as little as 0.1%. Note that differences in composition for samples with the same nominal values were reported (Geohegan et al, 1981) to be as large as 0.04%, which is clearly not negligible, and indicates that one factor causing the scatter could be compositional variations. Critical temperatures in Figure 5.34 were determined using magnetization measurements by Mirebeau et al, 1990, Yeshurun et al, 1981, and Manheimer et al, 1983. The T_c values obtained from susceptibility measurements by Geohegan et al, 1981 were simply determined from the point of maximum slope of the susceptibility versus temperature curve (inflection point), as opposed to the much more rigorous analysis performed here.

The critical exponents, δ and γ (Table 5.1) can now be discussed, as well

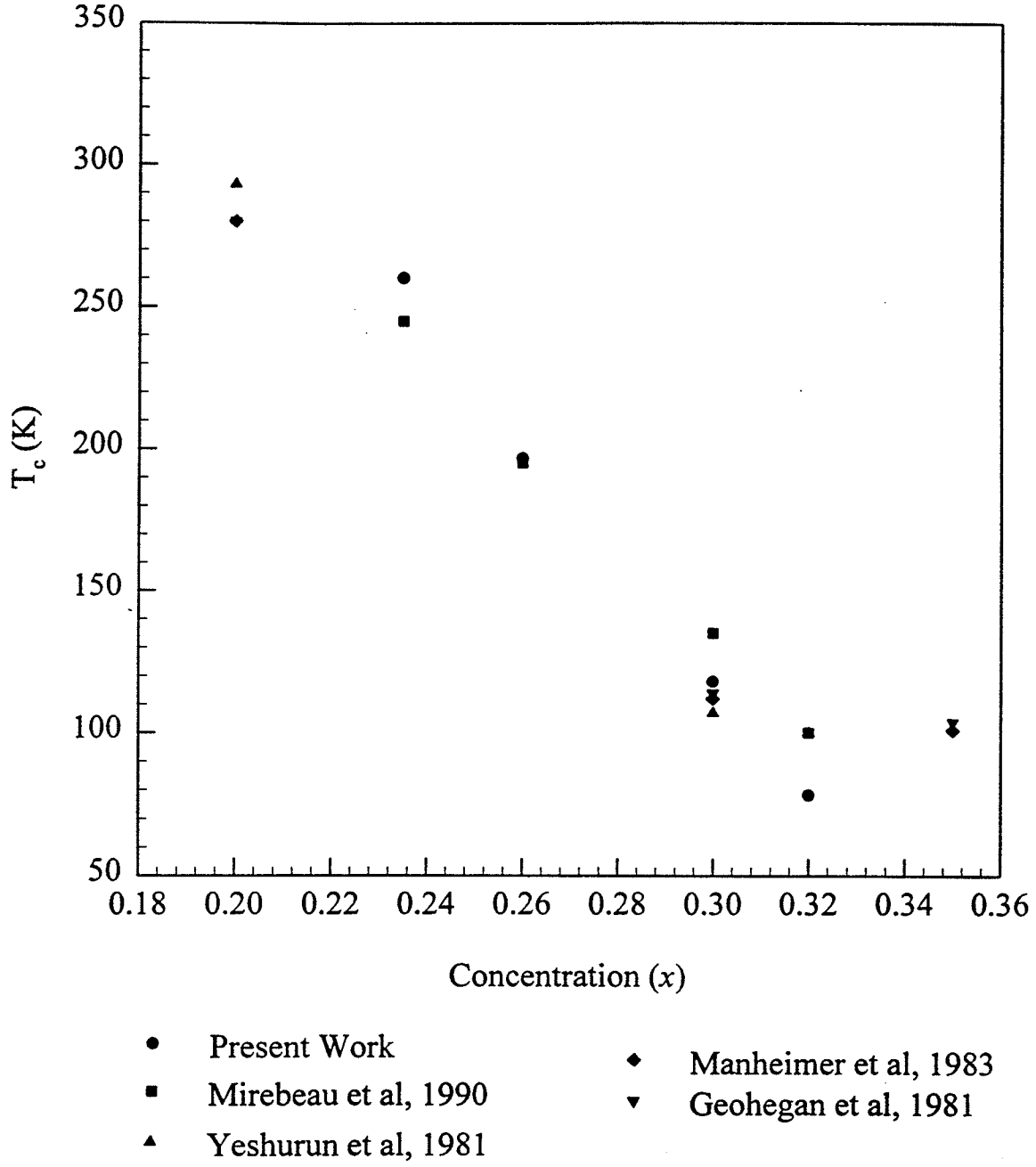

Figure 5.34: Critical temperature (in K) versus concentration, x.

Table 5.1: Critical temperature and exponents summary

Concentration	$x = 0.235$	$x = 0.26$	$x = 0.30$	$x = 0.32$
δ Range (Oe)	3.84 ± 0.03 $10 < H_i < 600$	4.69 ± 0.01 $6 < H_i < 1000$	4.86 ± 0.02 $12 < H_i < 1000$	6.99 ± 0.07 $95 < H_i < 1000$
$\gamma + \beta$ Range (Oe)	$1.7(6) \pm 0.1(0)$ $10 < H_i < 300$	$1.7(5) \pm .1(7)$ $8 < H_i < 82$	$1.7(5) \pm 0.1(3)$ $14 < H_i < 85$	$1.7(5) \pm 0.2(8)$ $95 < H_i < 295$
T_c (K) Range (Oe)	260.17 ± 0.09 $10 < H_i < 300$	196.6 ± 0.1 $8 < H_i < 82$	118.0 ± 0.2 $14 < H_i < 85$	78.2 ± 0.9 $95 < H_i < 295$
$\gamma^\dagger$ Range (Oe)	1.29 ± 0.01 $10 < H_i < 600$	1.477 ± 0.001 $6 < H_i < 1000$	1.53 ± 0.03 $12 < H_i < 1000$	1.54 ± 0.02 $95 < H_i < 1000$
$\gamma^\dagger$ Range (Oe)	1.24 ± 0.02 $10 < H_i < 300$	1.386 ± 0.003 $8 < H_i < 82$	1.31 ± 0.02 $14 < H_i < 85$	1.58 ± 0.02 $95 < H_i < 295$
$\gamma^*(t_{peak})$ t_{peak}	1.94 0.031	1.77 0.119	3.14 0.043	2.21 0.560

† From χ_p versus t_p plots – Figures 5.13, 5.19, 5.25 and 5.31.

as compared to the values found by other researchers, which are listed in Tables 3.1 and 3.2. Considering first the critical isotherm exponent, δ; the present values for $x = 0.26$ and 0.30 agree very well with the 3D Heisenberg model prediction (4.78), but the value at $x = 0.32$ is considerably higher, possibly because of the large coercivity present at this concentration - consequently this sample has a large regular contribution which is inadequately suppressed by the applied field, thus resulting in larger values for the critical peak susceptibility. For $x = 0.235$, a value of 3.84 was obtained here, which is also somewhat unusual, noting that this concentration is farthest from the multicritical point and is only weakly frustrated, and is therefore expected to be least affected by bond disorder. Comparison with previous results is somewhat difficult, as no results for this concentration are listed. Examining the closest concentration, $x = 0.20$, yields $\delta = 5.1 \pm 0.03$ (Table 3.1) and 3.5 (Table 3.2), from magnetization and susceptibility measurements respectively. As already discussed in Section 3.2.2, the latter value appears to be an average over low and high field data, which would account for the fact that it is much less than the Heisenberg model prediction of 4.78. The data collected here displays no curvature (Figure 5.10), but the value is nevertheless quite low, being about halfway between the two values listed above.

For the exponent γ, the two values found here for $x = 0.235$, 1.24 ± 0.02 (fit over 10 Oe $< H_i <$ 300 Oe) and 1.29 ± 0.01 (fit over 10 Oe $< H_i <$ 600 Oe), are both quite different from the $x = 0.20$ values given in

Table 3.1, namely, 1.64 (found using the Widom equality) and 1.45. The latter value (Manheimer et al, 1983) is in somewhat better agreement with the 3D Heisenberg prediction (1.388) than the value found here, but the Yeshurun et al value differs considerably. There is clearly considerable scatter in these values, as was the case for the critical temperature. Unfortunately, no previous results for the critical exponents exist for $x = 0.26$; the next highest concentration for which previous measurements exist is $x = 0.30$. The two γ values found here for $x = 0.30$, 1.53 ± 0.03 (fit over 12 Oe $< H_i <$ 100 Oe) and 1.31 ± 0.02 (fit over 14 Oe $< H_i <$ 85 Oe), are quite different from each other due to the curvature in the γ plot (Figure 5.25). Magnetization measurements give $\gamma = 1.60$ (found using the Widom equality), and 1.42 from the top and bottom of Table 3.1 respectively. There is again considerable scatter in the γ values, with none of the above values in agreement with any other. Finally, γ for the $x = 0.32$ sample was found to be 1.54 ± 0.02 (fit over 95 Oe $< H_i <$ 1000 Oe) and 1.58 ± 0.02 (fit over 95 Oe $< H_i <$ 295 Oe), which are both lower than the 1.72 (found using the Widom equality) determined by Yeshurun for $x = 0.32$, but agree very well with the value of 1.55, found for $x = 0.35$ by Manheimer. All of these values are substantially higher than the 3D Heisenberg value of 1.388.

Note that for the first three of the four concentrations examined in this study, the low-field γ values are either in good agreement with the Heisenberg value or slightly lower. Only for the $x = 0.32$ sample do we get a γ as large

as 1.58.; it should be recalled that the coercivity/regular contribution to the susceptibility is substantially larger for this particular sample, which could affect these results significantly. All previous measurements of γ are substantially higher than the Heisenberg value and likely do not represent asymptotic values; rather they are (average) values that are all influenced by the presence of bond disorder to some extent. Figures 5.15, 5.21, 5.27 and 5.33 show the effective Kouvel-Fisher susceptibility exponent γ^* as a function of temperature. Note that the value of γ^* rises as the reduced temperature increases, reaches a maximum value, $\gamma^*(t_{peak})$, at a reduced temperature, t_{peak}, and then falls monotonically to the mean field value of one. This initial rise is due to the presence of bond disorder (see Section 2.3.4). The effective exponent does not actually approach the Heisenberg value of 1.388 at small t because the susceptibility is unable to reach the demagnetizing limit because of the small demagnetizing factor. Kaul (Kaul, 1985) has reported that this temperature dependence of the Kouvel Fisher effective exponent broadens, $\gamma^*(t_{peak})$ increases and the peak position, t_{peak}, shifts up in temperature with increasing bond disorder. This behaviour was confirmed recently by Wang for a series of CeFeRu intermetallic compounds (Wang et al, 1995). Here the agreement is not as clear, since although the bond disorder generally increases with concentration, x, $\gamma^*(t_{peak})$ reaches a maximum at $x = 0.30$ and then decreases for $x = 0.32$; in addition, t_{peak} generally increases with x, except for a rather low value for $x = 0.30$.

5.5 Lower Transition

Previous studies (see Sections 2.3.4 and 2.3.5) suggest the presence of a second phase transition below the paramagnetic-ferromagnetic phase transition, with a critical temperature, T_f, coinciding with the drop in zero field susceptibility at $T \approx 28, 34, 55$ and 56 K, respectively, for the concentrations $x = 0.235, 0.26, 0.30$ and 0.32, as illustrated in Figure 5.1. However, to verify the presence of a true phase transition, a more rigorous analysis must be undertaken.

In an applied field the susceptibility, for all of the samples measured, displays at least one additional peak at a temperature below the ferromagnetic-paramagnetic peak. It has been suggested by some (Geohegan et al, 1981) that these features indicate re-entrant behaviour, or in other words, the presence of a ferromagnetic-spin glass transition (identified by the higher of the two low-temperature peaks, in the case of the $x = 0.235$ and 0.26 samples), where the paramagnetic - ferromagnetic phase boundary is now replaced by a similar line, known as the Gabay-Toulouse, or GT line.

Furthermore, a third peak appears in the presence of sufficiently large applied fields for $x = 0.235$ and 0.26, which can be more clearly seen in Figures 5.35 and 5.49, and may represent the transition from weak to strong irreversibility, delineated by the d'Almeida-Thouless, or AT line (de Almeida et at, 1978). It should be noted that although the vector spin mean field models do not predict the double peaked structure observed at low temperatures in

the $x = 0.235$ and 0.26 sample, it would be worthwhile to investigate if these two features coincide with the aforementioned transitions.

To study the characteristics of the GT transition in light of the experimental data collected, recall (2.67). From the latter equation, it is evident that the peak temperature plotted versus H_a, represented by the equation,

$$T_{GT}(H_a) = \sqrt{2}\frac{g\mu_B}{k_B} c H_a + T_{GT}(0). \tag{5.18}$$

gives a straight line with a slope of $\frac{\sqrt{2}g\mu_B}{k_B} c = -0.437$, where c is a constant defined in (2.68), and an intercept equal to the Gabay-Toulouse critical temperature, $T_{GT}(0)$. As an additional check to verify that the data is truly linear, $\log(T_{GT}(0) - T_{GT}(H_a))$ versus $\log(H_a)$ can be plotted. A slope of 1 for the resulting graph would verify that $T_{GT}(0) - T_{GT}(H_a) \sim H_a^n$ with $n = 1$ accurately describes the data. Since the mean field vector model does not specify the nature of any feature revealing the presence of the ferromagnetic to spin glass transition, the location of both low temperature peaks and the resulting intermediate trough (just below the proposed 'GT peaks') will be investigated for GT behaviour in the $x = 0.235$ and 0.26 samples.

As for the cross-over from weak to strong irreversibility, recall (2.69). Using a similar technique to that described previously for obtaining T_c and $\gamma + \beta$ (Section 5.3), both $T_{AT}(0)$ and n can be determined.

As discussed in Section 2.3.5, the presence of a phase transition can also be manifested by a peak (technically a divergence) in the non-linear, field-dependent component of the susceptibility. Using the technique de-

scribed there, analysis will be carried out to determine whether or not such a peak/anomaly occurs for the individual samples studied here.

5.5.1 $Fe_{1-x}Mn_x$ $(x = 0.235)$

Recalling the discussion above for the Gabay-Toulouse line, the theory can now be compared with the data collected. The temperatures at which the broad peaks illustrated in Figure 5.35 occur $(35\ \text{K} < T < 60\ \text{K})$ were found and plotted versus applied field, H_a, as illustrated in Figure 5.36. The large error bars reflect the difficulty in accurately determining the peak positions. A straight line through the data points gives an intercept of 65.8 ± 2.4 K, thereby identifying $T_{GT}(0)$, in accordance with (5.18). Performing the corresponding check recommended following the latter equation, the resulting double logarithmic plot in Figure 5.37 yields a slope of 0.95 ± 0.30, which agrees with the value of $n = 1$ proposed by the theory. However, the large error in both the temperature and exponent value (caused by the large error in the data), prevent a conclusive statement from being made about whether or not the data displays GT behaviour, based solely upon this analysis. Comparing the experimental slope of -4000 ± 500 to the theoretical slope of -0.44 indicates there is clearly no agreement, as the two values differ by four orders of magnitude! This suggests that the peaks are most likely not GT peaks, and arise due to some other effect.

The behaviour of the peak/trough features seen in the low temperature region of Figure 5.35, and shown more clearly in Figure 5.39 can also be

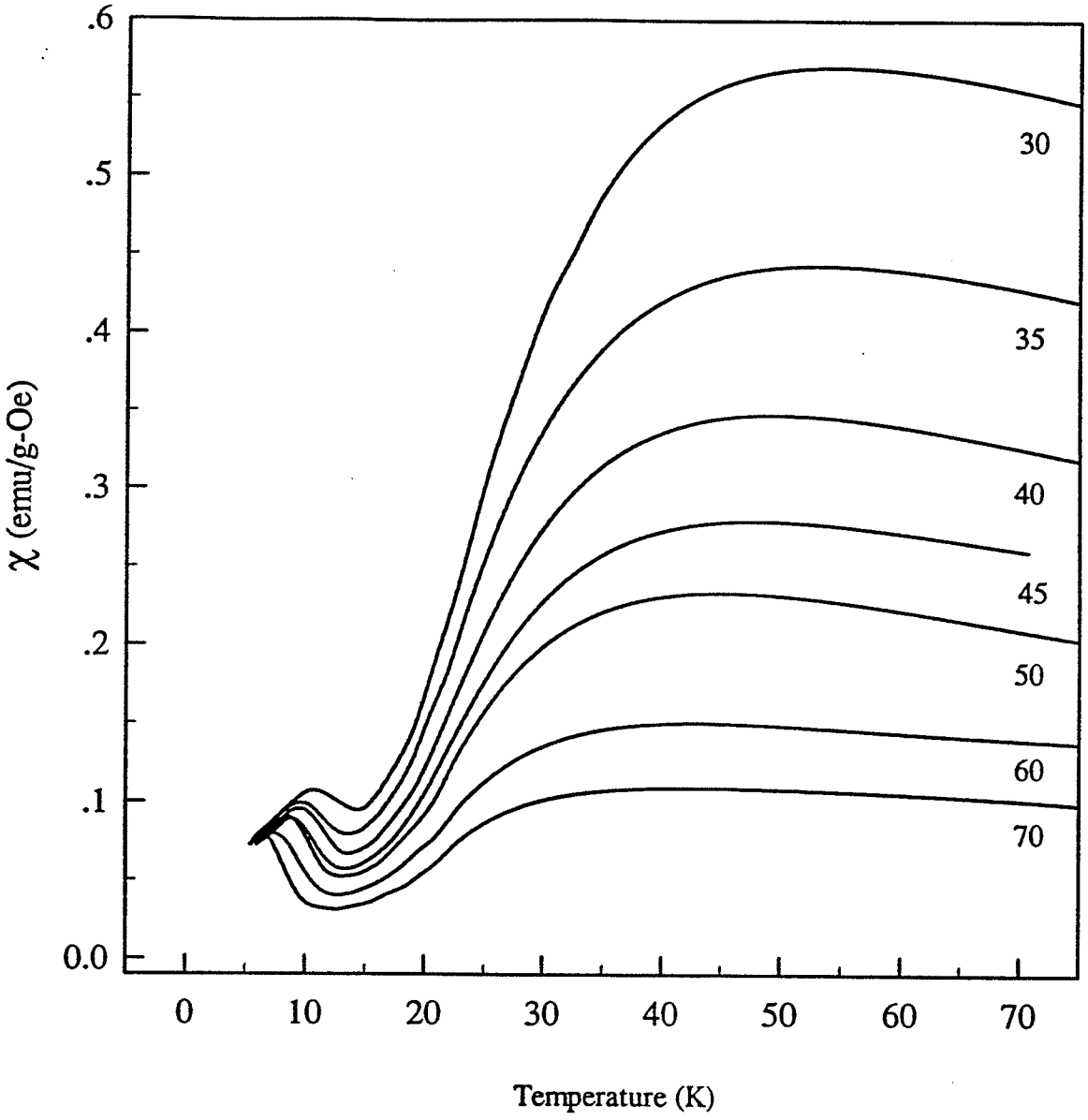

Figure 5.35: The a.c. susceptibility $\chi(H,T)$ (in emu/g-Oe), corrected for background and demagnetizing effects, plotted versus temperature (in K) for the $x = 0.235$ sample. The numbers beside each curve represent the static biasing field (in Oe).

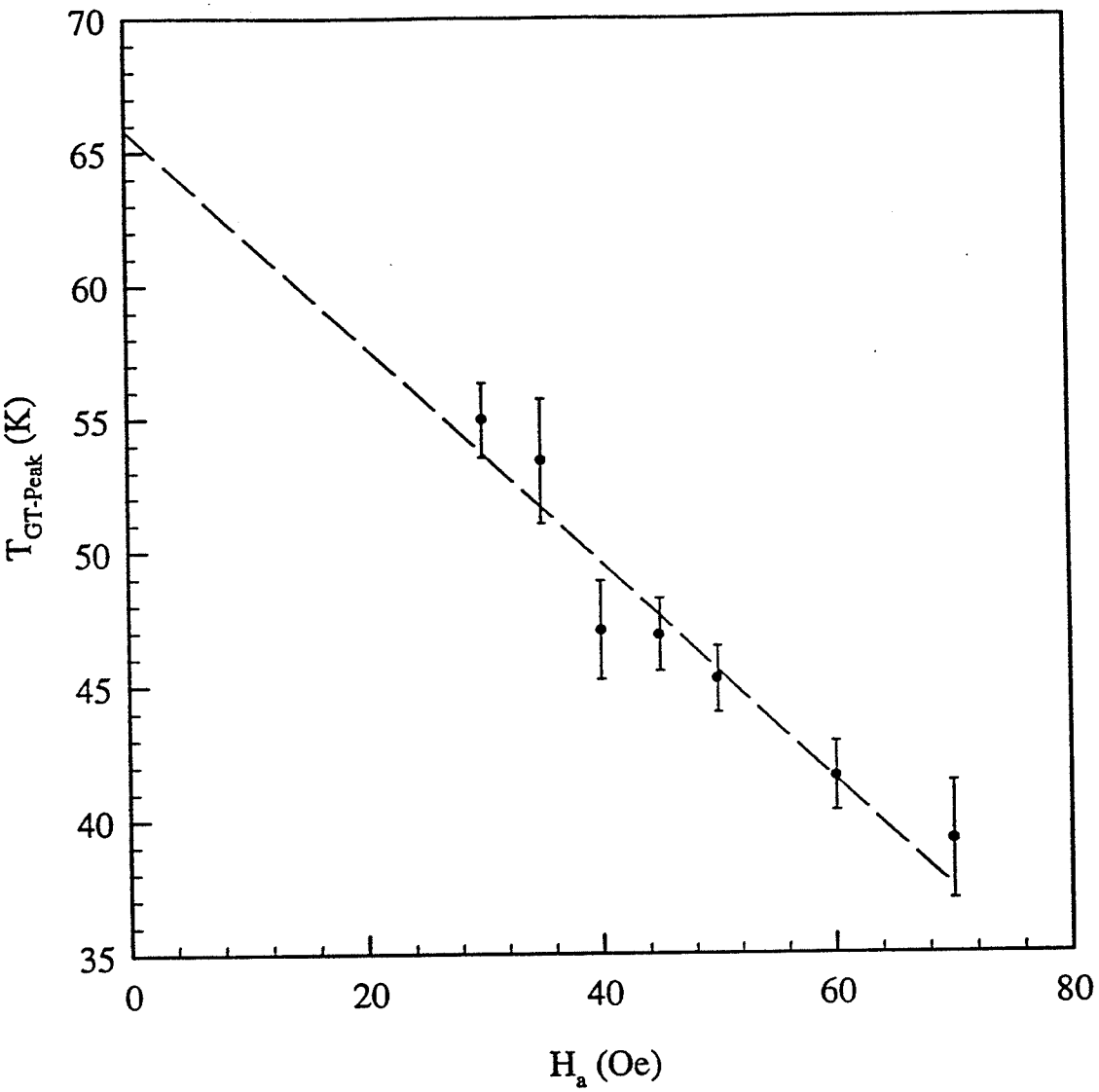

Figure 5.36: The proposed GT transition temperature (in K) (from peak) plotted versus the applied field (in Oe) for the $x = 0.235$ sample. The intercept of the best fit line gives $T_{GT}(0) = 65.8 \pm 2.4$ K, and the slope is -4000 ± 500.

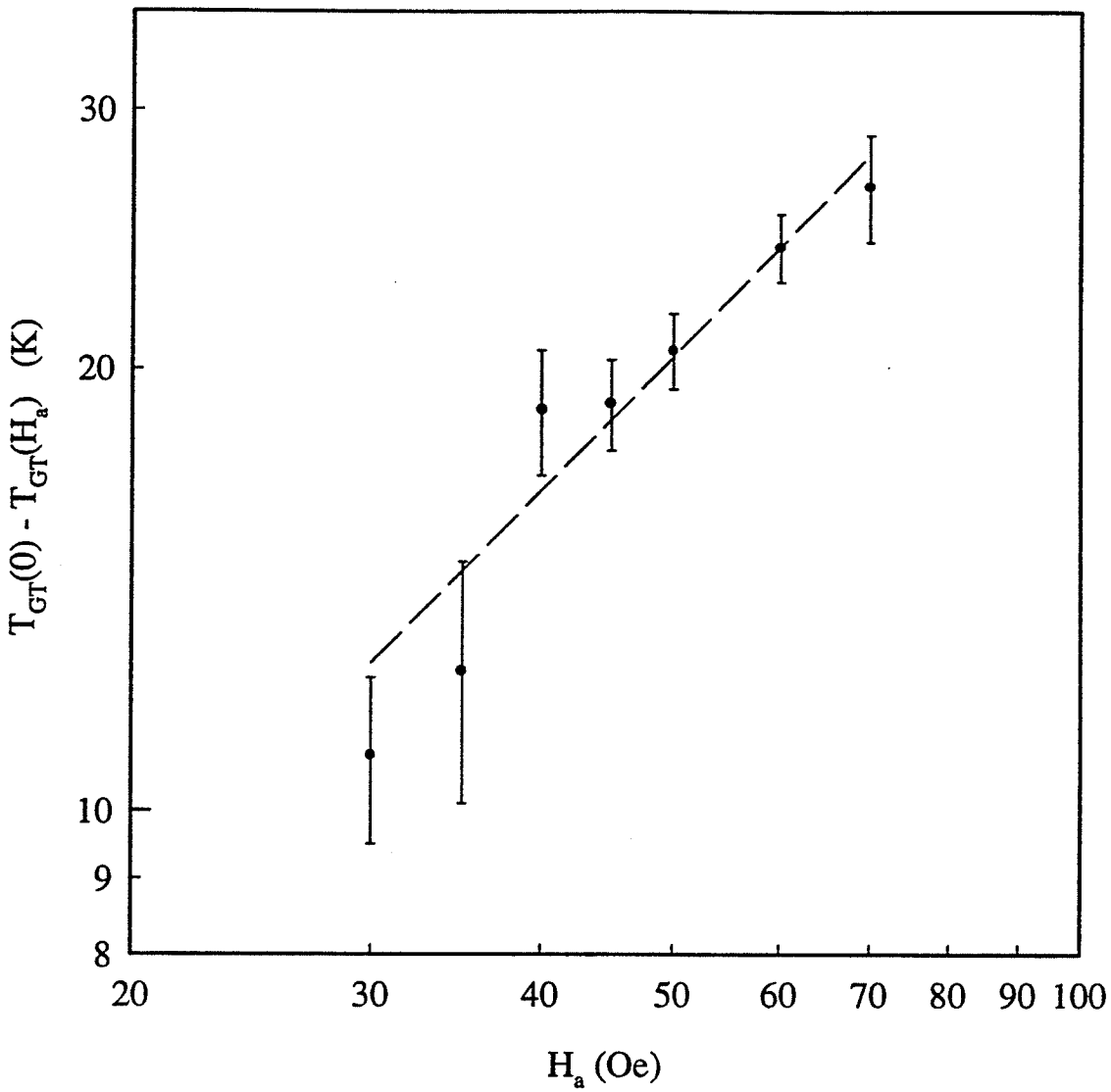

Figure 5.37: The logarithm of $T_{GT}(0) - T_{GT}(H_a)$ (in K) for the $x = 0.235$ sample plotted versus the logarithm of the applied field (in Oe). The slope of the best fit line gives $n = 0.9 \pm 0.3$.

analyzed for AT and GT behaviour respectively. Considering first the trough visible in the temperature range, 11 K $< T <$ 15 K; the T_{trough} versus H_a plot illustrated in Figure 5.38 gives a new estimate for $T_{GT}(0)$ of 15.4 ± 0.2 K, and the check procedure gives $n = 1.1 \pm 0.3$. Although the error in this second estimate of $T_{GT}(0)$ is reasonable, the large error in n, again prevents a conclusion from being drawn concerning the applicability of the GT model, considering only this result. The slope in Figure 5.39 is -450 ± 50, which is still three orders of magnitude larger than the expected value of -0.44, and suggests that the troughs also do not display GT behaviour.

Since an analysis of the trough structure gives an approximate straight line (Figure 5.39), this feature will not be reinvestigated for AT behaviour, for which it is predicted that the corresponding temperature versus field plot has substantial curvature. The lowest temperature peaks (6 K $< T <$ 14 K) will however by analyzed, and the peak temperatures versus field are plotted in Figure 5.40. The best fit curve has an intercept of 21 K, thereby giving $T_{AT}(0)$. A plot of $T_{AT}(0) - T_{AT}(H_a)$ versus H_a has a slope of 0.63 ± 0.03 using only the first four data points. This agrees quite well with the theoretical value of 2/3, which would support the presence of an AT transition. However, an AT transition is unlikely if a GT transition was absent at higher temperatures. Notice also that if all data points are used, a slope of 0.340 ± 0.003 is found, which is quite different from 2/3.

Finally, the behaviour of the non-linear component of the susceptibility

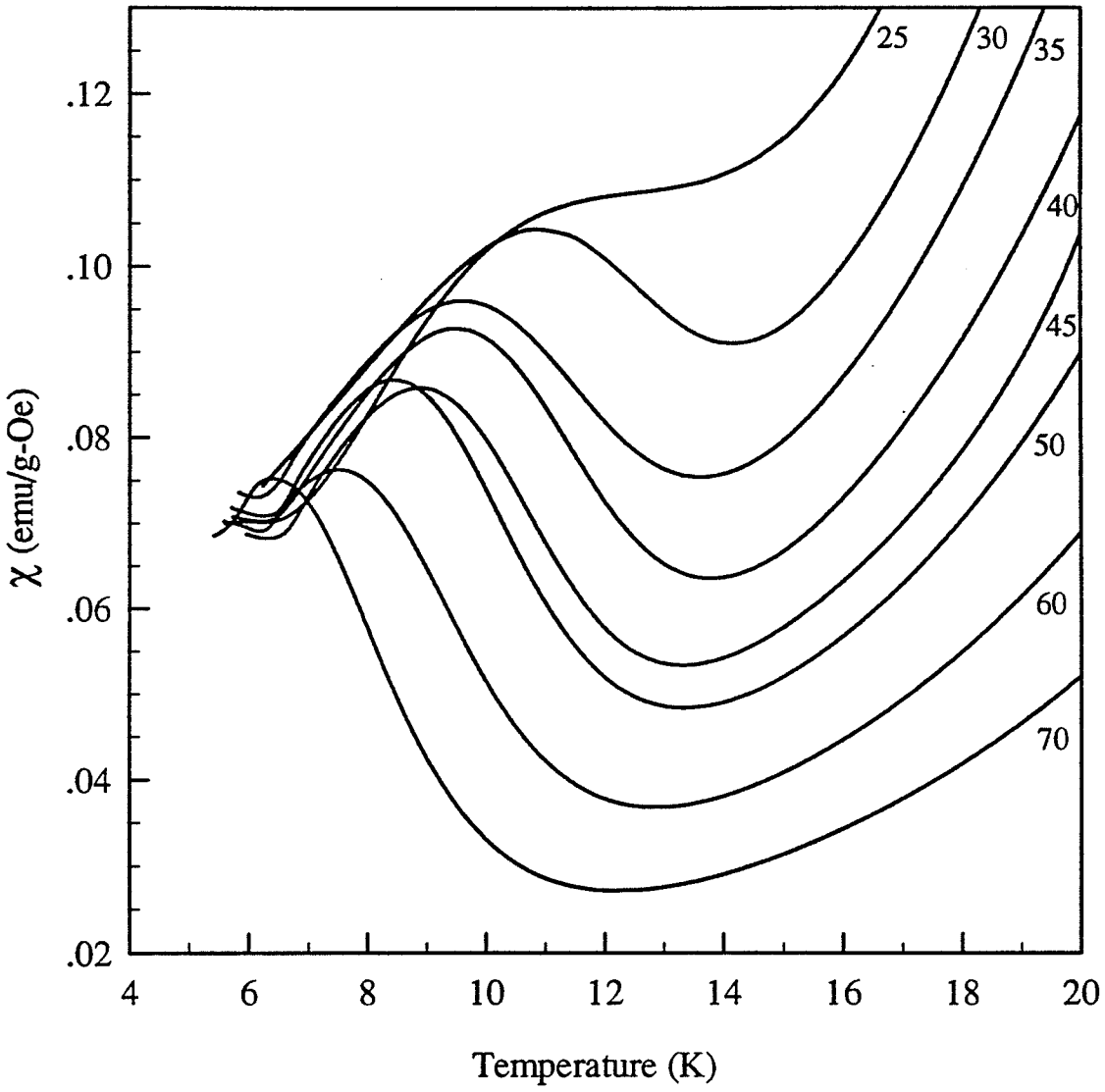

Figure 5.38: The a.c. susceptibility $\chi(H,T)$ (in emu/g-Oe), corrected for background and demagnetizing effects, plotted against temperature (in K) for the $x = 0.235$ sample. The numbers beside each curve represent the static biasing field (in Oe).

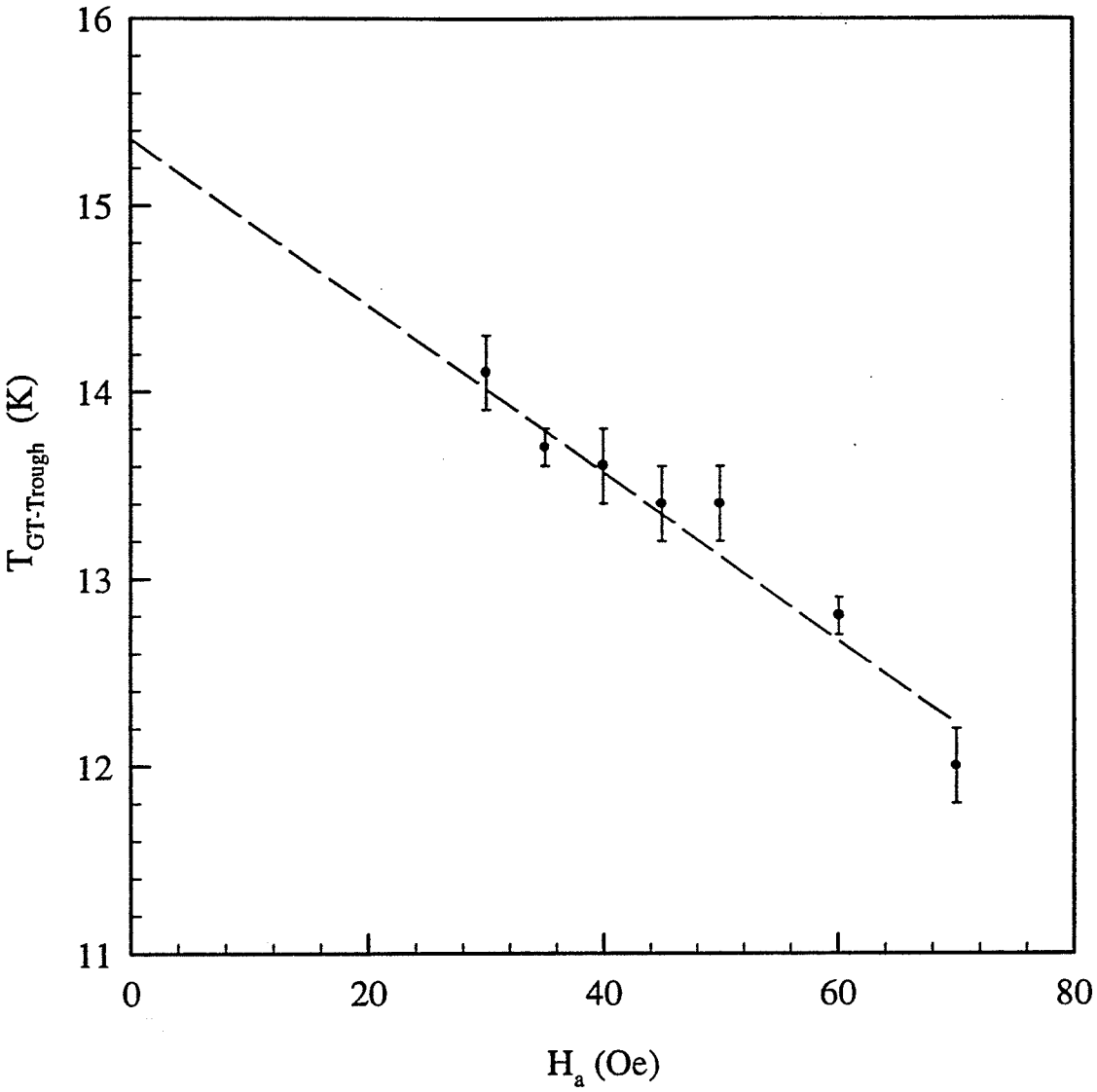

Figure 5.39: The proposed GT transition temperature (in K) (from trough) plotted versus the applied field (in Oe) for the $x = 0.235$ sample. The intercept of the best fit line gives $T_{GT}(0) = 15.4 \pm 0.2$ K, and the slope is -450 ± 50.

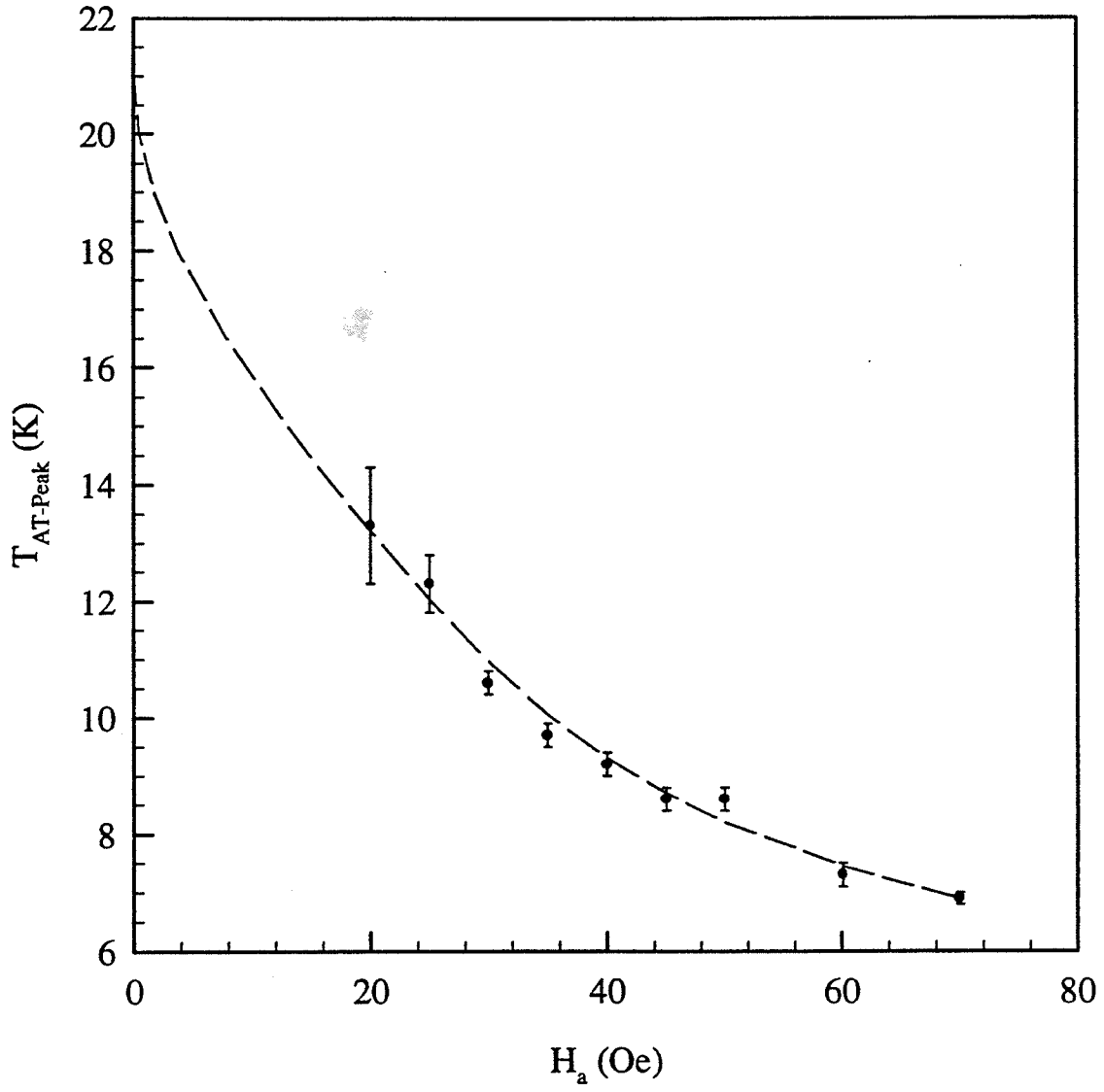

Figure 5.40: The proposed AT transition temperature (in K) (from lowest peak) plotted versus the applied field (in Oe) for the $x = 0.235$ sample. The intercept of the best fit curve gives $T_{AT}(0) = 21$ K.

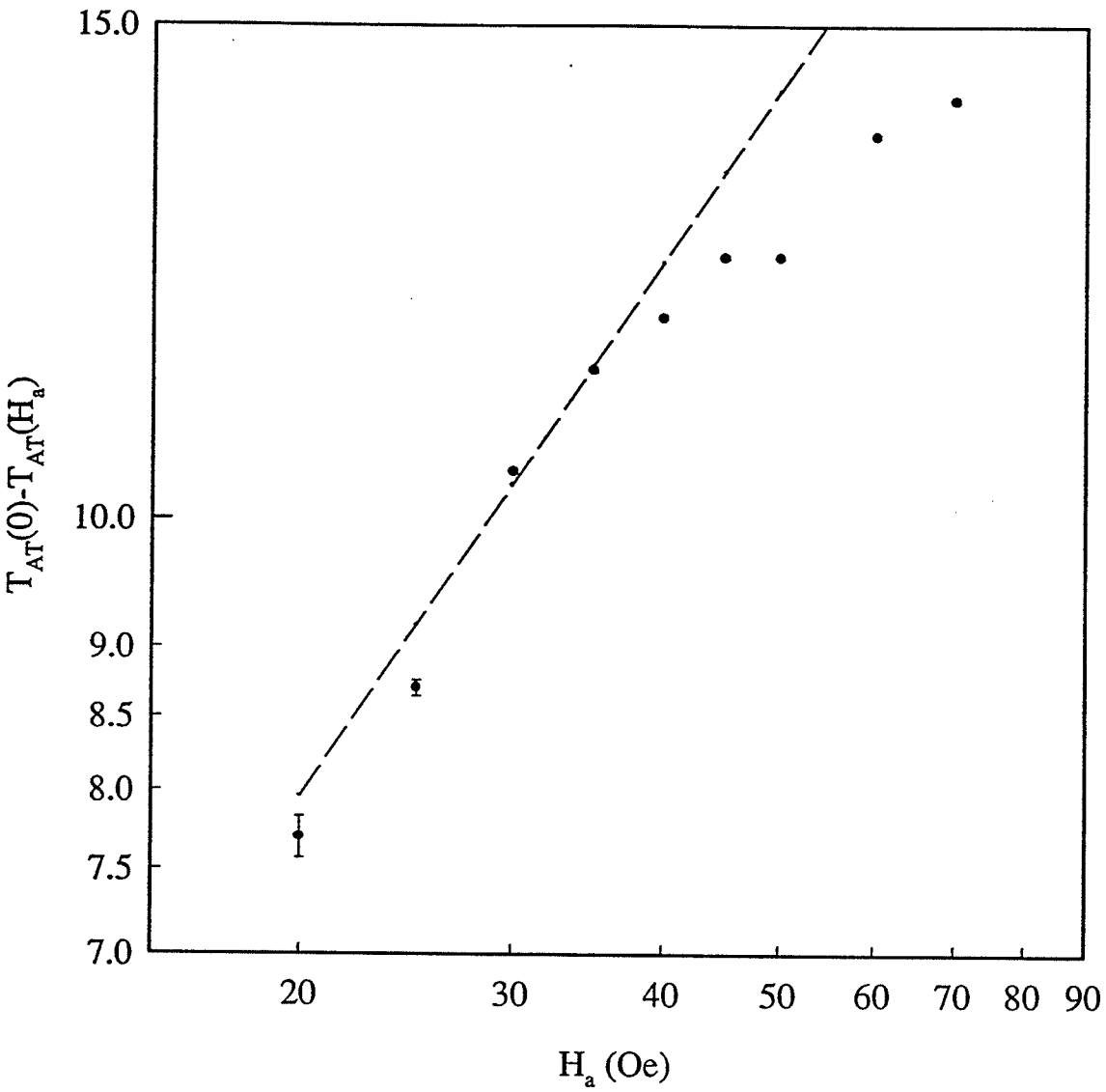

Figure 5.41: The logarithm of $T_{AT}(0) - T_{AT}(H_a)$ (in K) for the $x = 0.235$ sample plotted versus the logarithm of the applied field (in Oe). The slope of the best fit line is 0.63 ± 0.03 when the first four data points are used (dashed line) and 0.340 ± 0.003 when all of the data points are used (not shown).

can be examined using the procedure described above. Before continuing though, it would be useful to consider several typical plots of $\chi(H,t)$ versus H_i^2, as illustrated in Figures 5.42 to 5.45. The plot of $\chi(H,t)$ versus H_i^2 shown in Figure 5.45 is considered to be 'normal' with its immediate drop-off as the field rises from zero; however, as the temperature decreases and the coercive field [3] begins to increase (Figure 5.48), a 'plateau' appears at low fields. Examining Figures 5.42 to 5.44 it can be seen that this effect becomes more pronounced as the temperature decreases, and the coercivity continues to increase. This creates the problem of selecting the most appropriate linear fit for the low field data; it was decided to determine $a_2(T)$ using the higher field data beyond that affected by the coercive field, as illustrated in Figures 5.42 to 5.44. Whether or not this is the best technique for determining the slope is not absolutely certain; however, it does provide an upper limit. The resulting slopes found from all of the data collected are shown in Figure 5.46.

As can be seen, $a_2(T)$ increases as the temperature increases, without displaying any anomaly or peak in the vicinity of the shoulder appearing in the temperature dependent susceptibility data ($T \approx 28$ K). This reinforces the earlier conclusion that there is no true phase transition here, even though it would seem otherwise when considering the zero field temperature dependent data alone.

The question now arises as to the origin of the low temperature peak

[3] A detailed explanation of how the coercive field was determined is given in Section 5.5.2.

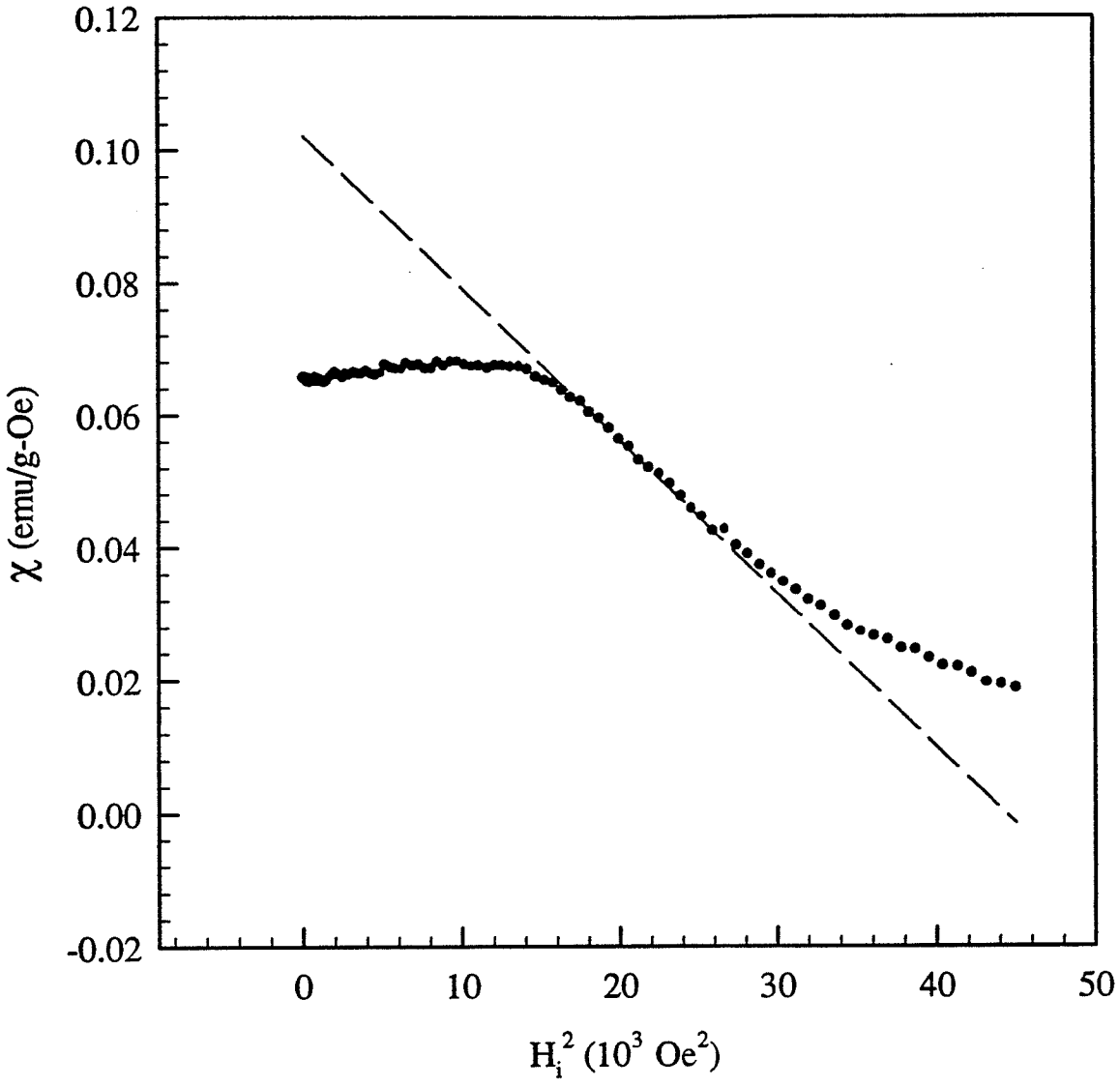

Figure 5.42: The a.c. susceptibility $\chi(H,T)$ (in emu/g-Oe) at $T = 4.2$ K, corrected for background and demagnetizing effects, plotted versus H_i^2 (in Oe^2) for the $x = 0.235$ sample. The dashed line represents the best fit line for the data above that affected by the coercive field.

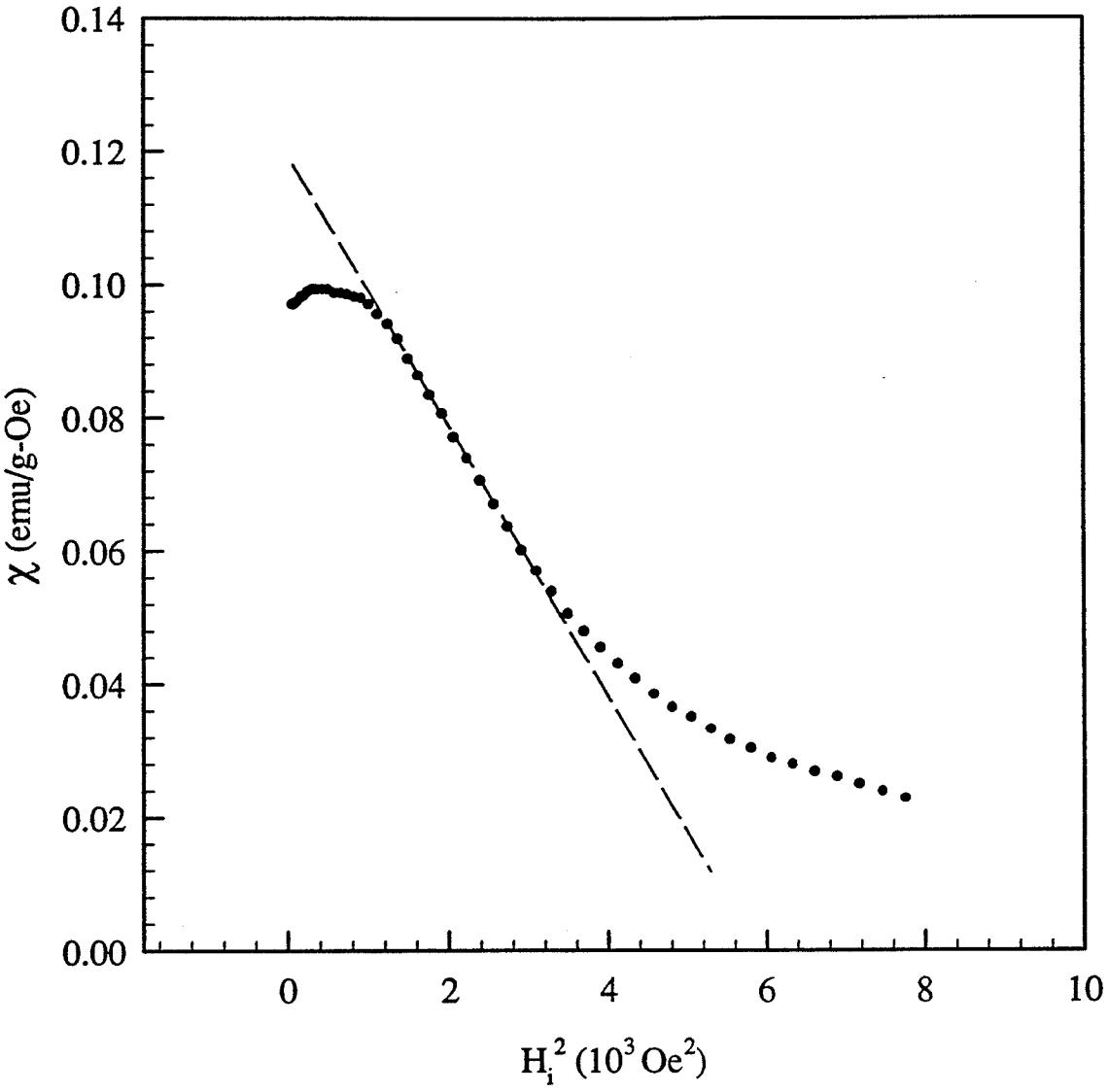

Figure 5.43: The a.c. susceptibility $\chi(H,T)$ (in emu/g-Oe) at $T = 10.0$ K, corrected for background and demagnetizing effects, plotted versus H_i^2 (in Oe^2) for the $x = 0.235$ sample. The dashed line represents the best fit line for the data above that affected by the coercive field.

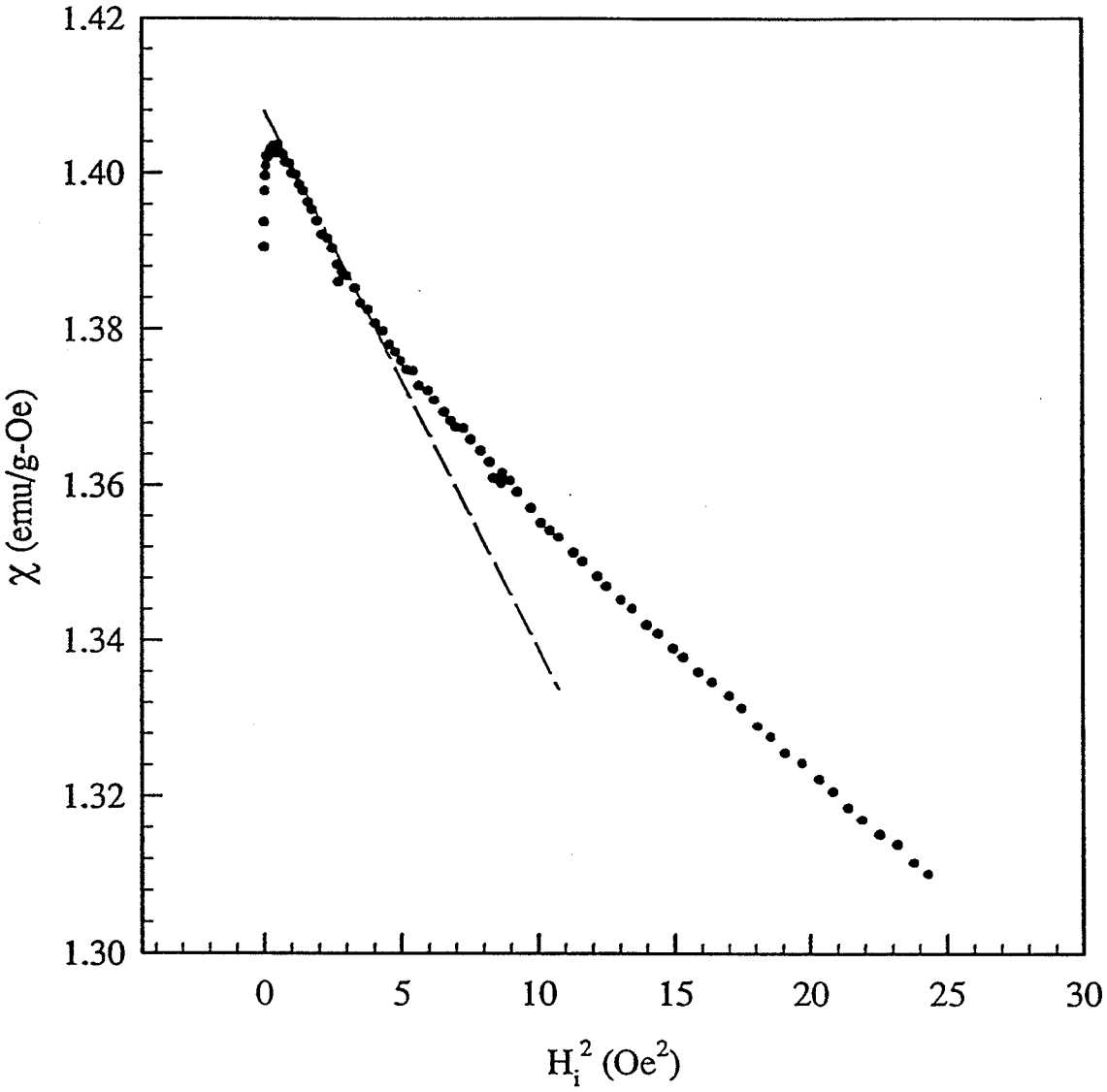

Figure 5.44: The a.c. susceptibility $\chi(H,T)$ (in emu/g-Oe) at $T = 35.3$ K, corrected for background and demagnetizing effects, plotted versus H_i^2 (in Oe^2) for the $x = 0.235$ sample. The dashed line represents the best fit line for the data above that affected by the coercive field.

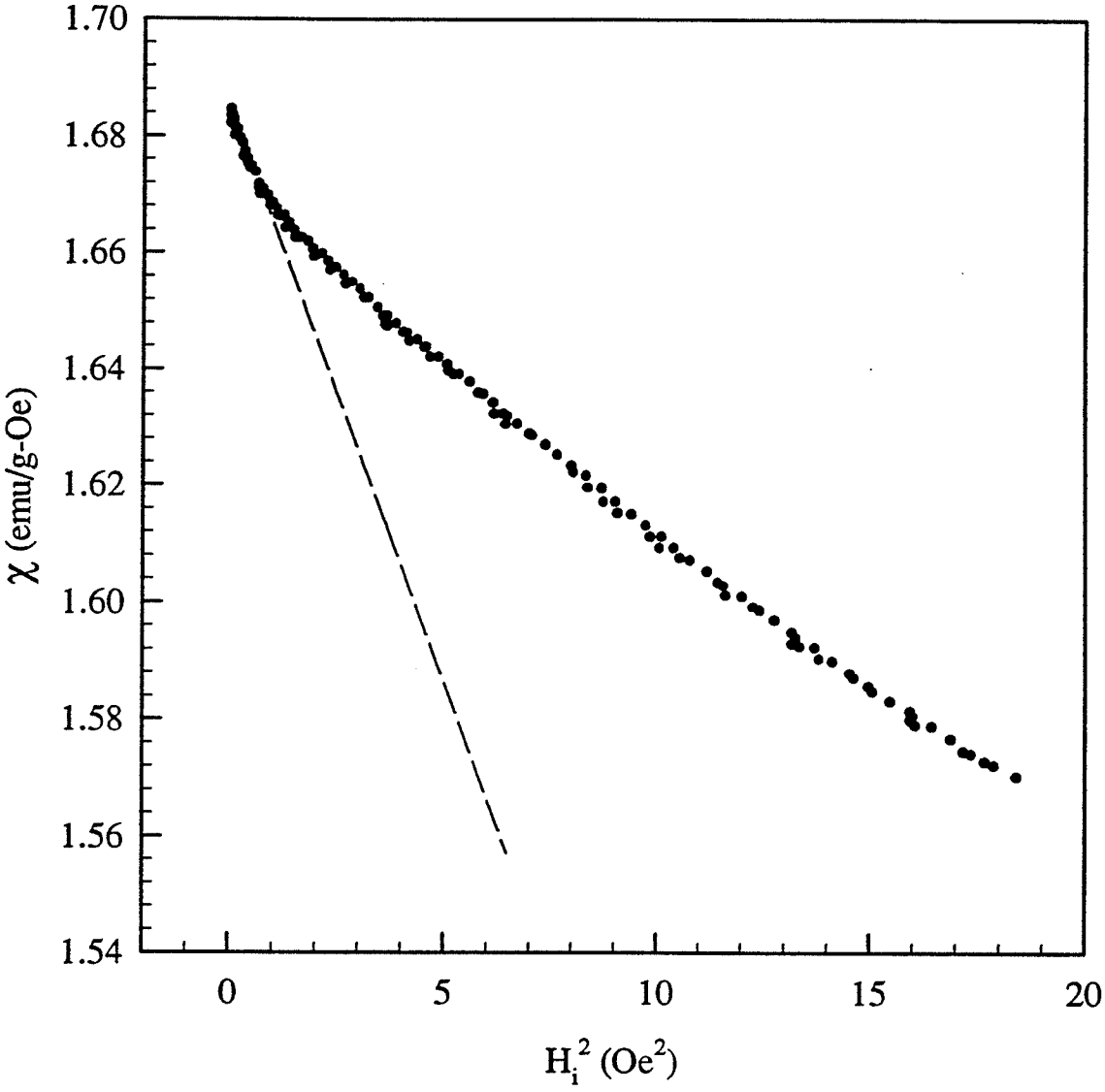

Figure 5.45: The a.c. susceptibility $\chi(H,T)$ (in emu/g-Oe) at $T = 50.9$ K, corrected for background and demagnetizing effects, plotted versus H_i^2 (in Oe^2) for the $x = 0.235$ sample.

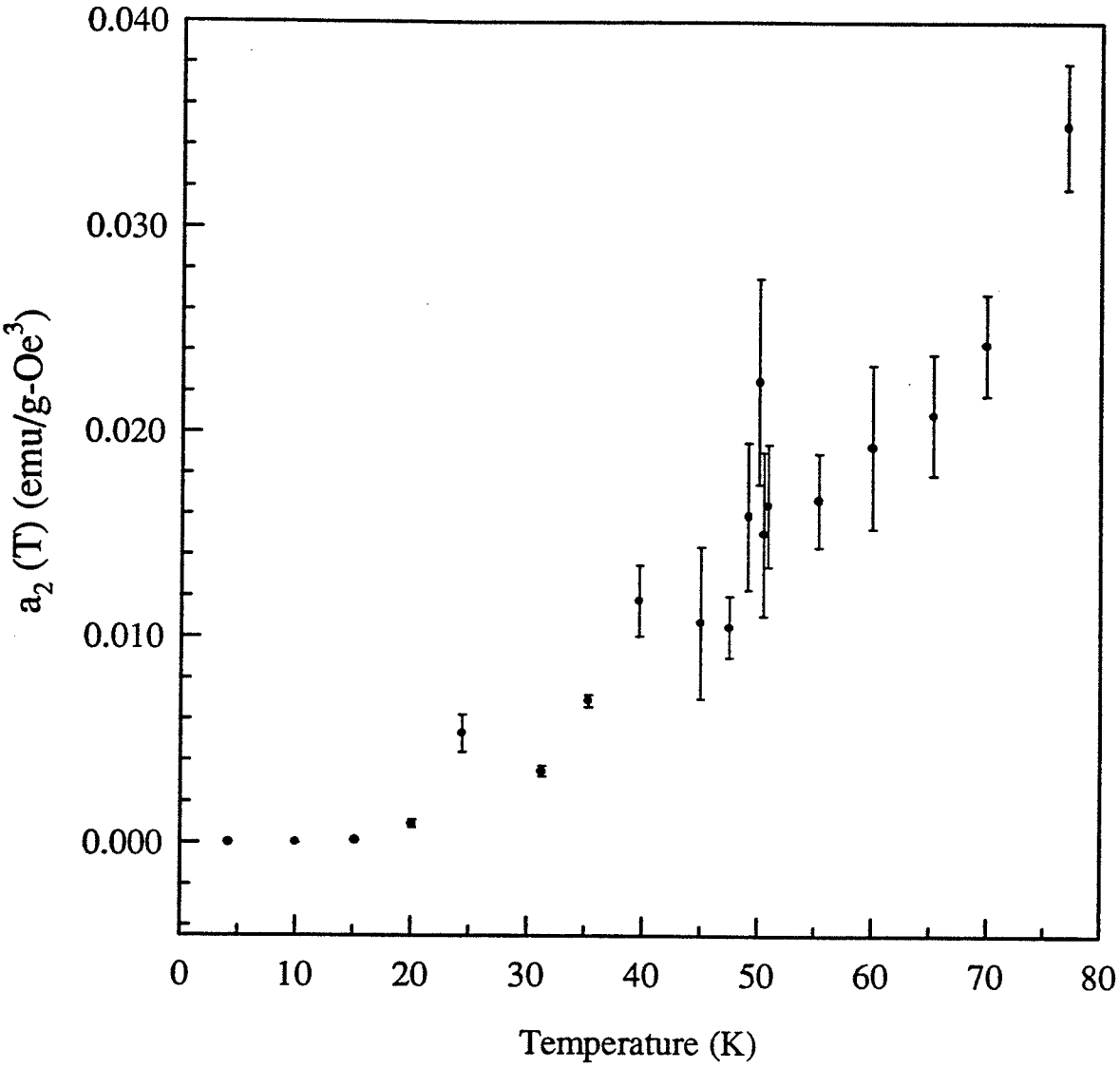

Figure 5.46: Non-linear coefficient, $a_2(T)$ (in emu/g-Oe^3) versus temperature (in K) for the $x = 0.235$ sample.

observed in the temperature sweeps. Looking at Figure 5.47 (for more detail, see Figure 5.48), it can be seen that the decrease in coercivity with increasing temperature is accompanied by an increase in susceptibility. Conversely this suggests the possibility that the decrease in a.c. susceptibility may simply be a consequence of the increasing coercive field, and thus the increasing difficulty in rotating the spins, moving domain walls, and other thermally activated blocking processes. This possibility could be explored, using for instance frequency dependent measurements. Unfortunately, our susceptometer operates at only two frequencies, 2400 and 714 Hz, with a considerably lower signal to noise ratio at 714 Hz.

5.5.2 $\mathbf{Fe}_{1-x}\mathbf{Mn}_x$ $(x = 0.26)$

The analysis of the $x = 0.26$ sample is very similar to that of the previous sample, due to the same general shape of the respective temperature sweeps, as illustrated in Figure 5.49. Analyzing the first set of broad peaks (35 K $< T <$ 65 K) appearing below the paramagnetic-ferromagnetic transition, the resulting plot of T_{peak} versus H_a, shown in Figure 5.50, gives a value for $T_{GT}(0)$ of 65.8 ± 0.4 K and a value for n of 0.9 ± 0.3. Although the error in $T_{GT}(0)$ is reasonable, the error in n, due to the scatter of the data points, is too large to decide if GT behaviour is exhibited. The slope of Figure 5.50 was found to be -2060 ± 50, which is four orders of magnitude larger than the theoretical value of -0.44, not unlike the $x = 0.235$ result. This suggests that the peaks observed are not GT peaks.

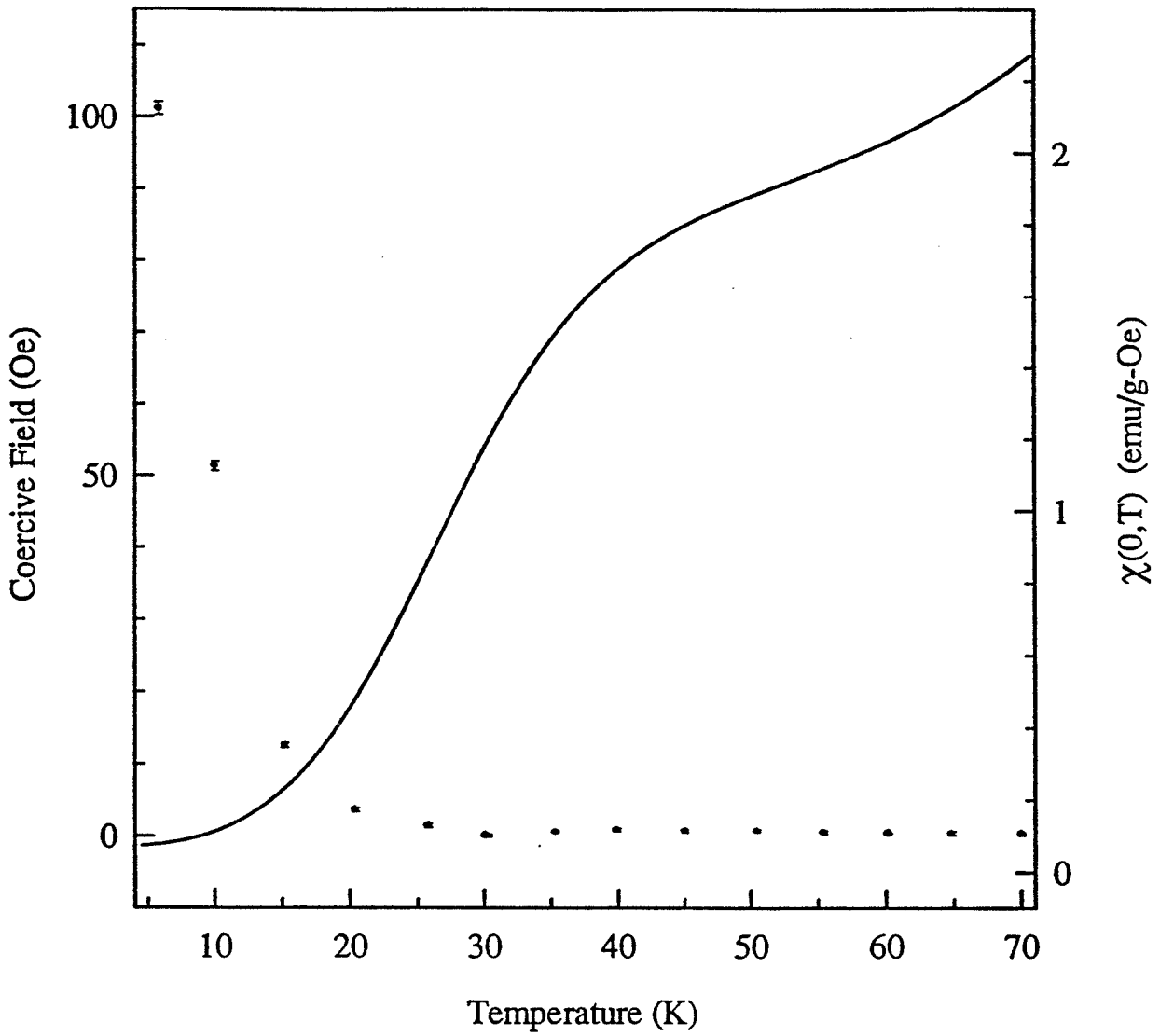

Figure 5.47: Coercive field (in Oe) for the $x = 0.235$ sample plotted versus temperature (in K) (dashed line), along with the zero field a.c. susceptibility $\chi(H,T)$ (in emu/g-Oe) corrected for background and demagnetizing effects plotted versus temperature (in K) (points).

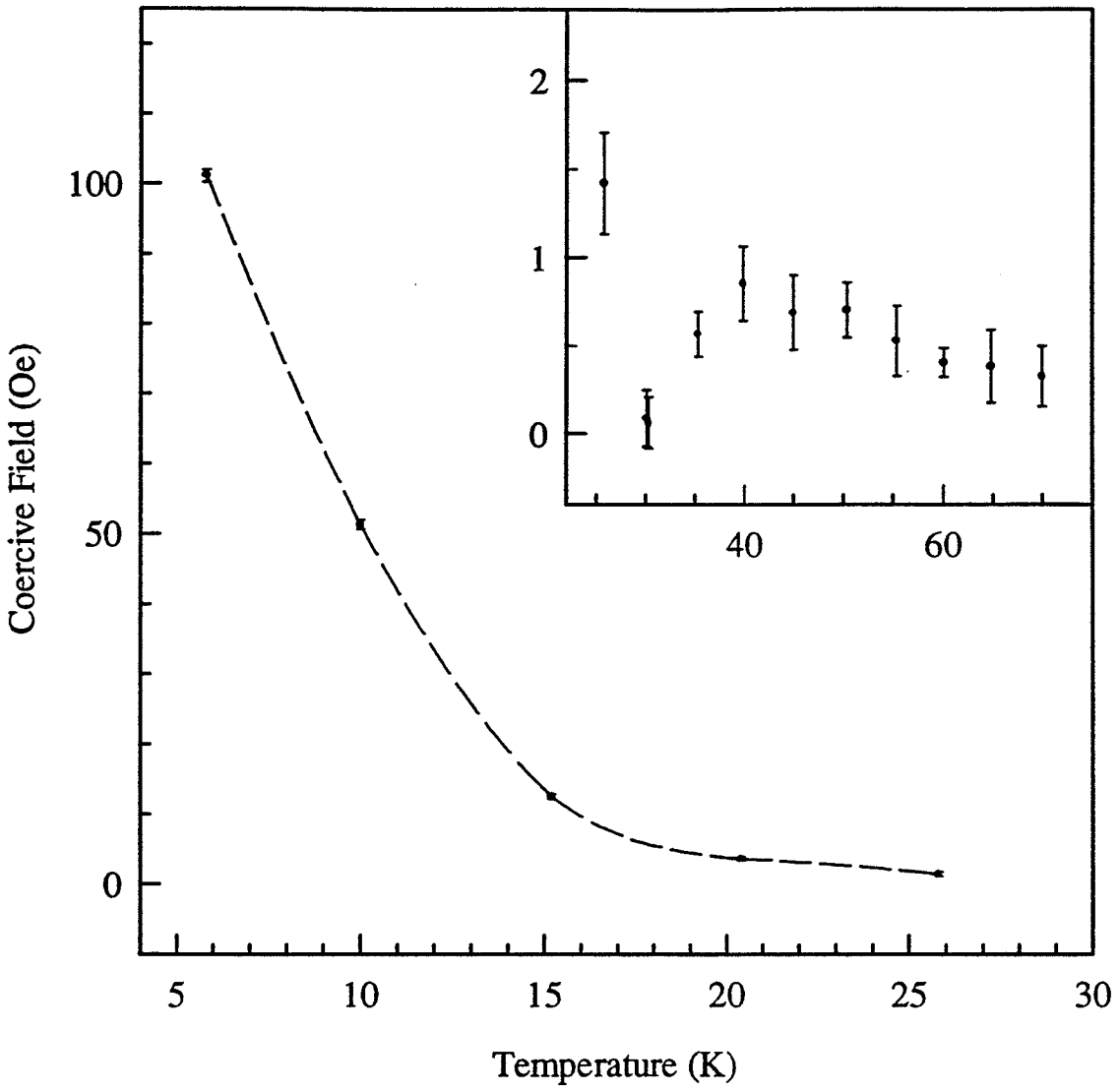

Figure 5.48: Coercive field (in Oe) for the $x = 0.235$ sample plotted versus temperature (in K). The insert shows the coercive field (in Oe) for the temperature range 30 K $< T <$ 70 K.

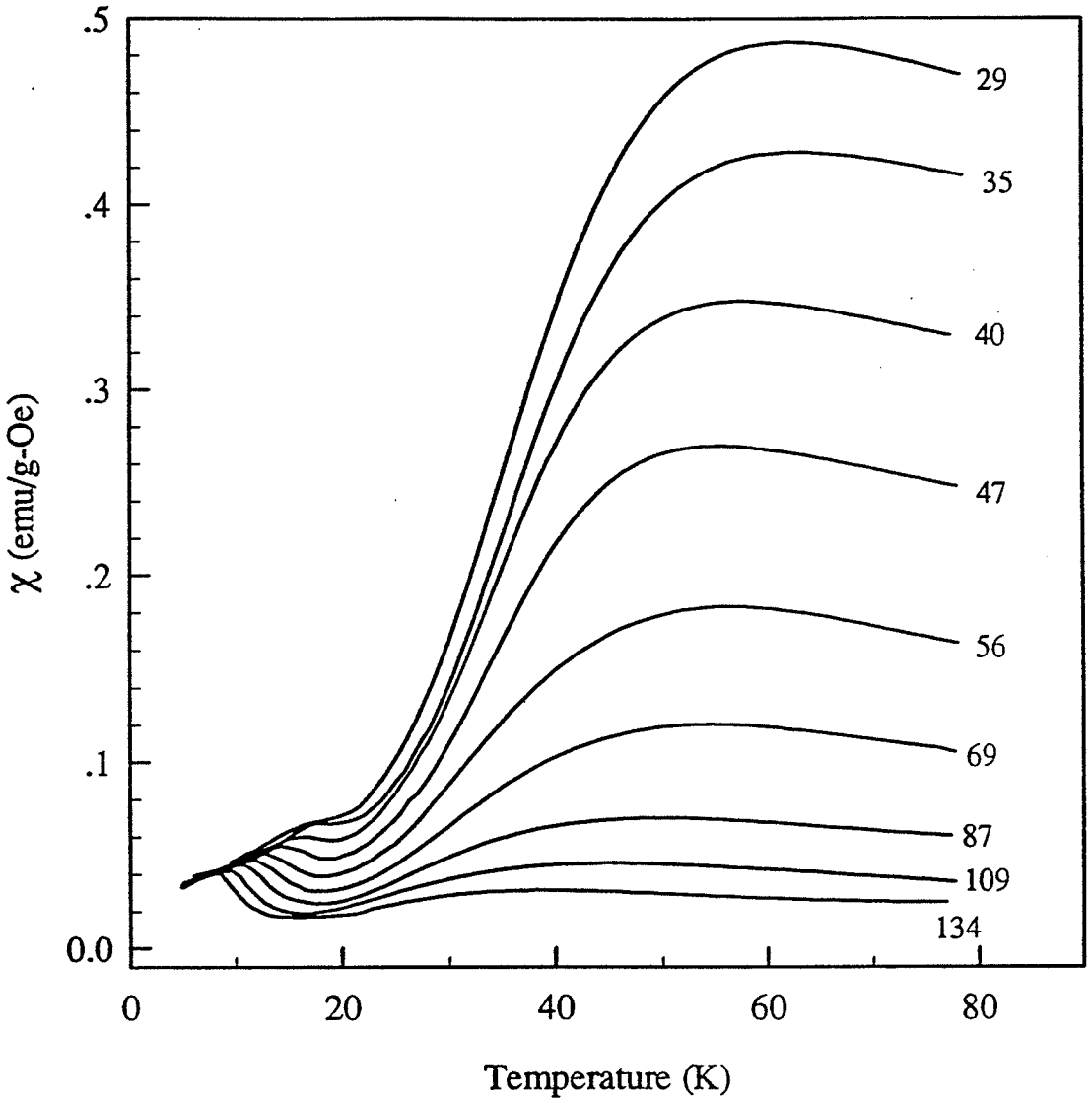

Figure 5.49: The a.c. susceptibility $\chi(H,T)$ (in emu/g-Oe), corrected for background and demagnetizing effects, plotted versus temperature (in K) for the $x = 0.26$ sample. The numbers beside each curve represent the static biasing field (in Oe).

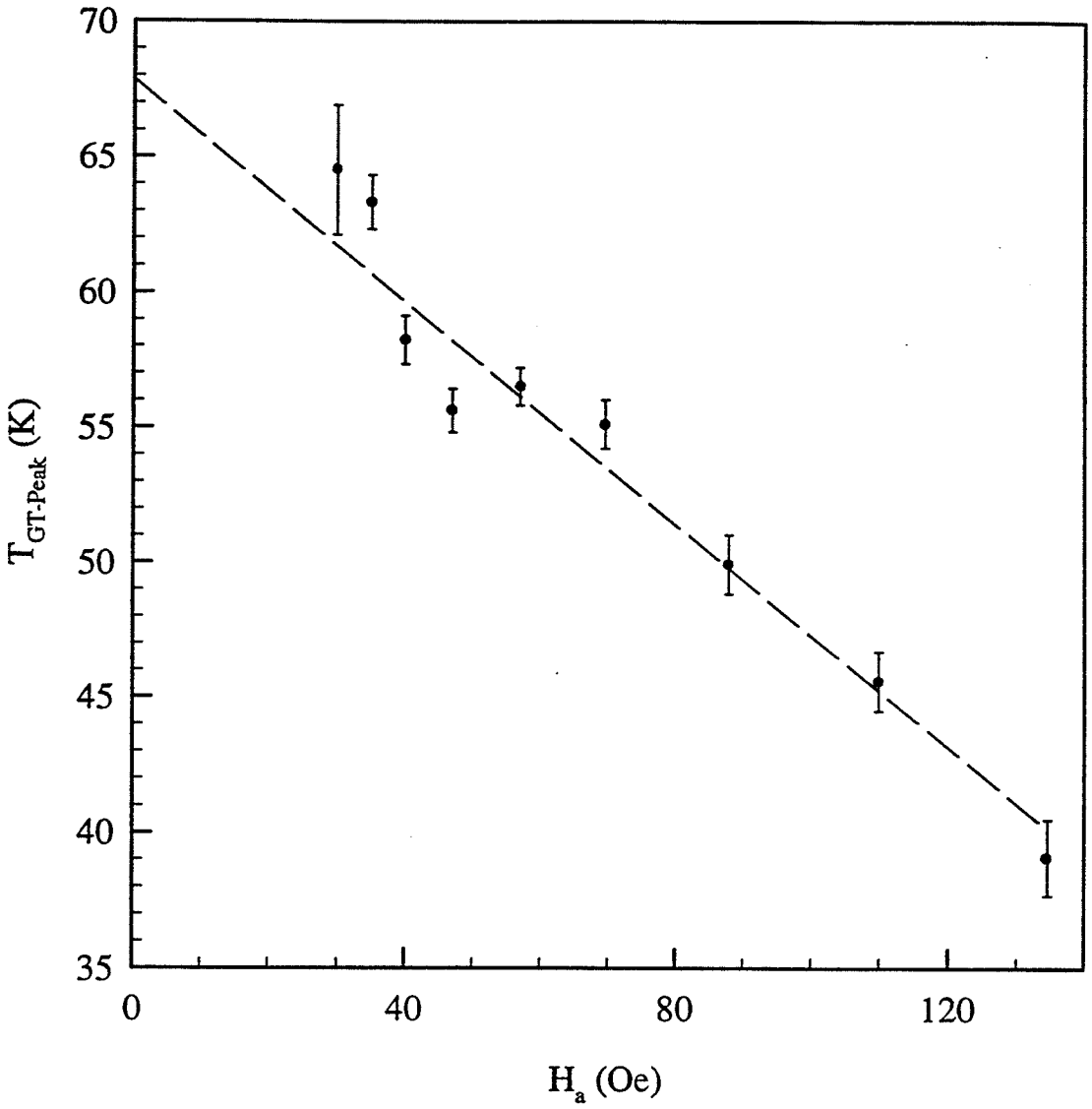

Figure 5.50: The proposed GT transition temperature (in K) (from peak) plotted versus the applied field (in Oe) for the $x = 0.26$ sample. The intercept of the best fit line gives $T_{GT}(0) = 65.8 \pm 2.4$ K, and the slope is -2060 ± 50.

Examining the trough structure in Figure 5.51 and plotting T_{trough} versus H_a gives the graph shown in Figure 5.52. The latter has an intercept of 20.0 ± 0.3 K and the corresponding check gives an exponent, n = 1.0 ± 0.3. As before, the error in the calculated value of n is simply too large to make a conclusive statement without further investigation. The slope of Figure 5.52 is -320 ± 40. Although this is much smaller than 2060 (from Figure 5.50), it is still three orders of magnitude larger than -0.44, thus suggesting that the trough structure is also not a result of the GT transition.

Proceeding to analyze the lowest temperature (6 K $< T <$ 18 K) peaks shown in Figure 5.51, the resulting plot of T_{peak} versus H_a can be seen in Figure 5.53. The best-fit curve intersects the $T_{AT-Peak}$ axis at 28 K, which will be taken to be $T_{AT}(0)$. Using this value to generate the data in Figure 5.54, the latter plot has a slope of 0.365 ± 0.002, when all of the data points are included. This agrees well with the value of 0.340 found for $x = 0.235$, but not with the expected value of 2/3, thereby reinforcing the earlier claim that the lowest set of peaks is not a manifestation of the AT transition.

Considering the behaviour of the non-linear component of the susceptibility, $a_2(T)$ was found as described above, and the resulting graph can be seen in Figure 5.55. As with $x = 0.235$, there is no anomaly or peak apparent in the data, other than the one occurring at the PM-FM transition. Along with the other results for this sample, this would lead to the conclusion that there is most likely no true FM-SG phase transition.

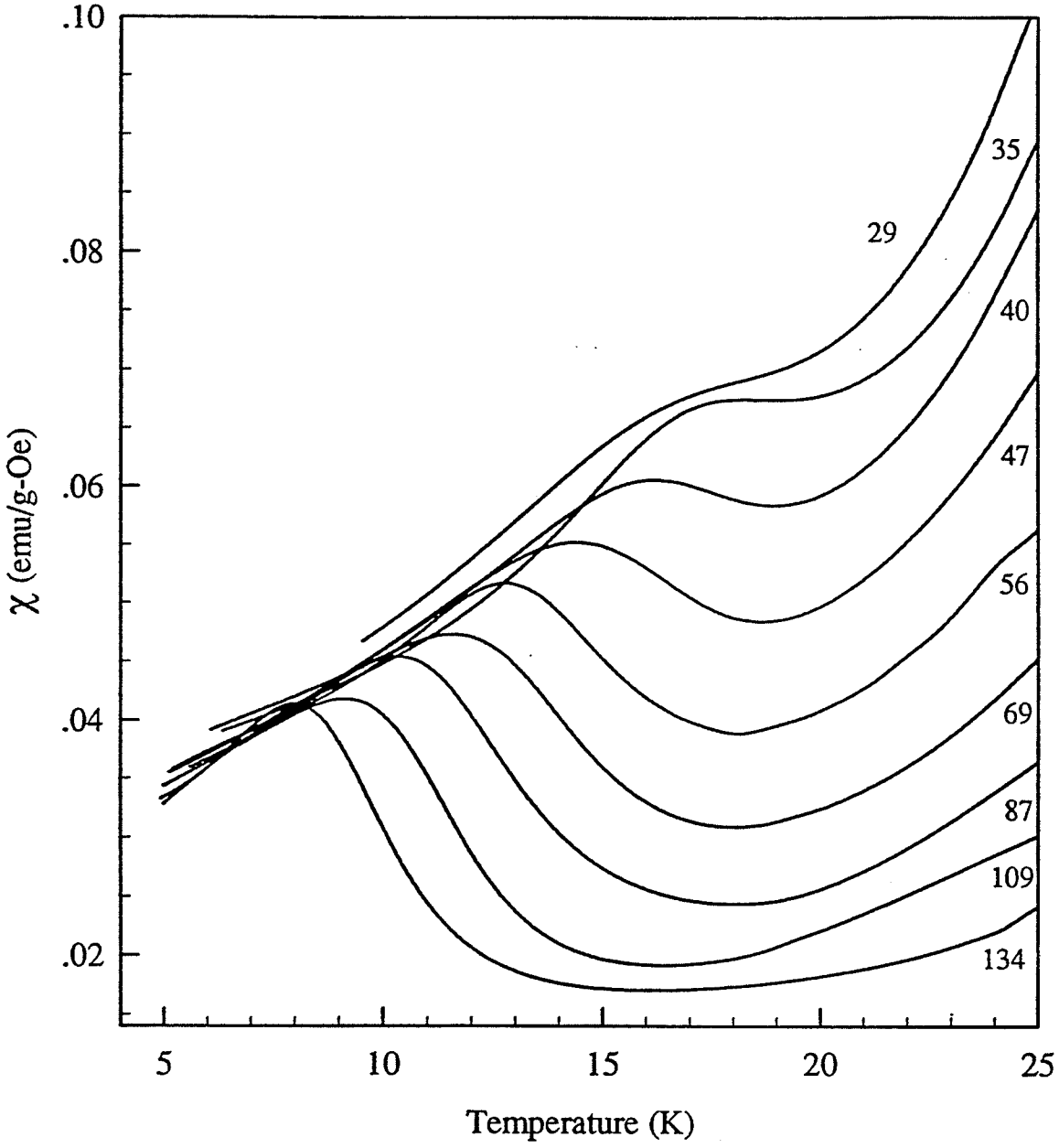

Figure 5.51: The a.c. susceptibility $\chi(H,T)$ (in emu/g-Oe), corrected for background and demagnetizing effects, plotted versus temperature (in K) for the $x = 0.26$ sample. The numbers beside each curve represent the static biasing field (in Oe).

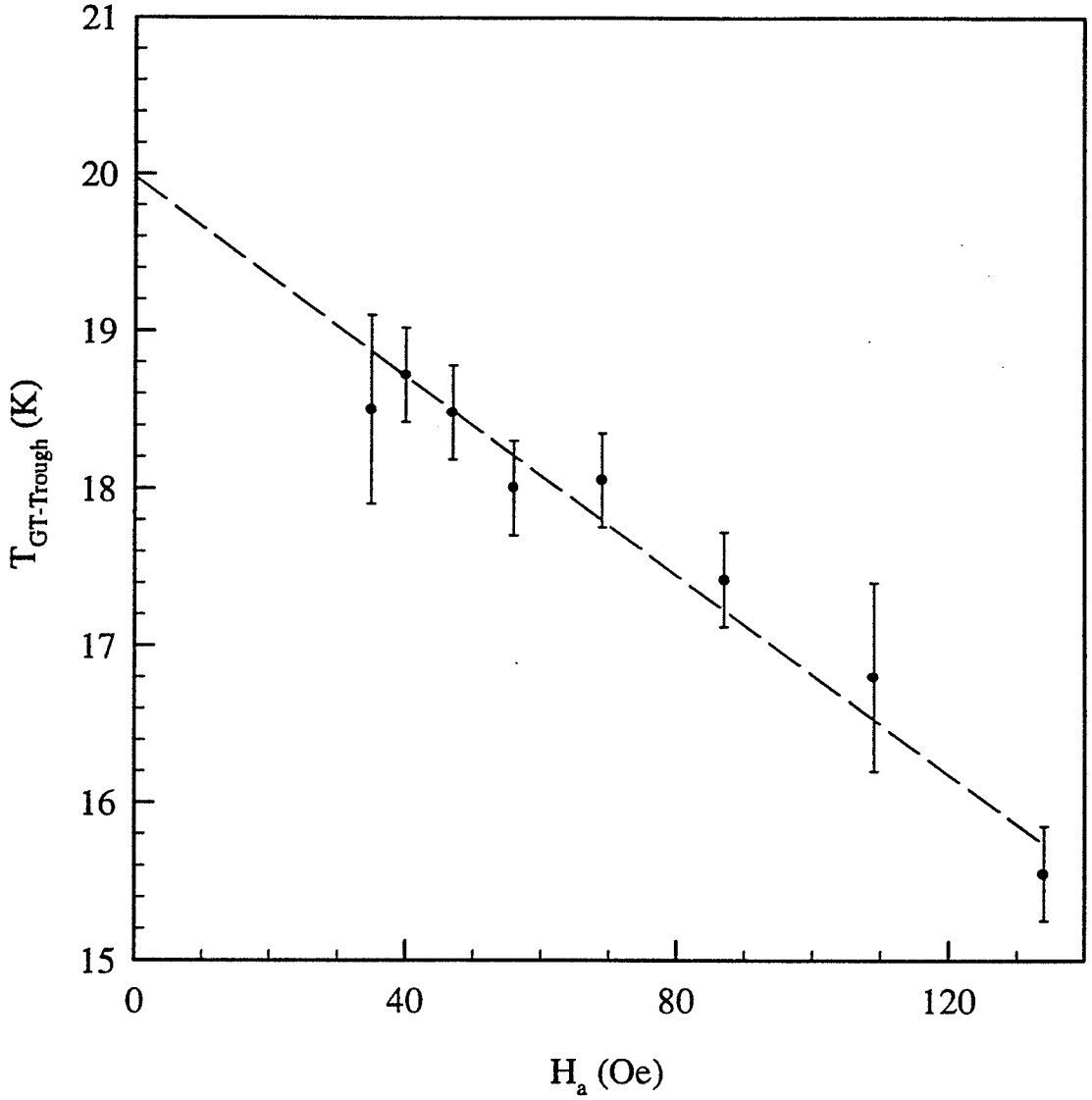

Figure 5.52: The proposed GT transition temperature (in K) (from trough) plotted versus the applied field (in Oe) for the $x = 0.26$ sample. The intercept of the best fit line gives $T_{GT}(0) = 20.0 \pm 0.3$ K, and the slope is -320 ± 40.

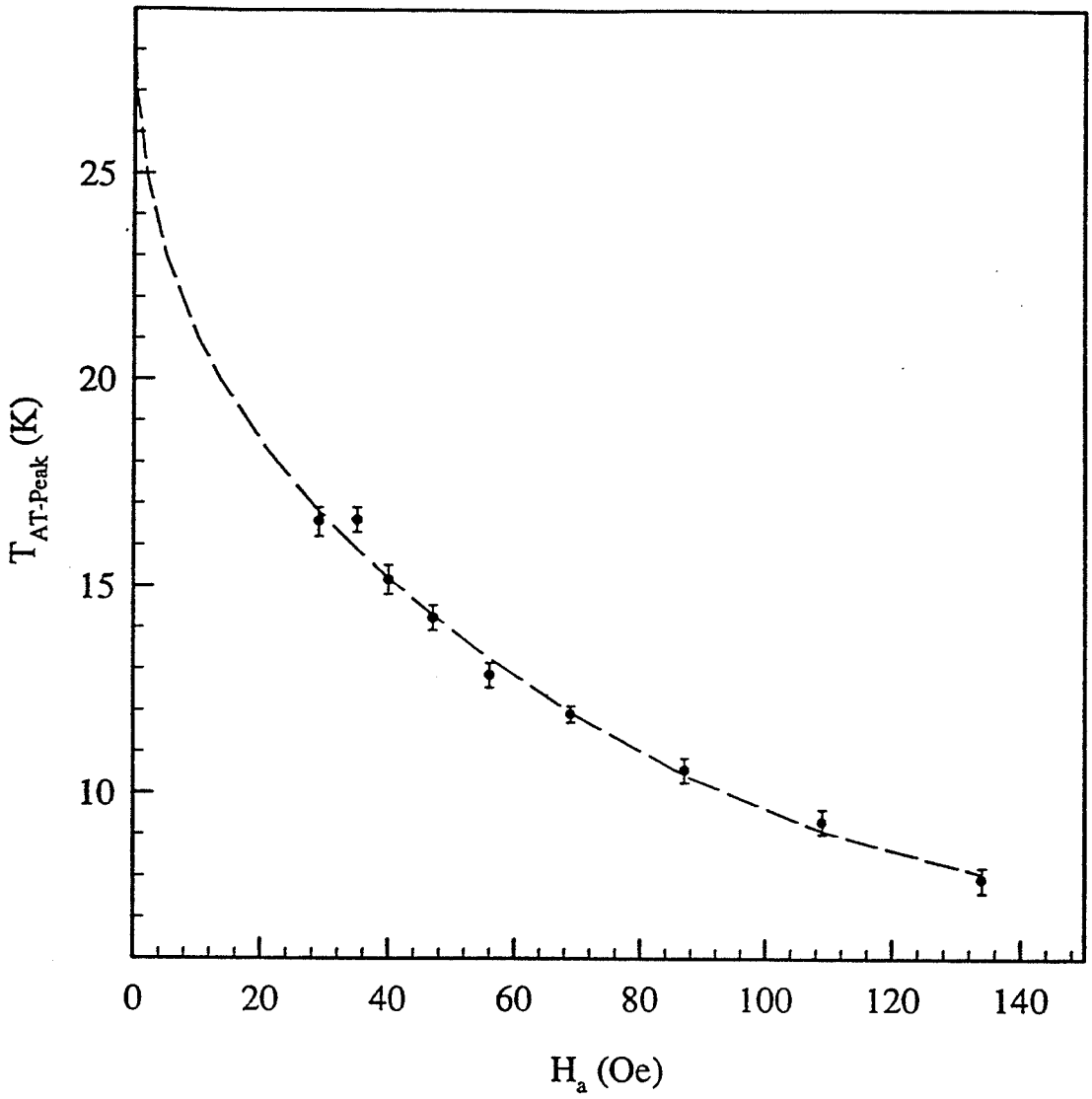

Figure 5.53: The proposed AT transition temperature (in K) (from lowest peak) plotted versus the applied field (in Oe) for the $x = 0.26$ sample. The intercept of the best fit curve gives $T_{AT}(0) = 28$ K.

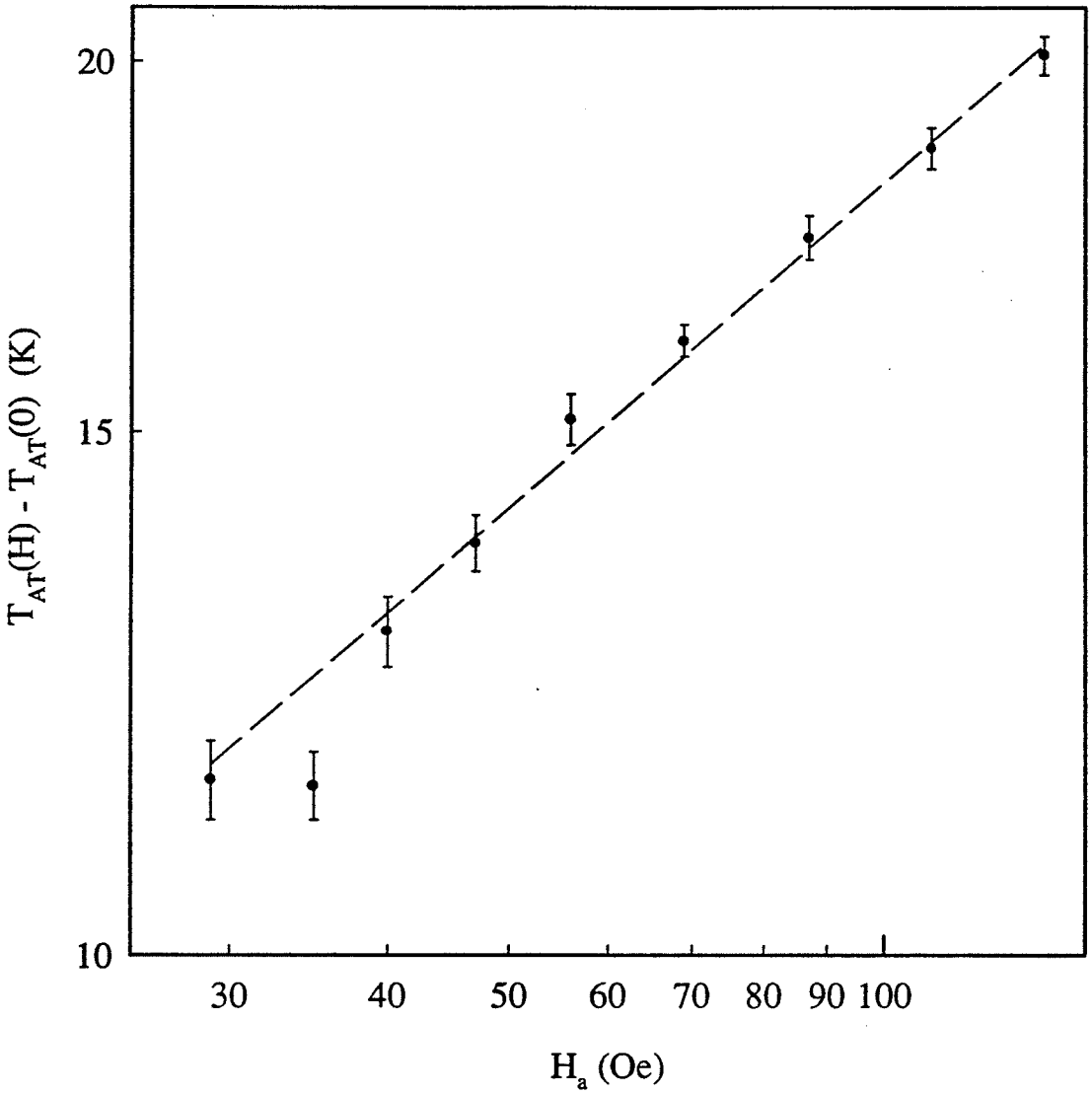

Figure 5.54: The logarithm of $T_{AT}(0) - T_{AT}(H_a)$ (in K) for the $x = 0.26$ sample plotted versus the logarithm of the applied field (in Oe). The slope of the best fit line is 0.365 ± 0.002 when all of the data points are used (dashed line).

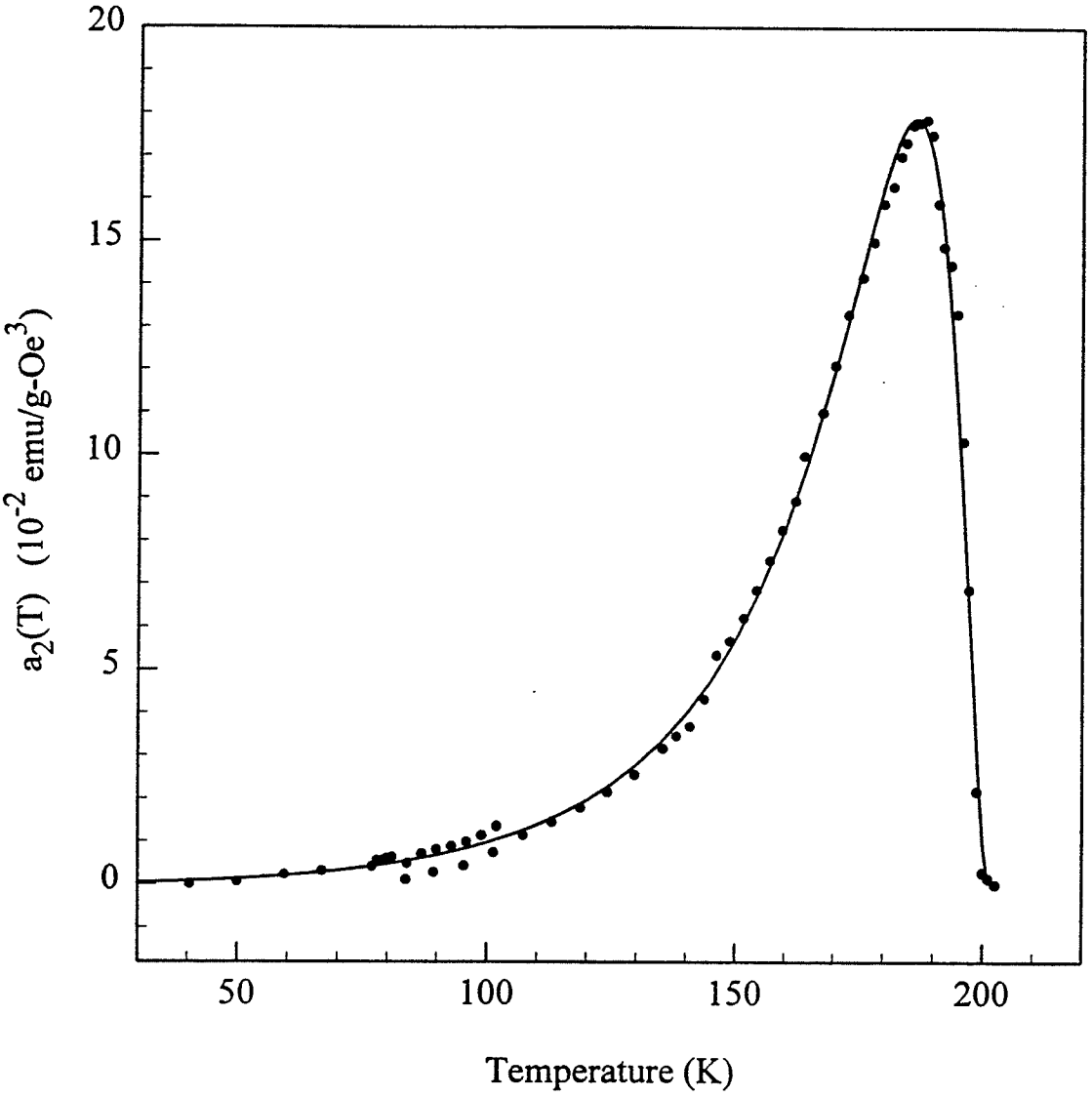

Figure 5.55: Non-linear coefficient, $a_2(T)$ (in emu/g-Oe^3) versus temperature (in K) for the $x = 0.26$ sample.

The origin of the low temperature peaks observed in the temperature sweep data is most likely due to the decrease in coercive field, similar to the $x = 0.235$ sample. The coercivity can be found using the 'butterfly sweeps' introduced in Section 4.3.3. Two representative butterflies are shown in Figures 5.56 and 5.57, where the first of the two is a complete butterfly, and the latter is a partial butterfly, showing only the essential peaks. The reason why the butterfly sweeps are a measure of the coercivity can be understood by realizing that the susceptibility versus field measurements represent the slope of the corresponding M versus H hysteresis loop. The greatest slope in the hysteresis loop occurs when $H = \pm H_c$ resulting in the two peaks in the butterfly loop. Thus

$$H_c = \frac{1}{2}(\textit{Field difference between susceptibility peaks}) \tag{5.19}$$

can easily be understood. Although not shown here, the shape of the H_c versus T_c plot for the $x = 0.26$ sample is similar to that for the $x = 0.235$ sample shown in Figure 5.48.

5.5.3 $\mathbf{Fe_{1-x}Mn_x}$ $(x = 0.30)$

The data for the $x = 0.30$ sample differs from the previous two lower concentration samples in that the additional low temperature peak/trough structure is absent here (Figure 5.58). In sufficiently strong fields, a broad peak still appears below the paramagnetic-ferromagnetic transition, which can be analyzed for GT behaviour, using the same procedure as before. The resulting

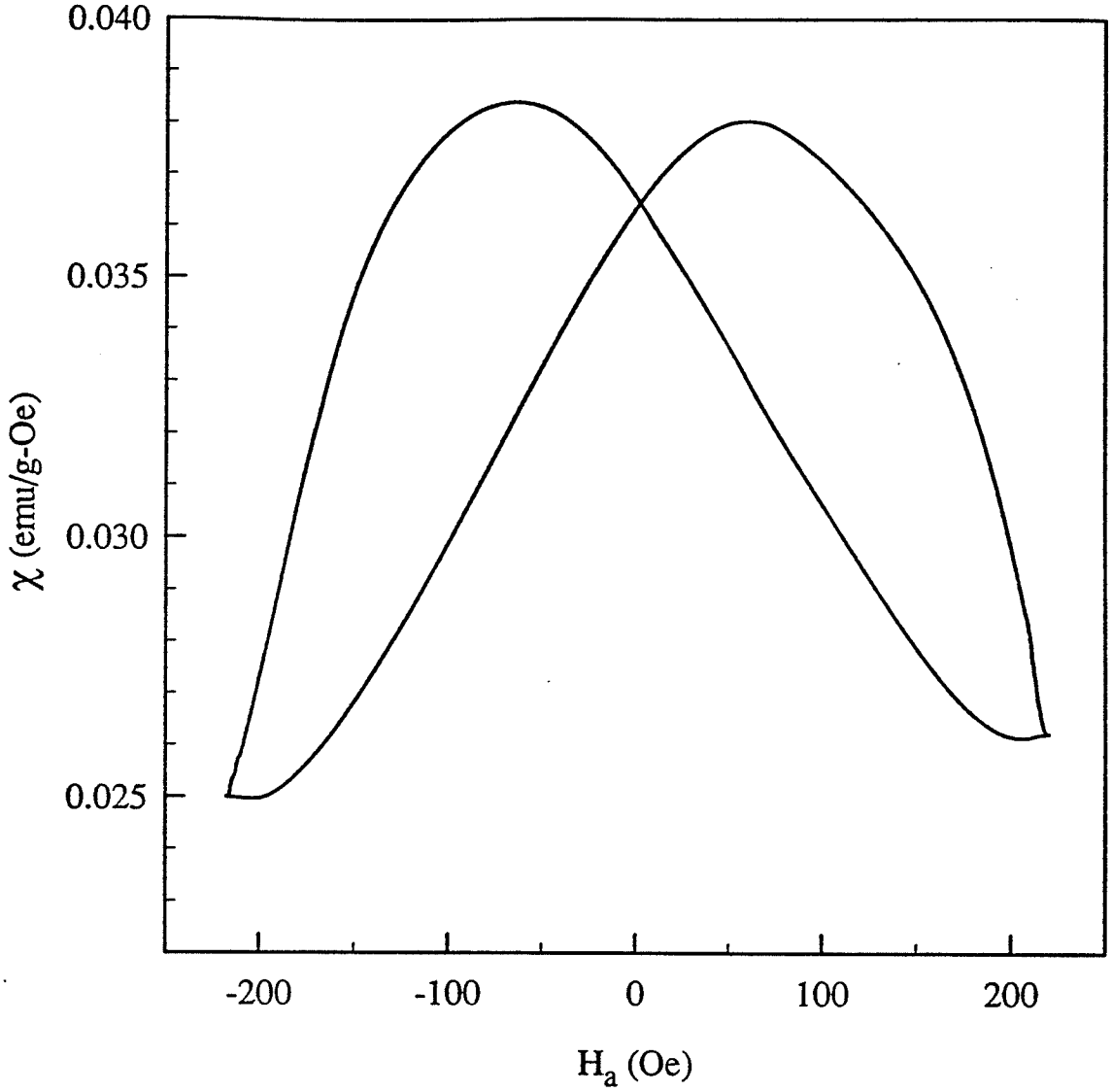

Figure 5.56: Complete butterfly loop: susceptibility (in emu/g-Oe) versus field (in Oe) for the $x = 0.26$ sample, at 4.2 K.

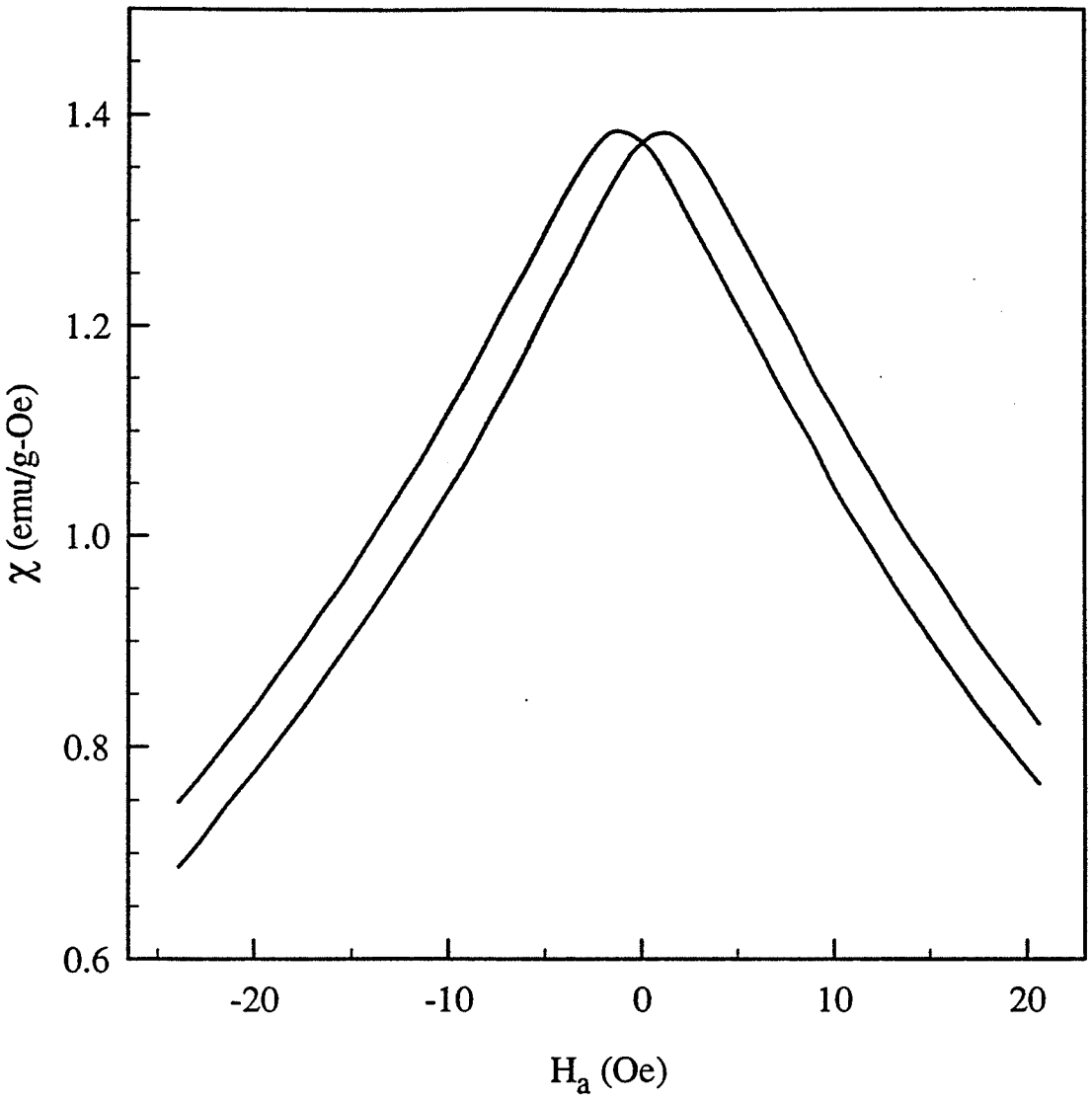

Figure 5.57: Partial butterfly loop: susceptibility (in emu/g-Oe) versus field (in Oe) for the $x = 0.26$ sample, at 77 K.

plot, shown in Figure 5.59 gives $T_{GT}(0) = 52.6 \pm 0.7$ and an exponent value of $n = 0.9 \pm 0.3$. As with the previous samples, the error is simply too large to make a conclusive statement, concerning whether or not GT behaviour is displayed, based only upon the above results. The slope of Figure 5.59 was found to be -930 ± 90, which is considerably smaller than the value for the previous two samples, but is still three orders of magnitude larger than the theoretical result of -0.44.

The behaviour of the non-linear component of the susceptibility was analyzed, and the results can be seen in Figure 5.60. Unlike the $x = 0.235$ and 0.26 samples, a small shoulder occurs in the vicinity of the low temperature drop-off in the susceptibility ($T \approx 55$ K).

In order to verify that this feature is not simply an artifact of the fitting procedure, a completely independent analysis was done using the temperature sweeps illustrated in Figure 5.57. By interpolating the temperature sweeps at various fixed temperatures, susceptibility versus H_i^2 curves similar to those illustrated in Figures 5.42 to 5.46, were obtained, albeit with far fewer data points. The magnetization, and therefore the internal fields were found by integrating the interpolated susceptibilities at a given temperature from zero up to its particular field using the trapezoidal rule (see Section 5.1.3). The initial slopes of these χ versus H_i^2 plots derived from temperature sweeps also give the $a_2(T)$ coefficients. The temperature dependence of the $a_2(T)$ coefficients obtained in this manner is shown in Figure 5.61 and is

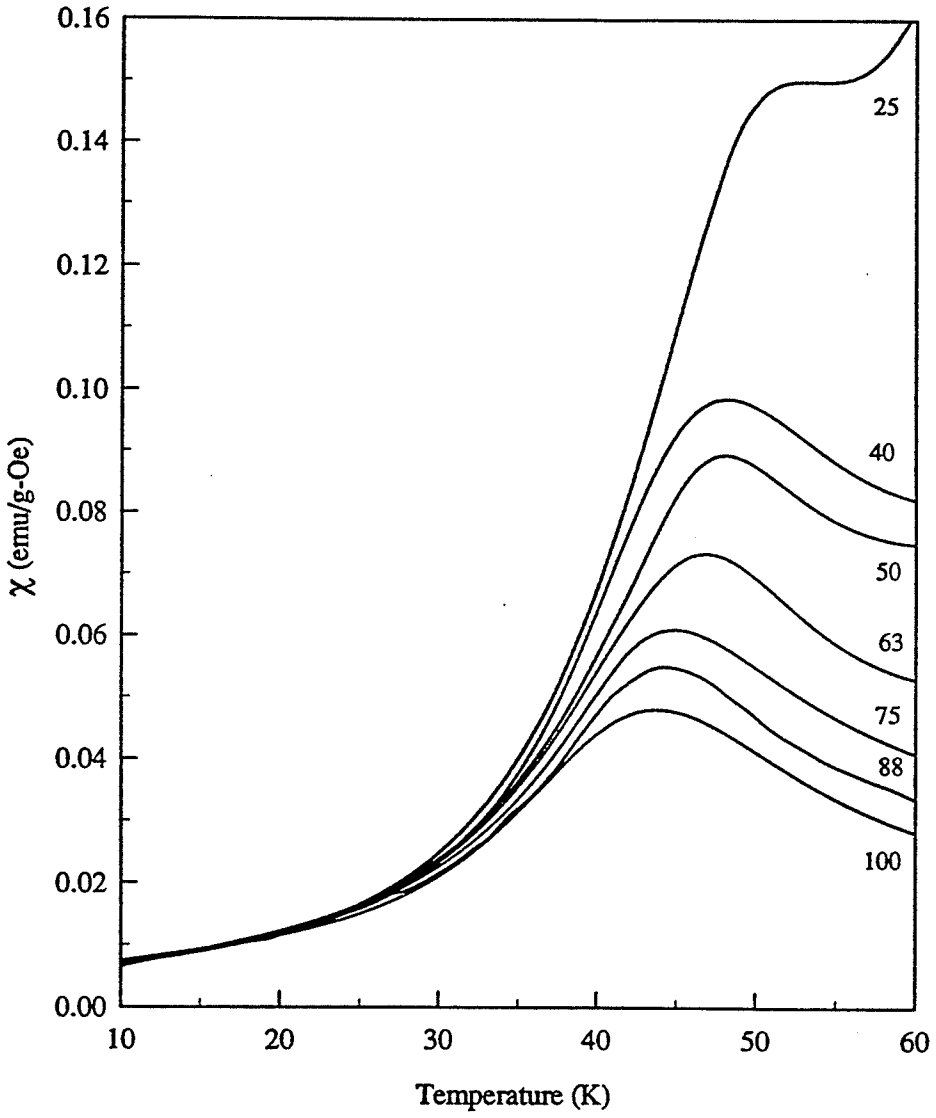

Figure 5.58: The a.c. susceptibility $\chi(H,T)$ (in emu/g-Oe), corrected for background and demagnetizing effects, plotted versus temperature (in K) for the $x = 0.30$ sample. The numbers beside each curve represent the static biasing field (in Oe).

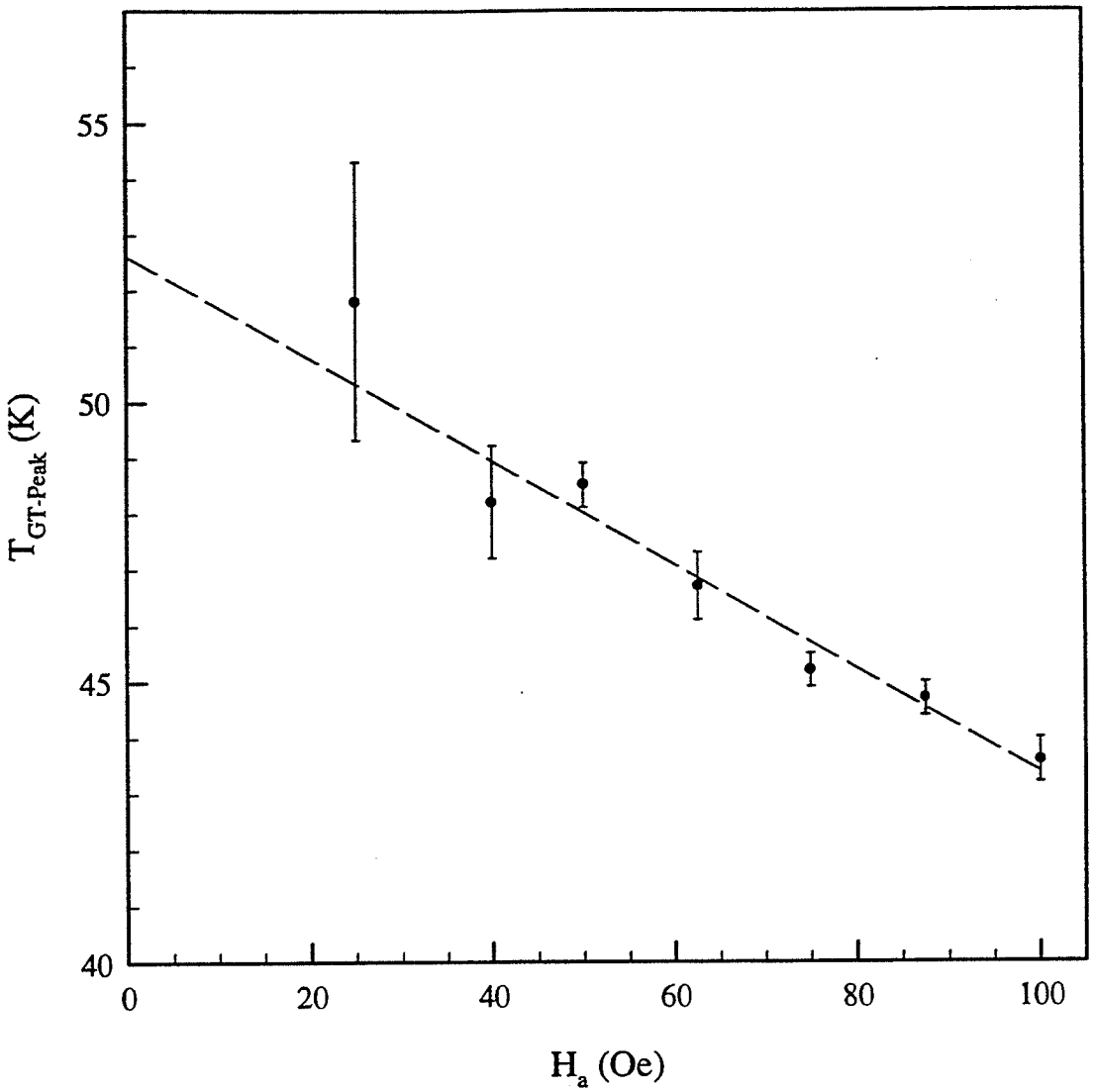

Figure 5.59: The proposed GT transition peak temperature (in K) plotted versus the applied field (in Oe) for the $x = 0.30$ sample. The intercept of the best fit line gives $T_{GT}(0) = 52.6 \pm 0.7$ K, and the slope is -930 ± 90.

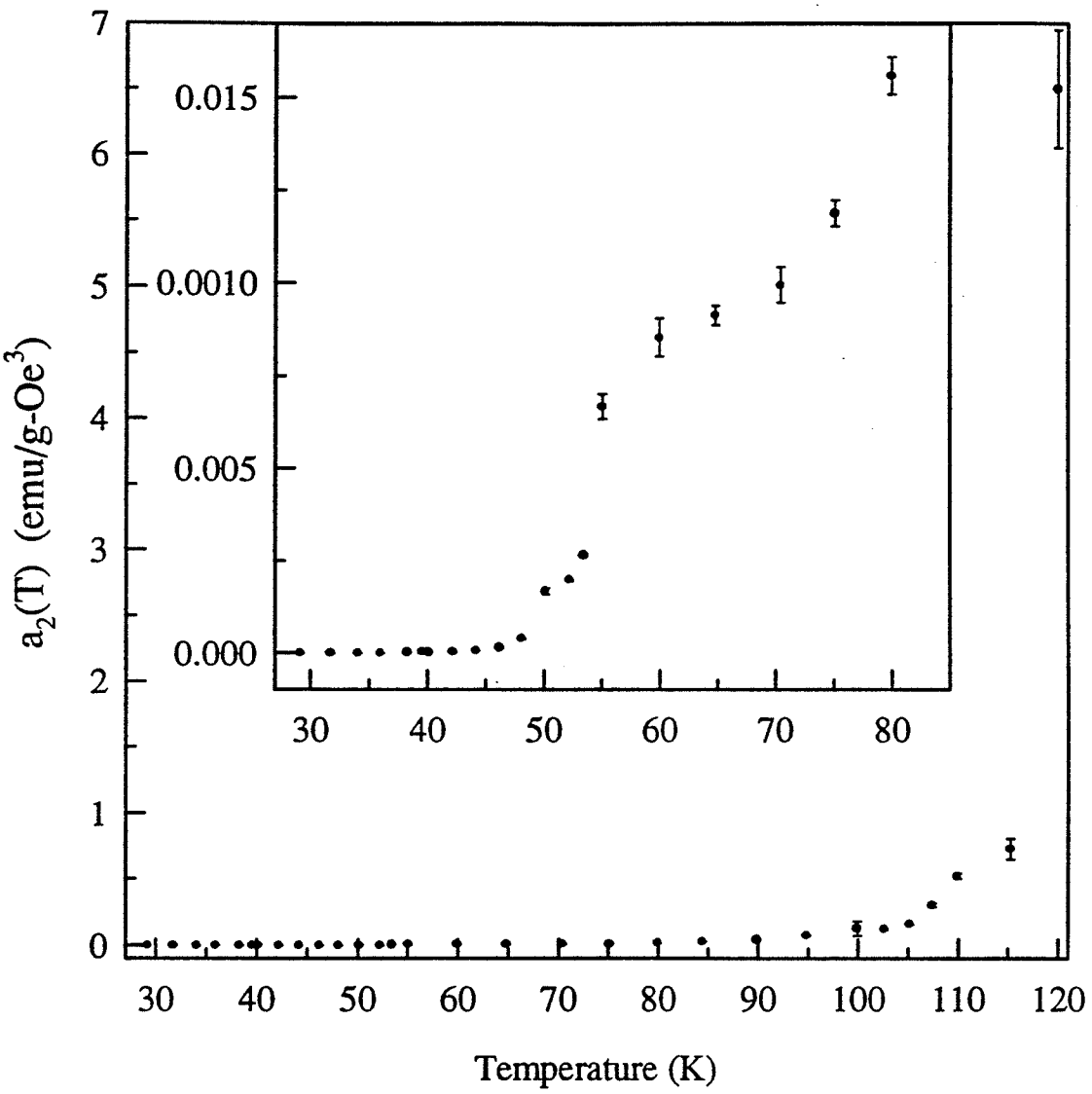

Figure 5.60: Non-linear coefficient, $a_2(T)$ (in emu/g-Oe^3) versus temperature (in K) for the $x = 0.30$ sample (from field sweeps).

in excellent agreement with the non-linear data obtained from field sweeps.

Finally, considering the coercive field, the drop in coercivity does not coincide with the zero field low-temperature shoulder (Figure 5.62). The susceptibility has already dropped before H_c begins to rise, suggesting that the behaviour of the coercive field is not solely responsible for the drop in the susceptibility. A more detailed plot of the coercive field versus temperature can be seen in Figure 5.63.

5.5.4 $\mathbf{Fe_{1-x}Mn_x}$ $(x = 0.32)$

Examination of the temperature sweeps illustrated in Figure 5.64, for the predicted GT behaviour of the low temperature peaks, yields, when plotting the peak temperature versus H_a, data that displays distinct curvature, as can be seen in Figure 5.64, and unlike the equivalent plots obtained for the other compositions. In comparing the latter graph to Figure 5.36 ($x = 0.235$, 30 Oe $< H_a <$ 700 Oe), Figure 5.50 ($x = 0.26$, 29 Oe $< H_a <$ 134 Oe) and Figure 5.59 ($x = 0.30$, 25 Oe $< H_a <$ 100 Oe), it can be seen that the latter three figures consist of data taken over a much smaller field range than Figure 5.65. This raises the possibility that perhaps the data for the compositions $x = 0.235, 0.26$ and 0.30 would also exhibit similar curvature had more data been collected at higher fields. Should this be the case, it would at the very least indicate that the quantitative predictions of the behaviour of the GT line by (Dubiel et al, 1987) are not confirmed by experiment.

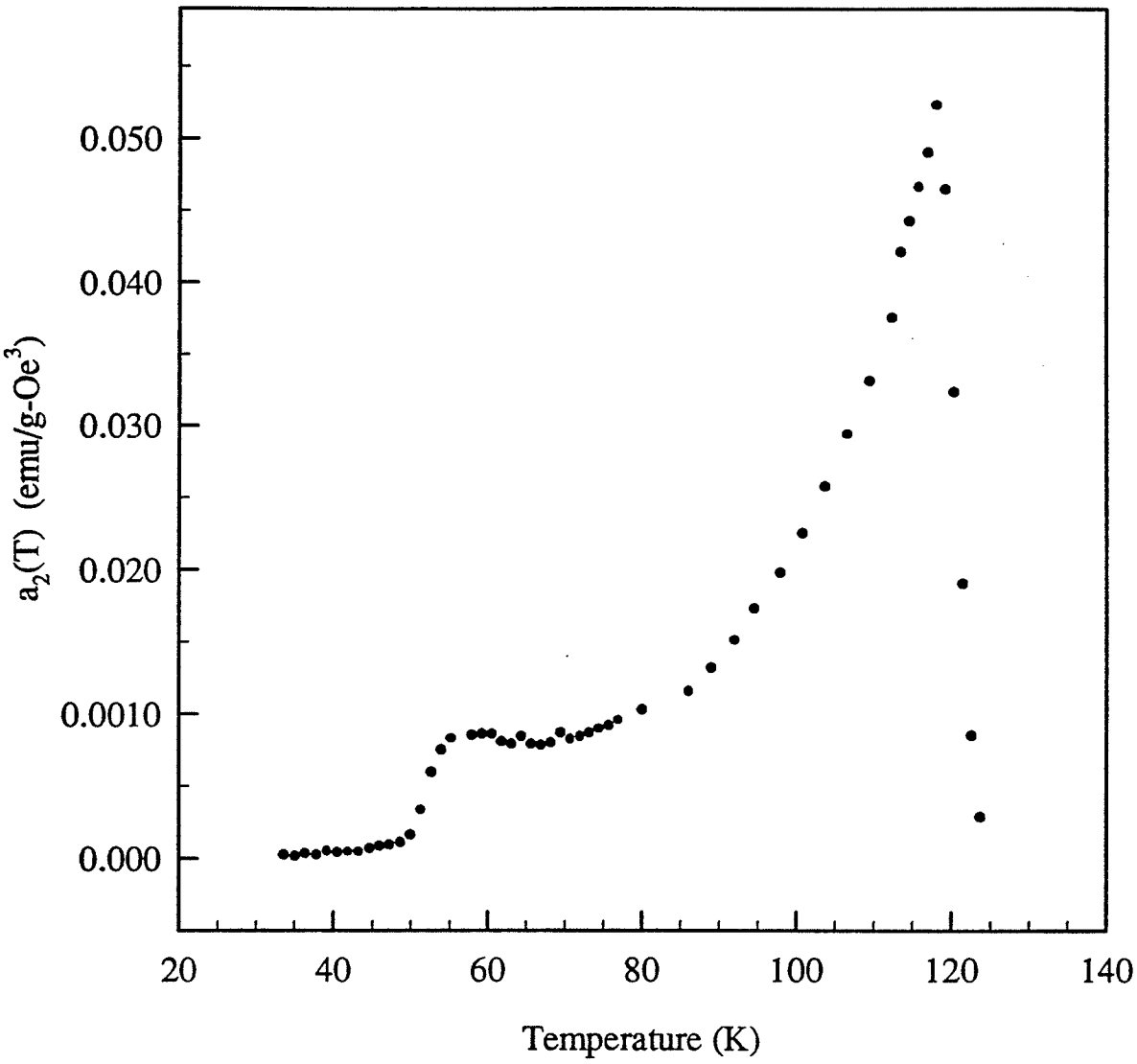

Figure 5.61: Non-linear coefficient, $a_2(T)$ (in emu/g-Oe^3) versus temperature (in K) for the $x = 0.30$ sample (from temperature sweeps).

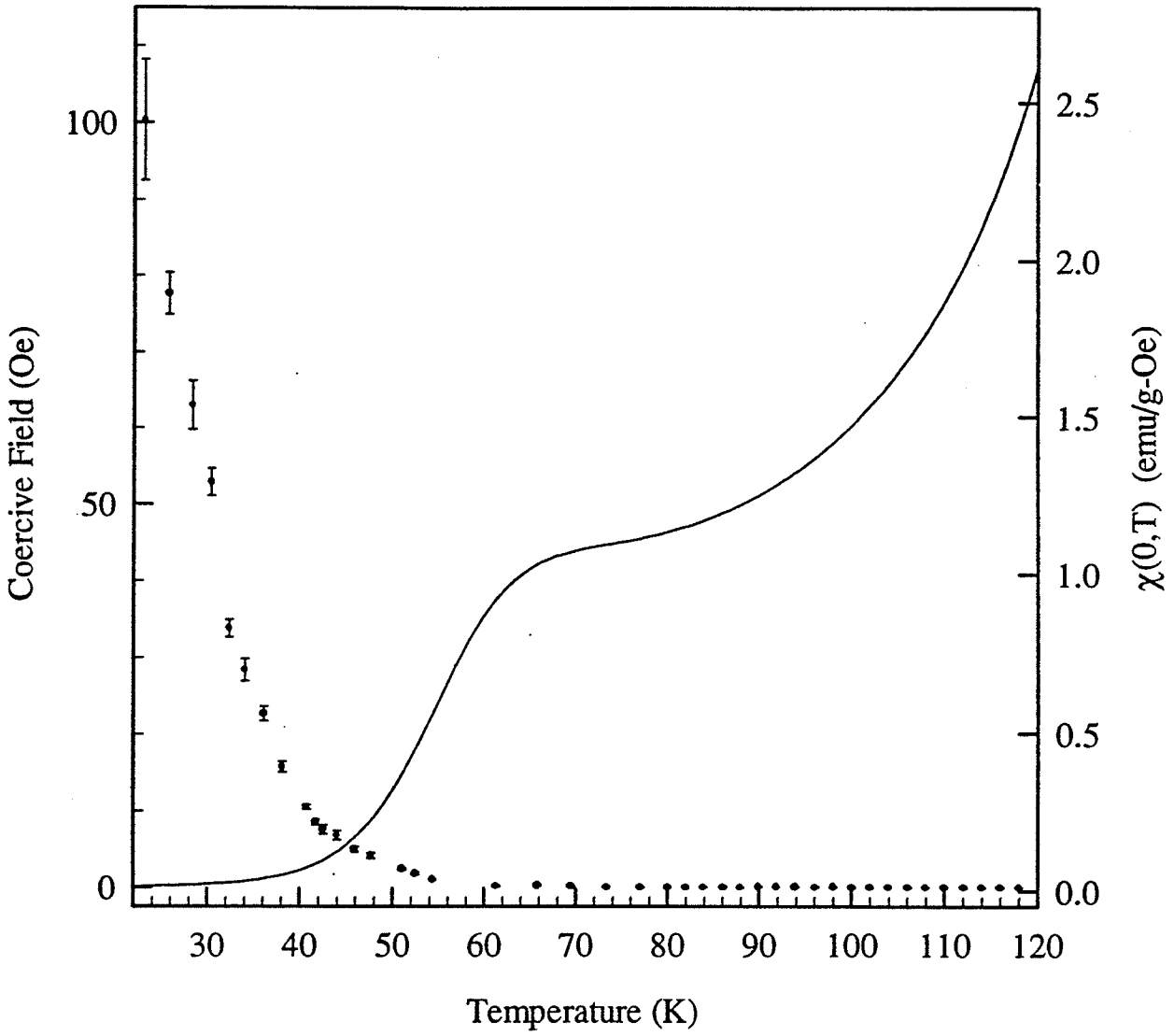

Figure 5.62: Coercive field (in Oe) for the $x = 0.30$ sample plotted versus temperature (in K) (points), along with the zero field a.c. susceptibility $\chi(H,T)$ (in emu/g-Oe) corrected for background and demagnetizing effects plotted versus temperature (in K) (solid line).

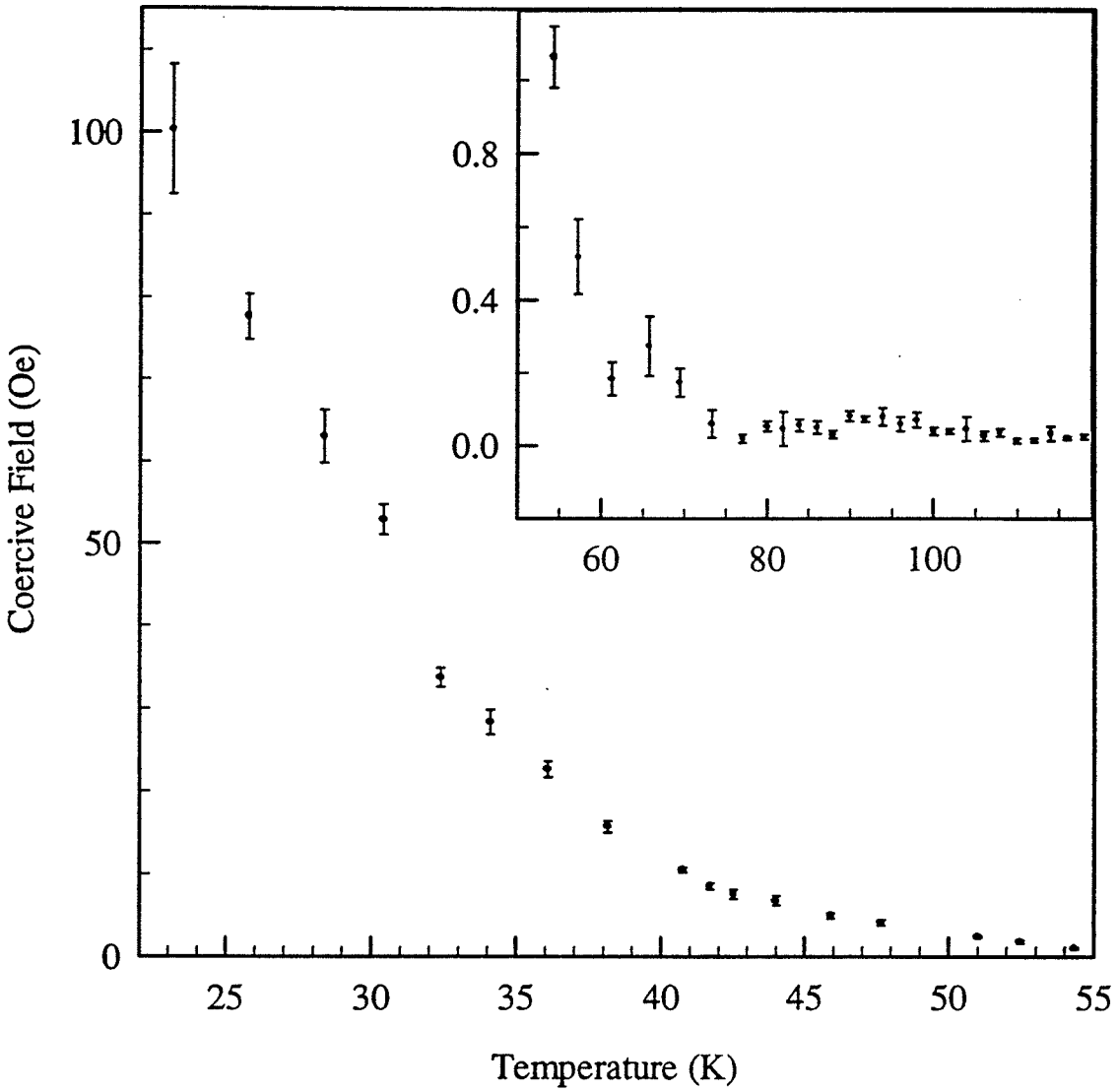

Figure 5.63: Coercive field (in Oe) for the $x = 0.30$ sample plotted versus temperature (in K).

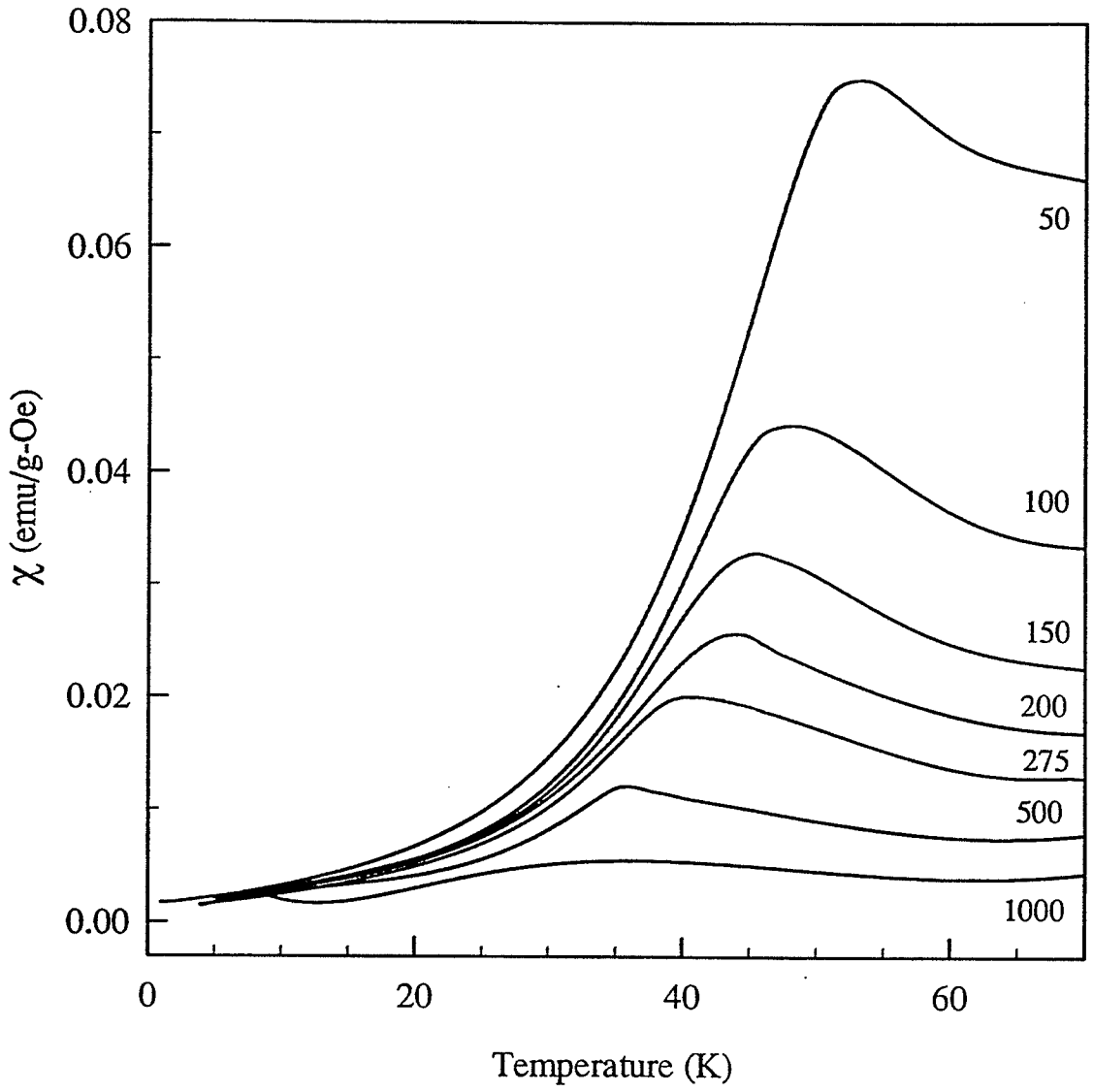

Figure 5.64: The a.c. susceptibility $\chi(H,T)$ (in emu/g-Oe), corrected for background and demagnetizing effects, plotted versus temperature (in K) for the $x = 0.32$ sample. The numbers beside each curve represent the static biasing field (in Oe). Note that the data has been smoothed for clarity of presentation.

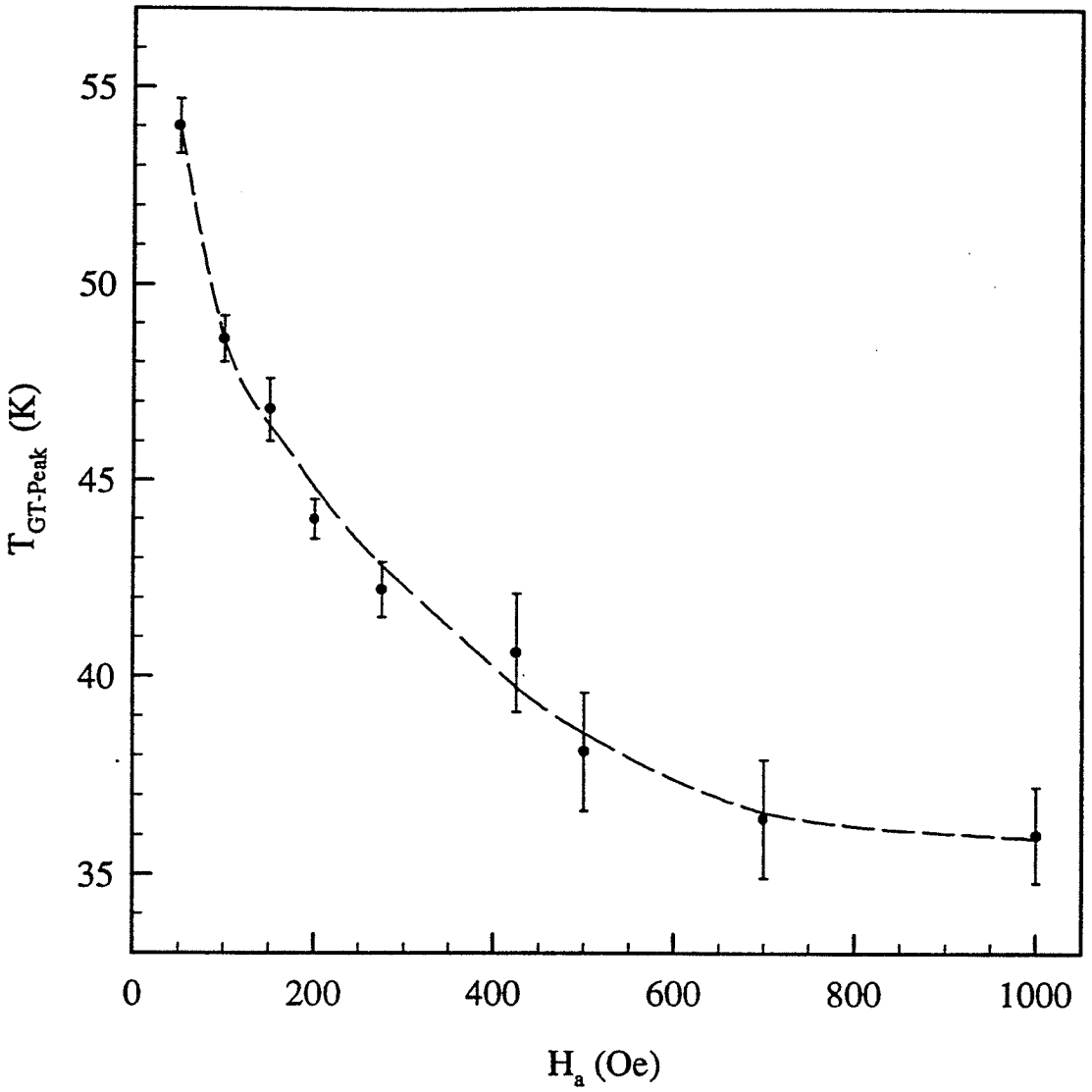

Figure 5.64: The proposed GT transition peak temperature (in K) plotted versus the applied field (in Oe) for the $x = 0.32$ sample.

Proceeding to analyze the behaviour of the non-linear component of the susceptibility, a plot of $a_2(T)$, obtained from field sweeps, versus temperature is shown in Figure 5.66. For this sample, there is a well defined peak in the temperature dependence of $a_2(T)$ in the vicinity of the low temperature drop-off of the zero field susceptibility ($T \approx 56$ K). However, $a_2(T)$ does not show a peak at T_c as is expected and as was the case for all of the previous samples. It was thought at first, that this may simply be due to an error in the thermometry, i.e. the 'anomaly' was simply the ferromagnetic-paramagnetic peak, shifted down in temperature. However, this would require an error in the temperature of about 20 K, which is unreasonably large, and highly unlikely, given our estimated error in the thermometry of ± 0.3 K. The other possibility is that the peak at T_c is simply much smaller than the peak at T_f and is therefore obscured.

An investigation of the $a_2(T)$ coefficients from the temperature sweep data yields a triple peaked structure, as can be seen in Figure 5.67 with the main peak in good agreement with that obtained from field sweeps. This result suggests that the peak in $a_2(T)$ at T_c is simply obscured in the field sweep measurements and the temperature sweep measurements are somewhat more sensitive. The high temperature peak in Figure 5.67 is at about 76 K, compared to $T_c = 78.2 \pm 0.09$ K, also in acceptable agreement. The middle peak is possibly due to the regular contribution to the susceptibility, which reaches a maximum at the Hopkinson peak.

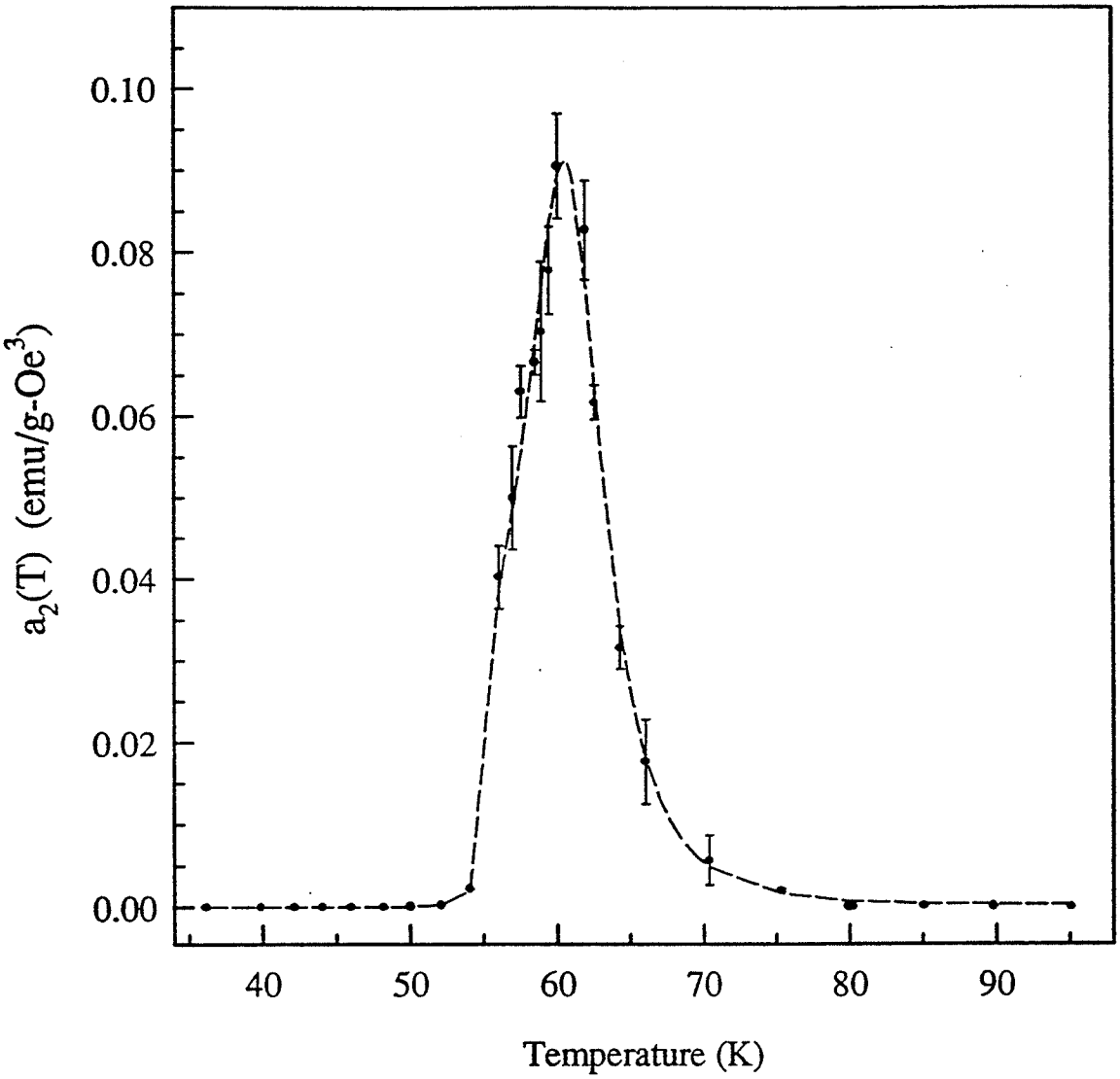

Figure 5.66: Non-linear coefficient, $a_2(T)$ (in emu/g-Oe^3) versus temperature (in K) for the $x = 0.32$ sample (from field sweeps).

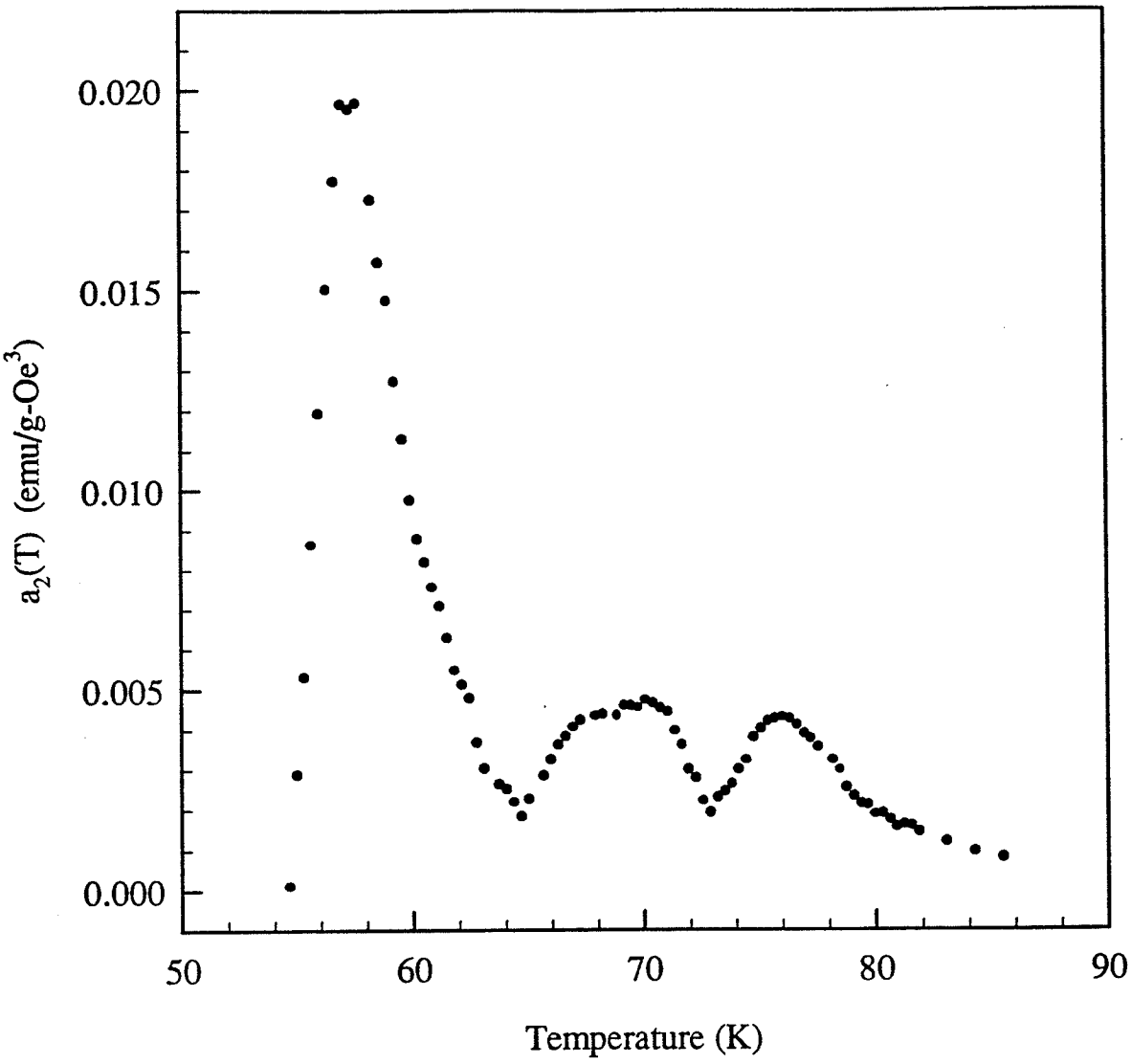

Figure 5.67: Non-linear coefficient, $a_2(T)$ (in emu/g-Oe^3) versus temperature (in K) for the $x = 0.32$ sample (from temperature sweeps).

As with the $x = 0.30$ sample, the coercive field drop does not correlate with the temperature at which the rise in zero field susceptibility is observed, which again suggests that the rise in susceptibility is not caused by the drop in H_c. This can be seen in Figure 5.68, and a more detailed plot of the coercivity can be seen in Figure 5.69.

5.6 Discussion: Re-entrant Transition

There are several factors which would contribute to the lack of success in confirming the presence of a phase transition of the predictions of the mean field vector model concerning the GT and AT transitions. Firstly, the model relies on several assumptions which are not necessarily upheld in physical systems. For instance, infinite-range interactions are assumed for GT behaviour to occur.

Discrepancies between theoretical predictions and experimental results have been reported by other researchers, especially in regards to the prefactor, c (2.68), which has often been found to be an order of magnitude larger than predicted in other systems. It should also be noted that 'c' depends upon the specific system being studied, a factor not incorporated in (2.68). Furthermore, it must be remembered that considerable ambiguity was found in the present results, preventing a conclusive statement from being made concerning possible AT and GT lines. Clearly, improved theories and additional experimental investigation is required before the ferromagnetic to spin

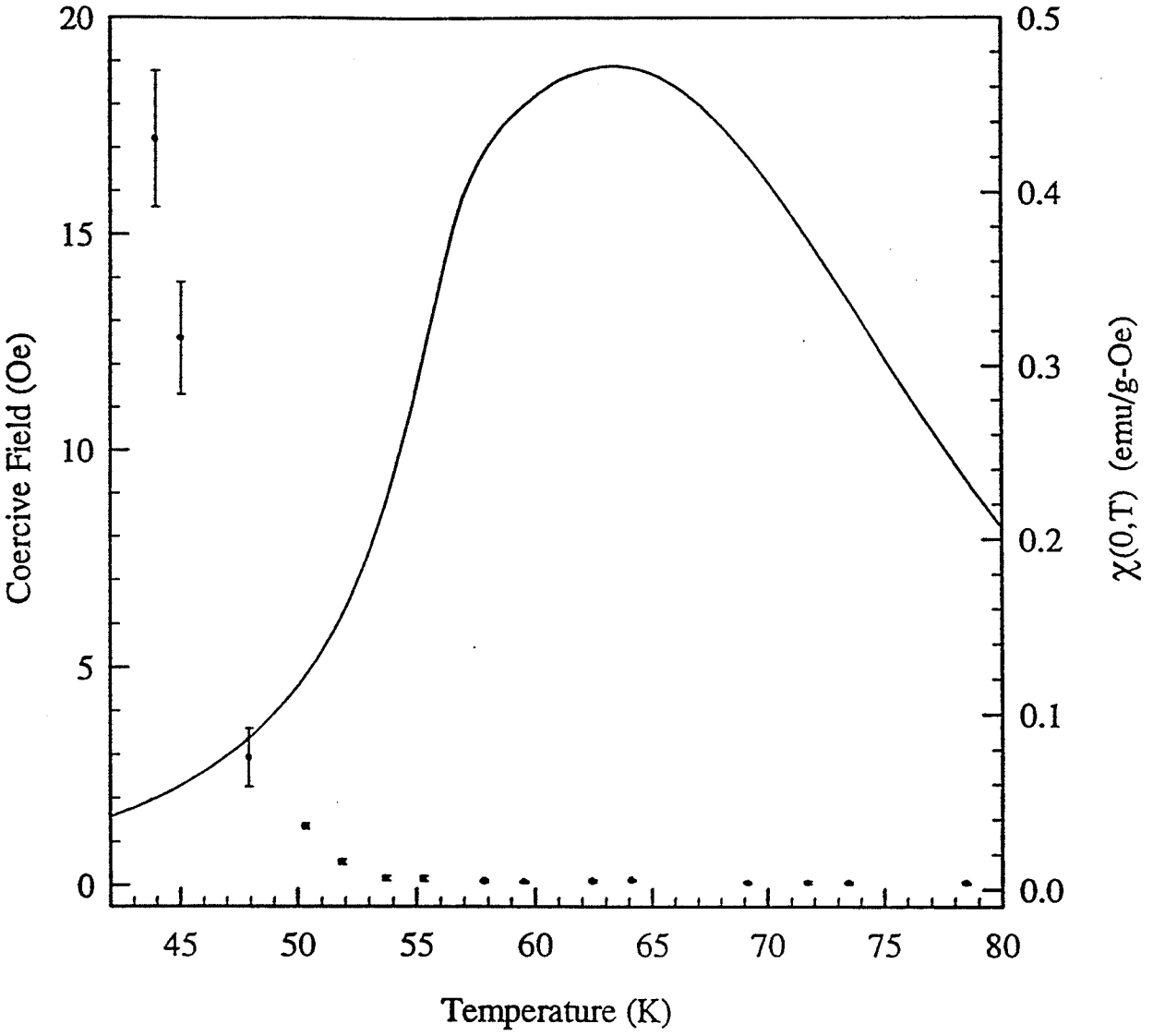

Figure 5.68: Coercive field (in Oe) for the $x = 0.32$ sample plotted versus temperature (in K) (points), along with the zero field a.c. susceptibility $\chi(H,T)$ (in emu/g-Oe) corrected for background and demagnetizing effects plotted versus temperature (in K) (solid line).

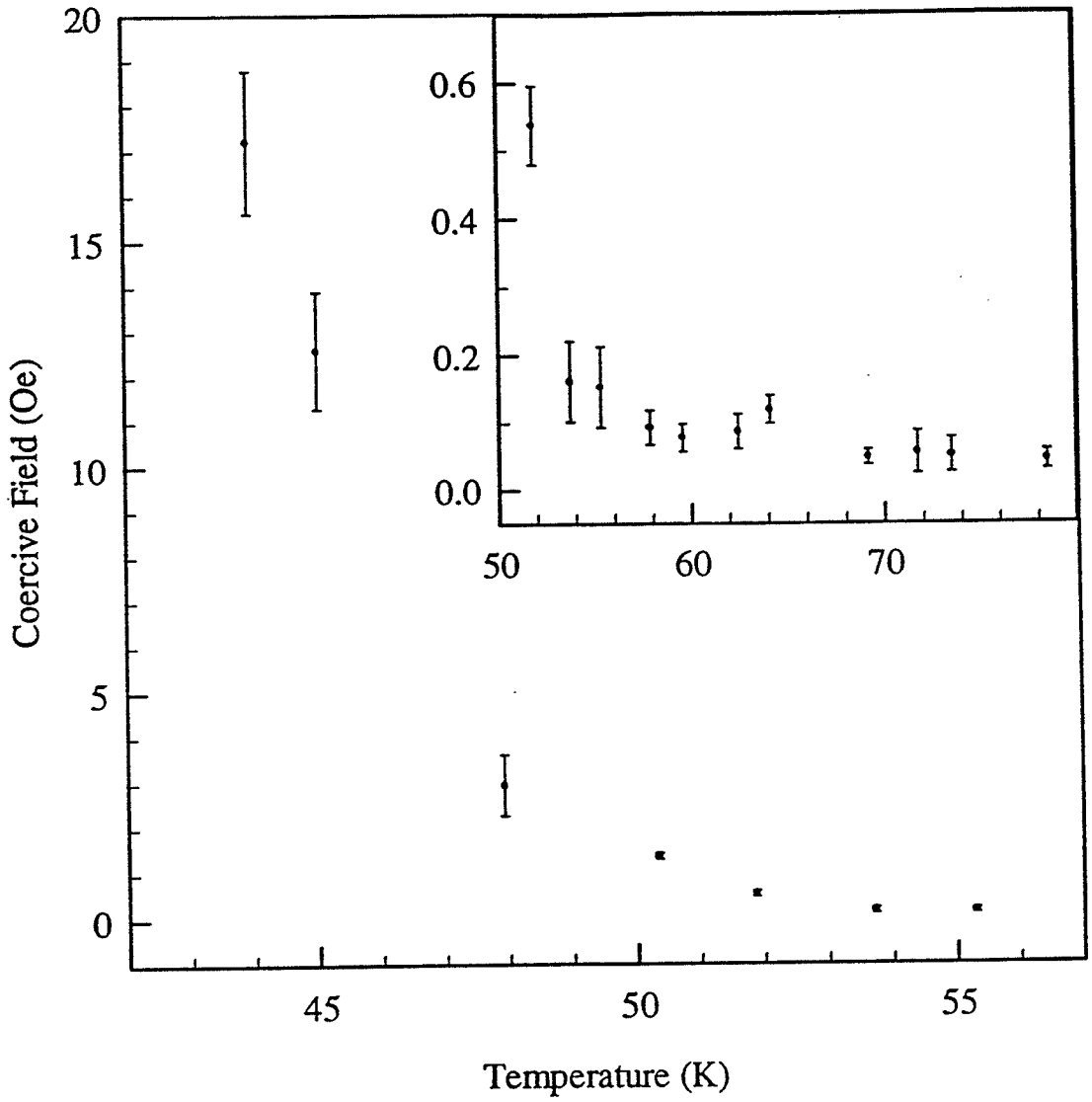

Figure 5.69: Coercive field (in Oe) for the $x = 0.32$ sample plotted versus temperature (in K).

glass transition is understood.

Considering the results of the non-linear analysis; although theory predicts a divergence in $a_2(T)$ at a re-entrant transition, only a small peak is observed experimentally for $x = 0.30$ with a much larger peak for $x = 0.32$. The anomaly observed here, however, is clearly weaker than Ising model predictions, possibly because the transverse spin freezing responsible for the anomaly may be only weakly coupled to the measured longitudinal response. It is also possible that finite frequency measurements are insensitive to the full spectrum of critical fluctuations as the freezing temperature is approached in particular from below (critical slowing down); the use of finite frequency measurements would then underestimate this coefficient close to the freezing temperature. Finally, above the freezing temperature, thermally activated blocking processes such as domain wall motion may obscure the non-linear response. Nevertheless, the measured $a_2(T)$ data does exhibit a distinct anomaly near the vicinity of the drop-off in the zero field susceptibility, and is strong evidence for the existence of a true re-entrant transition for the $x = 0.30$ and 0.32 alloys. No anomaly and therefore no evidence for a re-entrant transition is observed for the $x = 0.23$ and 0.26 alloys.

In light of neutron depolarization measurements by Mirebeau et al, 1990, which indicated that samples in the concentration range, $0.22 < x < 0.26$ were weakly frustrated, with a domain size which did not vary with temperature, even at the lowest temperatures, this evidence would suggest the

absence of a phase transition. On the other hand, the samples $x = 0.30$ and 0.32 were found to be strongly frustrated, with a decreased domain size, implying the presence of a new phase. These data are consistent with the presence of a re-entrant phase transition, thereby supporting the evidence from the non-linear analysis.

5.7 Spin Glass

Finally, one last sample, with a concentration of $x = 0.41$ was investigated. The resulting susceptibility versus temperature plot is illustrated in Figure 5.70, where it can be seen that the susceptibility is now several orders of magnitude smaller than for any of the previous samples. The sharp cusp at about 36 K and low susceptibility ($\chi_{peak} \approx 1.9\text{x}10^{-3}$ emu/g-Oe) are the identifying features for a spin glass, as described in Section 2.3.4, and illustrated in Figure 3.11 for the $x = 0.40$ sample. Geohegan (Table 3.2) found that $T_{SG} = 42$ K for the latter concentration, which seems to be consistent with the value found here, considering the slight differences in composition.

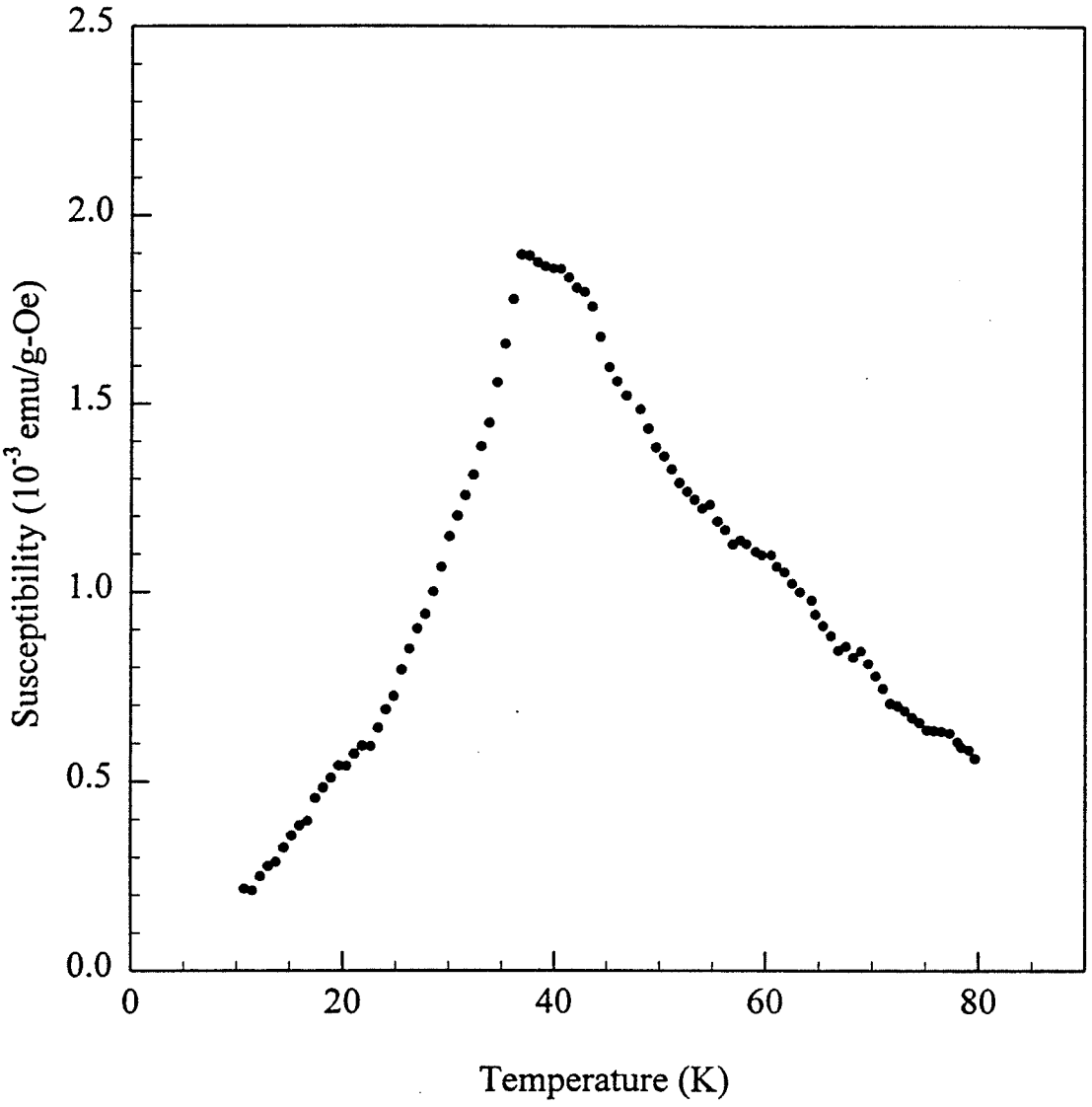

Figure 5.70: The zero field a.c. susceptibility, $\chi(H,T)$ (in emu/g-Oe), corrected for background and demagnetising effects, plotted against temperature (in K) for the x= 0.41 sample.

Chapter 6

Conclusion

The analysis of detailed measurements of the field and temperature dependent susceptibility of a series of $(Fe_{1-x}Mn_x)_{75}P_{16}B_6Al_3$ amorphous alloys confirms the occurrence of a paramagnetic to ferromagnetic phase transition with near Heisenberg model exponents in the vicinity of the critical point for the concentrations $x = 0.235$, 0.26, 0.30 and 0.32. The presence of considerable magnetic disorder becomes apparent away from the critical point. The sample with composition $x = 0.41$ displays the classic behaviour of a spin glass, a susceptibility reduced by several orders of magnitude and a cusp-shaped peak.

The zero field susceptibility for the compositions $x = 0.235$ to 0.32 displays features which are characteristic with re-entrant behaviour; a rapid increase in the susceptibility with decreasing temperature in the vicinity of the paramagnetic to ferromagnetic transition followed by a temperature independent plateau region which is not demagnetizing limited, and finally

an abrupt decrease in the susceptibility at the proposed re-entrant phase transition.

However, the low temperature features fail to satisfy the predictions of mean field vector spin models. The results found from AT and GT analysis proved inconclusive, likely due to unsatisfied assumptions and other limitations of the theory, in particular, its failure to identify specific physical features manifesting the AT and GT transitions. A non-linear analysis of the leading field dependent term in the susceptibility was used to locate the presence of a re-entrant phase boundary. Although the anomalies observed for $x = 0.30$ and 0.32 do not diverge (as predicted by the Ising mean field model but not unlike those observed in other re-entrant systems), this may be due to limitations imposed by the finite frequency at which the measurements were carried out and the complications associated with transverse spin freezing which might couple only weakly to the longitudinal response. Nevertheless, the anomaly is a quite well defined shoulder for the $x = 0.30$ sample, and a strong peak for $x = 0.32$. The behaviour of the non-linear component of the susceptibility, along with previous neutron depolarization results, suggest that the $x = 0.30$ and 0.32 samples are, indeed, re-entrant.

The zero field behaviour of the $x = 0.235$ and 0.26 samples might be interpreted to indicate that these samples are also re-entrant, but the non-linear analysis gives no indication of a low-temperature anomaly, at the very least emphasizing the need for more rigorous analysis techniques in the study

of the ferromagnetic to spin glass transition, as opposed to simple inspection of the zero field behaviour. Indeed, on the basis of the behaviour of $\chi(H,T)$ alone - specifically the presence of a very small, weakly temperature dependent non-linear susceptibility - would suggest that an explanation for the behaviour of these weakly frustrated samples be sought in terms of other processes, possibly thermally activated blocking processes.

Combining the results of all of the present data, a revised phase diagram shown in Figure 6.1 can be constructed. The phase diagram by Mirebeau shown in Figure 3.1, is qualitatively quite similar, but differs in the exact location of the various phase boundaries. The most pronounced difference lies in the location of the FM-SG line, which goes to zero much more abruptly in Figure 6.1 than in Figure 3.1 Clearly small changes in concentration can dramatically alter the magnetic properties of a sample. However, the present phase diagram (Figure 6.1) lacks considerable detail along certain boundaries (dashed lines). Further investigation, with a greater number of samples with appropriate concentrations is needed to complete the phase diagram.

Recalling the variations in the results reported by different investigators, specifically as related to the critical exponents and temperatures, further theoretical development and experimental work is clearly required before the magnetic properties of FeMn are completely understood, especially concerning the low-temperature transition.

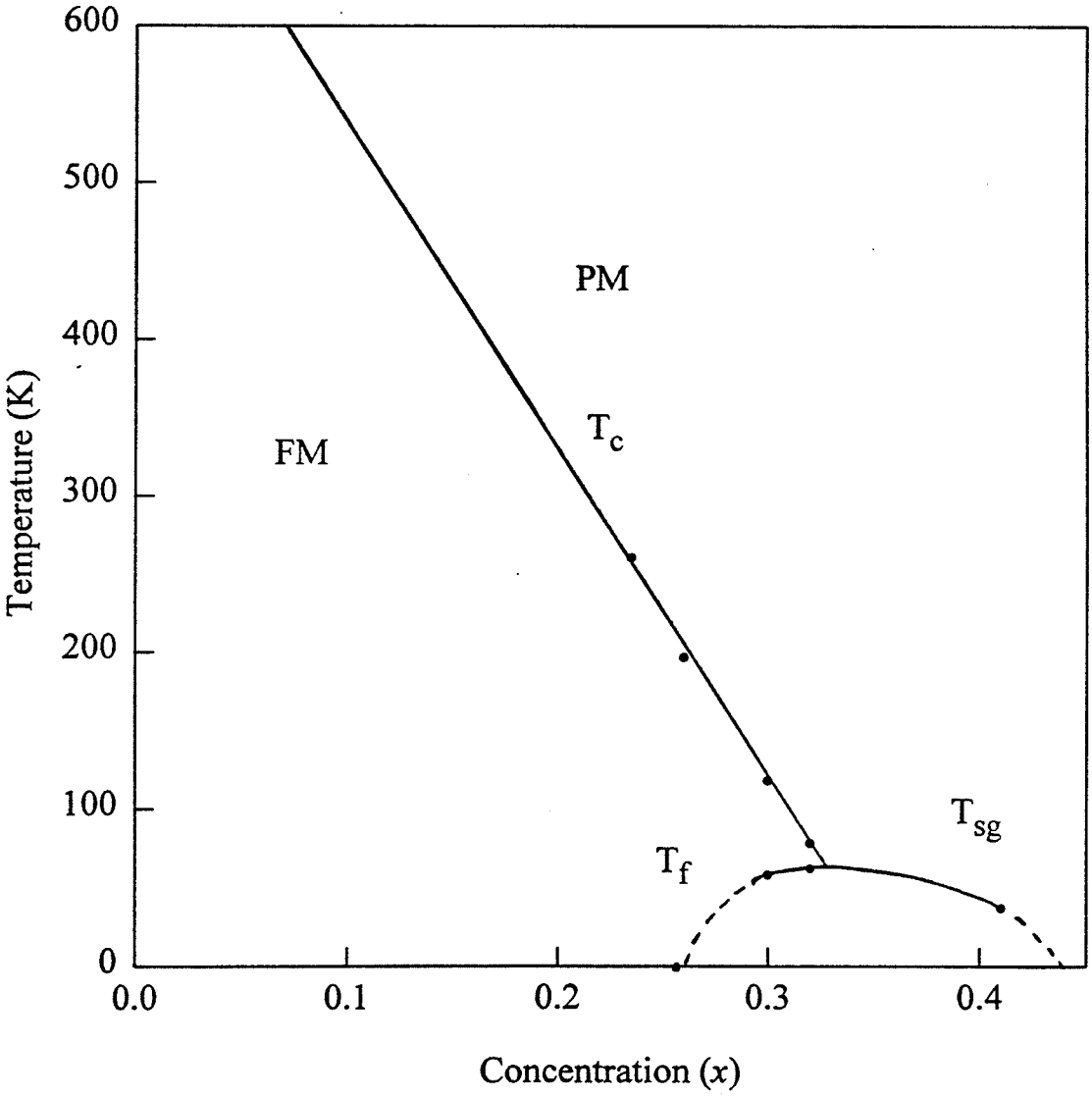

Figure 6.1: Revised FeMn phase diagram.

Appendix

The RKKY (Rudermann, Kittel, Kondo, Yoshida) model is applicable for solids consisting of a dilute solution of magnetic ions in a nonmagnetic host metal. Although the magnetic ions may not be adjacent to each other, they interact via an indirect exchange interaction which is mediated by the conduction electrons in the host material. The spatial dependence of the conduction band polarization near one of the magnetic ions is illustrated below.

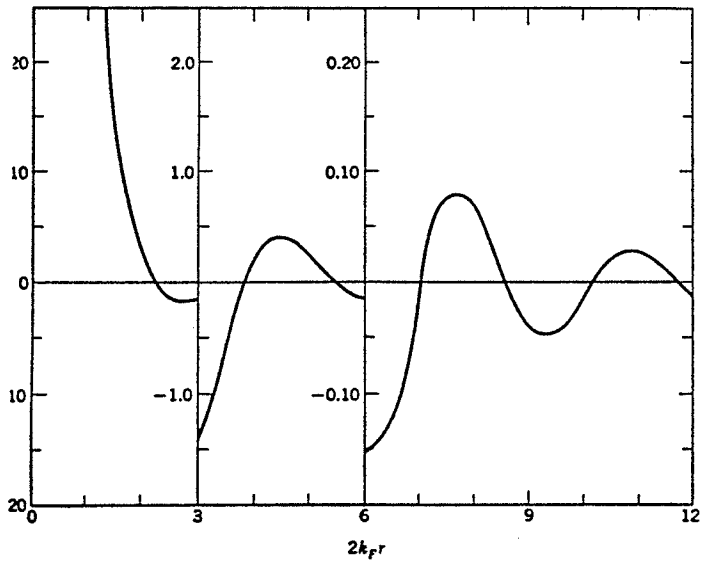

Figure A1: Polarization of a free electron gas in the neighbourhood of a point magnetic moment located at the origin $r = 0$, according to the RKKY theory. The horizontal axis is $2k_F r$, where k_F is the wave vector on the Fermi sphere. (Kittel, 1976)

Konczos, G. and B. Sas, Amorphous Metals, World Scientific, Singapore, 105 (1985).

Kornick, K. R., Master's Thesis, University of Manitoba (1990).

Kornik, K., R. M. Roshko and Gwyn Williams,*J. Mag. Mag. Mat.*, **81**, 323 (1989).

Krebs, H. U. and H. C. Freyhart, Rapidly Quenched Metals, Vol. 1, North Holland Publishing Company, 439 (1984).

I Kunkel, H. P. and Gwyn Williams, *J. Phys. F: Met. Phys.*, **18**, 1271 (1988).

II Kunkel, H. P. and Gwyn Williams, *J. Mag. Mag. Mat.*, **75**, 98 (1988).

III Kunkel, H. P., R. M. Roshko and Gwyn Williams, *Phys. Rev. B*, **37**(10), 5880 (1988).

Kunkel, H. P., R. M. Roshko, W. Ruan and Gwyn Williams, *Phil. Mag.*, **B63**, 1213 (1991).

Ma, Hao, Master's Thesis, University of Manitoba (1990).

Ma, H., H. P. Kunkel and Gwyn Williams, *J. Phys.: Condens. Matter*, **3**, 5563 (1991).

Maartense, I., *Rev. Sci. Instrum.*, **41**, 657 (1970).

Maartense, I., *J. Appl. Phys.*,**53** (3), 2466 (1982).

Manheimer, M. A., S. M. Bhagat and H. S. Chen, *Phys. Rev. B*, **26**, 456 (1982).

Mirebeau, I., S. Itoh, S. Mitsuda, T. Watanabe, Y. Endoh, M. Hennion, R. Papoular, *Phys. Rev. B*, **41**, 405 (1990).

Morrish, A. H., The Physical Principles of Magnetism, John Wiley & Sons, New York, (1965).

Osborn, J. A., *Phys. Rev.*, **67**, 351 (1945).

Patterson, J. D., Introduction to the Theory of Solid State Physics, Addison-Wesley Publishing Company, London (1971).

Pratten, N. A., *J. Mat. Sci.*, **16**, 1737 (1981).

Rhyne, J. J., R. W. Erwin, J. A. Fernandez-Baca and G. E. Fish, *J. Appl. Phys.*, **63**, 4080 (1988).

Roshko, R. M. and Gwyn Williams, *J. Mag. Mag. Mat.*, **50**, 311 (1985).

Ryan, D. H., J. M. D. Coey, E. Batalla, Z. Altoanian and J. O. Strom-Olsen, *Phys. Rev.*, **B35**, 8630 (1987).

Salamon, M. B., K. V. Rao and H. S. Chen, *Phys. Rev. Lett.*, **44**, 596 (1980).

Salamon, M. B., K. V. Rao and H. S. Chen, *J. Appl. Phys.*, **52** (3), 1687 (1981).

Schinkel, C. J. and W. D. Van Amstel, *Phys. Lett.*, 44A, **7**, 467 (1973).

Sherrington, D. and S. Kirkpatrick, *Phys. Rev. Lett.*, **B5**, 1792 (1975).

Southern, B. W., *J. Phys. C*, **9**, 4011 (1976).

Stanley H. E., Introduction to Phase Transitions and Critical Phenomena, Clarendon Press, Oxford (1971).

Verbeck, B. H., G. J. Nieuwenhuys, H. Stocker and S. A. Mydosh, *Phys. Rev. Lett.*, **40**, 586 (1978).

Wang, D., Master's Thesis, University of Manitoba (1993).

Wang, D., H. P. Kunkel and Gwyn Williams, *Phys. Rev. B*, **51** (5), 2872 (1995).

Wang, Z., Ph.D. Thesis, University of Manitoba (1990).

Wang, Z., H. P. Kunkel and G. Williams, *J. Phys.: Condens. Matter*, **4**, 10385 (1992).

Weiss, P., *J. Phys.*, **6**, 667 (1907).

White, R. M., Quantum Theory of Magnetism, McGraw-Hill Book Company, New York (1970).

Williams, G., *AC Susceptibility of Dilute Magnetic Systems*, Plenum Press, New York (1991).

Yeshurun, Y., M. B. Salamon, K. V. Rao, H. S. Chen, *Phys. Rev. B*, **24**, 1536 (1981).

Zallen, R., The Physics of Amorphous Solids, John Wiley & Sons, New York (1983).